



**STRUCTURE AND DYNAMICS OF HIGH  
LATITUDE MAGNETOSPHERIC BOUNDARIES**

*HUI ZHANG*

Dissertation submitted in partial fulfillment  
of the requirements for the degree of  
Doctor of Philosophy

**BOSTON  
UNIVERSITY**

BOSTON UNIVERSITY  
GRADUATE SCHOOL OF ARTS AND SCIENCE

Dissertation

**STRUCTURE AND DYNAMICS OF HIGH LATITUDE  
MAGNETOSPHERIC BOUNDARIES**

by

**HUI ZHANG**

M. A., Boston University, 2004

Submitted in partial fulfillment of the  
requirements for the degree of  
Doctor of Philosophy

2008

© Copyright by  
HUI ZHANG  
2007

Approved by

First Reader

---

Theodore A. Fritz, PhD  
Professor of Astronomy, Professor of Electrical and  
Computer Engineering  
Boston University

Second Reader

---

Harlan E. Spence, PhD  
Professor of Astronomy  
Boston University

Third Reader

---

Terrance G. Onsager, PhD  
Physicist  
NOAA Space Environment Center

## Acknowledgments

I am grateful to my advisor, Professor Theodore A. Fritz, who has been very supportive and helpful to this dissertation and my research in the past five years. Thanks for offering me a research assistant position, so that I was able to study at Boston University. Thanks for sending me to 20 conferences and workshops, from which I benefited a lot in the past five years. I am thankful for everything he has done for me to get to this point. He is a great mentor and friend. I feel very lucky to have him as my advisor.

I would like to give my special thanks to Professor Q.-G. Zong who has guided me through my research. Without his guidance and push, I could not have finished my Ph.D program in five years. Thanks for teaching me how to do research and write a research paper.

Thanks to Professor Alan Marscher, Dr. Terrance G. Onsager, Professor George L. Siscoe, and Professor Harlan E. Spence for serving in my dissertation committee along with my advisor. I am thankful for their valuable comments and suggestions to make this dissertation better.

I would also like to thank Professor W. Jeffrey Hughes, Professor Michael Mendillo, Professor Meers Oppenheim, Professor John Clarke, Professor James Jackson, and Professor Kenneth Janes for their great job in teaching very useful space physics and astronomy courses. I learned not only facts but also problem-solving skills, which is very useful in research. Thanks to Professor Nancy Crooker, Professor Charles Goodrich, and Professor Supriya Chakrabarti for their comments and support.

Thanks to Professor Bengt U. Ö. Sonnerup, Professor Malcolm W. Dunlop, Professor V. M. Vasyliunas, Yan Song, Naiguo Lin, David Sibeck, Yongli Wang, Guan Le, Meiqing Folk, Professor Xinlin Li, Shengwu Chang, Quanqi Shi, Xuzhi Zhou, Xianguo Zhang, Jue Wang, Jichun Zhang, Benoit Lavraud, Matt Taylor, Yulia V. Bogdanova, D. R. Weimer, Melissa Longmore, Aaron Ridley, and Homa Karimabadi for helpful discussions.

My gratitude goes to Professor Zuyin Pu, Professor Chuanyi Tu, Professor Zuo Xiao,

Professor Suiyan Fu, Associate Professor Xie, Lun at Peking Univeristy, China, from whom I first got knowledge about space physics which made me well-prepared for my graduate study. Their recommendations made it possible for me to pursue my degree at Boston University. They have also given me a lot of support and encouragement during my graduate study.

Thanks to my friends at BU, Chia-Lin Huang (Elly), Katherine Garcia, Cara Battersby, April Pinnick, Elizabeth Bass, Christina Prested, Pin (Penny) Wu, Sarah McGregor, Suwicha Wannawichian, Monica Young, Carol Carveth, Nicholeen Viall, Charlotte Wong, Francesca D’Arcangelo, Jonathan Niehof, Nicholas Lee, Joshua Wing, Christopher Mendillo, Majd Matta, Luke Moore, Andrew Jordan, Susanna Finn, Anthony Case, Carlos Martinis, Jody Wilson, Sonya Sherman, Susanna Lamey and Erin Buck. Thanks for your help and support during my graduate study, especially during the hardest time before my dissertation defence.

I would also like to thank my friends Xiaona Chen, Congxian Jia, Yunhui Lv, Xinlei Wu, Guoqing Lin, Li Gao, Jinling Dong, Liang Zhao, Zhixia Shen, Jing Zhang, Linghua Wang, Yajing Liu, Xia Cai, Zhao Chen, Dan Ruan, Huanwen Cao, Tianmeng Zhang, Wei Tang, Hui Zhang, Hao Yang and many more, your friendship has made my life happier.

Finally, I would like thank my parents and my sister for their endless love, understanding and support.



the magnetopause adjacent to the cusp is associated with sharp changes in plasma density, velocity, temperature and magnetic field. However, this interface becomes uncertain when the IMF turns southward. A superposed epoch analysis was applied to study the average variations of key plasma parameters across the magnetopause under different conditions for the first time. This dissertation reports the first in-situ observation of collisionless Hall reconnection at the high latitude magnetopause when the IMF  $B_y$  dominates. Finally, this dissertation compares observations to MHD simulations for a real cusp event. Although the simulated magnetospheres are smaller than the real magnetosphere, the simulated magnetic fields and the amplitude of the model-derived plasma parameters of density, velocity and temperature in the cusp region agree reasonably well with observations. The MHD code qualitatively simulated the responses of the cusp position to the solar wind azimuthal flow for the first time and the formation of the cold dense plasma sheet.

# Contents

<b>1</b>	<b>Introduction to the Earth's Outer Magnetospheric Boundaries</b>	<b>1</b>
1.1	MHD Discontinuities . . . . .	1
1.2	The Magnetopause . . . . .	4
1.2.1	Historical Review . . . . .	4
1.2.2	Magnetopause Shape and Position . . . . .	9
1.2.3	Magnetopause Structure . . . . .	14
1.2.4	Magnetic Reconnection at the Magnetopause . . . . .	15
1.2.5	Other Plasma Transport Mechanisms . . . . .	32
1.3	Magnetospheric Cusp . . . . .	36
1.4	Mantle . . . . .	37
1.5	Entry Layer . . . . .	38
1.6	Low Latitude Boundary Layer . . . . .	39
1.7	Goals of This Dissertation . . . . .	41
<b>2</b>	<b>Instrumentation</b>	<b>43</b>
2.1	Cluster Spacecraft . . . . .	43
2.2	Instruments onboard Cluster . . . . .	45
2.2.1	RAPID . . . . .	46
2.2.2	CIS . . . . .	49
2.2.3	PEACE . . . . .	51
2.2.4	FGM . . . . .	51
2.2.5	EFW . . . . .	51

<b>3</b>	<b>Methods</b>	<b>54</b>
3.1	Minimum Variance Analysis . . . . .	54
3.2	Multi-Spacecraft Timing Technique . . . . .	57
3.3	Walén Test . . . . .	57
3.3.1	HT frame . . . . .	58
3.3.2	Walén Test in HT frame . . . . .	59
3.4	Curlometer Technique . . . . .	60
<b>4</b>	<b>Magnetospheric Cusp</b>	<b>62</b>
4.1	Introduction . . . . .	62
4.2	Stagnant Exterior Cusp (SEC) Identification and its General Properties . .	68
4.3	Statistical SEC Position . . . . .	70
4.4	Presence of Energetic Particles . . . . .	72
4.5	Solar Wind Dependency of the Spectrum . . . . .	72
4.6	Turbulence in the Cusp Region Depends on the Magnetic Shear Angle . . .	75
4.7	Multiple Cusps: Temporal or Spatial Effect? . . . . .	79
4.7.1	Introduction . . . . .	79
4.7.2	Multiple Cusps under Variable IMF Conditions . . . . .	82
4.8	Conclusions . . . . .	88
<b>5</b>	<b>High Latitude Magnetopause</b>	<b>90</b>
5.1	Introduction . . . . .	90
5.2	Boundary and Clock Angle of the IMF . . . . .	95
5.3	Average Structure of the Magnetopause . . . . .	100
5.4	Under Extreme Solar Wind Conditions . . . . .	102
5.4.1	Quiet Time Vs. Extreme Storm Time . . . . .	102
5.4.2	High Solar Wind Density Vs. Low Solar Wind Density . . . . .	104
5.5	Geometry . . . . .	107
5.5.1	Case Events . . . . .	108

5.5.2	Crossing Survey . . . . .	111
5.6	Reconnection at Magnetopause . . . . .	114
5.7	Magnetopause Thickness . . . . .	126
5.8	Discussion and Conclusions . . . . .	126
<b>6</b>	<b>Comparison with MHD Simulations</b>	<b>131</b>
6.1	Introduction to Global MHD Simulation . . . . .	131
6.2	Comparison of Observation and MHD Simulation for a Multiple Cusp Event	132
6.2.1	General Properties . . . . .	132
6.2.2	Responses of Cusp Position to the Solar Wind . . . . .	134
6.2.3	Formation of the Cold Dense Plasma Sheet . . . . .	137
6.3	Discussion and Conclusions . . . . .	139
<b>7</b>	<b>Conclusions and Future Work</b>	<b>143</b>
7.1	Conclusions . . . . .	143
7.2	Future Work . . . . .	148
	<b>References</b>	<b>151</b>
	<b>Curriculum Vitae</b>	<b>165</b>

## List of Tables

1.1	Discontinuities in Ideal MHD (from Kivelson and Russell [1995]) . . . . .	4
2.1	Instruments onboard Cluster . . . . .	16
2.2	Characteristic parameters of the IIMS and IES sensor systems . . . . .	19
4.1	Cusp- Dayside Magnetosphere Interface Crossing . . . . .	57
5.1	Events prefer $B_y$ reconnection . . . . .	98

## List of Figures

1-1	The sketch shows the magnetic field of a dipole in the presence of an infinitely conducting plane. . . . .	5
1-2	The sketch shows the formation of the Chapman-Ferraro cavity [ <i>Chapman and Ferraro</i> , 1931]. . . . .	6
1-3	A perspective view of the northern portion of the Chapman-Ferraro current system, as seen from above the ecliptic plane. . . . .	7
1-4	A simple magnetopause current model proposed by <i>Ferraro</i> [1952]. . . . .	8
1-5	The earliest report of the subsolar magnetopause crossing taken by Explorer 12 on September 30, 1961. (from <i>Cahill and Amazeen</i> [1963]) . . . . .	10
1-6	The magnetic reconnection model of the magnetosphere for southward (top) and northward (bottom) IMF. (after <i>Dungey</i> [1961, 1963]) . . . . .	11
1-7	The pressure balance at the magnetopause. [after <i>Otto</i> , 2002] . . . . .	13
1-8	ISEE-1 observations of a magnetopause crossing on November 1, 1978 when the IMF is strongly northward. [ <i>Song et al.</i> , 1990] . . . . .	16
1-9	Illustration of the boundary normal coordinate system. [ <i>Russell and Elphic</i> , 1979] . . . . .	17
1-10	ISEE-1 observations of a subsolar magnetopause crossing on November 25, 1978 when the IMF is southward. [ <i>Song et al.</i> , 1993] . . . . .	18
1-11	Schematic of Sweet-Parker reconnection model [ <i>Parker</i> , 1957; <i>Sweet</i> , 1958].	19
1-12	Schematic of Petschek's reconnection model [ <i>Petschek</i> , 1964] with diffusion region indicated by the shaded rectangle. . . . .	20
1-13	Schematic of the multiscale structure of the dissipation region when the Hall term is important. (after <i>Oieroset et al.</i> [2001]) . . . . .	25

1-14	Schematic of the multiscale structure of the dissipation region when kinetic Alfvén waves play the role (the electron pressure is important). (after <i>Drake and Shay</i> [2007]) . . . . .	26
1-15	An example of the magnetopause as an rotational discontinuity. [ <i>Russell et al.</i> , 1990] . . . . .	28
1-16	Sketch of the reconnection region at the dayside magnetopause. (from <i>Gosling et al.</i> [1990]) . . . . .	30
1-17	ISEE-1 observations of He <sup>+</sup> and He <sup>2+</sup> distributions in the magnetosheath and magnetosheath boundary layer. (from <i>Fuselier</i> [1995]) . . . . .	31
1-18	A typical FTE observed by ISEE spacecraft. This figure is from <i>Russell and Elphic</i> [1978]. . . . .	33
1-19	Schematic of the Russell and Elphic model of FTEs [ <i>Russell and Elphic</i> , 1978].	33
1-20	Three-dimensional cutaway view of Earth's magnetosphere, showing signatures of Kelvin-Helmholtz (KH) vortices. (from <i>Hasegawa et al.</i> [2004]) . . .	34
1-21	Illustration of the magnetospheric boundary layers. (This figure is from <a href="http://www.oulu.fi/spaceweb/textbook/blayer.html">http://www.oulu.fi/spaceweb/textbook/blayer.html</a> .) . . . . .	37
1-22	Illustration of the formation of the mantle. ( <i>Paschmann</i> [1979]) . . . . .	38
1-23	Illustration of dual lobe reconnection model [ <i>Song and Russell</i> , 1992] for the formation of the low latitude boundary layer during periods of northward IMF. . . . .	40
2-1	Cluster orbit with the apogee at the day side during the northern hemisphere winter season every year. This figure is from ESA. . . . .	44
2-2	Cluster orbit with the apogee at the night side during the northern hemisphere summer season every year. This figure is from ESA. . . . .	44
2-3	The separation between four spacecraft during the Cluster mission. This figure is from ESA. . . . .	45

2-4	(a) A photograph of the RAPID instrument. (b) The cross section of one of the three ion sensors. (c) The complete set of azimuthal angles are covered as the spacecraft rotates. (d) Illustration of the complete $4\pi$ steradian sphere coverage. This figure is from <i>Wilken and Zong</i> [2001]. . . . .	48
2-5	The cross section of the IES head. This figure is from <i>Wilken et al.</i> [1997].	50
2-6	Energy range covered by RAPID, CIS and PEACE instruments onboard Cluster spacecraft. This figure is from <i>Wilken and Zong</i> [2001]. . . . .	52
3-1	Projection onto the the $xy$ plane of three $\mathbf{B}$ vectors measured during a spacecraft crossing of a 1-D current layer. . . . .	55
3-2	Walén test for two magnetopause crossings by the AMPTE/IRM spacecraft. This figure is from <i>Sonnerup et al.</i> [1990]. . . . .	60
4-1	An overview of RAPID, CIS, FGM and ACE data from 08:00 to 11:00 on Mar.4, 2002. . . . .	69
4-2	Cluster orbit from Jan.1, to Apr.30, 2001 and from Mar.1, to Apr.30, 2002 plotted in the GSM coordinate system. . . . .	71
4-3	The SEC extends from 7 to 14 MLT. . . . .	73
4-4	a) The proton spectra for the SEC events with extreme solar wind velocities (either $> 600\text{km/s}$ or $< 300\text{km/s}$ ). b) The power law spectral slopes for the energetic $H^+$ versus the solar wind velocity. c) Proton flux at 30 keV versus the solar wind velocity. . . . .	74
4-5	A) The proton spectra for the SEC events with extreme IMF $B_z$ and moderate solar wind velocities (between 350 km/s and 450 km/s). B) The power law spectral index $\gamma$ for all the SEC events identified versus the Dst index. C) The power law spectral index $\gamma$ for all the SEC events identified versus the turbulence of the magnetic field. D) The power law spectral index $\gamma$ for all the SEC events identified versus the magnetic shear angle. . . . .	76

4-6	The relationship between the turbulence of the magnetic field in the SEC and the magnetic shear angle. . . . .	78
4-7	An overview plot of the triple cusp event (from 16:00 to 19:00 UT, April 18, 2002). (from <i>Zong et al.</i> [2004a]) . . . . .	80
4-8	Panels 1-7: An overview plot of the multiple cusp event observed by Cluster C1. Panels 8-12: Zoom in view of the later three cusps. (from <i>Zong et al.</i> [2007]) . . . . .	81
4-9	Plasma density from Cluster C1 together with the time-shifted solar wind dynamic pressure, density, velocity $V_x$ component, eastward/westward flow and the IMF observed by the WIND spacecraft. (from <i>Zong et al.</i> [2007]) .	83
4-10	Cluster trajectory in GSM coordinates from 00:00 UT to 04:00 UT, March 2, 2002. . . . .	84
4-11	An overview plot of the multiple cusp event observed by Cluster C4 from 0000UT to 0400UT on March 2, 2002. . . . .	85
4-12	The spacecraft potential measured by EFW instrument [ <i>Gustafsson et al.</i> , 1997] onboard Cluster for boundary crossings 1 and 2 shown in Figure 4-11. . . . .	87
5-1	Schematic illustration of the high latitude boundaries viewed from dusk direction. . . . .	93
5-2	Cluster observation of the magnetopause crossing from the HLTR to the magnetosheath on March 2, 2002. . . . .	97
5-3	Examples for clear and unclear boundary between the cusp region and the magnetosheath. . . . .	98
5-4	The IMF clock angle dependence of the boundary between the magnetosheath and cusp. . . . .	99
5-5	Superposed epoch analysis of the energetic particle flux, the plasma temperature, density, and velocity change (a) from cusp region (41 crossings) (b) from HLTR (18 crossings) across the magnetopause in northern hemisphere. . . . .	101

5-6	Superposed epoch analysis of the energetic particle flux, the plasma temperature, density, and velocity change from cusp region across the magnetopause (a) under northward IMF (17 crossings)(b) during extreme storm time (Dst < -100nT) (5 crossings). . . . .	103
5-7	Superposed epoch analysis of the energetic particle flux, the plasma temperature, density, and velocity change from the cusp region across the magnetopause under northward IMF when solar wind density is low ( $n < 5$ p/cc). . . . .	105
5-8	Superposed epoch analysis of the energetic particle flux, the plasma temperature, density, and velocity change from the cusp region across the magnetopause under southward IMF a) when solar wind density is high ( $n > 40$ p/cc). b) when solar wind density is low ( $n < 5$ p/cc). . . . .	106
5-9	An overview of Cluster Ion Spectrometer (CIS), Fluxgate Magnetometer (FGM), and Advanced Composition Explorer (ACE) data from 0800 to 1100 UT on 4 March 2002. . . . .	109
5-10	a) The geometry of the boundaries surrounding the cusp in the northern hemisphere deduced from a few crossings. b) The geometry of the boundaries in the southern hemisphere deduced from a few crossings. . . . .	110
5-11	a) Normal directions for the interface between cusp and magnetosheath in the X-Z plane in the GSM coordinate system. b) Normal directions for the interface between HLTR and magnetosheath in the X-Z plane in the GSM coordinate system. . . . .	112
5-12	This figure shows the same crossing sets as those in Figure 5-11, but in the GSM-XY plane, where a) gives normal directions for the Cusp/magnetosheath interface and b) gives normal directions for the HLTR/magnetosheath boundary. . . . .	113
5-13	Cluster orbit on Mar. 23, 2002 plotted in the GSM coordinate system together with magnetic field vectors. . . . .	116

5-14	An overview of Cluster Ion Spectrometer (CIS), Fluxgate Magnetometer (FGM) and Research with Adaptive Particle Imaging Detectors (RAPID) data from 1000 to 1300 UT on 23 March 2002. . . . .	117
5-15	The magnetic field data obtained from the ACE (interplanetary magnetic field, IMF) and Cluster spacecraft. . . . .	118
5-16	The detailed view of the magnetopause crossing (from 1133UT to 1145 UT, 12 minutes time interval). . . . .	120
5-17	The pitch angles of electrons with different energies. . . . .	121
5-18	The geometry of the reconnection region. It is viewed from $x$ direction. . .	123
5-19	The magnetic field data projected in a local coordinate system where $L$ , $M$ and $N$ are the maximum, medium and minimum variance directions respectively. . . . .	124
5-20	High resolution magnetic field data in GSE coordinate system from all 4 spacecraft. . . . .	125
6-1	Comparison of Cluster C1 observation (black), outputs from the Open GGCM (red) and BATSRUS (blue) codes at CCMC ( <a href="http://ccmc.gsfc.nasa.gov/">http://ccmc.gsfc.nasa.gov/</a> ), run numbers Hui.Zhang_050707_1a and Hui.Zhang_051707_2 respectively. .	133
6-2	Contours in $xy$ plane of the thermal pressure at the time Cluster crossed the magnetopause at 0248UT. . . . .	135
6-3	Response of the simulated cusp position to the solar wind azimuthal flow.	136
6-4	Geotail observations of the cold dense plasma population at the duskside tail-flank. (from [Zong <i>et al.</i> , 2007]) . . . . .	138
6-5	BATRUS simulation of the formation of the cold dense plasma sheet. . . .	139
6-6	The plasma density, temperature and flow $V_x$ component derived by BATRUS along the straight line which connecting two points $(-7, -30, 2)$ GSM $R_E$ and $(-7, 30, 2)$ GSM $R_E$ . . . . .	140

6.7	The profile of the magnetosphere in $xz$ -plane as seen in contours of plasma pressure at 0248UT when Cluster crossed the magnetopause at (7.3, 1.0, 8.9) GSE ((7.3, -3.4, 8.3) $R_E$ in GSM). . . . .	141
-----	--	-----

## List of Abbreviations

ACE	.....	Advanced Composition Explorer
amu	.....	atomic mass unit
ASPOC	.....	Active spacecraft potential control
BATSRUS	.....	Block-Adaptive-Tree-Solarwind-Roe-Upwind-Scheme
BMXR	.....	Bursty Multiple X-Line Reconnection
CCMC	.....	Community Coordinated Modelling Center
CIS	.....	Cluster Ion Spectrometer
CODIF	.....	COmposition and DIstribution Function analyser
CTIM	.....	Couple Thermosphere Ionosphere Model
DA	.....	Discontinuity Analyzer
DWP	.....	Digital wave processing experiment
EDI	.....	Electron drift instrument
EFW	.....	Electric field and wave experiment
FGM	.....	Fluxgate Magnetometer
FTEs	.....	Flux Transfer Events
GSE	.....	Geocentric Solar Ecliptic
GSM	.....	Geocentric Solar Magnetospheric
HCS	.....	Heliospheric Current Sheet
HIA	.....	Hot Ion Analyser
HLTR	.....	High Latitude Trapping Region
HT	.....	deHoffmann-Teller

IES	Imaging Electron Spectrometer
IIMS	Imaging Ion Mass Spectrometer
IMF	interplanetary magnetic field
KH	Kelvin-Helmholtz
LLBL	low latitude boundary layer
MCP	micro channel plate
MHD	magnetohydrodynamic
MK	millions of degrees
MLAT	Magnetic Latitude
MLT	Magnetic Local Time
MPI	Message Passing Interface
MVA	Minimum Variance Analysis
Open GGCM	Open Geospace General Circulation Model
PA	Pitch Angle
PEACE	Plasma electron and current experiment
PTE	Plasma Transport Event
RAPID	Research with Adaptive Particle Imaging Detectors
$R_E$	radius of the Earth
SEC	Stagnant Exterior Cusp
SSD	solid state energy detector
STAFF	Spatio-temporal analysis of field
TOF	Time of Flight
WBD	Wide band data
WHISPER	Waves of high frequency and sounder for probing of electron density by relaxation
UT	Universal Time

## Chapter 1

# Introduction to the Earth's Outer Magnetospheric Boundaries

The Earth's magnetospheric boundaries are interfaces that separate different regions of geospace. A magnetospheric boundary is defined by discontinuous fluid parameters (density, temperature and velocity) and electromagnetic fields. The large scale properties of the plasma boundaries can be obtained by the magnetohydrodynamic (MHD) continuum theory of fluids if the dimensions of the boundary are much larger than the ion Larmor radius [*Parks*, 2004].

### 1.1 MHD Discontinuities

The complete set of ideal MHD equations are:

Continuity equation:

$$\frac{\partial \rho}{\partial t} + \nabla \cdot (\rho \mathbf{u}) = 0 \quad (1.1)$$

Momentum equation:

$$\rho \frac{\partial \mathbf{u}}{\partial t} + \rho (\mathbf{u} \cdot \nabla) \mathbf{u} = -\nabla p - \nabla \left( \frac{B^2}{2\mu_0} \right) + (\mathbf{B} \cdot \nabla) \frac{\mathbf{B}}{\mu_0} \quad (1.2)$$

Energy equation:

$$\frac{\partial w_{total}}{\partial t} = -\nabla \cdot \left[ \left( \frac{1}{2} \rho u^2 + \frac{\gamma p}{\gamma - 1} + \frac{1}{\mu_0} B^2 \right) \mathbf{u} - \frac{\mathbf{u} \cdot \mathbf{B}}{\mu_0} \mathbf{B} \right] \quad (1.3)$$

Maxwell's equations:

$$\frac{\partial \mathbf{B}}{\partial t} = \nabla \times (\mathbf{u} \times \mathbf{B}) \quad (1.4)$$

$$\nabla \cdot \mathbf{B} = 0 \quad (1.5)$$

where  $\rho$  is mass density,  $\mathbf{u}$  is bulk flow velocity,  $p$  is thermal pressure,  $\mathbf{B}$  is the magnetic field vector,  $\mu_0$  is magnetic permeability of free space,  $\gamma$  is the ratio of specific heat, and the total energy

$$w_{total} = \frac{1}{2}\rho u^2 + \frac{p}{\gamma - 1} + \frac{1}{2\mu_0}B^2 \quad (1.6)$$

Assuming that a boundary is stable and in equilibrium with the surrounding plasma medium, the set of ideal MHD equations can be written as

Continuity equation:

$$\nabla \cdot (\rho \mathbf{u}) = 0 \quad (1.7)$$

Momentum equation:

$$\rho(\mathbf{u} \cdot \nabla)\mathbf{u} + \nabla p + \nabla\left(\frac{B^2}{2\mu_0}\right) - (\mathbf{B} \cdot \nabla)\frac{\mathbf{B}}{\mu_0} = 0 \quad (1.8)$$

Energy equation:

$$\nabla \cdot \left[ \left( \frac{1}{2}\rho u^2 + \frac{\gamma p}{\gamma - 1} + \frac{1}{\mu_0}B^2 \right) \mathbf{u} - \frac{\mathbf{u} \cdot \mathbf{B}}{\mu_0} \mathbf{B} \right] = 0 \quad (1.9)$$

Maxwell's equations:

$$\nabla \times (\mathbf{u} \times \mathbf{B}) = 0 \quad (1.10)$$

$$\nabla \cdot \mathbf{B} = 0 \quad (1.11)$$

Assuming a one-dimensional boundary with zero width, we can construct the so-called Rankine Hugoniot conditions:

Continuity equation:

$$[\rho u_n] = 0 \quad (1.12)$$

Momentum equation:

$$[\rho u_n \mathbf{u} + (p + \frac{B^2}{2\mu_0})\mathbf{n} - \frac{1}{\mu_0} B_n \mathbf{B}] = 0 \quad (1.13)$$

Energy equation:

$$[\rho u_n (\frac{1}{2} u^2 + \frac{\gamma}{\gamma - 1} \frac{p}{\rho}) + u_n \frac{B^2}{\mu_0} - \mathbf{u} \cdot \mathbf{B} \frac{B_n}{\mu_0}] = 0 \quad (1.14)$$

Maxwell's equations:

$$[B_n] = 0 \quad (1.15)$$

$$[u_n \mathbf{B}_t - B_n \mathbf{u}_t] = 0 \quad (1.16)$$

where  $[ ]$  denotes the difference between the values of the quantity on the two sides of the discontinuity, subscripts  $n$  and  $t$  indicate the components normal and tangential to the discontinuity respectively.

The solutions of these equations describe a number of different types of MHD discontinuities including shocks. Based on the behavior of the  $u_n$  and  $B_n$ , the discontinuities can be divided into the six types as summarized in Table 1.1

Table 1.1: Discontinuities in Ideal MHD (from *Kivelson and Russell [1995]*)

Contact discontinuity	$u_n = 0, B_n \neq 0$	Density jump arbitrary, but pressure and all other quantities are continuous
Tangential discontinuity	$u_n = 0, B_n = 0$	Plasma pressure and field change, maintaining static pressure balance
Rotational discontinuity	$u_n = \frac{B_n}{\sqrt{\mu_0 \rho}}$	Large-amplitude intermediate wave; in isotropic plasma, field and flow change direction, but not magnitude
Parallel shock	$u_n \neq 0, B_t = 0$	Magnetic field unchanged by shock
Perpendicular shock	$u_n \neq 0, B_n = 0$	Plasma pressure and field strength increase at shock
Oblique shock	$u_n \neq 0, B_t \neq 0$	

## 1.2 The Magnetopause

### 1.2.1 Historical Review

The concept of the existence of a boundary to the Earth's magnetic field originated from the work of Chapman and Ferraro [*Chapman and Ferraro, 1931; Chapman and Bartels, 1940*]. To explain the features of magnetic storms, Chapman and his graduate student Ferraro proposed that a stream of ionized but neutral gas, what would nowadays be called a plasma, emitted by solar flare travelled to the Earth and compressed the sunward portion of the Earth's magnetic field until the stream dynamic pressure is balanced by the Earth's magnetic pressure.

Figure 1.1 shows the Earth's dipole magnetic field in the presence of an infinitely conducting plane. When the non-magnetic superconducting gas approaches the Earth's magnetic field, since the ionized gas can not penetrate into the Earth's magnetic field, a strong shielding current sheet would be induced in front of the conducting gas. There would be a repulsion between the Earth's magnetic field and the current sheet. The magnetic field is distorted by the current sheet as if there is an image dipole on the right hand side of the current sheet. The magnetic field strength at the equatorial plane is doubled. There are two points (labelled Q) at the high latitude where the magnetic field is zero. The two magnetic field lines which extend from the Earth's surface to these two points are called Chapman-Ferraro cusps.

The super conducting plane in Figure 1.1 is rigid. In reality, it is a gas instead of a rigid

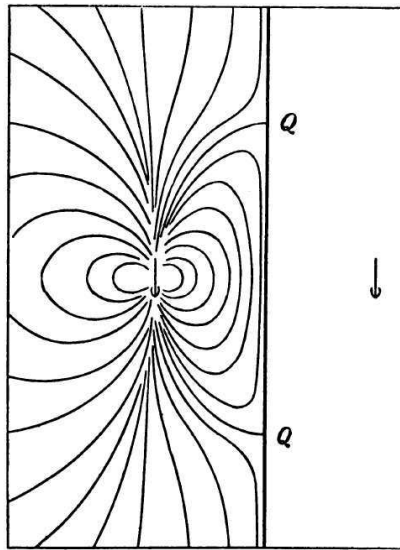


Figure 1-1: The sketch shows the magnetic field of a dipole in the presence of an infinitely conducting plane. When the super conducting gas (now known as solar wind) approaches the Earth's dipole field on the left hand side, an image dipole forms on the right hand side. The superconducting property of the boundary and the nature of the dipole field combine to produce magnetic nulls at high latitudes (labelled Q). The two magnetic field lines which extend from the Earth's surface to these two magnetic nulls are now called Chapman-Ferraro cusps. (from *Chapman and Bartels* [1940])

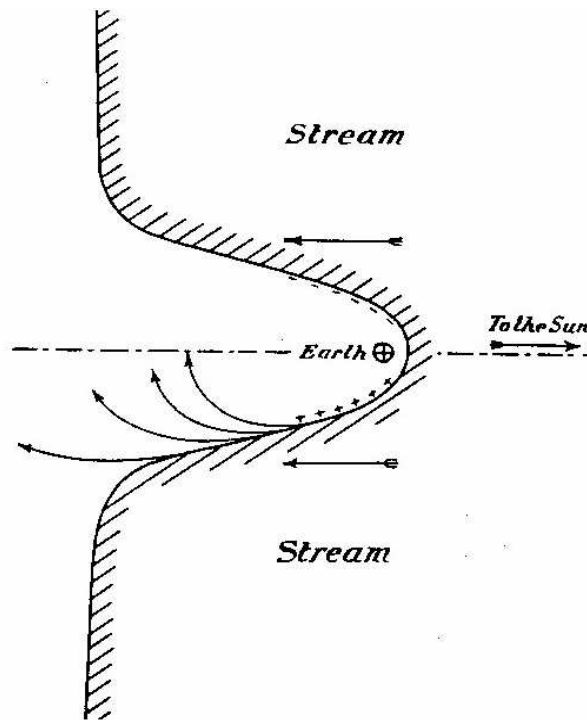


Figure 1-2: The sketch shows the formation of the Chapman-Ferraro cavity [*Chapman and Ferraro, 1931*]. When the non-magnetic super conducting gas approaches the Earth's magnetic field, a strong shielding current would be induced and confine the Earth's magnetic field in a cavity.

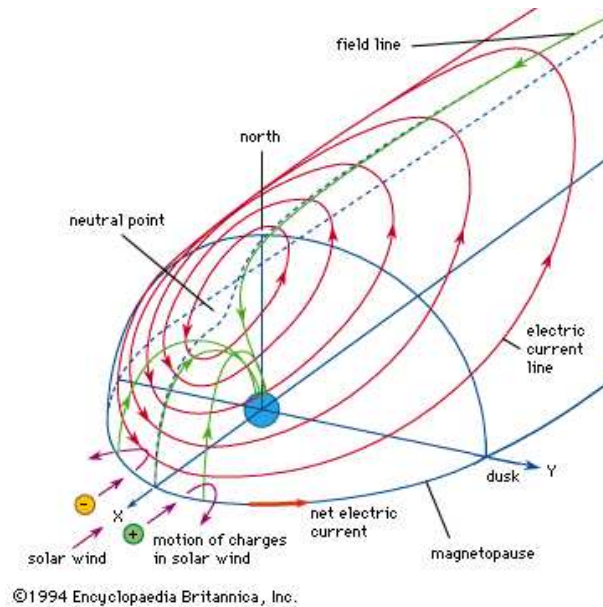


Figure 1-3: A perspective view of the northern portion of the Chapman-Ferraro current system, as seen from above the ecliptic plane. Charged particles in the solar wind are deflected by the Earth's magnetic field, creating a boundary current. This current confines the field inside the Chapman-Ferraro cavity (the magnetosphere). [This Figure is from "Chapman-Ferraro current system." Online Art. Encyclopedia Britannica Online. <http://www.britannica.com/eb/art-1167>.]

plane. Owing to the unequal repulsion forces at different latitudes, the induced current sheet would close around the Earth and form a cavity as shown in Figure 1-2. The Earth's magnetic field is confined in this cavity which was named "the magnetosphere" by *Gold* [1959]. The shielding current is referred to as the Chapman-Ferraro current. Figure 1-3 shows the northern portion of the Chapman-Ferraro current system.

The first simple model for the structure of the magnetopause current was proposed by *Ferraro* [1952]. As shown in Figure 1-4, when solar wind particles encounter the Earth's field, they are bent from their paths by the Lorentz force. Protons gyrate in a left-handed sense around a magnetic field and electrons in a right-handed sense. Since the particles are coming from the Sun and the direction of the Earth's field is upward parallel to its rotation axis, this gyration creates an electric current flowing from dawn to dusk in the equatorial plane as shown in Figure 1-4 and Figure 1-3. The thickness of this current sheet should be

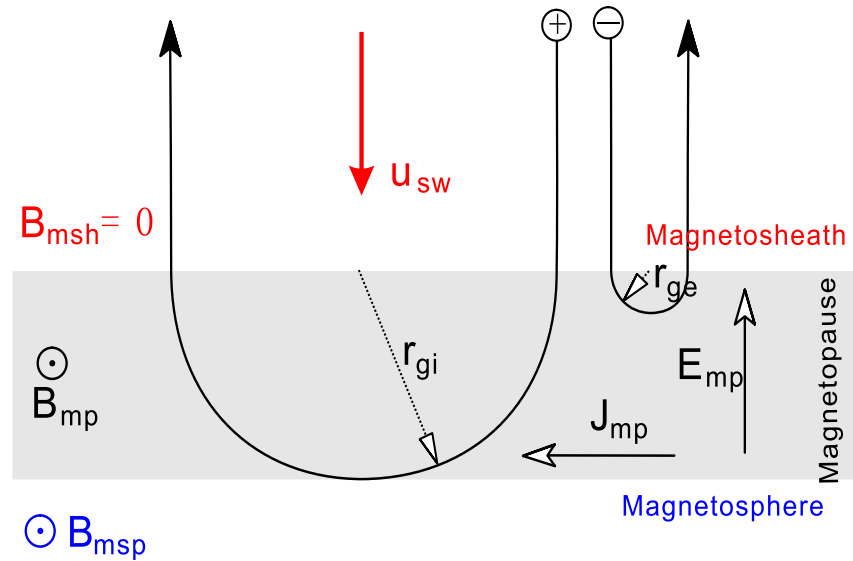


Figure 1-4: A simple magnetopause current model proposed by *Ferraro* [1952]. When solar wind particles encounter the Earth's field, they are bent from their paths by the Lorentz force. Protons gyrate in a left-handed sense around a magnetic field and electrons in a right-handed sense, forming a current flowing from dawn to dusk. (after *Ferraro* [1952])

around the ion gyro radius.

In Chapman and Ferraro's concept, the stream of ionized gas emitted by a solar flare is not continuous, there is no interplanetary magnetic field and the Earth's magnetosphere is a vacuum. These deficiencies were soon filled. The concept of continuous emission of ionized gas from the sun emerged in the 1950's. Observations of comet tails [*Biermann*, 1957] as the comet passed close to the sun indicated that a stream of ionized particles emitted from the sun were needed. *Parker* [1959] showed that the solar corona must expand at velocity higher than 500 km/s. He named this streaming solar corona gas the "solar wind". *Parker* [1958] showed that the outward motion of the solar wind would pull out the solar magnetic field and form a spiral shape with the rotation of the sun. The observations of whistlers [*Storey*, 1953] indicated that the magnetosphere is filled with charged particles instead of being a vacuum. In addition, theoretical studies [*Dungey*, 1958; *Dessler*, 1958; *Dessler and Parker*, 1959] showed that magnetic pulsations and sudden commencement

must travel through the magnetosphere in the form of hydromagnetic waves which requires the presence of charged particles.

Chapman and Ferraro's concept about the magnetopause was not well accepted until the early 1960's when the in-situ magnetic field measurements were taken across the magnetopause [Cowley, 1995]. Figure 1-5 shows the earliest report of the subsolar magnetopause crossing taken by Explorer 12 on September 30, 1961 [Cahill and Amazeen, 1963]. In Figure 1-5, the magnetopause at  $10.5 R_E$  is clearly seen as a sharp, large change in the magnetic field direction and an increase in fluctuations. In addition, the magnitude of the magnetic field inside the magnetopause is about double the predicted dipole magnetic field magnitude.

In the same year that Explorer 12 was launched, based on the work of Giovanelli [1947], Dungey [1961] proposed his classical model of magnetic reconnection between the interplanetary magnetic field (IMF) and the Earth's magnetic field where the magnetic field lines are antiparallel. Figure 1-6 shows the magnetic topology in the noon-midnight meridian for the two cases when the IMF is southward (top) and when it is northward (bottom). In the former case the internal convection is driven by the reconnection in the subsolar magnetopause and a circulation pattern is set up. When the interplanetary magnetic field is northward, reconnection still occurs but this time on open magnetic field lines in the high latitude region.

Three years after Dungey proposed the open model of the magnetosphere, Petschek [1964] conceived a detailed rapid reconnection theory which allows for the required fast reconnection rate. The detailed introduction to this model is presented in section 1.2.4.

### 1.2.2 Magnetopause Shape and Position

The shape of the magnetopause is crucial to many space physics problems and its precise calculation has been a fundamental problem for many years [Beard, 1967]. After Chapman and Ferraro [1931] proposed the existence of the magnetopause, more rigorous theoretical work on the shape of the magnetopause has been done. In 1960, the shape of the mag-

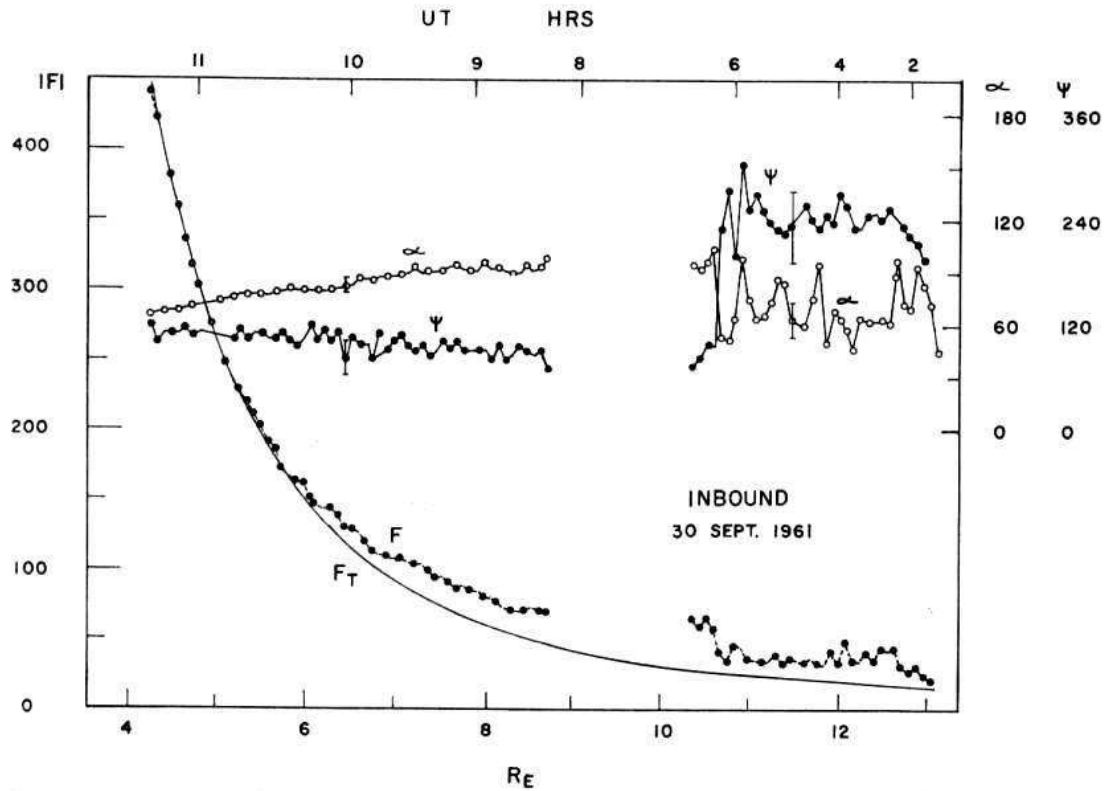


Figure 1-5: The earliest report of the subsolar magnetopause crossing taken by Explorer 12 on September 30, 1961.  $|F|$  is the magnitude of the magnetic field.  $\alpha$  is the angle between the magnetic field and the spin axis of the spacecraft.  $\psi$  is the dihedral angle between the plane that contains the magnetic field vector and the spin axis and the plane that contains the spin axis and the satellite sunline. The solid line represents  $r^{-3}$  dependence of the dipole field. (from *Cahill and Amazeen* [1963])

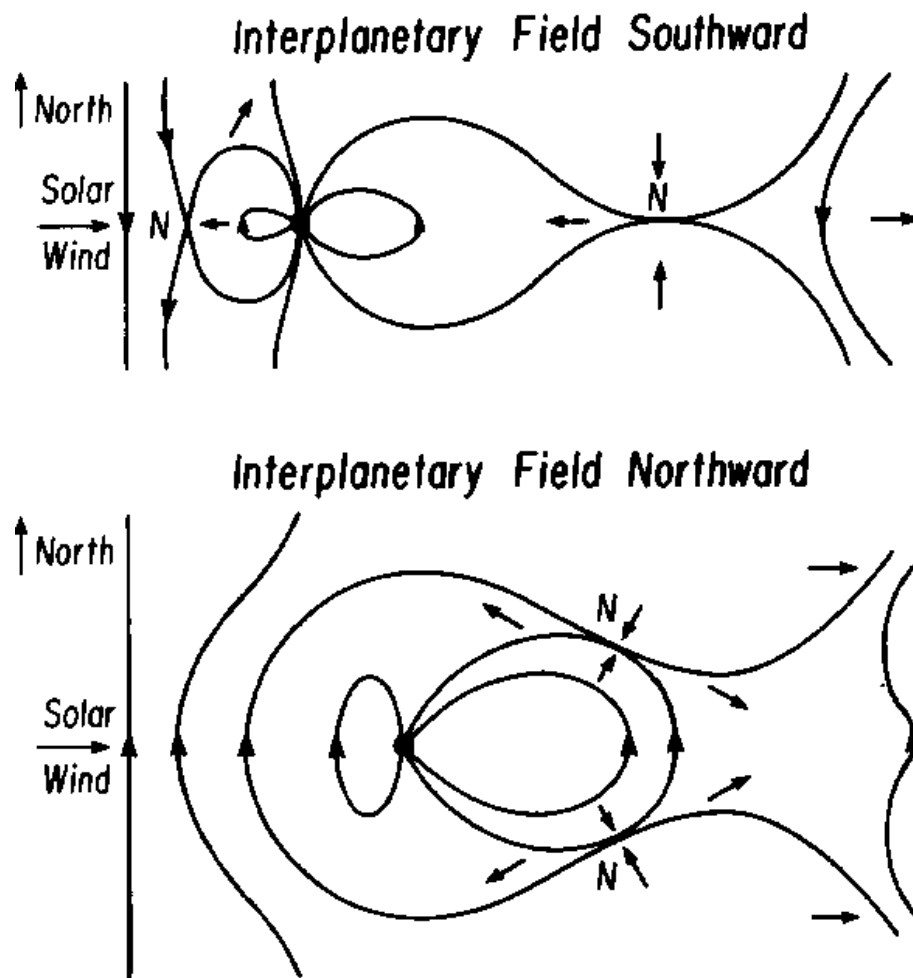


Figure 1-6: The magnetic reconnection model of the magnetosphere for southward (top) and northward (bottom) IMF. (after *Dungey* [1961, 1963])

netopause in two dimensions was derived [*Beard*, 1960; *Ferraro*, 1960] followed by more detailed computational models in the 1960's and the early 1970's [*Spreiter and Briggs*, 1962; *Midgeley and Davis*, 1963; *Mead and Beard*, 1964; *Olson*, 1969; *Choe et al.*, 1973].

All of these magnetopause models are based on the pressure balance at the magnetopause. When the charged particles in the solar wind approach the Earth's magnetic field, they are deflected by the geomagnetic field. Since these particles experience a change in momentum at the magnetopause, they exert a dynamic pressure on the magnetopause which must be balanced by the magnetic pressure inside the magnetopause. Because of the presence of the IMF, the particles flow tangentially to the magnetopause rather than being reflected back to the solar wind. The tangential component of the particle momentum remains unchanged if the viscous effects are neglected. Therefore the dynamic pressure is due only to the change in the perpendicular portion of the particle momentum. Because the solar wind is supersonic, a bow shock is formed in front of the magnetopause to decelerate and heat the solar wind plasma. The solar wind dynamic pressure perpendicular to the bow shock surface is transmitted to the magnetopause via the transition region – the magnetosheath. Since the presence of the bow shock has little effect on the angular dependence of the dynamic pressure on the magnetopause, it can be ignored in the derivation of the magnetopause shape [*Beard*, 1967].

As shown in Figure 1-7, the momentum change of a particle deflected by the magnetopause is equal to  $mv\cos\theta$ , where  $mv$  is the momentum of the particle and  $\theta$  is the angle between the solar wind direction and the normal of the magnetopause. The number of particles striking the magnetopause per second per unit area is  $nv\cos\theta$ , thus the solar wind dynamic pressure exerted on the magnetopause is  $p_{sw} = nmv^2\cos^2\theta$ .

A conducting fluid flowing in the electric and magnetic field can be described by the ideal MHD momentum equation 1.2. By assuming that a steady state exists, equation 1.2 can be rewritten as equation 1.8. The last term  $(\mathbf{B} \cdot \nabla) \frac{\mathbf{B}}{\mu_0}$  indicates the change of the magnetic field in the direction of the magnetic field. If the magnetopause can be regarded as tangential discontinuity, the last term is negligible compared with the other three terms.

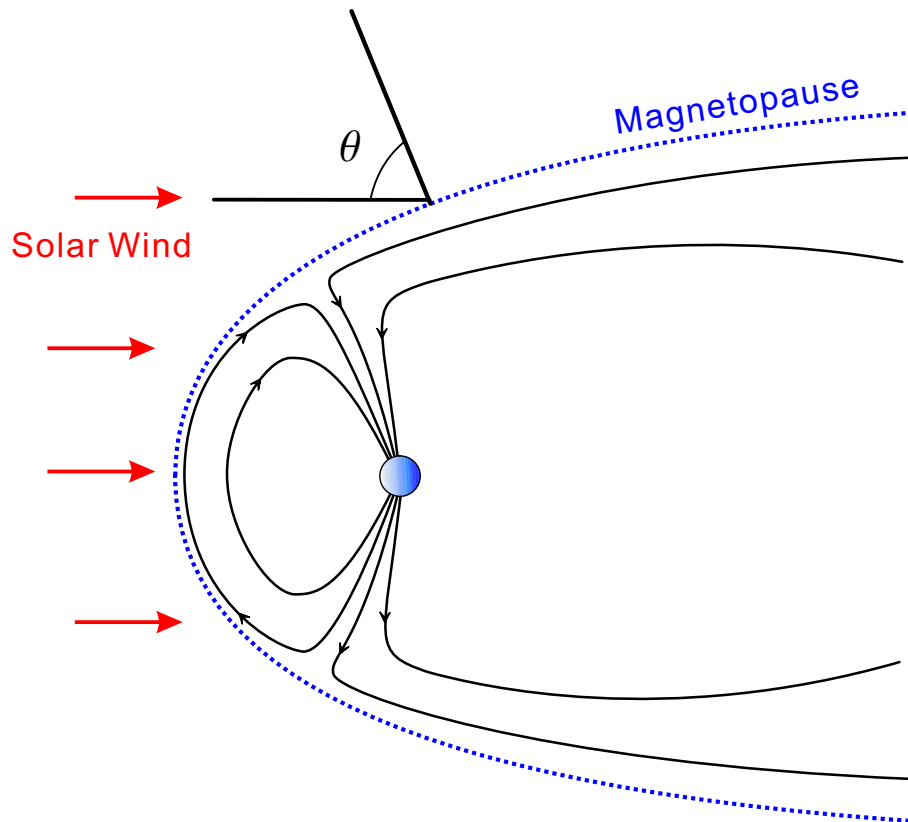


Figure 1.7: The pressure balance at the magnetopause. The component of solar wind dynamic pressure normal to the magnetopause is balanced by the magnetic pressure at the inner edge of the magnetopause. [after Otto, 2002] (<http://what.gi.alaska.edu/ao/msp/index.html>)

By integrating equation 1.8 we get the well-known Bernoulli's equation:

$$\rho u^2 + p + \frac{B^2}{2\mu_0} = \text{constant} \quad (1.17)$$

Let the constant be the solar wind dynamic pressure transmitted to the magnetopause  $p_{sw} = nmv^2 \cos^2\theta$ , then Bernoulli's equation can be rewritten as

$$\rho u^2 + p + \frac{B^2}{2\mu_0} = nmv^2 \cos^2\theta \quad (1.18)$$

which is the equation that determines the shape of the magnetopause.

The first empirical model of the magnetopause and bow shock was established by *Fairfield* [1971]. The average shape and size of the magnetopause was obtained by a fit to crossing positions of the magnetopause by several different spacecraft *Fairfield* [1971]. Similar empirical fits to additional magnetopause crossings for later missions have been performed [*Holzer and Slavin*, 1978; *Formisano et al.*, 1979; *Sibeck et al.*, 1991; *Petrinec et al.*, 1991; *Shue et al.*, 1997]. The shapes of the magnetopause in these studies are fitted to conic sections, with the nose standoff distance of about  $10 R_E$ .

The shape and size of the dayside magnetopause are found to be influenced by other factors besides solar wind dynamic pressure. It has been observed that the interplanetary magnetic field (IMF) can also affect the position of the magnetopause. The magnetopause moves closer to the Earth when the IMF  $B_z$  is southward [*Sibeck et al.*, 1991; *Petrinec and Russell*, 1993]. Oscillations of the magnetospheric boundaries could also be driven by the IMF rotations [*Laakso et al.*, 1998].

### 1.2.3 Magnetopause Structure

The magnetopause is a complicated plasma boundary which has not been fully understood yet. Figure 1-8 shows the ISEE-1 observations of a magnetopause crossing on November 1, 1978 when the IMF was strongly northward. The plasma density, temperature, velocity,

and pressure are shown in the top four panels. The bottom four panels show the magnetic field components in boundary normal coordinates [*Russell and Elphic, 1978*] as illustrated in Figure 1.9 and the magnitude of the magnetic fields. Five regions are labelled in this figure. The region on the left is the magnetosheath with ion density as high as  $40 \text{ cm}^{-3}$  and low temperature. As the spacecraft moved closer to the Earth, it encountered a region with piled up magnetic field and decreased ion density which is called the plasma depletion layer. In the subsolar region close to the magnetopause, the plasma flow is slow. The thermal motion of particles allows them to escape along the magnetic field and evacuate the magnetic field lines near the magnetopause. In the plasma depletion layer, the plasma is strongly anisotropic [*Song et al., 1993; Phan et al., 1994; Anderson and Fuselier, 1993*]. On the inner edge of the plasma depletion layer, there is a small but abrupt change in the magnetic field and plasma data which may correspond to the Ferraro current layer with a thickness of an ion gyro radius as shown in Figure 1.4. After passing the outer boundary layer, the spacecraft encountered the inner boundary layer with lower density and higher temperature than the outer layer. Finally the spacecraft entered the magnetosphere.

When the IMF is southward the structure of the magnetopause is different from the northward case because of the presence of magnetic reconnection between the magnetic fields in the magnetosheath and the magnetosphere. Figure 1.10 shows ISEE-1 observations of a subsolar magnetopause crossing on November 25, 1978 when the IMF is southward. Comparing this figure with Figure 1.8, one of the differences is that no plasma depletion layer is observed for the southward IMF case. Another difference is that there is a broad current sheet in which the magnetic field direction rotates and the total magnetic field is depressed. In addition, there is plasma heating and flow acceleration in the current sheet.

#### 1.2.4 Magnetic Reconnection at the Magnetopause

The concept of magnetic reconnection originated with *Giovanelli* [1947] who attempted to explain the solar flare. Then *Dungey* [1961] applied magnetic reconnection to the magnetosphere. Magnetic reconnection provides an efficient mechanism for the conversion of

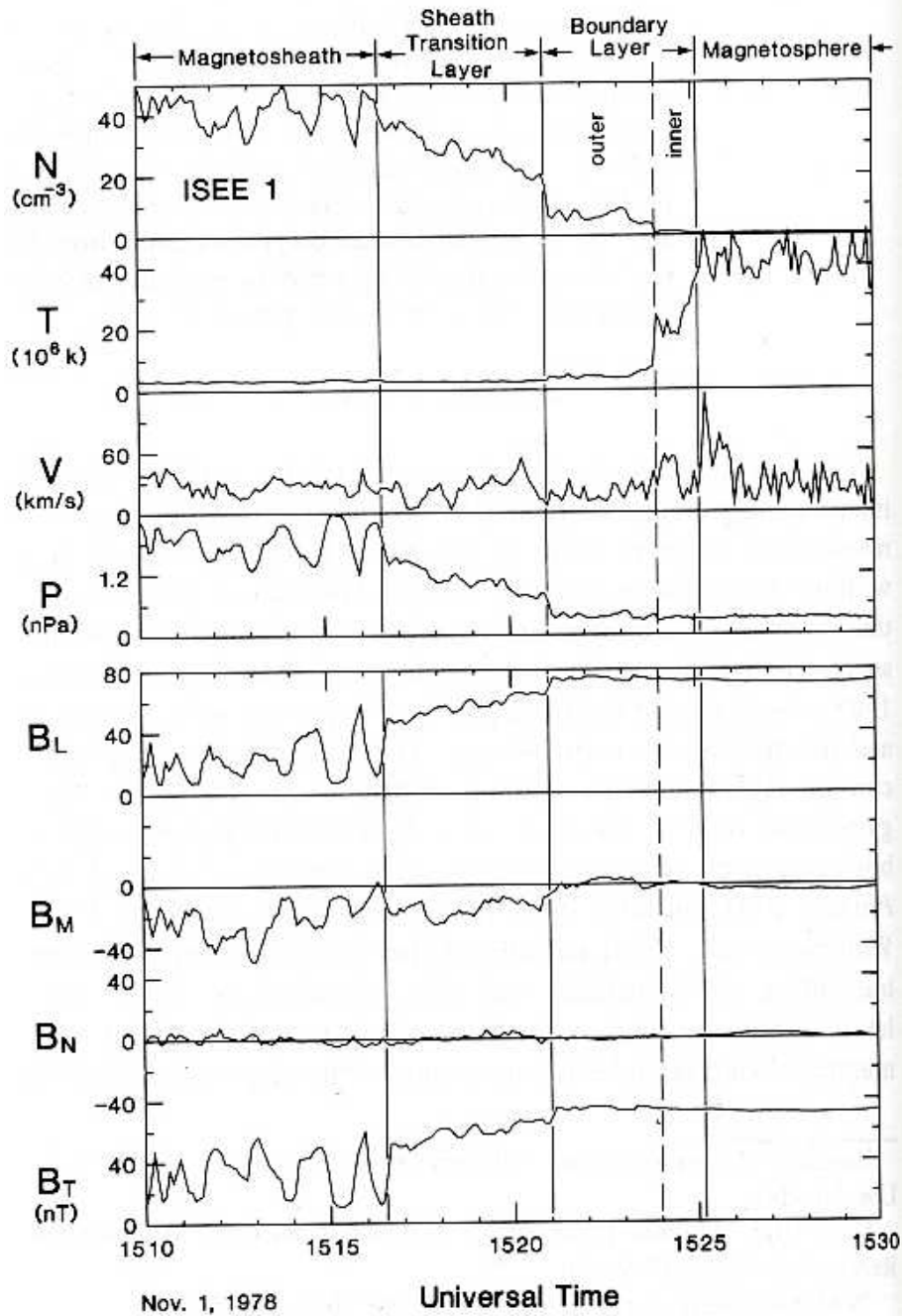


Figure 1-8: ISEE-1 observations of a magnetopause crossing on November 1, 1978 when the IMF is strongly northward. The top four panels show the plasma ion density in  $\text{cm}^{-3}$ , the ion temperature in millions of degrees (MK), the plasma velocity in  $\text{km/s}$  and the plasma pressure in  $10^{-8} \text{ dyne cm}^{-2}$ . The bottom four panels show the magnetic field components in boundary normal coordinates [Russell and Elphic, 1978] as illustrated in Figure 1-9 and the magnitude of the magnetic fields in  $\text{nT}$ . [Song et al., 1990]

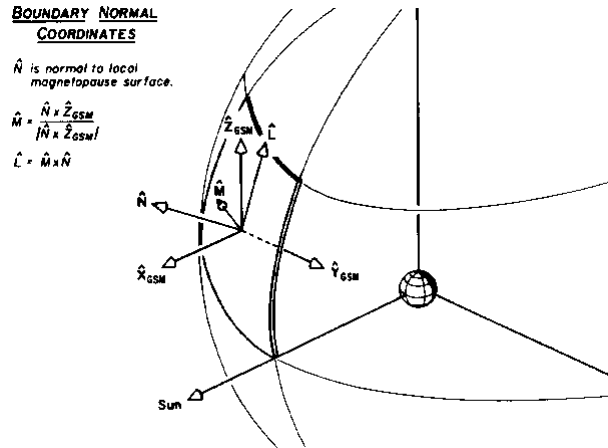


Figure 1-9: Illustration of the boundary normal coordinate system. The N direction is chosen to be along the magnetopause normal. The L direction is northward along the magnetic field and the M direction is tangential to the boundary toward dawn. [Russell and Elphic, 1979]

magnetic energy to kinetic energy and the change of magnetic topology. Various models of reconnection have been proposed in the past half century. In the following sections, I will briefly review the reconnection models, both MHD and kinetic treatments, and show the observations of the magnetic reconnection at the magnetopause.

### MHD Reconnection Models

In ideal MHD theory, there is no resistivity and the magnetic field is frozen into the plasma flow. The local breakdown of the frozen-in condition is necessary for magnetic reconnection to happen. The MHD reconnection models are based on the assumption that the resistivity breaks down the frozen-in condition. From Ohm's law:

$$\mathbf{E} + \mathbf{v} \times \mathbf{B} = \eta \mathbf{j} \quad (1.19)$$

and Faraday's law:

$$\frac{\partial \mathbf{B}}{\partial t} = -\nabla \times \mathbf{E} \quad (1.20)$$

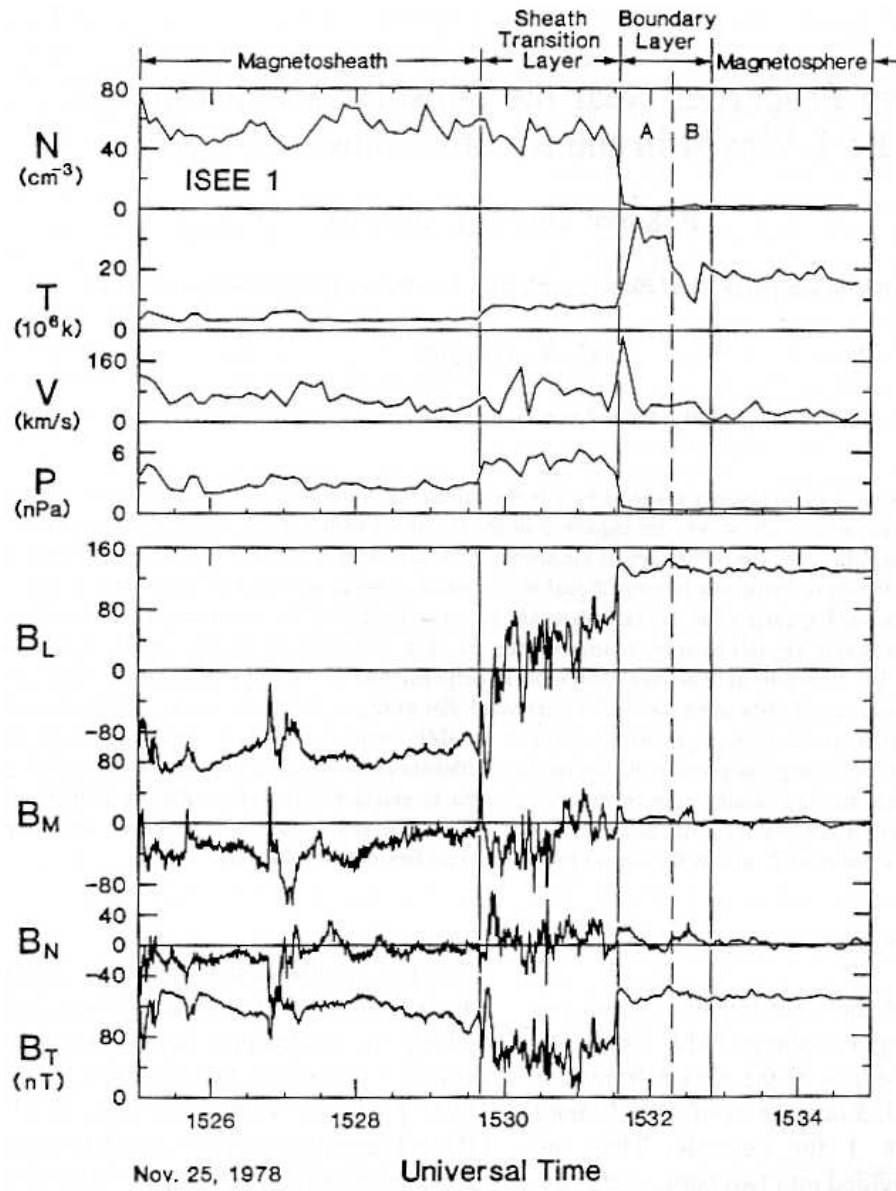


Figure 1-10: ISEE-1 observations of a subsolar magnetopause crossing on November 25, 1978 when the IMF is southward. The format of this plot is the same as Figure 1-8 [Song *et al.*, 1993]

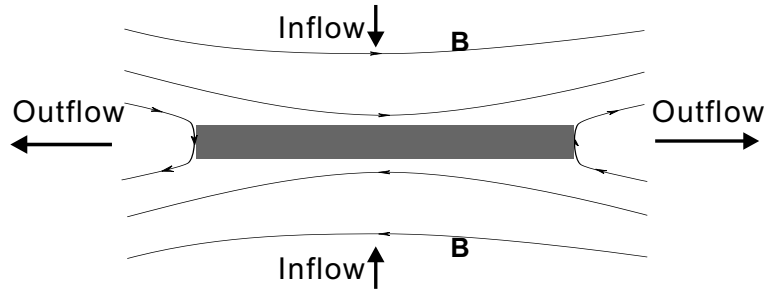


Figure 1.11: Schematic of Sweet-Parker reconnection model [*Parker, 1957; Sweet, 1958*]. The plasma flow is shown in short arrows. The grey rectangular box marks the diffusion region.

the induction equation (or dynamo equation) which governs the magnetic reconnection process is obtained:

$$\frac{\partial \mathbf{B}}{\partial t} = \nabla \times (\mathbf{v} \times \mathbf{B}) + \frac{\eta}{\mu_0} \nabla^2 \mathbf{B} \quad (1.21)$$

The first term on the right hand side of equation 1.21 is the convection term and the second term is the diffusion term.

The first self-consistent reconnection model is the Sweet-Parker model [*Parker, 1957; Sweet, 1958*]. This model shows for the first time how the localized magnetic reconnection causes the observed macroscopic changes. An illustration of Sweet-Parker model is shown in Figure 1.11. The plasma flow is shown in short arrows. The horizontal opposing magnetic field lines at the top and bottom of this plot are convected toward each other by the inflowing plasma. The key element of the Sweet-Parker model is the existence of a "diffusion region" – a rectangular box (grey box in Figure 1.11) where the frozen-in condition is broken down allowing the magnetic field to diffuse and reconnect. The newly reconnected field lines try to straighten out and carry the plasma flow outward. The dimensions of the diffusion region are important because the geometry determines the magnetic reconnection rate by balancing the incoming and outgoing plasma and magnetic flux flow. The length of this box is of macroscopic scale and the width is determined by the local resistivity. An important consequence of the long and thin diffusion region and associated thin current

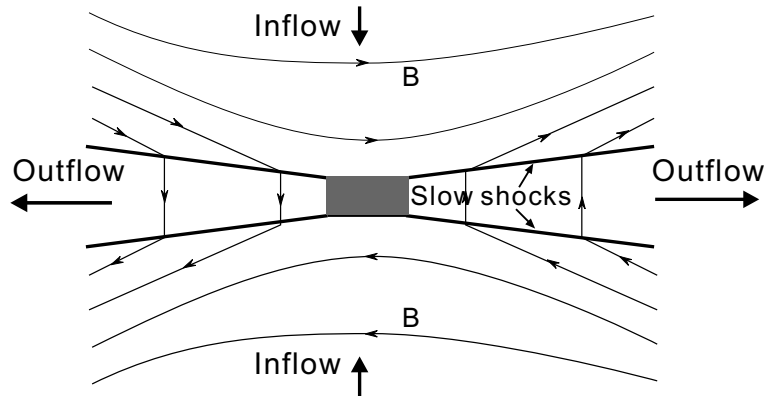


Figure 1.12: Schematic of Petschek's reconnection model [*Petschek*, 1964] with diffusion region indicated by the shaded rectangle. The plasma outflow is bounded by two pair of slow shocks in a wedge-shaped region.

layer is that this layer could be unstable and produce many small magnetic islands [*Biskamp and Welter*, 1980] which is the basis of the Russell-Elphic model of flux transfer events [*Russell and Elphic*, 1978] at the day side magnetopause. The reconnection rate given by Sweet-Parker model is too low to explain the magnetic explosions such as solar flares.

Following the Sweet-Parker's reconnection model, *Petschek* [1964] proposed a rapid reconnection model which allows for the required faster reconnection rate. An illustration of Petschek model is shown in Figure 1.12. The long thin current sheet (Y-type) in Sweet-Parker model (Figure 1.11) is replaced by an open X-type geometry in Petschek model (Figure 1.12). The diffusion region is confined to a small region in the center area. The magnetic field lines in the inflow regions are convected to the central diffusion region. In Petschek's model it is the two pair of slow shocks that accelerates the plasmas and bound the high speed outflow in the wedge-shaped region. This model can produce much higher reconnection rates than the Sweet-Parker model because the magnetic energy is converted to plasma kinetic energy through slow shocks and only a small fraction of plasma needs to go through the small diffusion region. The reconnection rate provided by this mechanism is fast enough to explain the solar flares.

The success of Petschek model in providing a fast reconnection rate was revolutionary, however, it was found later that a microscopic diffusion region in Petschek model is not ca-

pable of supporting an open outflow geometry unless the resistivity is spatially nonuniform (the anomalous resistivity) [Ugai and Tsuda, 1977; Sato and Hayashi, 1979; Biskamp, 1986; Scholer, 1989]. Efforts have been made to explain the anomalous resistivity. In collisionless plasmas, such as in the Earth's magnetotail, anomalous resistivity could be caused by the onset of micro-instabilities at small scale length, such as the lower hybrid drift instability [Huba *et al.*, 1977], ion-acoustic instability [Coroniti and Eviatar, 1977] or Buneman instability [Drake *et al.*, 2003]. However, in collisional plasma such as the solar flare, how to explain the anomalous resistivity is still an open question. Although anomalous resistivity has been widely used in MHD simulations, the establishment and the role of anomalous resistivity in the reconnection process is not well understood [Papadopoulos, 1977; Galeev and Sagdeev, 1984; Drake *et al.*, 2003].

### **Kinetic Treatments**

In the Earth's magnetosphere where the plasma density is only a few particles per cubic centimeter or less, the collisional mean free path is large enough that classical collisions are negligible. In addition, the thickness of the magnetopause current layer is usually a few ion gyro radii. One may argue that the MHD description of reconnection at the magnetopause would be inappropriate. However the reconnection process involves large scale structures, e.g., the normal component of the magnetic field and the accelerated outflow jets [Sonnerup *et al.*, 1995]. Although the MHD description of the plasma dynamics in the magnetic reconnection process is quite accurate at large scales [Drake, 1995], there are still observations which can not be understood with resistive MHD theory, e.g., the sudden onsets of the magnetic reconnection in solar flares and magnetospheric substorms, energetic electrons released during magnetic reconnection [Drake and Shay, 2007]. Since MHD is a single fluid model, it can not describe the high energy tails in the particle distribution which can only be treated with kinetic models [Drake and Shay, 2007].

In the resistive MHD reconnection model, the structure of the diffusion region is controlled by Ohm's law. To understand the influence of non-MHD behavior on the magnetic

reconnection, the generalized Ohm's law must be take into account:

$$\mathbf{E} + \mathbf{v} \times \mathbf{B} = \frac{1}{en} \mathbf{j} \times \mathbf{B} + \frac{1}{en} \nabla \cdot \mathbb{P} + \frac{1}{\epsilon_0 \omega_{pe}^2} \frac{d\mathbf{j}}{dt} + \eta \mathbf{j} \quad (1.22)$$

There are four possible processes to break down the frozen-in flux condition so that reconnection can happen. The terms on the right hand side of the generalized Ohm's law are the Hall term, the electron pressure term, the electron inertial term, and the resistive term respectively. To estimate the relative importance of each term on the right hand side, we can compute the scale length  $L$  required to to make the term comparable to the  $\mathbf{v} \times \mathbf{B}$  term [*Priest and Forbes, 2000*].

For the Hall term  $\frac{1}{en} \mathbf{j} \times \mathbf{B}$  (the first term on the right hand of Equation 1.22), assuming  $\nabla \approx 1/L$ ,  $|\mathbf{j}| \approx B/(\mu_0 L)$ , where  $L$  is the typical scale length, it will be comparable to the  $\mathbf{v} \times \mathbf{B}$  term if

$$\frac{B^2}{en\mu_0 L} \approx VB \quad (1.23)$$

or

$$L_{Hall} \approx \frac{B}{en\mu_0 V} = \frac{\sqrt{m_i}}{\sqrt{n\mu_0 e} V} \frac{B}{\sqrt{\mu_0 n m_i}} = \sqrt{\frac{m_i}{\mu_0 n}} \frac{1}{e} \frac{V_A}{V} = \sqrt{\frac{m_i c^2 \epsilon_0}{n}} \frac{1}{e} \frac{V_A}{V} = \frac{c}{\omega_{pi}} \frac{V_A}{V} = \frac{\lambda_i}{M} \quad (1.24)$$

where

$$\lambda_i = \frac{c}{\omega_{pi}}$$

is the ion-inertial length or ion skin depth and  $\omega_{pi}$  is the ion plasma frequency,

$$M = \frac{V}{V_A}$$

is the Alfvén Mach number.

For the electron pressure term  $\frac{1}{en} \nabla \cdot \mathbb{P}$  (the second term on the right hand of Equation

1.22), assuming  $|\mathbb{P}| = nk_B T_e$  we can write

$$\frac{nk_B T_e}{e n L} \approx V B \quad (1.25)$$

Solving for  $L$ , we get

$$L_{pressure} \approx \frac{k_B T_e}{e V B} \quad (1.26)$$

If we assume  $T_e \approx T_i$ , Equation 1.26) can be rewritten as

$$L_{pressure} \approx \frac{k_B T_e}{e V B} \approx \frac{\sqrt{k_B T_e} V_A}{V_A} \frac{\sqrt{k_B T_i}}{V} \frac{1}{e B} = \frac{\sqrt{k_B T_e/m_i} V_A}{B/\sqrt{\mu_0 \rho}} \frac{\sqrt{k_B T_i m_i}}{e B} \quad (1.27)$$

$$= \sqrt{\frac{nk_B T_e}{B^2/\mu_0}} \frac{V_A}{V} \frac{\sqrt{k_B T_i m_i}}{e B} \approx \frac{\beta^{1/2}}{M_A} R_{gi} \quad (1.28)$$

where

$$\beta = \frac{nk_B T_e}{B^2/2\mu_0}$$

is the plasma beta, and

$$R_{gi} = \frac{\sqrt{k_B T_i m_i}}{e B}$$

is the ion gyro-radius.

If we further assume  $V_{thermal} = \sqrt{3k_B T_i/2m_i} \approx V$ , Equation 1.26) can be rewritten as

$$L_{pressure} \approx \frac{k_B T_e}{e V B} = \frac{m_i}{e B} \frac{k_B T_e}{m_i V} \approx \frac{\sqrt{k_B T_e/m_i}}{\omega_{ci}} \frac{\sqrt{k_B T_i/m_i}}{V} \approx \frac{\sqrt{k_B T_e/m_i}}{\omega_{ci}} = r_{ci} \quad (1.29)$$

where  $r_{ci} = \frac{\sqrt{k_B T_e/m_i}}{\omega_{ci}}$  is the effective ion Larmor radius.

For the electron inertial term  $\frac{1}{\epsilon_0 \omega_{pe}^2} \frac{d\mathbf{j}}{dt}$  (the third term on the right hand of Equation 1.22), assuming  $d/dt \approx V/L$ , we can write

$$\frac{1}{\epsilon_0 \omega_{pe}^2} \frac{V B}{\mu_0 L^2} \approx V B \quad (1.30)$$

or

$$\frac{c^2}{\omega_{pe}^2} \frac{VB}{L^2} \approx VB$$

Solving for  $L$ , we get

$$L_{inertia} \approx \frac{c}{\omega_{pe}} = \lambda_e \quad (1.31)$$

where  $\omega_{pe}$  is the electron plasma frequency and

$$\lambda_e = \frac{c}{\omega_{pe}}$$

is the electron inertial length or skin depth.

For the resistive term  $\eta \mathbf{j}$  (the last term on the right hand of Equation 1.22),

$$\eta \frac{B}{\mu_0 L} \approx VB \quad (1.32)$$

Solving for  $L$ , we get

$$L_{resistive} \approx \frac{\eta}{\mu_0 V} = \lambda_{res} \quad (1.33)$$

The relative importance of these terms is related to four characteristic scale lengths, the ion inertial length  $\lambda_i = c/\omega_{pi}$ , the effective ion Larmor radius  $r_{ci} = (\kappa_B T_e/m_i)^{1/2}/\omega_{ci}$ , electron inertial length  $\lambda_e = c/\omega_{pe}$  and the resistive scale length  $\lambda_{res} = \eta/\mu_0 |\mathbf{v}|$ . When the current sheet is thin enough to be comparable to a characteristic scale length, the magnetic reconnection is likely to happen. So the process with the largest scale length dominates in the reconnection process. When the resistive scale length is small compared to other terms, the reconnection is regarded as collisionless reconnection.

When the Hall term is important, ions decouple from the magnetic field at the ion inertial length while electrons are still frozen in to the magnetic field but they will decouple with the magnetic field at the electron inertial length. The different behaviors of ions and electrons results in quadrupolar magnetic fields (Hall perturbation) as shown in Figure

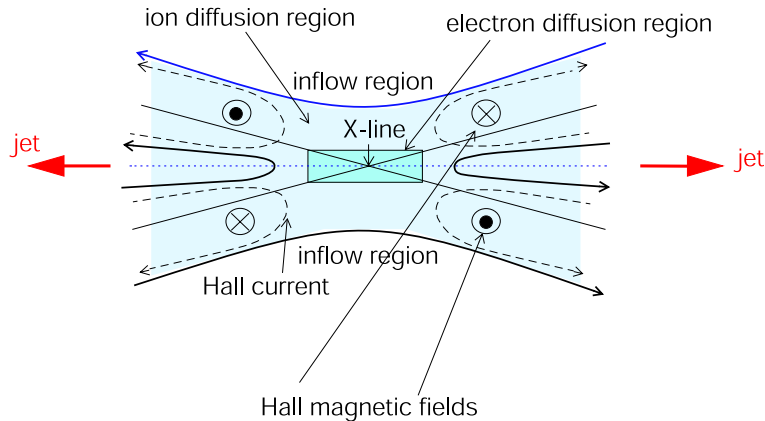


Figure 1-13: Schematic of the multiscale structure of the dissipation region when the Hall term is important. The small box marks the electron diffusion region. Outside of the electron diffusion region is the ion diffusion region. In this region ions are decoupled from the electrons and magnetic field, creating the quadrupolar Hall magnetic field in or out of the plane. Hall related currents are shown as dashed lines. The red arrows indicate reconnection outflow jets. (after *Oieroset et al.* [2001])

1-13 [*Sonnerup*, 1979].

The decoupling of the electrons and ions at small spatial scales implies that the Alfvén wave no longer controls the collective behavior of the plasma at these scales. Close to the X-line the whistler or kinetic Alfvén wave takes over the role [*Drake and Shay*, 2007].

The Hall term in the generalized Ohm’s law (equation 1.22) introduces whistler waves into the system [*Drake*, 1995]. In the scale length smaller than ion inertial length  $\lambda_i$ , the magnetic field is frozen into the electron fluid and the ions are left behind. Quadrupolar magnetic fields are a signature of the role of the whistler wave in driving magnetic reconnection [*Drake*, 1995].

The electron pressure term in the generalized Ohm’s law (equation 1.22) brings kinetic Alfvén waves into the system [*Drake*, 1995]. Figure 1-14 illustrates how the electron pressure term affects the structure of the dissipation region. The electron flow parallel to the magnetic field leads to a density asymmetry structure in contrast to the symmetric system as shown in Figure 1-13. The ions drift across the magnetic field lines to neutralize the electrons.

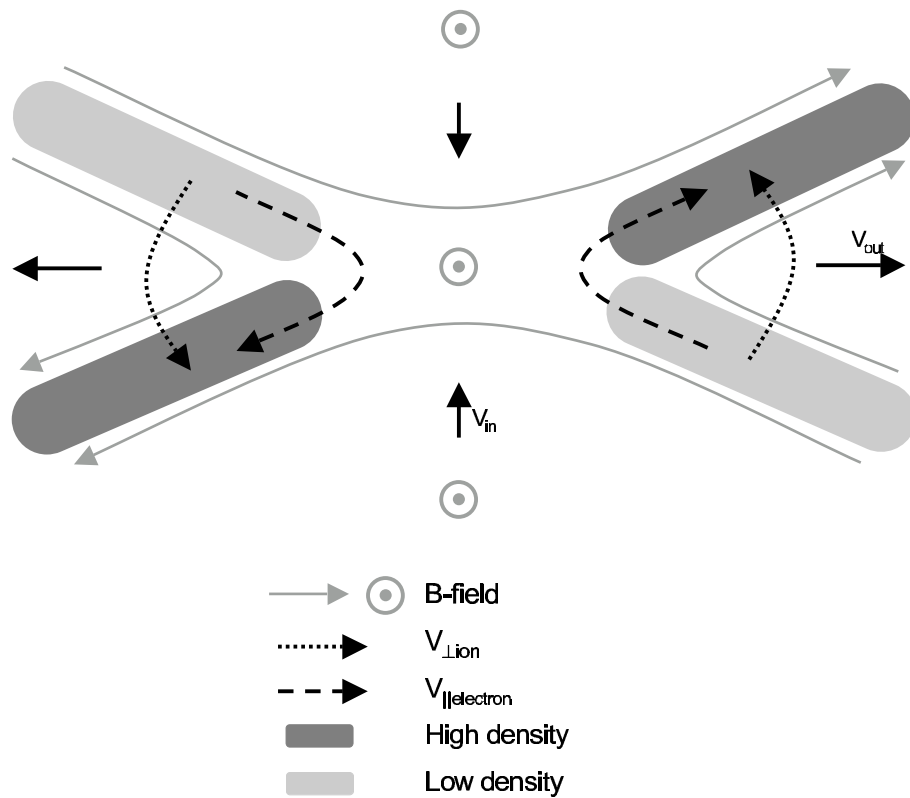


Figure 1·14: Schematic of the multiscale structure of the dissipation region when kinetic Alfvén waves play the role (the electron pressure is important). The electron flow parallel to the magnetic field leads to a density asymmetry structure in contrast to the symmetric system as shown in Figure 1·13. (after *Drake and Shay* [2007])

## Observations

Direct in-situ evidence for the occurrence of reconnection at the magnetopause is as follows:

(a) Minimum Variance Analysis (MVA, introduction to this technique is presented in Chapter 3 of this dissertation) of measured magnetic fields indicates the existence of a significant nonzero field component perpendicular to the magnetopause [e.g., *Sonnerup and Ledley, 1979; Gosling et al., 1982*] which is a topological requirement for reconnection to occur.

Figure 1.15 shows hodograms of the variation of the magnetic field through the magnetopause in boundary normal components. The  $B_L - B_M$  plane is the plane of the magnetopause. From Figure 1.15, it is clearly seen that the magnitude of the magnetic field is nearly constant and the tangential field vector rotated about  $120^\circ$  through the magnetopause. In addition there is a non-zero normal component. All of these signatures indicate that the magnetopause was approximately a rotational discontinuity.

(b) Plasma jets along the magnetopause away from the reconnection site and the plasma velocity and magnetic field satisfy the Walén [*Walén, 1944*] relation, i.e., the accelerated plasma flow is Alfvénic in the deHoffmann-Teller (HT) frame [*de Hoffman and Teller, 1950*] (a frame in which the electric field vanishes). This evidence has been called the "smoking-gun" evidence of reconnection at the subsolar magnetopause [*Sonnerup et al., 1995*].

As the magnetosheath plasma moves across the magnetopause in which the normal component of the magnetic field is not zero, its momentum components tangential to the magnetopause change in response to the tangential Maxwell stresses or the  $\mathbf{j} \times \mathbf{B}$  force. This process can be described by an ideal MHD rotational discontinuity for which the following relations are valid [*Hudson, 1970*]:

$$\rho(1 - \alpha) = \text{constant} \quad (1.34)$$

$$\mathbf{V} - \mathbf{V}_{HT} = \pm \mathbf{V}_A \quad (1.35)$$

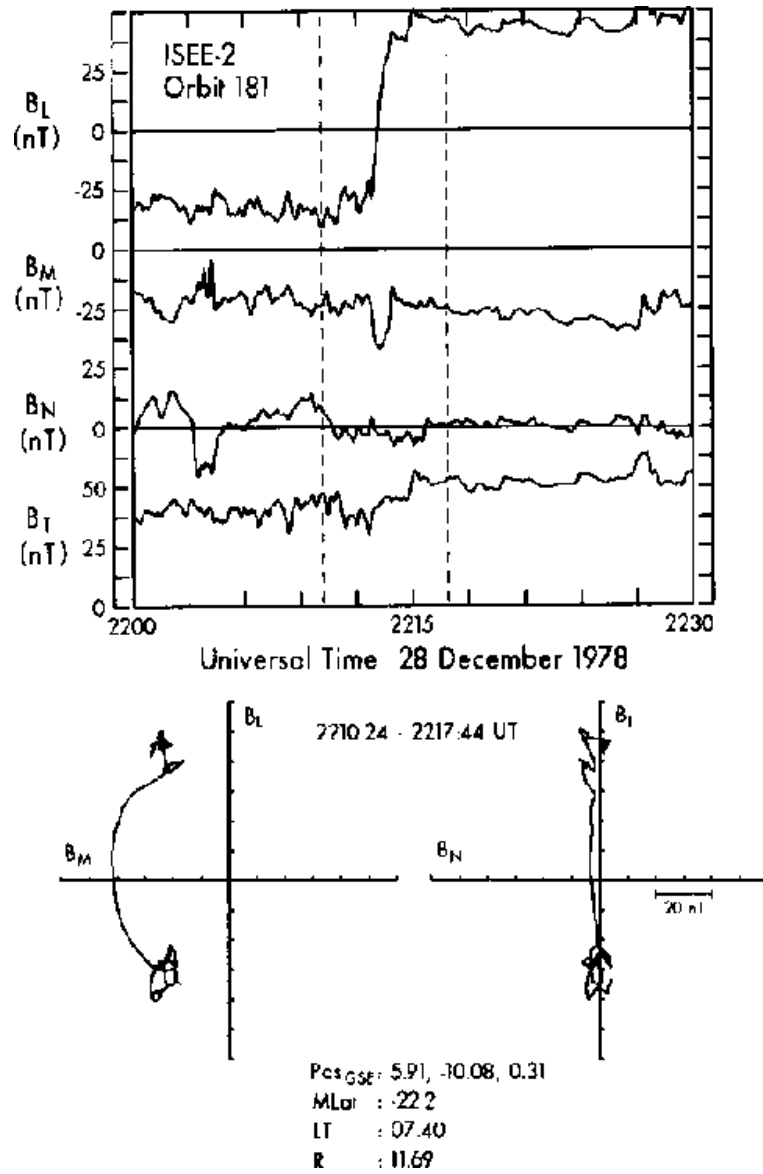


Figure 1-15: An example of the magnetopause as a rotational discontinuity. Top: Components and magnitude of the magnetic field in boundary normal coordinates for a magnetopause crossing observed by ISEE-2 on December 28, 1978. Bottom: Hodogram of the variation of the magnetic field vector through the magnetopause. [Russell *et al.*, 1990]

where

$$\alpha = (p_{\parallel} - p_{\perp})\mu_0/B^2$$

is the pressure anisotropy factor,  $\mathbf{V} - \mathbf{V}_{HT}$  is the plasma velocity observed in the HT frame [*de Hoffman and Teller, 1950*], and  $\mathbf{V}_A = \frac{\mathbf{B}}{\sqrt{\mu_0\rho}}$  is the Alfvén velocity. Equation 1.35 is called the Walén relation. More detailed information about HT frame and Walén test is presented in Chapter 3 of this dissertation. Two examples of the Walén test for two magnetopause crossings by the AMPTE/IRM spacecraft are shown in Figure 3.2. In example (a) on the left hand side, the Walén relation is not satisfied since the plasma flow velocities in the HT frame are much smaller than the Alfvén velocities. By contrast, example (b) on the right hand side shows a good agreement with the Walén relation.

(c) The reflection and transmission of magnetospheric and magnetosheath ion species occurs at the magnetopause [*Fuselier, 1995*]. This evidence strongly supports the kinetic description of quasi-static reconnection at the magnetopause [*Fuselier, 1995*] while the evidences (a) and (b) supports the fluid description of the magnetic reconnection [*Sonnerup et al., 1995*].

*Gosling et al. [1990]* first qualitatively described the particle behavior for quasi-stationary reconnection at the subsolar magnetopause as illustrated in Figure 1.16. When reconnection occurs, magnetosheath ions either reflect off the magnetopause or cross the boundary and enter the magnetosphere. Similarly the magnetospheric ions will either reflect off the magnetopause or cross the magnetopause and enter the magnetosheath [*Gosling et al., 1990*]. Thus two boundary layers which contains both magnetosheath and magnetospheric ion populations form, the magnetosheath boundary layer and the magnetospheric boundary layer.

Qualitative prediction of the ion distribution function near the magnetopause has been performed [*Cowley, 1980, 1995; Fuselier, 1995*]. In particular, only ions with velocities in excess of a threshold are able to cross the boundary and lead to the so-called "D-shaped" distributions for transmitted ions [*Sibeck et al., 1999*]. An example of the ion reflection and transmission at the magnetopause is shown in Figure 1.17. It shows ISEE-1 observations of



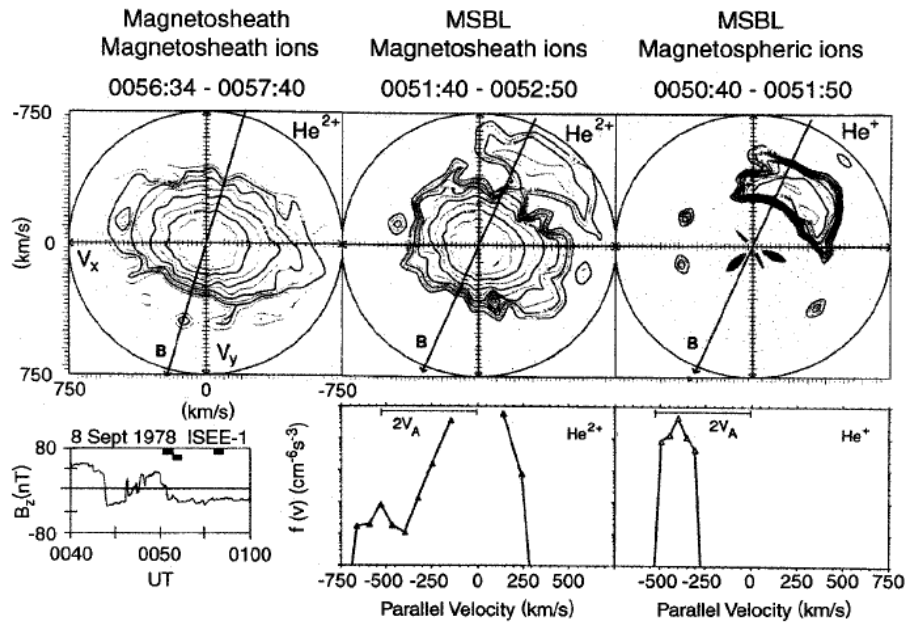


Figure 1-17: ISEE-1 observations of He<sup>+</sup> and He<sup>2+</sup> distributions in the magnetosheath and magnetosheath boundary layer. The upper three panels show contours of the ion velocity distribution in two-dimensional velocity space. Bottom panels show  $B_z$  together with cuts through the ion distribution along the field direction. The black horizontal bars mark the time interval when the distributions have been measured. (from *Fuselier* [1995])

He<sup>+</sup> and He<sup>2+</sup> distributions in the magnetosheath and the magnetosheath boundary layer. The upper three panels show contours of the ion velocity distribution in two-dimensional velocity space. Bottom panels show  $B_z$  together with cuts through the ion distribution along the field direction. Data are shown for He<sup>+</sup> of ionosphere origin and He<sup>2+</sup> of solar origin. The top left panel shows the He<sup>2+</sup> distribution in the magnetosheath. The top middle panel shows the He<sup>2+</sup> distribution in the magnetosheath boundary layer which consists of a central core of inflowing ions and an accelerated reflected component flowing antiparallel to the field. The top right panel shows that He<sup>+</sup> distribution is a D-shaped distribution with a cut-off at the field line speed implying that they are transmitted magnetospheric ions. These observations provides striking evidence in support of the kinetic picture of reconnection at the magnetopause [Fuselier *et al.*, 1991].

(d) The magnetic flux transfer events (FTEs) are observed at the vicinity of the magnetopause [Russell and Elphic, 1978]. Since their discovery [Haerendel *et al.*, 1978; Russell and Elphic, 1978], FTEs have been connected with patchy magnetic reconnection. One of the principal identifying marks of FTEs is the characteristic bipolar signature in the  $B_N$  component which is normal to the plane of the magnetopause. Another characteristic is the enhanced magnetic field strength at center of the event. Figure 1-18 shows a typical FTE identified by Russell and Elphic [1978]. Russell and Elphic [1978] proposed that the localized patchy reconnection leads to the formation of the FTEs. Figure 1-19 illustrates the Russell-Elphic model of elbow-shaped FTEs. This twisted magnetic flux tube connects the magnetosheath and the magnetosphere.

### 1.2.5 Other Plasma Transport Mechanisms

Magnetic reconnection has been regarded as a dominant mechanism for the transfer of mass, momentum and energy from the solar wind to the magnetosphere because of the good agreement between the observations and reconnection model predictions. Besides magnetic reconnection, several other mechanisms are also thought to be important for the transfer of plasma across the magnetopause. In this section, I briefly review these

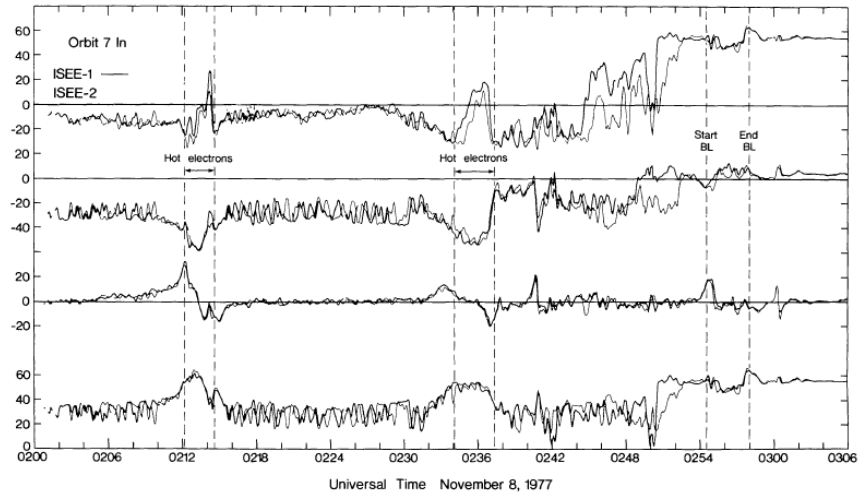


Figure 1-18: A typical FTE observed by ISEE spacecraft. This figure is from *Russell and Elphic* [1978].

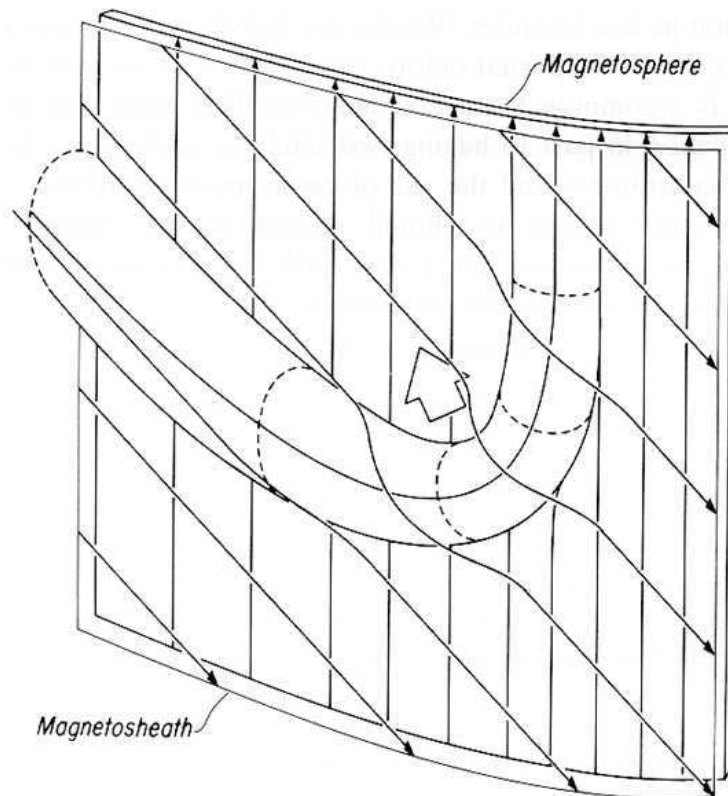


Figure 1-19: Schematic of the Russell and Elphic model of FTEs [*Russell and Elphic*, 1978].

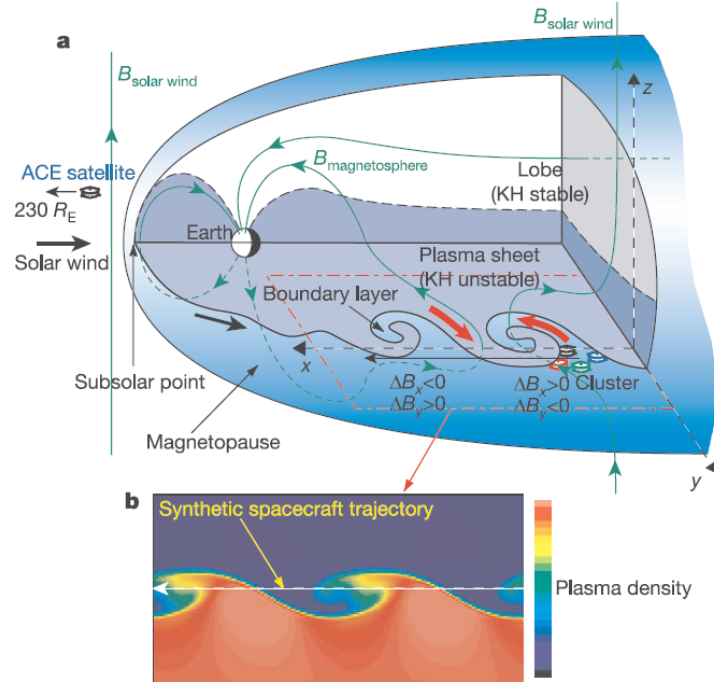


Figure 1-20: Three-dimensional cutaway view of Earth's magnetosphere, showing signatures of Kelvin-Helmholtz (KH) vortices. (a) Cutaway view of the magnetosphere with the KH vortices at the duskside magnetopause. (b) Vortex structure from a 3D numerical simulation of the magnetohydrodynamic KH instability under a magnetosphere-like geometry. Color-coded is the plasma density in an x-y cross-section cut below the equatorial plane. (from *Hasegawa et al.* [2004])

mechanisms.

### K-H Instability

The magnetopause is an ideal location for the development of the Kelvin-Helmholtz (KH) instability since it is a thin boundary with considerable velocity shear. Both MHD and hybrid simulations have been performed to investigate the role which the KH instability plays in the plasma transport process. Hybrid simulation results showed that the KH instability in an uniform plasma produced enhanced mixing inside the vortices and this mixing layer was identified as the low latitude boundary layer [*Fujimoto and Terasawa, 1994*].

Unambiguous evidence for rolled-up vortices at the flank magnetopause was reported by *Hasegawa et al.* [2004]. The authors argue that nonlinear Kelvin-Helmholtz (KH) instabilities along the flanks of the magnetosphere can lead to rolled-up small-amplitude vortices along the magnetopause surface as illustrated in Figure 1.20. These vortices can engulf plasma from either side of the magnetopause, allowing transport of solar wind plasma across the boundary. Observations of these KH vortices by the Cluster spacecraft have been reported by *Hasegawa et al.* [2004]. In addition, the co-location of two distinct plasma populations (cold solar wind  $< 2$  keV, and hot magnetospheric  $> 5$  keV) provides strong evidence that the transport of plasma had occurred [*Hasegawa et al.*, 2004].

### Diffusion

Diffusion is basically a resistive process which dominates only when high resistivity is present and other competing plasma transport process can be ignored [*Sibeck et al.*, 1999]. Diffusion requires a distortion of particle orbits. Collision is an obvious way to distort the particle orbit, however the plasma in the Earth's magnetosphere is almost collisionless. Thus mechanisms that can provide sufficiently strong particle scattering are required to distort the particle orbit. In the absence of the actual particle collision, wave particle interaction can provide such mechanisms which are called "anomalous resistive" diffusion [*Sibeck et al.*, 1999]. Many candidate instabilities has been proposed for anomalous diffusion, e.g., lower-hybrid drift instability and eddy turbulence [*Sibeck et al.*, 1999]. When the magnetic field varies in a small spatial scale or a short time scale, the first adiabatic invariants  $\mu = \frac{mv_{\perp}^2}{2B}$  of the charged particles are not conserved. The nonconservation of  $\mu$  can lead to velocity-space diffusion for the charged particles in the fluctuating magnetic field.

*Terasawa et al.* [1997] did a statistical survey of the properties of the near-Earth plasma sheet based on GEOTAIL observations. They found that during the periods when the northward IMF dominates, the plasma sheet becomes significantly cold and dense and the best correlations between the plasma sheet and the IMF parameters occur when the latter

quantities are averaged over 9 hours prior to the plasma sheet observations. Based on these results, they argued that there is a slow diffusive transport of the plasma from the solar wind into the plasma sheet through the magnetotail flanks.

### **Impulsive Penetration**

*Lemaire and Roth* [1978] first proposed that solar wind irregularities containing excess momentum can perturb the magnetopause boundary. Under certain conditions these irregularities are able to penetrate impulsively through the magnetopause, allowing the magnetosheath plasma to migrate onto the closed field lines in Earth's magnetosphere.

### **Direct Entry via Cusp**

The cusp is identified by the presence of magnetosheath plasma at high latitudes on the dayside magnetosphere [*Heikkila and Winningham, 1971*]. The cusp is like a window of the magnetosphere which allows the direct penetration of magnetosheath plasma to low altitudes. Observations show that the cusp is continuously open to the solar wind/magnetosheath, independent of the IMF direction [*Sibeck et al., 1999*].

## **1.3 Magnetospheric Cusp**

The existence of the magnetospheric cusp was first proposed by *Chapman and Ferraro* [1931]. As illustrated in Figure 1.1, the superconducting property of the magnetopause and the nature of the dipole field combine to produce magnetic nulls at high latitudes (labelled Q). The singular magnetic field line which extends from the Earth's surface to the magnetic null Q at the magnetopause is called the Chapman-Ferraro cusp. The stagnant flow in the cusp region was first predicted by a gas dynamic model [*Spreiter and Briggs, 1962*].

The launches of polar orbiting satellites provided the opportunity to investigate the cusp region with in-situ measurements. The magnetic cusp was first discovered by the presence of magnetosheath plasma at low altitudes on the dayside magnetosphere [*Heikkila and Winningham, 1971*]. The center location of the magnetospheric cusp is usually observed

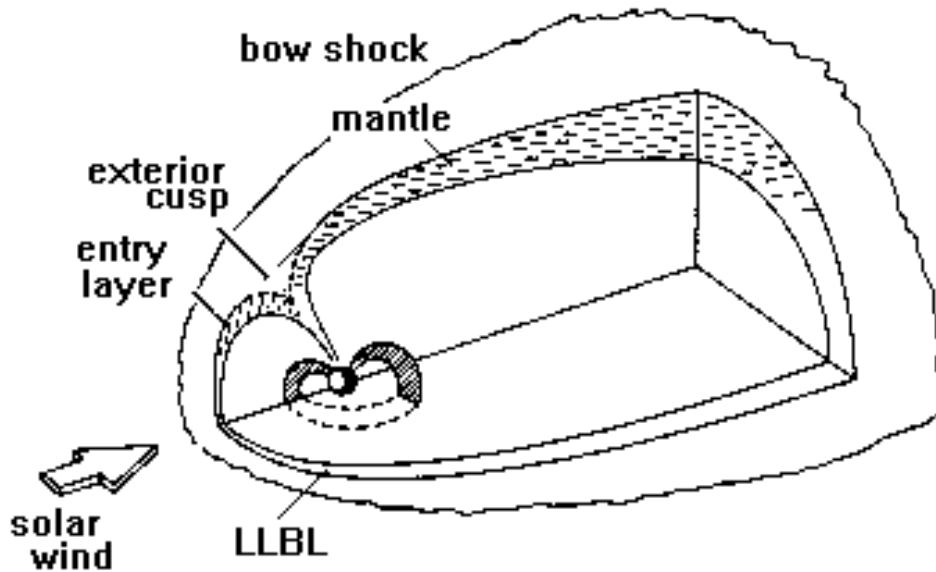


Figure 1·21: Illustration of the magnetospheric boundary layers. (This figure is from <http://www oulu.fi/ spaceweb/textbook/blayer.html>.)

at local noon (12 MLT) from  $75^\circ - 80^\circ$  invariant latitude, although it can vary over a few hours in MLT [e.g., *Heikkila and Winningham, 1971; Newell and Meng, 1988*]. Observations implied that the cusp is a funnel as illustrated in Figure 1·21. The outer part of the cusp with weak magnetic field is called the exterior cusp.

The magnetospheric cusp is a very complex region of the magnetosphere and it is greatly affected by the solar wind dynamic pressure and the IMF orientation. A detailed review of cusp observations is presented in Chapter 4.1.

#### 1.4 Mantle

The plasma mantle, which is located on the field lines where the injected magnetosheath plasma continues tailward, was first reported by *Rosenbauer et al. [1975]*. The plasma mantle covers the high-latitude magnetosphere poleward of the magnetospheric cusp region as illustrated in Figure 1·21. The plasma density in the mantle varies from 0.01 to  $1 \text{ cm}^{-3}$ . The temperature is about 100 eV and the tailward flow velocities is 100-200 km/s

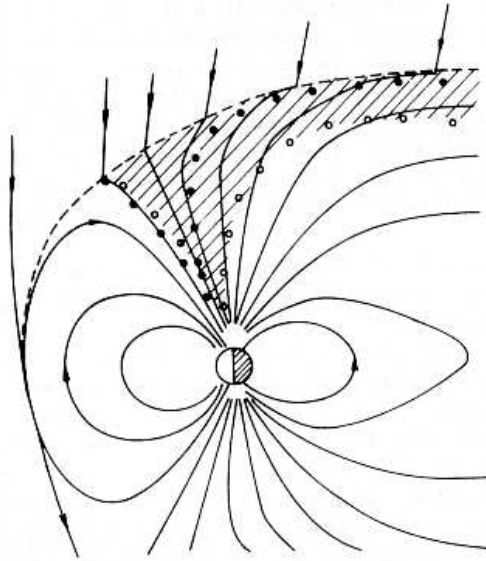


Figure 1-22: Illustration of the formation of the mantle. (from *Paschmann* [1979])

[*Rosenbauer et al.*, 1975].

The plasma mantle is formed when magnetic reconnection processes occur at the sub-solar point when the IMF is southward [*Kivelson and Russell*, 1995]. The newly opened magnetic field lines carrying the magnetosheath and magnetospheric plasma convect to the tail and form the mantle as illustrated in Figure 1-22.

### 1.5 Entry Layer

The entry layer [*Paschmann et al.*, 1976] is located on the magnetospheric field lines just equatorward of the cusp as shown in Figure 1-21. It is a region of diffusive, turbulent entry of magnetosheath plasma onto closed field lines probably caused by the eddy flow that maps to the low-altitude cusp [*Haerendel et al.*, 1978]. It has been found that in the entry layer the plasma density is almost as high as the magnetosheath but generally lacking the strong antisunward plasma flow. In fact sunward flow has even been reported by *Paschmann et al.* [1976]. *Lundin* [1985] suggested that a characteristic feature of the entry layer is a strong variability of magnetosheath plasma entry with frequent plasma

injection. However, the entry layer is basically a region occurring during southward IMF [Zong *et al.*, 2005a] since the cusp geometry will be changed by high latitude reconnection when the IMF is northward.

## 1.6 Low Latitude Boundary Layer

The low latitude boundary layer contains both magnetosheath and magnetospheric plasma and is located earthward of the magnetopause [Eastman, 1976]. The low latitude boundary layer extends from dayside to nightside along the flanks (see Figure 1.21).

The low latitude boundary layer has been observed both on open field lines [Fuselier *et al.*, 1991] and on closed field lines [e.g., Williams, 1985; Song *et al.*, 1993]. The low latitude boundary layer on open field lines results from magnetic reconnection at the magnetopause as illustrated in Figure 1.16. The mechanisms for the formation of the low latitude boundary on closed field lines are still under debate. There are at least six mechanisms have been proposed: (1) local diffusive entry (2) interchange mixing in the exterior cusp (3) gradient drift entry (4) impulsive penetration (5) stochastic "re-reconnection" (6) high latitude reconnection [Lotko and Sonnerup, 1995]. Some of these mechanisms have been reviewed in section 1.2.5. The high latitude reconnection mechanism is a promising mechanism and has attracted much attention.

Dual lobe reconnection, proposed first by Dungey [1961], occurs tailward of the cusp region where magnetospheric magnetic fields are antiparallel to the IMF during periods of northward IMF. Song and Russell [1992] further developed this model. As shown in Figure 1.23, simultaneous or near-simultaneous reconnection in both the north and the south high-latitudes results in a closed flux tube that contains magnetosheath plasma. This flux tube then relaxes, expands and sinks into the magnetosphere. This expansion of plasma of magnetosheath origin along the magnetopause forms a low latitude boundary layer extending toward the terminator. The magnetosheath plasma on these closed LLBL flux tubes continues to flow anti-sunward. Although field line tension decelerates the plasma, it continues to move toward the tailward flanks of the magnetopause. The Dual-

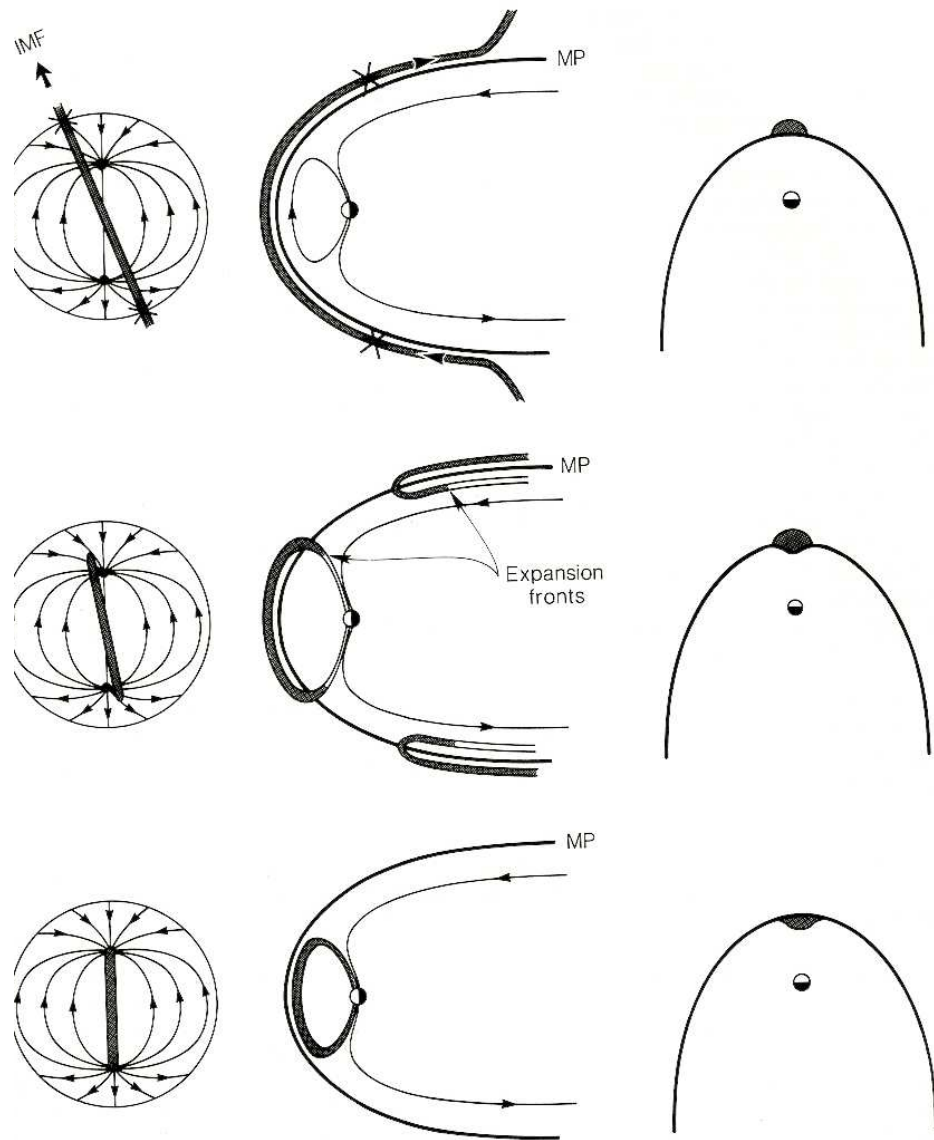


Figure 1-23: Illustration of dual lobe reconnection model [Song and Russell, 1992] for the formation of the low latitude boundary layer during periods of northward IMF. (a) During periods of northward IMF, reconnection takes place at high latitudes at both hemispheres. (b) The dual lobe reconnection results in a closed flux tube containing sheath plasma. (c) The closed flux tube then contracts as it moves in radially through the magnetopause, resulting in magnetosheath plasma in the magnetosphere. (This figure is from Song and Russell [1992].)

Lobe Reconnection Model is also a promising model for the formation of the cold dense plasma sheet during times of northward IMF.

## 1.7 Goals of This Dissertation

Mass, momentum and energy are transferred from the solar wind into the magnetosphere via their interface, the magnetospheric boundaries. Many fascinating plasma phenomena and processes happen at the magnetospheric boundaries such as magnetic reconnection, particle acceleration, wave particle interactions and so on. High latitude boundaries including the high latitude magnetopause, cusp, entry layer and mantle have been rarely studied compared to the subsolar magnetopause and low latitude boundary layer since only a few spacecraft have visited there.

Most of the previous studies on the magnetospheric boundaries are based on single spacecraft data which is not able to distinguish between the spatial and temporal variations. The magnetospheric boundaries are very dynamic regions which are very sensitive to the solar wind and IMF condition. Thus the separation of spatial and temporal effects is very important in the study of magnetospheric boundaries. The Cluster spacecraft with four identical satellites forming a tetrahedron in space can help to distinguish spatial from temporal variations.

There are many long standing open questions about high latitude boundaries, e.g.,

- What is the magnetic structure of high latitude boundaries during various interplanetary magnetic field (IMF) conditions?
- Do the boundaries lose their distinct well-defined edge during southward IMF conditions?
- How do they respond to outside (solar wind) and inside (magnetic storm and sub-storm) conditions?
- What is the behavior of energetic particles in these regions?

This dissertation addresses these questions via extensive Cluster data analysis and comparison with global MHD simulations.

This dissertation is organized as follows: Chapter 2 presents an introduction to the Cluster mission and instruments onboard. Chapter 3 presents a description of the analysis methods used in this dissertation. Chapter 4 and 5 present the main results on the cusp region and high latitude magnetopause respectively. A comparison of observations to MHD simulations for a real cusp event is presented in chapter 6. Chapter 7 summarizes the main results and proposes future works.

## Chapter 2

# Instrumentation

### 2.1 Cluster Spacecraft

The aim of the ESA/NASA Cluster mission is to investigate small scale structures of the Earth's plasma environment in three dimensions [Escoubet *et al.*, 1997]. With four identical spacecraft in a tetrahedral configuration, the Cluster spacecraft will permit the accurate determination of three-dimensional and time-varying phenomena and will make it possible to distinguish between spatial and temporal variations.

The four Cluster spacecraft were launched as two pairs in July and August, 2000. They orbit the Earth in an elliptical polar orbit with a perigee of  $3 R_E$  and an apogee of  $19 R_E$ . The orbiting period is 57 hours. The plane of the Cluster orbit will cross all regions of scientific interest (solar wind and bow shock, magnetopause, polar cusp, magnetotail and auroral zone) during a year. The apogee of the Cluster orbit is in the day side during the northern hemisphere winter season as shown in Figure 2-1. The night side auroral zone, both northern and southern exterior cusp regions, the magnetopause and the bow shock are crossed by Cluster along this orbit. In this dissertation, the Cluster data obtained during the winter season of the year 2001 to 2004 were used to study the high latitude magnetopause and the exterior cusp region. During the northern hemisphere summer season, the apogee precesses to the night side as shown in Figure 2-2. When the apogee is in the magnetotail, the regions crossed by Cluster are mid-altitude cusp, the polar cap, lobe and the plasma sheet.

The orbital parameters of the four spacecraft are slightly different to form a tetrahedral configuration. Figure 2-3 shows the separation between four spacecraft during the Cluster

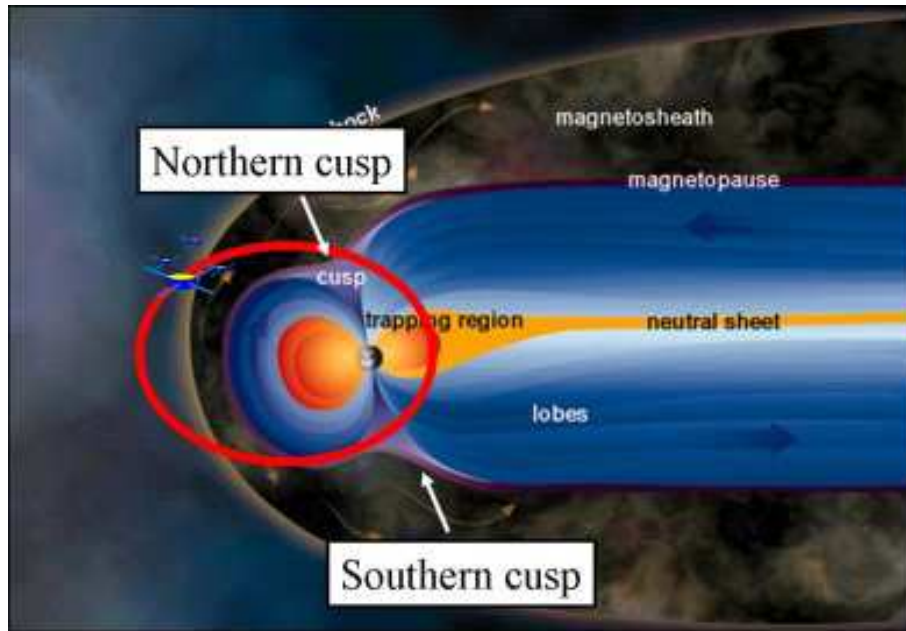


Figure 2-1: Cluster orbit with the apogee at the day side during the northern hemisphere winter season every year. This figure is from ESA.

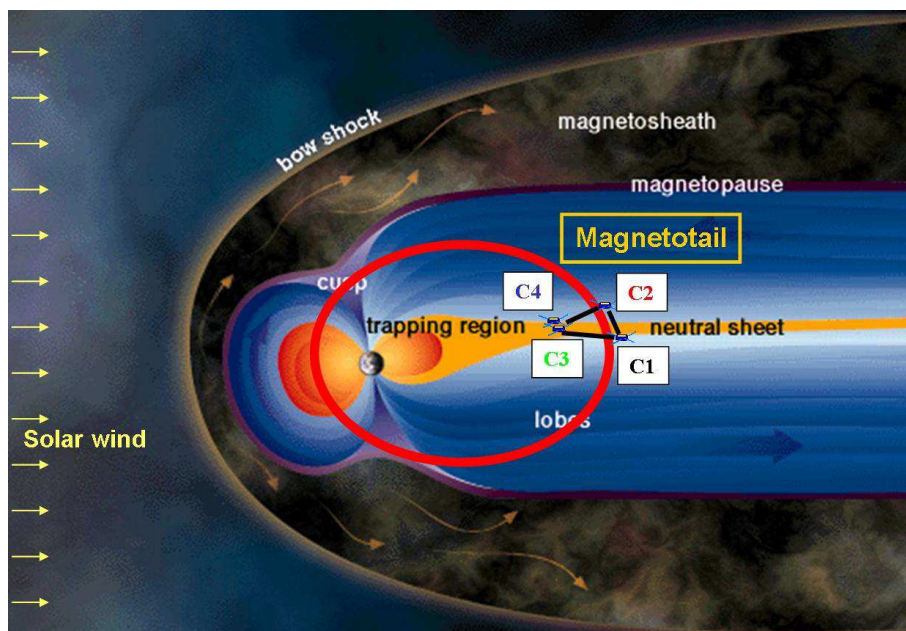


Figure 2-2: Cluster orbit with the apogee at the night side during the northern hemisphere summer season every year. This figure is from ESA.

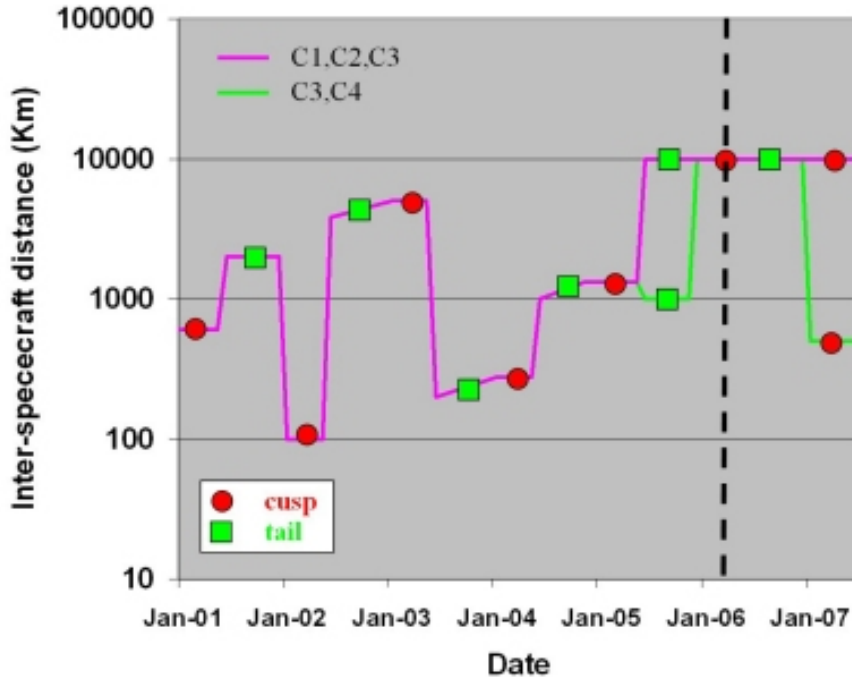


Figure 2-3: The separation between four spacecraft during the Cluster mission. This figure is from ESA.

mission. The separation is around 600 km for the cusp crossing during the first year (2001) [Escoubet *et al.*, 1997]. For the following years the separation varies from 100 km (year of 2002) to 10000 km (year of 2006).

Each Cluster spacecraft is spin-stabilized at 15 rpm with spin axis pointing toward the South ecliptic pole [Escoubet *et al.*, 1997]. Most of the data used in this dissertation is spin averaged (4-second resolution) data. In case studies, higher resolution data, e.g., 5 Hz spacecraft potential data and 23 Hz magnetic field data, are used.

## 2.2 Instruments onboard Cluster

The instruments on board four Cluster spacecraft are identical. Table 2.1 lists the 11 instruments onboard each Cluster spacecraft and their Principal Investigators. The data used in this dissertation is obtained by the RAPID, CIS, PEACE, FGM and EFW instruments. We will introduce these instruments briefly in the following sections.

Table 2.1: Instruments on cluster

Acronym	Instrument	Principal investigator
FGM	Fluxgate magnetometer	A. Balogh (IC, U.K.)
STAFF	Spatio-temporal analysis of field fluctuation experiment	N. Cornilleau-Wehrlin (CETP, France)
EFW	Electric field and wave experiment	G. Gustafsson (IRFU, Sweden)
WHISPER	Waves of high frequency and sounder for probing of electron density by relaxation	P. M. E. Décréau (LPCE, France)
WBD	Wide band data	D. A. Gurnett (Iowa U., U.S.A.)
DWP	Digital wave processing experiment	L. J. C. Woolliscrooftb, H. Alleyne (Sheffield U., U.K.)
EDI	Electron drift instrument	G. Paschmann (MPE, Germany)
ASPOC	Active spacecraft potential control	W. Riedler (IWF, Austria)
CIS	Cluster ion spectrometry	H. Rème (CESR, France)
PEACE	Plasma electron and current experiment	A. D. Johnstone (MSSL, U.K.)
RAPID	Research with adaptive particle imaging detectors	P. W. Daly (MPA, Germany)

### 2.2.1 RAPID

The RAPID (Research with Adaptive Particle Imaging Detectors) instrument is an advanced particle detector which records high energy electrons and ions present in geospace [Wilken *et al.*, 1997]. The novel detector design allows the measurement of angular distribution over a range of  $180^\circ$  in the polar angle. The identification of ions is based on an analysis of the particle's velocity and energy and the identification of electrons is based on the energy-range relationship. The energy ranges are 30 to 4000 keV for ions and 30 to 500 keV for electrons [Wilken *et al.*, 1997].

Figure 2·4(a) shows a photograph of of the RAPID instrument. The ion sensor, the Imaging Ion Mass Spectrometer (IIMS), is on the left hand side and the electron sensor the Imaging Electron Spectrometer (IES) is on the right hand side.

#### Imaging Ion Mass Spectrometer (IIMS)

The IIMS is composed of three identical sensor heads. Figure 2·4(b) shows the cross section of one of the three ion sensor heads. Each ion sensor head is composed of a Time of Flight (TOF) and energy detection system. The purpose of the Time of Flight (TOF) system is to obtain the particle velocity by measuring the flight time  $T$  it takes the particle to travel a known distance in the detector geometry. The mass of a particle can be uniquely

determined by the measurements of the energy  $E$  and velocity  $V$  since  $E = \frac{1}{2}MV^2$ . The TOF system is the entry element of the sensor. The TOF system is composed of a thin foil and the front surface of the solid state energy detector (SSD, energy detector) which is mounted at the rear of the system. When energetic particles travel through the foil, a small fraction of their energy is absorbed by the foil and secondary electrons are released. These secondary electrons are accelerated and detected by a micro channel plate (MCP). The output signal of MCP is used as the START signal for the  $T$  measurement. When the energetic particles impact the surface of the energy detector, secondary electrons are released similarly and the signals are used as the STOP signal for the  $T$  measurements. The remaining energy  $E$  of the particles is measured by the energy detector. The particles of different mass, hydrogen, helium and CNO, can be identified in the  $E - T$  plots [Wilken *et al.*, 1997].

Two collimators in front of the TOF system as shown in Figure 2.4(b) define a field of view of  $6^\circ$  lateral and  $60^\circ$  polar angle. Three identical sensor heads covers  $180^\circ$  in polar angle. The complete azimuthal angles are covered as the spacecraft rotates. As shown in Figure 2.4(c), the azimuthal coordinate is divided by 16 sectors with sector #13 pointing to the sun. The unique design features of IIMS provides the complete  $4\pi$  steradian sphere overview as shown in Figure 2.4(d).

Converting the observed counting rates  $n$  (cts/s) to particle flux  $j$  in physical units is represented by functions of the form

$$j = \frac{n}{GF \cdot \varepsilon(E, M)} \quad (2.1)$$

where  $GF$  denotes the geometric factor and  $\varepsilon$  describes the detection efficiency as a function of particle energy  $E$  and mass  $M$ . The performance parameters are summarized in Table 2.2.

## RAPID/CLUSTER II

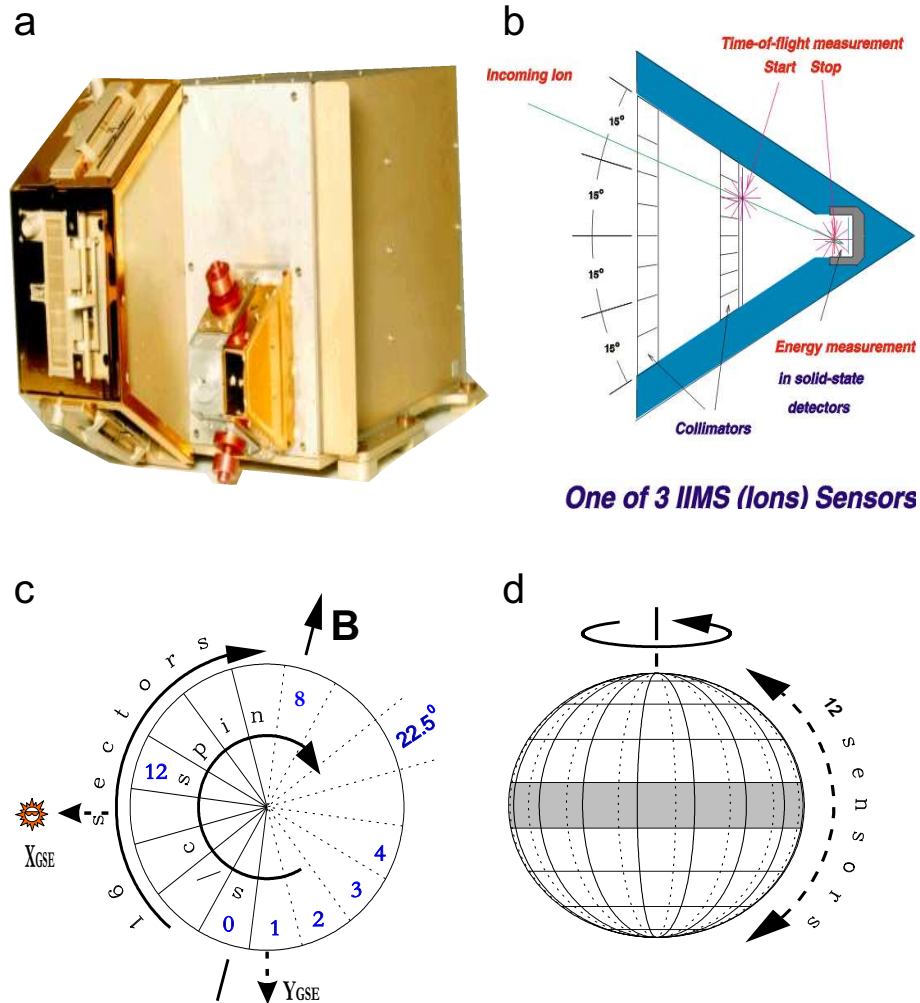


Figure 2-4: (a) A photograph of the RAPID instrument. The ion sensor IIMS is on the left hand side and the electron sensor IES is on the right hand side. (b) The cross section of one of the three ion sensors. The TOF system is composed of a thin foil and the front surface of the solid state energy detector (SSD, energy detector) which is mounted at the rear of the system. The foil and the front surface of the solid state detector define the START and STOP points of the  $T$  measurements. (c) The complete set of azimuthal angles are covered as the spacecraft rotates. The azimuthal coordinate is divided by 16 sectors with sector #13 pointing to the sun. (d) Illustration of the complete  $4\pi$  steradian sphere coverage. This figure is from *Wilken and Zong* [2001].

Table 2.2: Characteristic parameters of the IIMS and IES sensor systems

	IIMS	IES
<b>Energy range (keV)</b>		
Hydrogen	30 - 4000	
Helium	30 - 4000	
CNO	210-1500 (oxygen)	
Electrons		30 - 500
ENA	40 -200	
Mass classes (amu)	1, 4, 12-16, 28-56	
Mass resolution (A/dA)	4 (oxygen)	
Field-of-view	$\pm 3^\circ \times 180^\circ$	$\pm 17.5^\circ \times 180^\circ$
<b>Angular coverage</b>		
Polar (range/intervals)	180°/12	180°/9
Azimuthal (range/sectors)	360°/16	360°/16
<b>Deflection voltage (kV)</b>		
Range/steps	0-10/16	
<b>Geometric factor (<math>cm^2 sr</math>)</b>		
Total (180°)/per pixel	$2.7 \times 10^{-2}/2.2 \times 10^{-3}$	$2.0 \times 10^{-2}/2.2 \times 10^{-3}$

### Imaging Electron Spectrometer (IES)

The Imaging Electron Spectrometer (IES) is designed to detect electrons from 30 to 500 keV. Figure 2-5 shows the cross section of the IES head. The solid state detectors with three individual elements detect electrons passing through the pinslit which divides the 60° segment into three 20° angular intervals. Three of these detector assemblies as shown in the sketch at the top left corner of Figure 2-5 cover 180° in polar angle [Wilken *et al.*, 1997].

### 2.2.2 CIS

The Cluster Ion Spectrometry (CIS) experiment is a comprehensive plasma spectrometry which is capable of obtaining full three-dimensional ion distributions [Rème *et al.*, 1997]. The CIS experiment consists two instruments, a Hot Ion Analyser (HIA) and a time-of-flight ion COmposition and DIstribution Function analyser (CODIF). CODIF measures the distribution of the major ion species ( $H^+$ ,  $He^+$ ,  $He^{++}$ , and  $O^+$ ) with energies less than 40 keV/e with angular resolution of  $22.5^\circ \times 10.25^\circ$ . HIA measures the distribution of ions of 5 eV/e to 32 keV/e with an angular resolution of  $5.6^\circ \times 5.6^\circ$  [Rème *et al.*,

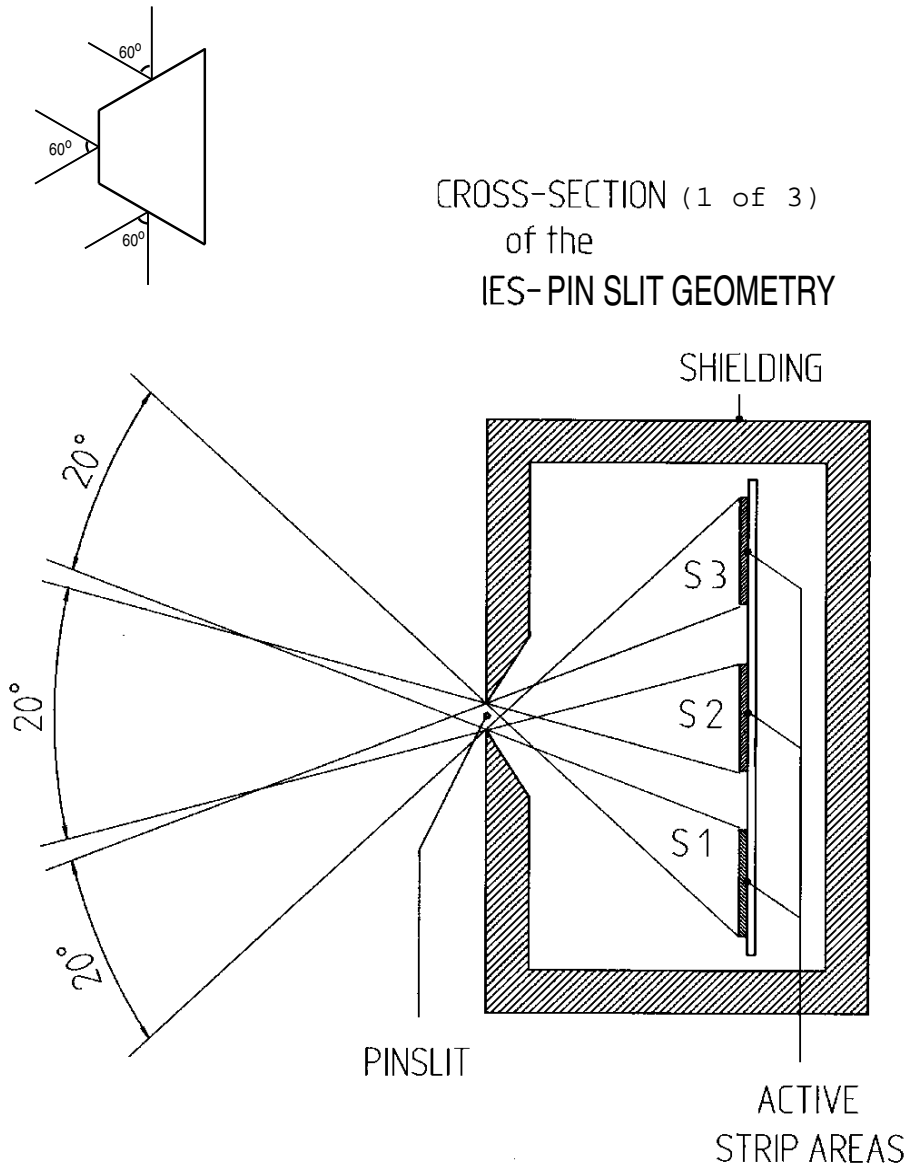


Figure 2-5: The cross section of the IES head. The solid state detectors with three individual elements detect electrons passing through the pin slit which divides the  $60^\circ$  segment into three  $20^\circ$  angular intervals. The sketch at the top left corner shows that three of these detector assemblies cover  $180^\circ$  in polar angle. This figure is from *Wilken et al.* [1997].

1997]. The plasma ion density, temperature and flow velocity are obtained based on the ion distribution function. The time resolution of CIS measurements is 4 seconds.

### 2.2.3 PEACE

The Plasma Electron and Current Experiment (PEACE) measures the three-dimensional velocity distribution of electrons in the energy range from 0.59 eV to 26.4 keV. The PEACE instrument normally scans the electron distribution in half a spacecraft rotation or 2 second which is the fastest time resolution for complete distributions. Partial distributions can be obtained in as little as 62.5 ms and angular distributions at a fixed energy in 7.8 ms [Johnstone *et al.*, 1997].

Figure 2-6 summarizes the energy range covered by RAPID, CIS and PEACE instruments onboard Cluster spacecraft.

### 2.2.4 FGM

The Fluxgate magnetometer (FGM) is designed to measure the magnetic field vectors at high time resolution (up to 67 vectors  $s^{-1}$ ) [Balogh *et al.*, 1997]. Combining the magnetic field data from four Cluster spacecraft is able to provide parameters such as the current density vector and the geometry and structure of discontinuities. More detailed information is provided in Chapter 3.

### 2.2.5 EFW

The Electric Field and Wave (EFW) experiment is designed to measure the electric-field and density fluctuations [Gustafsson *et al.*, 1997]. The EFW instrument is capable of measuring:

- Spin plane components ( $E_x$  and  $E_y$ ) of the quasi-static electric-field vector, over a dynamic range of 0.3 to 700  $mV m^{-1}$ , with time resolution down to 0.1 ms.
- Oscillating electric-field in the range 50-8000 Hz and amplitude range 10  $mV m^{-1}$  to 1  $\mu V m^{-1}$ .
- The thermal plasma density, over a dynamic range of 1 to 100  $cm^{-3}$ .

## Particle Instrumentation on Cluster II

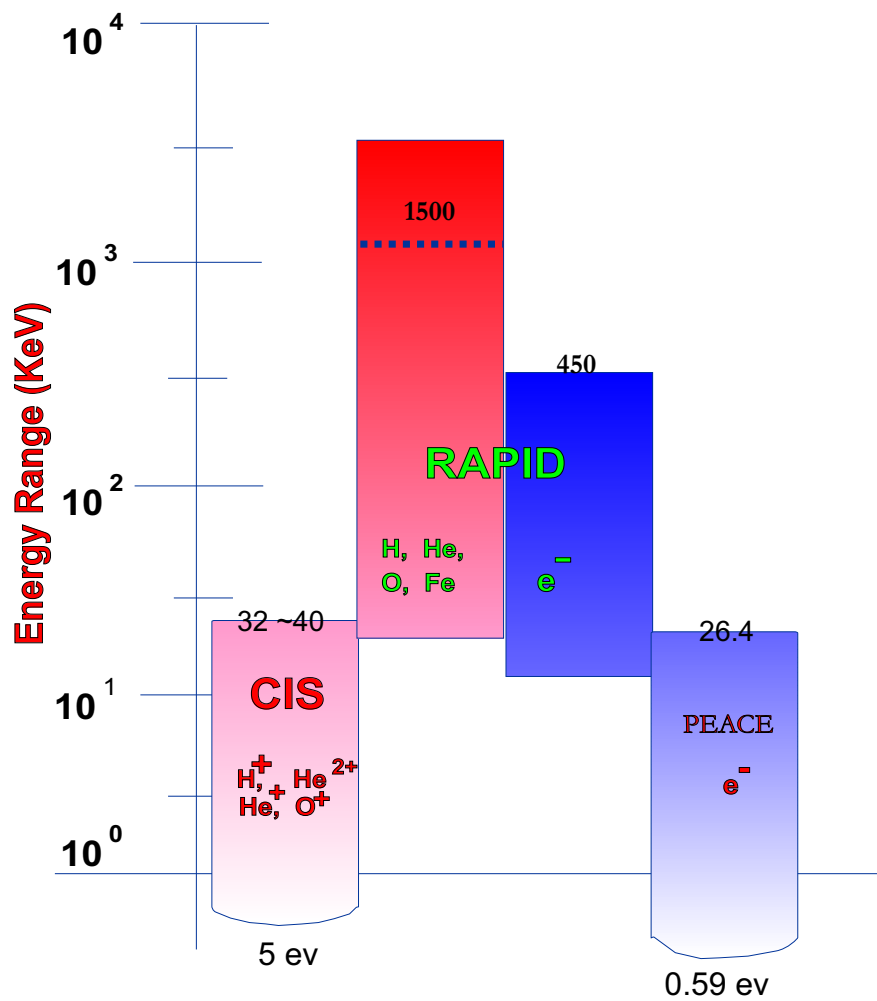


Figure 2-6: Energy range covered by RAPID, CIS and PEACE instruments onboard Cluster spacecraft. This figure is from *Wilken and Zong [2001]*.

- Plasma density fluctuations over a dynamic range of 1 to 50% with a time resolution of 0.1 ms.
- Time delays between signals from up to four different antenna elements on the same spacecraft, with a time resolution of 110  $\mu\text{s}$ .
- The spacecraft potential which can give information about electron density in the range  $10^{-2}$ - $10\text{ cm}^{-3}$  with time resolution down to 0.2 s [*Gustafsson et al., 1997*].

## Chapter 3

### Methods

This chapter presents an introduction to the main methods used in this dissertation: Minimum Variance Analysis (MVA) method, multi-spacecraft timing technique, Walén test and the curlometer technique.

#### 3.1 Minimum Variance Analysis

The Minimum Variance Analysis (MVA) technique was first developed by *Sonnerup and Cahill* [1967] to determine the normal direction of a one-dimensional or approximately one-dimensional current layer, wave front, or other transition layer. The MVA method is based on the solenoidality of the magnetic field:

$$\nabla \cdot \mathbf{B} = 0 \tag{3.1}$$

For an idealized one dimensional ( $\partial/\partial x = 0$ ,  $\partial/\partial y = 0$ ) transition layer, equation 3.1 can be rewritten as

$$\partial B_z / \partial z = 0 \tag{3.2}$$

In other words, the normal component of the magnetic field is continuous across this transition layer. If three distinct magnetic field vectors,  $\mathbf{B}_b$  (before crossing),  $\mathbf{B}_d$  (during crossing) and  $\mathbf{B}_a$  (after crossing) as shown in Figure 3.1, can be measured at the same time, the normal vector  $\mathbf{n}$  can be determined. Since

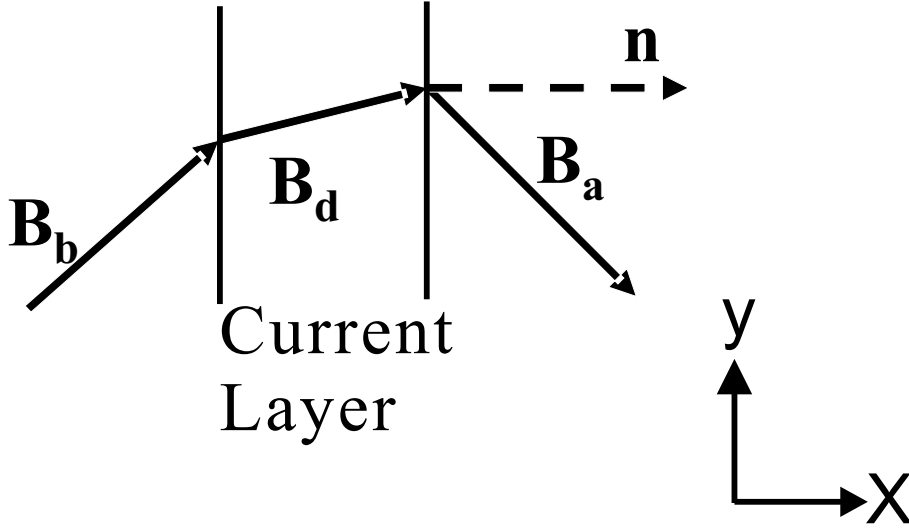


Figure 3-1: Projection onto the the  $xy$  plane of three  $\mathbf{B}$  vectors measured during a spacecraft crossing of a 1-D current layer.

$$\mathbf{B}_b \cdot \mathbf{n} = \mathbf{B}_d \cdot \mathbf{n} = \mathbf{B}_a \cdot \mathbf{n} \quad (3.3)$$

the vectors  $(\mathbf{B}_b - \mathbf{B}_a)$  and  $(\mathbf{B}_b - \mathbf{B}_d)$  are tangential to the current layer so that their cross product, if it is not zero, is along  $\mathbf{n}$ :

$$\mathbf{n} = \pm \frac{(\mathbf{B}_b - \mathbf{B}_a) \times (\mathbf{B}_b - \mathbf{B}_d)}{|\mathbf{B}_b - \mathbf{B}_a| \times |\mathbf{B}_b - \mathbf{B}_d|} \quad (3.4)$$

For real transition layer crossings there are usually more or less pronounced deviations from the ideal 1-D model described above. The transition layer is likely to have 2-D or 3-D structures which evolve in time and to have temporal fluctuations in the normal orientation as well. Considering the real situation that many magnetic field vector measurements,  $\mathbf{B}^i$  ( $i = 1, 2, 3 \dots N$ ) can be made by the high time resolution magnetometer experiments, *Sonnerup and Cahill* [1967] designed the MVA technique to minimize the non-ideal effects mentioned above. As the best estimate of  $\mathbf{n}$ , the MVA method identifies the direction along which the field-component set  $\mathbf{B}^i \cdot \mathbf{n}$  ( $i = 1, 2, 3 \dots N$ ) has minimum variance, i.e.,  $\mathbf{n}$

is determined by minimization of

$$\sigma^2 = \frac{1}{N} \sum_{i=0}^N |(\mathbf{B}^i - \langle \mathbf{B} \rangle) \cdot \mathbf{n}|^2 \quad (3.5)$$

where the average  $\langle \mathbf{B} \rangle$  is defined by

$$\langle \mathbf{B} \rangle = \frac{1}{N} \sum_{i=0}^N \mathbf{B}^i \quad (3.6)$$

Minimization of Equation 3.5 is equivalent to finding the eigenvalues of the magnetic variance matrix

$$M_{\alpha\beta} \equiv \langle B_\alpha B_\beta \rangle - \langle B_\alpha \rangle \langle B_\beta \rangle \quad (3.7)$$

Since  $M_{\alpha\beta}$  is symmetric, the eigenvalues  $\lambda_1$ ,  $\lambda_2$  and  $\lambda_3$  (given in order of decreasing magnitude) are all real and the corresponding eigenvectors,  $\mathbf{x}_1$ ,  $\mathbf{x}_2$ ,  $\mathbf{x}_3$  are orthogonal. The three eigenvectors represents the directions of maximum, intermediate and minimum variance of the magnetic field along each vector. The eigenvector  $\mathbf{x}_3$  associated with the smallest eigenvalue  $\lambda_3$  is used as the estimator for the normal direction of the transition layer. The other two eigenvectors  $\mathbf{x}_1$  and  $\mathbf{x}_2$ , corresponding to maximum and intermediate variance, are tangential to the transition layer and the set  $\mathbf{x}_1$ ,  $\mathbf{x}_2$ ,  $\mathbf{x}_3$  arranged as a convenient local coordinate system are called the *LMN* coordinate system where *L*, *M* and *N* represents the maximum, intermediate and minimum variance direction respectively. The MVA method had been used to determine the normal direction of various boundaries in Chapter 5 of this dissertation.

When the three eigenvalues of the variance matrix are distinct, the matrix is non-degenerate. This is the most common situation in practice but there are also a significant number of cases where near degeneracy occurs. When two eigenvalues are nearly the

same, the uncertainty in the corresponding eigenvectors is large. So to obtain a reliable estimator of the normal direction of a transition layer, the ratio of intermediate to minimum eigenvalue should be large.

When the MVA method is not valid, e.g., intermediate eigenvalue = minimum eigenvalue, a timing technique is used to obtain the normal direction of a boundary in this dissertation.

### 3.2 Multi-Spacecraft Timing Technique

The timing (or triangulation) technique was first applied by *Russell et al.* [1983] to determine the normal direction of a boundary and the velocity of the boundary motion in the normal direction using four spacecraft data.

Small spacecraft separation scales are particularly well-suited for examining the boundary motion of structures. If the same planar boundary, moving at a constant velocity, passes several spacecraft, the relative positions and timings can be used to construct the boundary normal direction and speed, since

$$V_n = \frac{\mathbf{r}_{\alpha\beta} \cdot \mathbf{n}}{t_{\alpha\beta}} \quad (3.8)$$

where  $\mathbf{r}_{\alpha\beta}$  is the separation vector between any spacecraft pair and  $t_{\alpha\beta}$  is the time difference between this pair for a particular boundary. Thus, given 4 spacecraft, the normal vector and normal propagation velocity  $V_n$  can be determined. The timing technique is used to determine the normal direction and velocity of a structure in this dissertation.

### 3.3 Walén Test

The Walén test requires a determination of the plasma velocities in the deHoffmann-Teller frame, hereafter referred to as the HT frame, and their relation to the local measured Alfvén velocities  $\mathbf{V}_A = \frac{\mathbf{B}}{\sqrt{\mu_0 \rho}}$ , where  $\rho$  is the measured mass density. It is one of the major methods to identify the magnetic reconnection process. To understand how the Walén test

works, one has to know what the HT frame is and how to determine an HT frame from experimental data.

### 3.3.1 HT frame

The HT frame [*de Hoffman and Teller*, 1950] is a frame in which the electric field vanishes, i.e.,

$$\mathbf{E}' = \mathbf{E} + \mathbf{V}_{HT} \times \mathbf{B} = 0 \quad (3.9)$$

It follows from Faraday's law, in the HT frame, that  $\nabla \times \mathbf{E}' = -(\partial \mathbf{B} / \partial t)' = 0$ . In other words, the existence of an HT frame indicates that the magnetic field structure sampled is quasi-stationary when viewed in this frame. The HT frame facilitates further analysis and interpretation of the data.

*Sonnerup et al.* [1987] developed a least-squares analysis technique to find a HT frame based on single spacecraft data. To obtain  $\mathbf{V}_{HT}$  from a set of measurements of plasma bulk velocity,  $\mathbf{v}^m$ , and magnetic field,  $\mathbf{B}^m$ ,  $m = 1, 2, \dots, M$ , one may seek a frame in which the mean square of the electric field is as small as possible. In other words, the purpose is to find an approximate value  $\mathbf{V}_{HT}$  which minimizes the quantity:

$$D(\mathbf{V}) = \frac{1}{M} \sum_{i=0}^M |\mathbf{E}'|^2 = \frac{1}{M} \sum_{i=0}^M |\mathbf{v}^m - \mathbf{V} \times \mathbf{B}^m|^2 \quad (3.10)$$

The minimization condition  $\nabla_{\mathbf{V}} D = 0$  leads to the linear equation for  $\mathbf{V}_{HT}$ :

$$K_0 \mathbf{V}_{HT} = \langle K^m \mathbf{v}^m \rangle \quad (3.11)$$

The solution is

$$\mathbf{V}_{HT} = K_0^{-1} \langle K^m \mathbf{v}^m \rangle \quad (3.12)$$

where

$$K_{\mu\nu}^m = B^{m2} \left( \delta_{\mu\nu} - \frac{B_\mu^m B_\nu^m}{B^{m2}} \right) \quad (3.13)$$

$$K_0 \equiv \langle K^m \rangle \quad (3.14)$$

### 3.3.2 Walén Test in HT frame

For a rotational discontinuity, ideal MHD theory predicts that the accelerated plasma flow is Alfvénic in the HT frame [*Paschmann et al.*, 1979]. This is called Walén relation:

$$\mathbf{V} - \mathbf{V}_{HT} = \pm \mathbf{V}_A \quad (3.15)$$

The choice of plus or minus signs on the right hand side depends on whether the flow is parallel (+) or antiparallel (-) to the magnetic field.

The Walén Test has been used to check if there is reconnection process. Figure 3-2 shows two examples of the Walén Test for two magnetopause crossings by the AMPTE/IRM spacecraft. In example (a) on the left hand side, the Walén relation is not satisfied since the plasma flow velocities in the HT frame are much smaller than the Alfvén velocities. By contrast, example (b) on the right hand side shows a good agreement with the Walén relation.

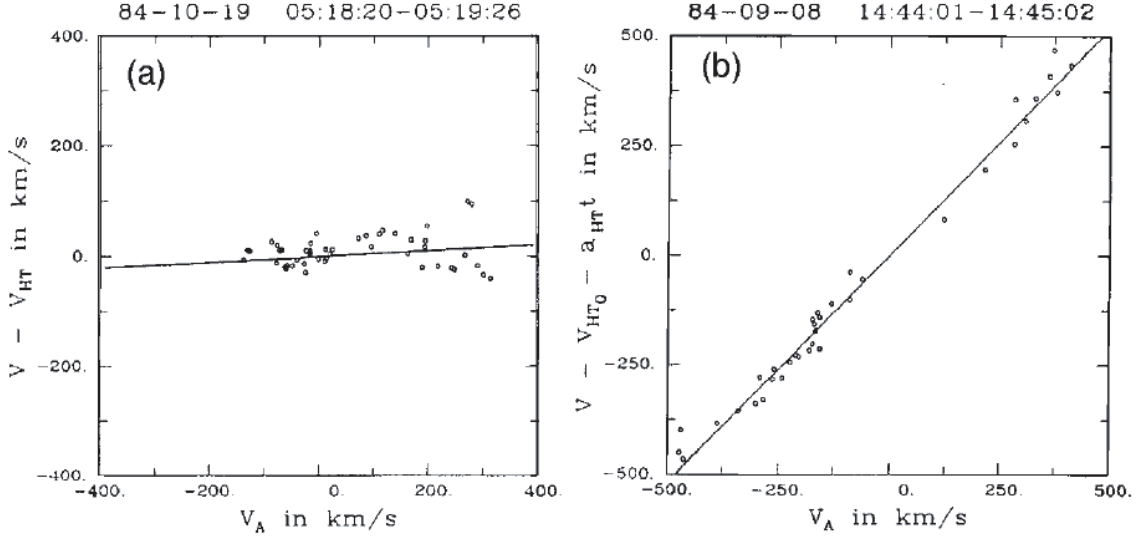


Figure 3-2: Walén test for two magnetopause crossings by the AMPTE/IRM spacecraft. In example (a) on the left hand side, the Walén relation is not satisfied since the plasma flow velocities in the HT frame are much smaller than the Alfvén velocities. By contrast, example (b) on the right hand side shows a good agreement with the the Walén relation. (The HT frame was assumed to be accelerating for better agreement in example (b). This figure is from *Sonnerup et al.* [1990].

### 3.4 Curlometer Technique

The curlometer technique [*Robert et al.*, 1998] is a method used to calculate the current density based on magnetic field measurements from four spacecraft. Assuming the current density is constant over the tetrahedral volume formed by the four spacecraft, it can be estimated based on Ampere's law:

$$\nabla \times \mathbf{B} = \mu_0 \mathbf{J} \quad (3.16)$$

In reality, the current will always vary to some degree over the tetrahedron and the best knowledge of this lies in estimating  $\nabla \cdot \mathbf{B}$  under the same assumptions. Because of the solenoidality of the magnetic field, any non-zero result of  $\nabla \cdot \mathbf{B}$  arises from the neglected nonlinear gradients in  $\mathbf{B}$  [*Robert et al.*, 1998]. The value of  $\nabla \cdot \mathbf{B} / |\nabla \times \mathbf{B}|$  can serve as a

quality indicator of the current estimate [*Robert et al.*, 1998].

## Chapter 4

# Magnetospheric Cusp

### 4.1 Introduction

The magnetospheric cusp is the region where the shocked solar wind plasma (magnetosheath plasma) can most easily access into dayside magnetosphere [Heikkila and Winningham, 1971; Frank, 1971]. The magnetospheric cusp is believed to be one of the major regions for the transfer of mass and energy from the solar wind into the magnetosphere.

The cusp at low altitudes can be identified in general by intense fluxes of low-energy ions, mostly in the energy range from a few hundred eV to a few keV [e.g., Heikkila and Winningham, 1971; Frank, 1971]. However, the presence of intense fluxes of low-energy ( $< 50$  eV) electrons have also been used to identify the cusp [e.g., Meng *et al.*, 1981]. The cusp has been further studied by using mid-altitude satellite data [e.g., Menietti and Burch, 1988] as well as highly eccentric satellites such as HEOS 2 and Prognoz 7 [Paschmann *et al.*, 1976; Haerendel *et al.*, 1978]. The high-altitude data have provided a perspective of the external cusp region [Haerendel *et al.*, 1978; Zong *et al.*, 2004b]. The region we deal with in this chapter is the Stagnant Exterior Cusp (SEC) at the high altitude region which resembles the one proposed by Haerendel *et al.* [1978] and Lavraud *et al.* [2002]. Numerous case studies have been done based on Cluster data [e.g., Zong *et al.*, 2003, 2004b; Lavraud *et al.*, 2002].

The indications of the existence of a boundary layer adjacent to the magnetopause from energetic particle measurements were provided in the 1960's. Energetic particles ( $> 25$  keV) at the dusk-side are found very often in the magnetosheath just outside the magnetosphere [Anderson *et al.*, 1965; Haskell, 1969; West and Buck, 1976; Eccles and

*Fritz*, 2002]. Observations from Geotail showed that the energetic ions of terrestrial origin (e.g., singly charged oxygen ions) leak out of the magnetosphere and can form layers in the equatorial magnetosheath (in the vicinity of the magnetopause) during intense storm activities [*Zong et al.*, 1998, 2001]. At the high latitude region, energetic ions have been observed adjacent to the magnetopause outside the magnetosphere during southward IMF, whereas energetic ions have been observed inside the magnetosphere during northward IMF [e.g., *Meng et al.*, 1981].

Energetic ions with energies from tens of keV up to MeV have been observed in the cusp region [*Aparcio et al.*, 1991; *Kremser et al.*, 1995; *Chen et al.*, 1997; *Fritz et al.*, 1999; *Chang et al.*, 2000; *Fritz*, 2000, 2001; *Trattner et al.*, 2001]. The physical origin of energetic particles in the cusp region has been a subject of controversy, although *Roederer* [1970] showed that the drift paths of energetic particles in the outer magnetosphere intersect with the high latitude magnetopause. The theoretical work by *Roederer* [1970] implies that the energetic particles can be quasi-trapped in the high latitude/cusp region temporarily, but such energetic particles can not be stably trapped in the high latitude cusp region.

*Chen et al.* [1997] and *Fritz* [2000] suggested that the particles observed in the cusp region by Polar satellite are the result of a localized acceleration mechanism and thus should be one of the major sources for magnetospheric energetic particles. On the other hand, *Chang et al.* [1998] and *Trattner et al.* [2001] argued that the presence of energetic particles in the cusp region could originate from either the bow shock or magnetosphere itself and no local acceleration is needed.

Further, *Delcourt and Sauvaud* [1999] proposed an additional interpretation for the appearance of energetic particles in the magnetospheric cusp region. They suggest that energetic particles in the high latitude region could be generated from the de-trapping of the trapped equatorial magnetospheric ions. Another possible clue for the solution to this puzzle has been suggested by *Sheldon et al.* [1998] and *Delcourt and Sauvaud* [1998]. They found that particles can drift on a closed path around the front of the dayside magnetosphere and suggested that a possible stable trapping region may exist in the outer

magnetospheric cusp region. This kind of particle trajectories have been further explored by *Fritz* [2000] and has been applied to explain the origin of energetic particles in the high latitude boundary during very quiet geomagnetic conditions for both northward and southward IMF conditions [*Zong et al.*, 2002]. On the spectrum of the energetic particles measured in the cusp region, it has been observed by Prognoz-10 that a power law energy spectra in the range of 15-950 keV is harder close to the magnetopause than it is deep in the magnetosheath [*Kudela et al.*, 1998]. This suggested that there are two populations in the sheath, the particles leaking from the magnetosphere and the particles accelerated at the bow shock. *Trattner et al.* [2001] showed that the exponential spectral slope of ions ( $< 150$  keV) in the cusp region increased (harder spectra) with increasing solar wind velocity. Further measurements of energetic particles are therefore essential in the search for answers to these questions.

The center location of the magnetospheric cusp is usually observed at local noon (12 MLT) from  $75^\circ - 80^\circ$  invariant latitude, although it can vary over a few hours in MLT [e.g., *Heikkila and Winningham*, 1971; *Newell and Meng*, 1988]. Statistical results from the DMSP satellites have shown that the location of the cusp not only depends on solar wind dynamic pressure but also on the IMF orientation. The location of the cusp moves equatorward or poleward in response to solar wind pressure change [*Newell and Meng*, 1994]; and moves equatorward (poleward) when the IMF orientation is southward (northward) [*Burch*, 1973].

Further studies have found that IMF  $B_y$  can also affect the location of the cusp. The cusp would shift prenoon (postnoon) when IMF  $B_y$  is negative (positive) in the northern hemisphere [*Newell et al.*, 1989]. The average width of the cusp proper is approximately 2 to 3 hours in MLT and about  $1$  to  $5^\circ$  in invariant latitude ( $1^\circ \sim 100$  km) [*Newell and Meng*, 1988; *Lundin et al.*, 1988; *Aparcio et al.*, 1991] centered at noon and about  $78^\circ$  IL. Although its location and size vary with changes in the IMF direction and solar wind velocity, the magnetospheric cusp is always present [*Newell and Meng*, 1988].

*Wing et al.* [2001] found that the cusp width at low-altitude appears to increase with

magnitude of IMF  $B_z$ . The shift of the low-altitude cusp position by the change of IMF direction is confirmed by a comprehensive statistical study [Merka *et al.*, 2002].

The physical mechanism driving cusp dynamics is believed to be the magnetic field reconnection process. Under northward IMF, cusp or lobe reconnection occurs between the magnetosheath and lobe magnetic field lines [Gosling *et al.*, 1991; Kessel *et al.*, 1996; Phan *et al.*, 2003]. Since the reconnection process may occur at both the northern and southern hemispheres simultaneously, Song and Russell [1992] proposed that the low latitude boundary layer (LLBL) with newly closed magnetospheric field lines at the dayside magnetopause can be formed when the IMF is strongly northward. This suggestion has been supported by case studies [Le *et al.*, 1996; Onsager *et al.*, 2001] and MHD simulations [Raeder *et al.*, 1997].

Beside the LLBL, inside the cusp, different subregions may be formed depending on whether the reconnection at both the northern and southern hemispheres occurs simultaneously or not. As stated by Trattner *et al.* [2002] that if the major substructures in the cusp are interpreted as spatial features this does not eliminate the importance of patchy or transient reconnection at the magnetopause. In a recent study, Bogdanova *et al.* [2005] found three distinct plasma regions inside the main cusp by checking low energy plasma electron data when high latitude reconnection is occurring. The first region was found to be associated with injections of magnetosheath-like plasma which are believed to be associated with dawnward and sunward convection indicating Cluster crossed newly-reconnected field lines related to the dusk reconnection site. The second region, a Stagnant Exterior Cusp (SEC) characterized by nearly isotropic and quasi-stagnant plasma was observed. The last region was found to be associated with significant anti field-aligned flows. The last region is close to the magnetosheath.

The existence of three different plasma sub-regions inside the cusp can be explained by asymmetry in the lobe reconnection geometry with either single (one hemisphere) or dual (both northern and southern hemisphere) reconnection sites [Bogdanova *et al.*, 2005]. It is found that heated magnetosheath electrons are present in a boundary layer outside

the magnetopause (magnetosheath boundary layer [*Fuselier et al.*, 1997]) at high latitudes under northward IMF [*Onsager et al.*, 2001; *Lavraud et al.*, 2005b]. The directionality of those heated electrons can be used to identify whether high latitude reconnection is occurring in one or the other, or both, hemispheres.

Electrons with energy larger than 30 keV are able to trace the topology of the magnetic field lines and can be used to distinguish open or closed field lines. Clearly delineated regions of open and closed magnetic field lines in the high latitude/cusp region are crucial to understanding the dynamics of the magnetic cusp [*Zong et al.*, 2005a].

Although the reconnection process has been regarded as an important mechanism for the energy transport into and through the cusp region, it has been suggested that the solar wind plasma penetrating into the magnetosphere can be also explained by a non-reconnection process, known as "Plasma Transport Event" (PTE) [e.g., *Lundin et al.*, 2003]. Also, the Kelvin-Helmholtz instability occurring along the flanks of the magnetosphere has been considered to produce a viscous interaction which can cause a transfer of mass into the magnetotail during times of northward IMF [*Hasegawa et al.*, 2004]. The vortex motion of Kelvin-Helmholtz waves can twist the magnetic field strongly to form multiple current layers. Small scale magnetic reconnection may occur at those multiple current sheets within a vortex which would then be responsible for the plasma transport through the magnetopause [*Nykyri and Otto*, 2001]. In non-reconnection models the cusp position and extent are less sensitive to the IMF, but more strongly dependent on the solar wind ram pressure [*Yamauchi and Lundin*, 1998]. This seems to be in agreement with results obtained by *Newell and Meng* [1994] and *Frey et al.* [2002], who found a better correlation of the cusp area with the solar wind dynamic pressure than with the magnitude of the IMF  $B_z$ .

As we already know, the magnetospheric cusp is a highly dynamic region since it is a region where plasma and magnetic pressures are balanced by the solar wind and IMF pressure, so a small change in the solar wind may lead to a large effect. The cusp contains many different plasma instabilities [*Cargill et al.*, 2004]. The spatial and temporal

variations of the high-altitude cusp are very complex. The spatial variations of the cusp have focused on the dispersion of plasma ions in the cusp region [Wing *et al.*, 2001; Nemecek *et al.*, 2004].

It is also suggested that the factors controlling the overall high latitude boundary configuration are dipole tilt and the solar wind pressure with the IMF effects being secondary [Eastman *et al.*, 2000].

The windsock effect due to the deviation of the solar wind flow from the Sun-Earth line has been indeed observed by the Hawkeye satellite [Boardsen *et al.*, 2000]. Further, a physical explanation of the dawn-dusk displacement of the cusp which was strongly connected to the solar wind component flow (which is probably deflected by the large scale heliosphere current sheet/plasma sheet) was given by Lundin *et al.* [2001]. The existence of a bifurcated cusp geometry or so called "double cusp" during extreme conditions has been suggested by the low altitude DMSP satellite observations [Wing *et al.*, 2001]. The double cusp has been suggested to be the result of merging simultaneously occurring at the low- and high-latitude magnetopause during periods of large IMF  $|B_y|$  and small IMF  $|B_z|$  [Weiss *et al.*, 1995; Wing *et al.*, 2001]. In this way, a satellite travelling in the meridional direction near noon observed two different ion populations caused by the low and high latitude reconnection. The cusp latitudinal width increases with IMF  $|B_y|$  and the equatorward boundary moves to lower latitude with increasing IMF  $|B_y|$ . Trattner *et al.* [2002] concluded that major double cusp structures that they examined are not the signature of pulsed reconnection [Lockwood and Smith, 1992]; they believed that these were spatial structures in nature. A Bursty Multiple X-Line Reconnection (BMXR) mechanism [Boudouridis *et al.*, 2001] was proposed to interpret the overlap between the two ion energy dispersions observed at low altitude cusp. Multiple cusp phenomena have been observed [Wing *et al.*, 2001; Zong *et al.*, 2004a; Pitout *et al.*, 2006]. The multiple cusps have been suggested to be either spatial [Wing *et al.*, 2001] or temporal effect (windsock effect) [Zong *et al.*, 2004a] or a combination of a spatial feature and temporal effect [Zong *et al.*, 2004a]. Zong *et al.* [2004a] and Zong *et al.* [2007] reported multiple cusp events which were interpreted to be

the result of a temporal effect.

Understanding the magnetospheric cusp physical processes is essential and important for a thorough understanding of the entire field of space plasma physics, and of the interaction or coupling processes between the solar wind plasma and any planetary magnetospheric plasma. There are still many outstanding questions for the cusp region. For example, what is the behavior of the energetic particles in the cusp region? What is the major source of the magnetic turbulence in the cusp region? Are the observed multiple cusps temporal or spatial effect? I address these questions in this chapter. In section 4.2-4.6, I present statistical results on the cusp properties, energetic particles and magnetic turbulence in the cusp region. In section 4.7, I present in detail one of the multiple cusp events I analyzed to show the multiple cusp encounters were a temporal effect.

## 4.2 Stagnant Exterior Cusp (SEC) Identification and its General Properties

In the following sections (4.2-4.4), we present statistical properties of the SEC calculated from SEC crossing data recorded by Cluster during two periods in a total of 6 months. The identification of the SEC was made on the basis of the following criteria: 1. High density plasma (comparable to that in the sheath); and 2. Small or stagnant plasma flow ( $V_x < 60$  km/s). These criteria have been used by *Zong et al.* [2004a] and *Lavraud et al.* [2002].

The cusp is one of the main regions for transport of plasma into the magnetosphere and contains magnetosheath-like (high density) plasma [e.g., *Frank, 1971; Newell and Meng, 1988*]. Another characteristic of the cusp is the low and fluctuating flow velocity (as compared with that of the magnetosheath) [*Haerendel et al., 1978*]. Adding all these selection criteria together, we obtained a data set containing the 40 most clear SEC crossings. An example of the SEC selected using our criteria is presented in figure 4-1.

Figure 4-1 gives an overview of the RAPID, CIS, FGM and ACE measurements between 0800 and 1200 UT on Mar. 4, 2002. At 9:30 Cluster is located at (2.7, 1.1, 8.1)  $R_E$  (in GSM coordinates). From the top the panels show energetic electron and proton fluxes and the

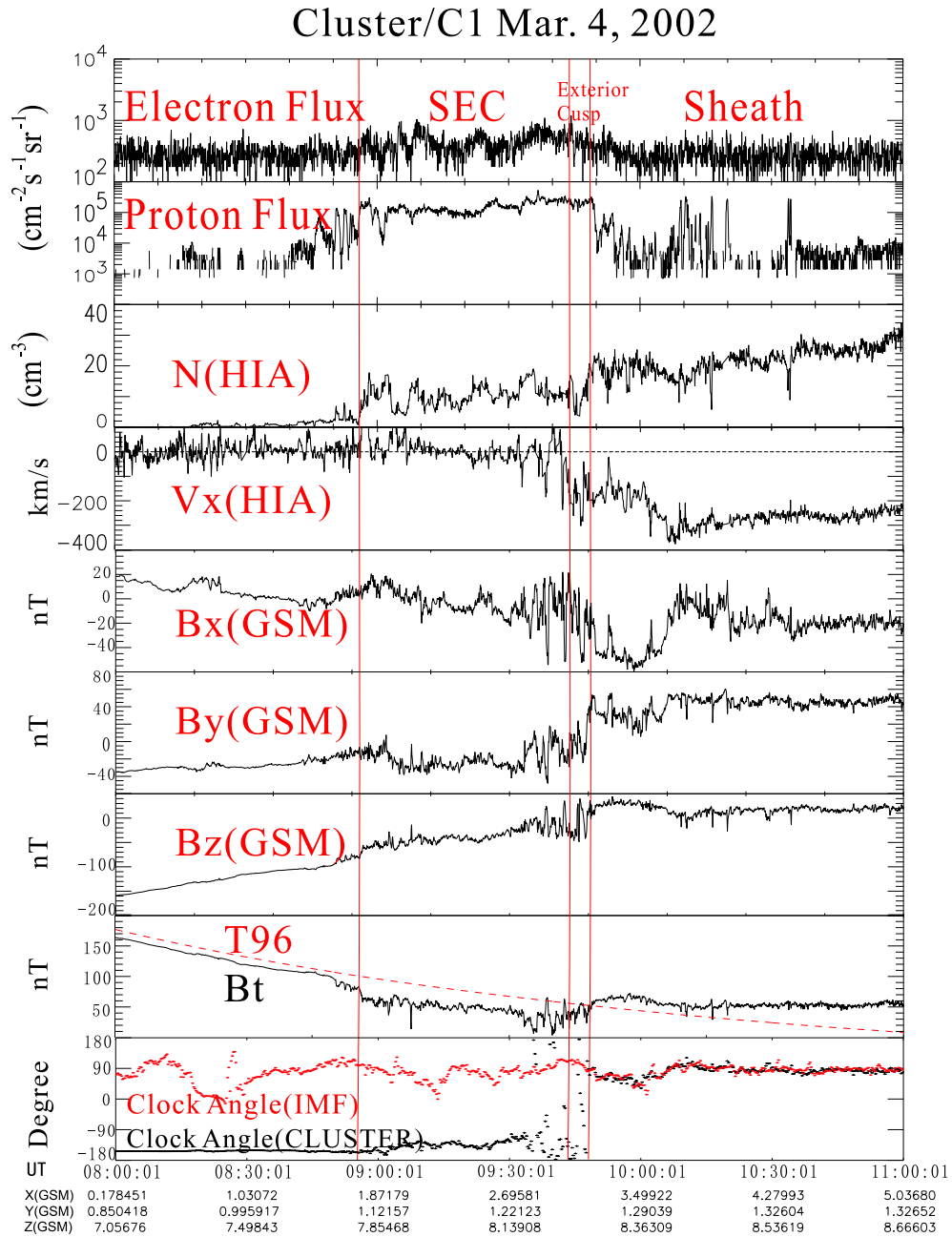


Figure 4-1: An overview of RAPID, CIS, FGM and ACE data from 08:00 to 11:00 on Mar.4, 2002. From the top panels show: integral electron flux ( $> 30$  keV); proton flux ( $> 30$  keV); plasma density; plasma velocity  $V_x$  component; magnetic field components in the GSM coordinate system and magnitude (in nT). The magnetic field clock angle obtained by ACE (IMF) and Cluster spacecraft (local) are plotted in the bottom panel. The region between the vertical lines is identified as the SEC. The solar wind data were lagged by 50 minutes to allow for the plasma to travel from the ACE spacecraft to the SEC.

plasma flow velocity  $V_x$  component, together with the magnetic field in GSM coordinates and clock angles of both the IMF and local magnetic field. The Stagnant Exterior Cusp was identified as a region with high density plasma, a stagnant flow ( $V_x$  around 0), and highly turbulent magnetic field. The SEC region is also accompanied by the depressed magnetic field and it is clear that large magnetic shears (changes in the field direction) are also present.

To ensure the SEC regions we identified were not a part of the magnetosheath, we correlated the clock angle of the IMF with this angle within the SEC regions. The clock angle of the magnetic field is the angle between the projection of the magnetic field on the  $YZ$  plane and the  $z$  axis of GSE coordinates, or  $\arctan(B_y/B_z)$ . The clock angle should remain essentially unchanged across the bow shock according to the coplanarity theorem [Song *et al.*, 1992; Zong *et al.*, 2004b] although the magnitudes of  $B_z$  and  $B_y$  will increase in a stagnant region, e.g. the SEC region [Spreiter and Stahara, 1980]. The clock angle should be well correlated for the IMF and the dayside magnetosheath field if there is only a bow shock in between. As we can see from the bottom panel in Figure 4-1, a quite large angular difference between the IMF and local clock angles can be seen in the region identified as SEC, but these angles are very similar in the region denoted as sheath. The proper lags from ACE to Cluster are adjusted by the time for the solar wind to travel from the location of ACE to the Earth. The angular difference between clock angles further confirmed the identification of the SEC region. This criterion has been applied to distinguish the cusp and magnetosheath by Maynard *et al.* [2003].

Kaymaz *et al.* [1992] pointed out that in the nightside, it is expected that the draping should increase  $B_y$  relative to  $B_z$ . Hence, the clock angle would change from that of the IMF. In this section we try to study how effective the draping is in the high latitude region, or in other words, if the angular difference between the IMF and local clock angles is a good criterion to identify the SEC region. Our results show that it is a good criterion for 72.5 % of all the events.

Another purpose of this section is to test whether the depressed magnetic field is a

good criterion to identify the SEC region. Our statistical study based on the 40 SEC events shows that 72.5 % of all the events are characterized by a depressed magnetic field.

### 4.3 Statistical SEC Position

The extension of the cusp in magnetic local time and invariant latitude has been investigated by *Meng et al.* [1981]. According to the DMSP electron measurements, the cusp lies predominantly within the 0800 to 1400 MLT sector. Figure 4-2 shows the Cluster trajectory from Jan.1, to Apr.30, 2001 and from Mar.1, to Apr.30, 2002 plotted in the GSM coordinate system. The red segments are SEC regions identified by the criteria mentioned in section 2.1 above. There is a dawn-dusk asymmetry partly because more dawn side than dusk side orbits are included in our statistical study. Figure 4-3 shows the occurrence of the SEC in 1 hour MLT sectors covering the interval 0700-1400 MLT. This distribution is based on all of the 40 events (including northern and southern SEC crossings) selected. From Figure 4-3 we can see that the SEC lies predominantly within the 0800 to 1300 MLT sector which is similar to the position of the low latitude cusp [*Newell and Meng, 1988*].

### 4.4 Presence of Energetic Particles

The energetic particle data presented in this section were obtained by the RAPID instrument on board the Cluster spacecraft [*Wilken et al., 1997*]. The background level of the electron and proton flux is of the order of  $< 10^3 \text{ cm}^{-2} \text{ s}^{-1} \text{ sr}^{-1}$  (1 count level) based on RAPID measurements. We define the presence of energetic particles as the presence of fluxes higher than  $10^4 \text{ cm}^{-2} \text{ s}^{-1} \text{ sr}^{-1}$  ( $> 10$  counts). We find that energetic ions are present on 32 passes ( $\sim 80$  % of such opportunities) through the SEC region. The energetic electrons are present 22.5 % of these opportunities.

### 4.5 Solar Wind Dependency of the Spectrum

To study the relationship between the hardness of the ion spectra and the solar wind velocity, a power law function  $f = f_0(E/E_0)^{-\gamma}$  (above 30 keV) has been used to fit the

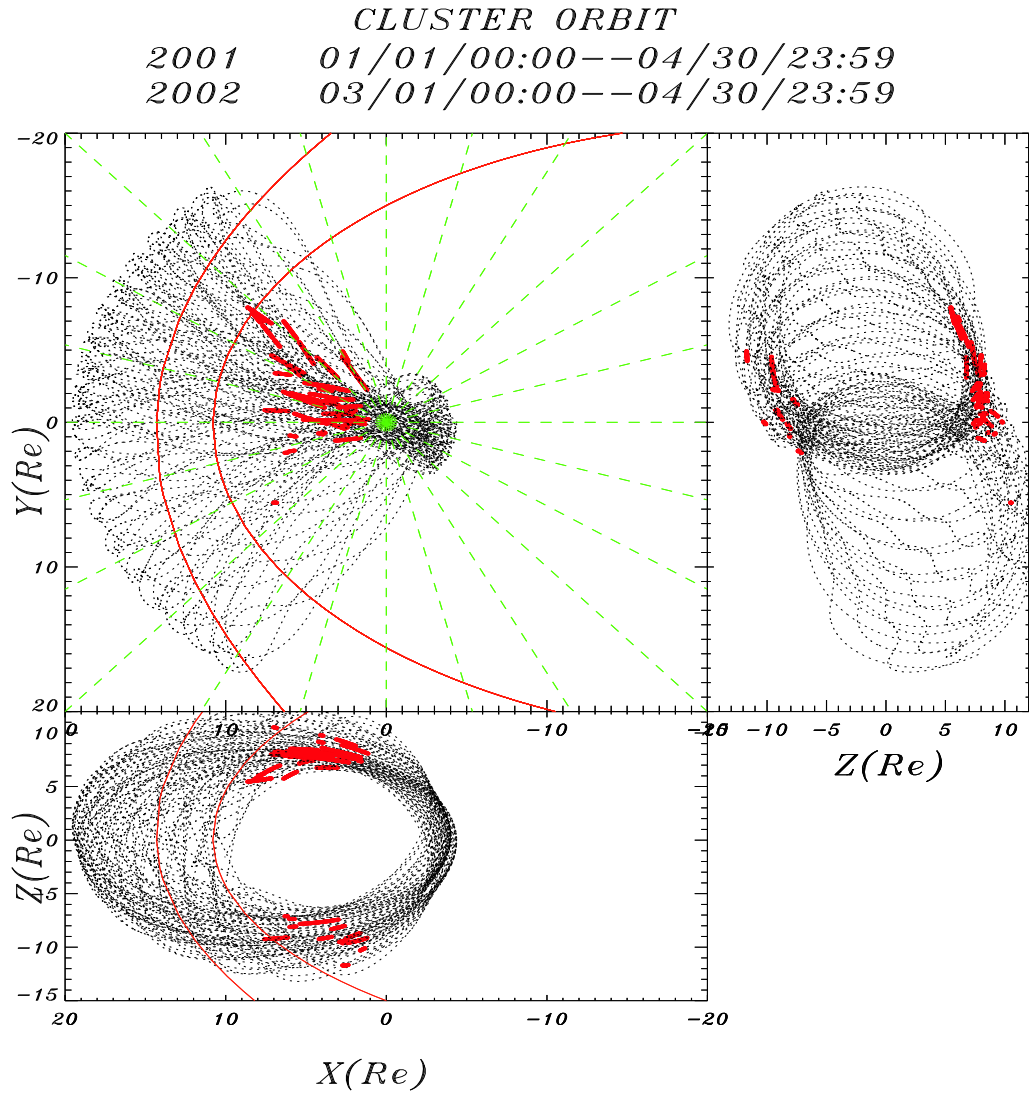
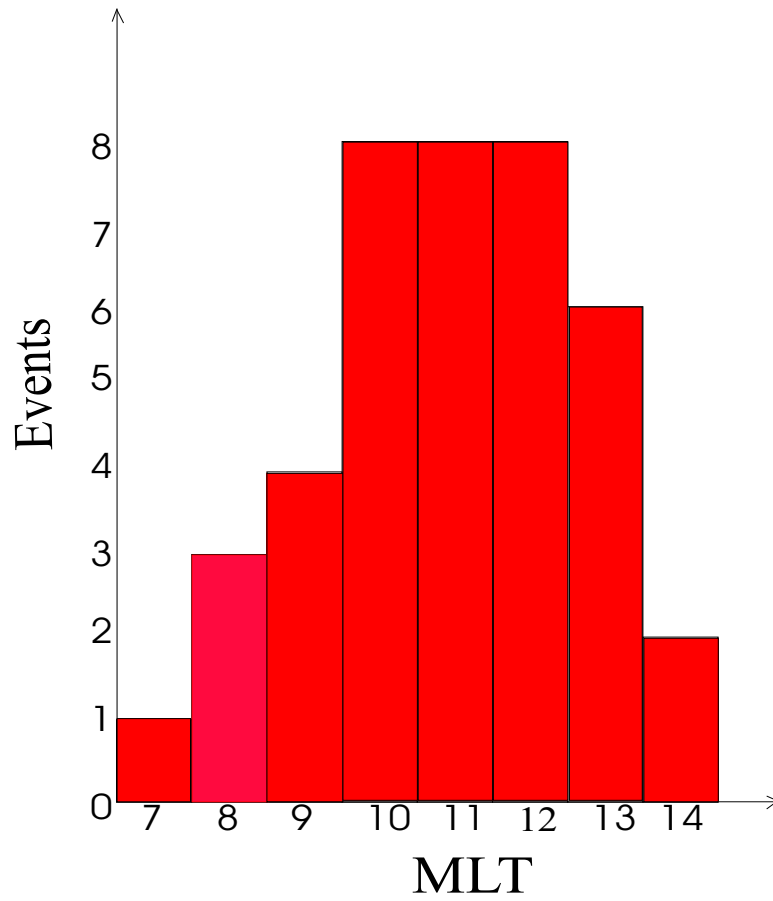


Figure 4-2: Cluster orbit from Jan.1, to Apr.30, 2001 and from Mar.1, to Apr.30, 2002 plotted in the GSM coordinate system. The red segments indicate SEC regions identified by the criteria mentioned in section 4.2.



## 40 Events

Figure 4-3: The SEC extends from 7 to 14 MLT.

## Spectra

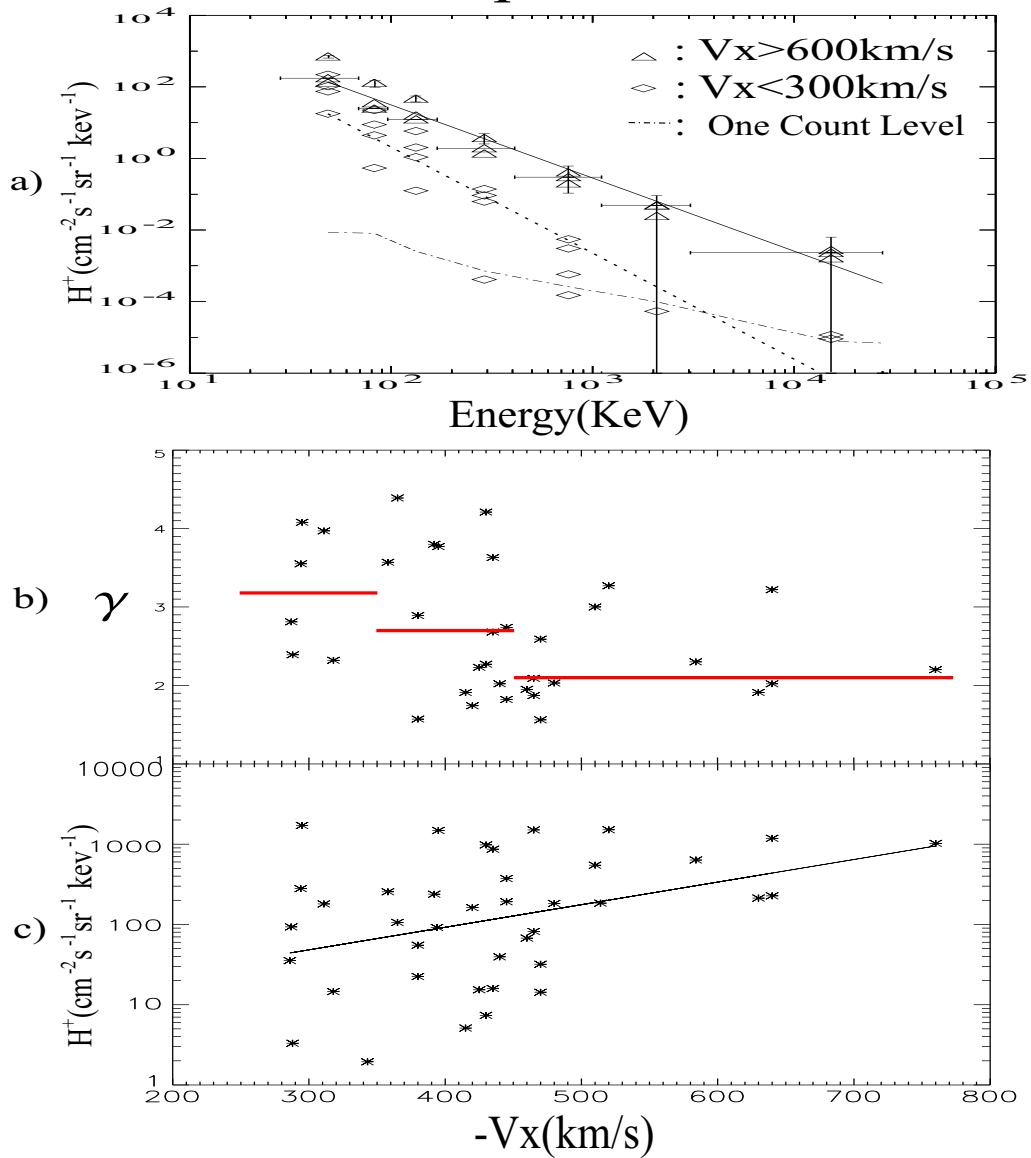


Figure 4-4: a) The proton spectra for the SEC events with extreme solar wind velocities (either  $> 600 \text{ km/s}$  or  $< 300 \text{ km/s}$ ). b) The power law spectral slopes for the energetic  $H^+$  versus the solar wind velocity. The horizontal bars indicate the median spectral slope in three ranges of solar wind velocity, from 250 km/s to 350 km/s, from 350 km/s to 450 km/s and beyond 450 km/s. c) Proton flux at 30 keV versus the solar wind velocity.

spectra. The spectrum is likely to be more complicated than that of a single power law and the choice of a single power law was made to simplify the analysis and to indicate general trends in the data. The solar wind data with 1 minute resolution were time-shifted to allow for the plasma to travel from the ACE spacecraft to the position of Cluster. For each SEC event, an average solar wind speed over the time interval of the SEC event was obtained. Figure 4-4 a) is the proton spectra for the SEC events with extreme solar wind velocities (either  $> 600\text{km/s}$  or  $< 300\text{km/s}$ ). Plotted on the x-axis is energy in keV and plotted on the y-axis is the differential proton flux in  $\text{cm}^{-2}\text{s}^{-1}\text{sr}^{-1}\text{keV}^{-1}$ . The flux is averaged over the time period when Cluster is in the SEC region so a single differential proton flux value is obtained per energy channel for each SEC event. The error bars on the energy represent the width of the energy passbands. The widths of the energy passbands are small relative to the total energy range of the data, making systematic errors due to finite passband width negligible. Altogether, the data cover three orders of magnitude in energy from 28 keV to 30 MeV and 8 orders of magnitude in flux. The best fit power law function is indicated by the solid line for the large solar wind velocities and dotted line for small solar wind velocities. The spectra are harder for higher solar wind velocity. *Trattner et al.* [2001] showed the exponential spectral slope of ions in SEC region increased (harder spectra) with increasing solar wind velocity.

Figure 4-4 b) shows the power law spectral indices for the energetic  $H^+$  versus the solar wind velocity. The horizontal bars indicate the median spectral slope in three ranges of solar wind velocity, from 250 km/s to 350 km/s, from 350 km/s to 450 km/s and beyond 450 km/s. Case studies of energetic ion ( $<150\text{keV}$ ) spectra in the SEC region have been investigated previously [*Trattner et al.*, 1994; *Kudela et al.*, 1998; *Fritz et al.*, 2003; *Chang et al.*, 1998]. However, the ion energy range was limited to below a few hundred keV for most of the previous studies. In this section, the ion spectra with energy range from 30 keV to 4 MeV for SEC crossings have been studied statistically. The particle spectra are characterized by a power law with spectral indices  $\gamma$  varying from 1 to 5. Furthermore, the power law indices are found to be closely related to solar wind velocity, which is consistent

with previous studies for lower energy particles by *Trattner et al.* [1994] and *Kudela et al.* [1998].

The proton flux dependence on the solar wind velocity has also been studied. Figure 4.4 c) shows the proton flux  $f_0$  (at 30 keV) versus the solar wind velocity. We can see the tendency that the flux increases with increasing solar wind velocity. The magnetospheric energetic particle environment is affected by the high speed solar wind. *Paulikas and Blake* [1979] reported that the flux of energetic electrons at geosynchronous orbit enhanced when the solar wind was fast. Cluster observations reported in the section show that the flux of energetic particles in the cusp region also increases during time period when the solar wind speed is high.

#### 4.6 Turbulence in the Cusp Region Depends on the Magnetic Shear Angle

Figure 4-5A shows the proton spectra for the SEC events with extreme IMF  $B_z$  and moderate solar wind velocities (between 350 km/s and 450 km/s). Figure 4-5B, C and D show the power law spectral index  $\gamma$  for all the SEC events identified versus the Dst index, the turbulence of the magnetic field (defined below), and the magnetic shear angle. The horizontal bars indicate the median power law spectral indices. The power law spectral indices are well correlated (see Figure 4.4b) with the solar wind speed using 40 events, whereas no clear relationship between the power law spectral index and IMF  $B_z$ , solar wind Mach number, Dst, turbulence of the magnetic field (defined below) or even magnetic shear angle has been found (see Figure 4.5, Mach number plot is not shown). The magnetic shear angle is the difference between local  $B$  vector and IMF clock angle projected on the plane perpendicular to the shock normal. Therefore  $0^\circ$  ( $180^\circ$ ) magnetic shear angle indicates the IMF is parallel (anti-parallel) to the local magnetic field in the cusp region. As shown in the Figure 4-5D, the power law spectral index has no clear relationship with the magnetic shear angle which indicates the energetic particles observed in the cusp region are not provided by high latitude reconnection process.

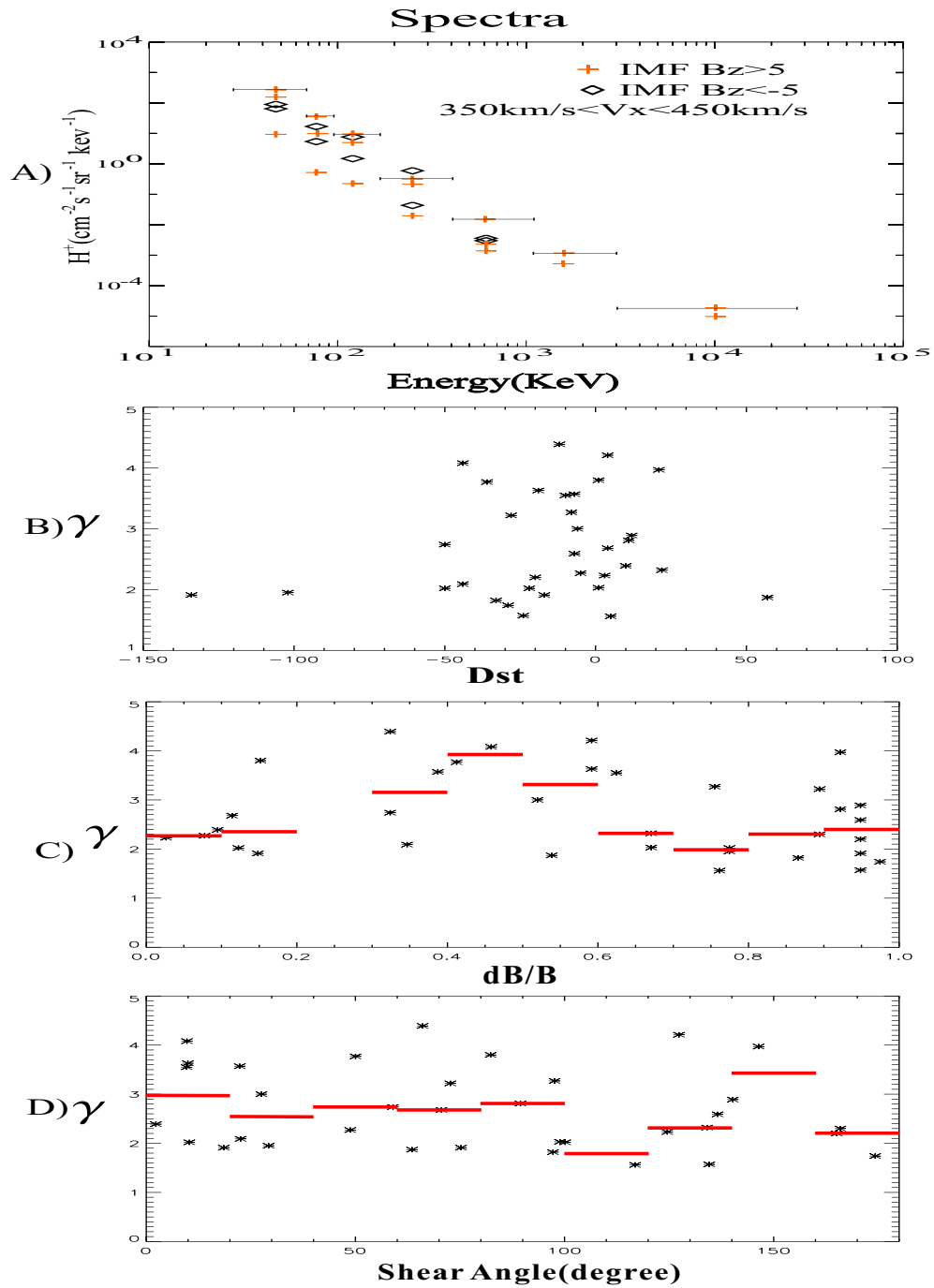


Figure 4-5: A) The proton spectra for the SEC events with extreme IMF  $B_z$  and moderate solar wind velocities (between 350 km/s and 450 km/s). B) The power law spectral index  $\gamma$  for all the SEC events identified versus the Dst index. C) The power law spectral index  $\gamma$  for all the SEC events identified versus the turbulence of the magnetic field. The horizontal bars indicate the median power law spectral indices. D) The power law spectral index  $\gamma$  for all the SEC events identified versus the magnetic shear angle.

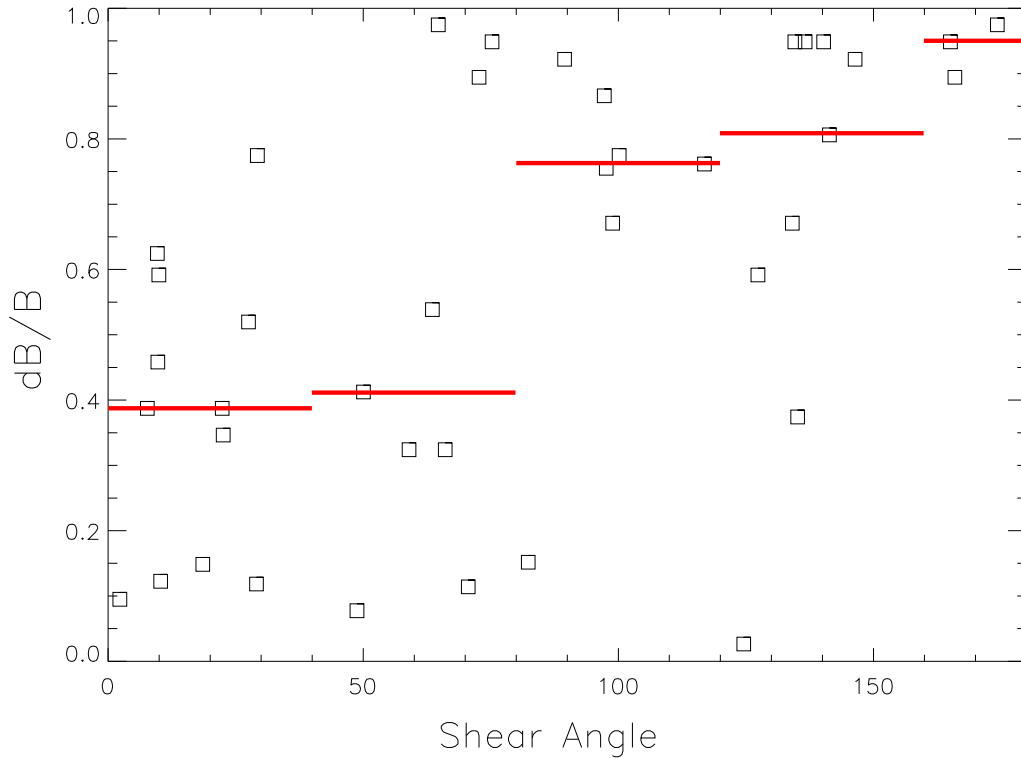


Figure 4-6: The relationship between the turbulence of the magnetic field in the SEC and the magnetic shear angle (the clock angle difference between the IMF and SEC magnetic field). The horizontal bars indicate the median of the turbulence of the magnetic field.

At high altitudes, fluctuations in the magnetic field strength are expected because the plasma in the polar cusp region has an energy density that is significant relative to background magnetic field in contrast to low altitudes where the magnetic energy density is far greater than that of the plasma [Zhou *et al.*, 2000]. Alternatively, the turbulence in the high latitude cusp could also be caused by the shear flow or the high latitude reconnection process [Nykyri *et al.*, 2004; Khotyaintsev *et al.*, 2004]. The velocity shear presumably arises from the lobe reconnection process and is a well-known source of plasma instabilities at around the ion cyclotron frequency [Ganguli and Palmadesso, 1988; Nykyri *et al.*, 2004]. On the other hand, the high-frequency turbulence waves are suggested to be related to a reconnection region [Khotyaintsev *et al.*, 2004].

To perform a statistical study, the turbulence of the magnetic field in this section is

assumed to be represented by  $dB/B$  where  $dB/B$  is the normalized standard deviation, i.e.

$$dB/B = \sqrt{(\langle |B|^2 \rangle - |\langle B \rangle|^2) / \langle |B|^2 \rangle}$$

where  $\langle B \rangle$  is one minute averaged magnetic field.  $dB/B$  data with 4 seconds resolution obtained by FGM instrument was used in this study. Considering the particles are possibly energized by strong field turbulence, the maximum value of the  $dB/B$  is selected to be the representative of turbulent level for each SEC event. The magnitude of the turbulence in the SEC is found to be associated with the magnetic shear angle between the magnetosheath and SEC. When the magnetic shear angle is large enough, reconnection (merging) may occur [Crooker, 1979; Luhmann *et al.*, 1984].

Figure 4-6 shows the relationship between the turbulence of the magnetic field in the SEC and the magnetic shear angle. From Figure 4-6 we can see that the larger the magnetic shear angle is, the more turbulent the magnetic field in the SEC. In our statistical study, 80% of the SEC events have turbulent magnetic field ( $dB/B > 0.3$ ). We find that the magnetic turbulence is closely associated with the magnetic shear angle. This result strongly suggests that turbulence in the high latitude/ SEC region is mainly the result of the high latitude reconnection process.

## 4.7 Multiple Cusps: Temporal or Spatial Effect?

### 4.7.1 Introduction

Zong *et al.* [2004a] reported Cluster observations of multiple cusp crossings during southward IMF on April 18, 2002. Figure 4-7 gives an overview of the triple cusp event as viewed by Cluster between 1600 and 1900 UT on April 18, 2002. The three cusp regions were identified by high density plasma, stagnant plasma flow ( $V_x$  around 0), and highly turbulent and depressed magnetic field.

As strong evidence of a temporal cause of the triple cusp event, Zong *et al.* [2004a] showed that the order of the Cluster spacecraft crossing the magnetopause five times (la-

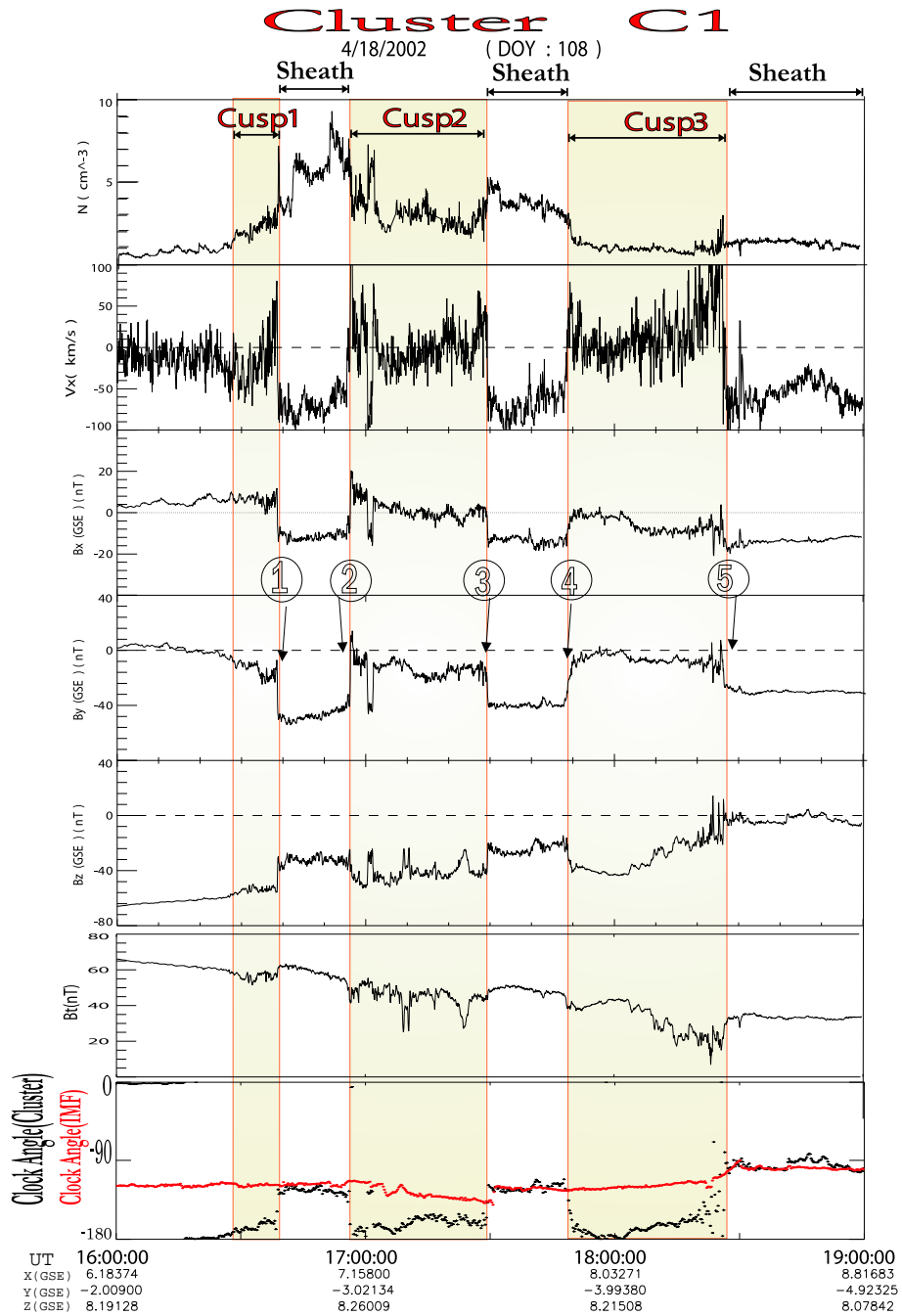


Figure 4-7: An overview plot of the triple cusp event (from 16:00 to 19:00 UT, April 18, 2002). From the top, the panels show: plasma density, plasma velocity  $V_x$  component, the magnetic field components and magnitude and the magnetic field clock angles obtained by ACE (IMF, in red line) and Cluster spacecraft (in black line). The three shaded regions are identified as cusp regions. (after Zong *et al.* [2004a])

belled 1 to 5 in Figure 4.7) is consistent with the cusp moving forward and retreating.

Another multiple cusp event during a period of highly radial IMF on Feb. 26, 2001 was reported by *Taylor et al.* [2004]. A multiple cusp event during northward IMF on March 21-22, 2001 was reported by *Zong et al.* [2007]. An overview plot of this event is shown in Figure 4.8. Evidence showed that the Cluster spacecraft had been observing the same cusp and it appeared as 4 cusp-like regions due to possible magnetospheric oscillations. The authors interpreted that the cusp motion was possibly due to the change of the solar wind azimuthal flow (see Figure 4.9).

#### 4.7.2 Multiple Cusps under Variable IMF Conditions

We have seen from the previous section that the multiple cusp events are observed during both northward and southward IMF conditions. In this section, we present in detail a multiple cusp event under variable IMF conditions based on Cluster observations.

Cluster was travelling outbound in the northern hemisphere from 0000UT to 0400UT on March 2, 2002 as shown in Figure 4.10, in which the scale size of the Cluster tetrahedron has been enlarged 300 times. The separation of the Cluster satellites is about 100 km which was perfect to use four spacecraft data to do a timing analysis (will show timing results later in this section).

An overview of Cluster measurements between 0000UT and 0400UT on March 2, 2002 is presented in Figure 4.11. Panel 1 shows the plasma ion spectrum obtained by the CIS instrument [*Rème et al.*, 1997] over-plotted with the integral flux of energetic ions (30-4000 keV, solid black line) and electrons (30-500 keV, dashed black line) obtained by the RAPID instrument [*Wilken et al.*, 2001]. Panel 2 shows the three components of the plasma velocity in GSE coordinates. Panel 3 shows the ion parallel (red line) and perpendicular temperature. Panel 4 shows the ion density. The three components and the magnitude of the magnetic field are shown in panels 5 and 6. The vertical blue dashed line marks the location of the magnetopause which is associated with the sharp transition of all the parameters shown in Figure 4.11. The magnetosheath is on the right hand side

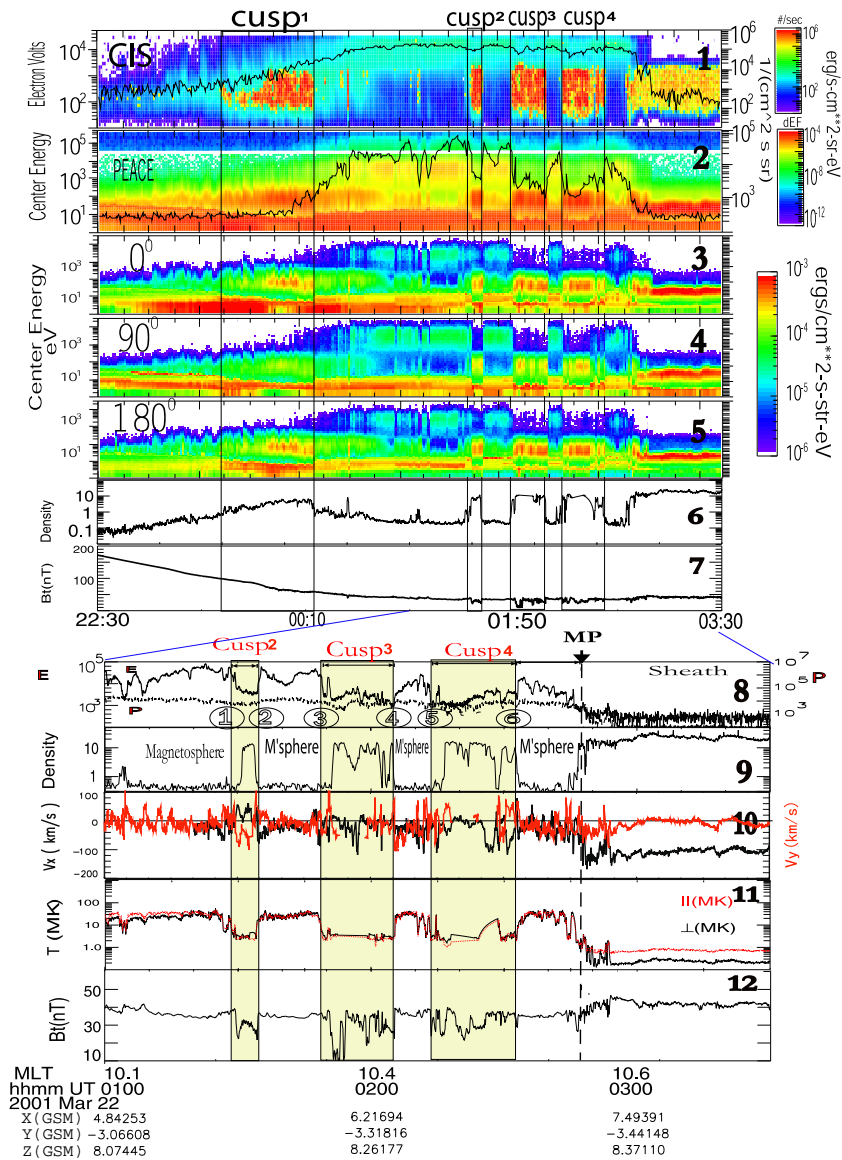


Figure 4-8: Panels 1-7: An overview plot of the multiple cusp event observed by Cluster C1. Panels 1 and 2 show the plasma ion, electron spectrum over-plotted with energetic particle (energy ranges are 30-500 keV for electrons and 30-4000 keV for ions) fluxes. Panels 3-5 show the electron spectrograms for 3 different pitch angles ( $0^\circ$ ,  $90^\circ$ ,  $180^\circ$ ) obtained by PEACE. Panels 6 and 7 show the ion density ( $\text{cm}^{-3}$ ) and the magnitude of the magnetic field. Panels 8-12: Zoom in view of the later three cusps. Panel 8 shows Energetic ion (30-4000 keV) and electron (30-500 keV) flux. Panel 9 shows plasma density ( $\text{cm}^{-3}$ ). Panel 10 shows velocity  $V_x$ ,  $V_y$  components in GSE coordinates. Panel 11 shows the plasma temperature. Panel 12 shows the magnitude of the magnetic field. MP marks the location where Cluster crossed the magnetopause. (after Zong *et al.* [2007])

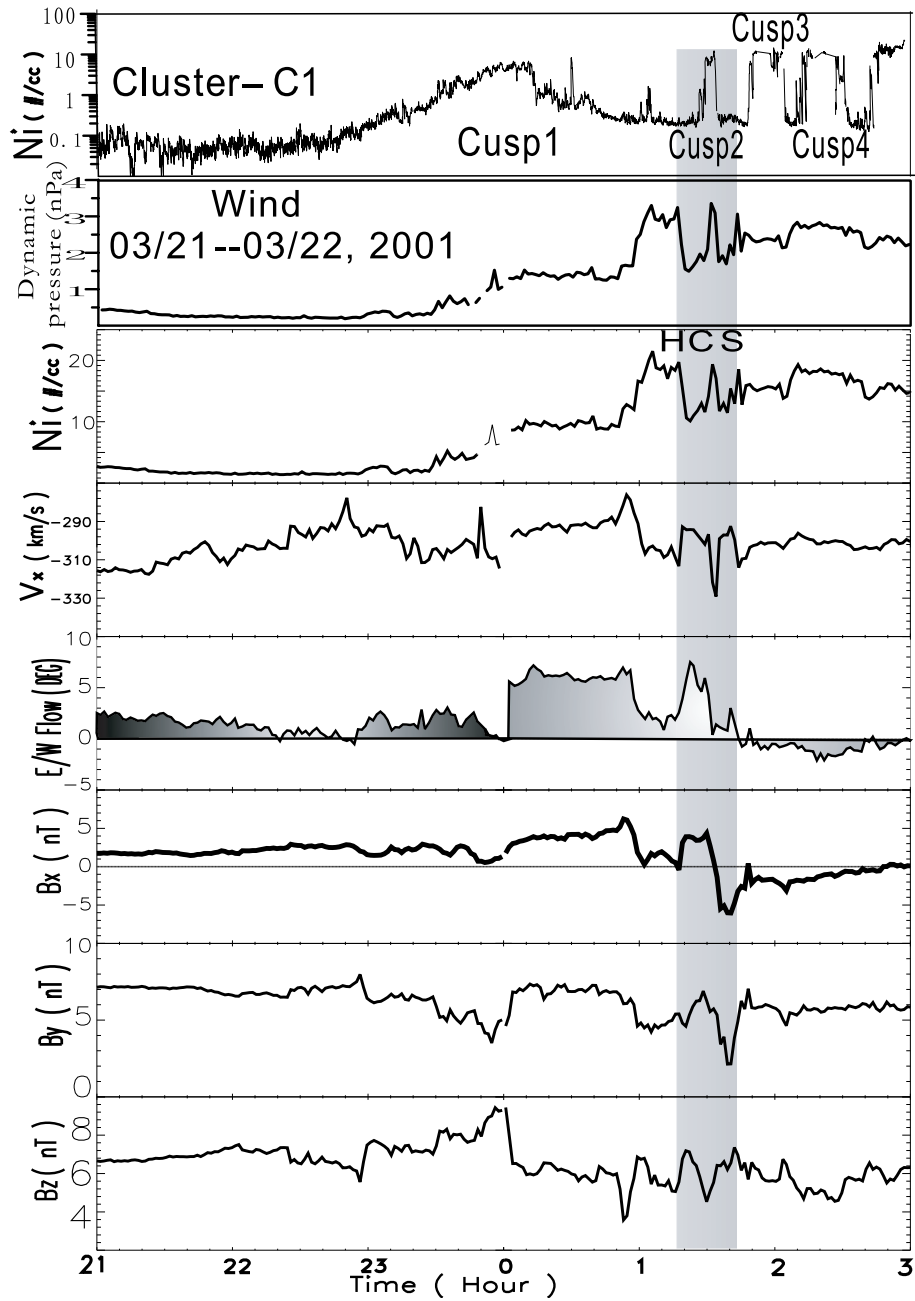


Figure 4-9: Plasma density from Cluster C1 together with the time-shifted solar wind dynamic pressure, density, velocity  $V_x$  component, eastward/westward flow and the IMF observed by the WIND spacecraft. The shaded area is the Heliospheric Current Sheet (HCS) which is identified by the high plasma density and sign change of the IMF  $B_x$ . (from Zong *et al.* [2007])

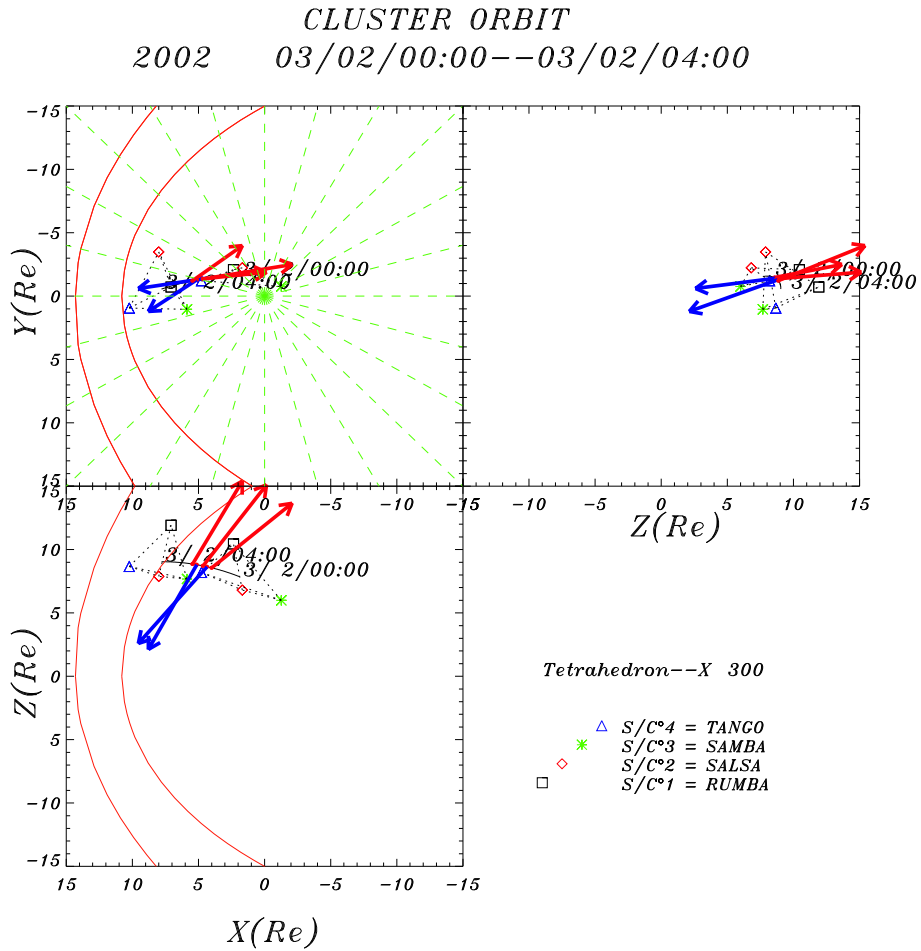


Figure 4-10: The solid black lines show Cluster trajectory in GSM coordinates from 00:00 UT to 04:00 UT, March 2, 2002. The scale size of the Cluster tetrahedron has been enlarged in 300 times. The normal directions of the boundaries Cluster encountered along its outbound journey are presented by red (northward motion) and blue (southward motion) arrows (see text for details). The nominal positions (unlabelled solid red lines) of the magnetopause and the bow shock have been plotted according to the Fairfield model [Fairfield, 1971].

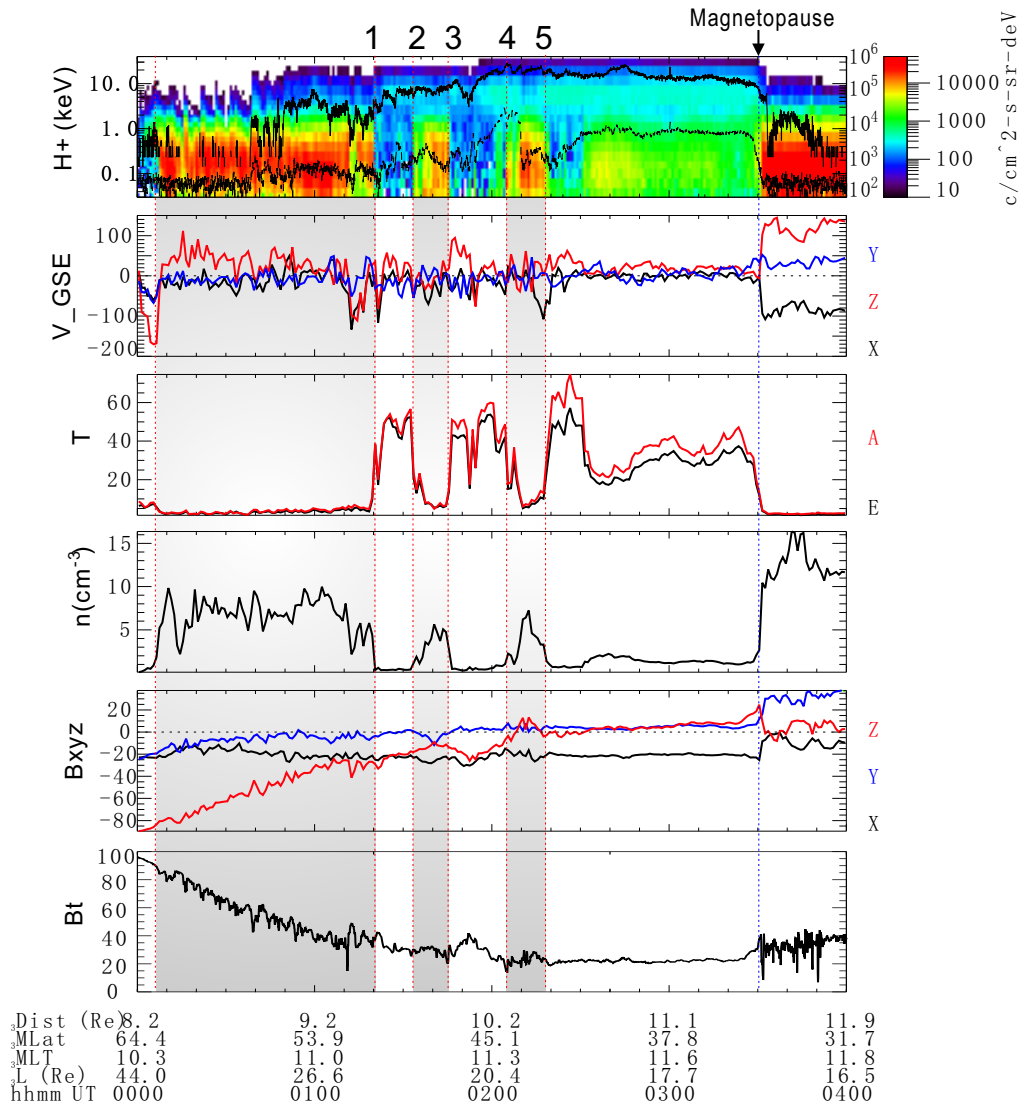


Figure 4-11: An overview plot of the multiple cusp event observed by Cluster C4 from 0000UT to 0400UT on March 2, 2002. Panel 1 shows the plasma ion spectrum obtained by CIS instrument [Rème *et al.*, 1997] over-plotted with the integral flux of energetic ions (30-4000 keV, solid black line) and electrons (30-500 keV, dashed black line) obtained by the RAPID instrument [Wilken *et al.*, 2001]. Panel 2 shows the three components of the plasma velocity in GSE coordinates. Panel 3 shows the ion parallel (red line) and perpendicular temperature. Panel 4 show the ion density. The three components and the magnitude of the magnetic field are shown in panels 5 and 6. Three shaded regions are identified as cusp regions. The red dashed vertical lines labelled 1-5 mark 5 boundaries between the cusp region and the high latitude trapping region. The vertical blue dashed line marks the location of the magnetopause. The magnetosheath is on the right hand side of the magnetopause.

of the magnetopause which is characterized by the shocked solar wind plasma (panels 1 and 4) and strong anti-sunward and northward plasma flow (panel 2). Three cusp regions (shaded regions) can be clearly identified by the enhanced thermalized sheath plasma ions (panels 1), quasi-stagnant plasma flow (compared to that in the magnetosheath, panel 2), low temperature (panel 3) and the high plasma density (panel 4). The time intervals of these three cusps on March 2, 2002 are from 00:06UT to 01:20UT (lasted 1 hour and 14 minutes); from 01:33UT to 01:45UT (lasted 12 minutes) and from 02:05UT to 02:18UT (lasted 13 minutes). The unshaded regions on the left hand side of the magnetopause are the high latitude trapping regions which are characterized by the magnetospheric ion population (panel 1), high temperature (panel 3) and the low plasma density (panel 4). The red dashed vertical lines labelled 1-5 mark 5 boundaries between the cusp region and the high latitude trapping region.

A multiple spacecraft timing method [*Russell et al.*, 1983] has been performed to investigate the five interfaces between the cusp and the high latitude trapping region (labelled 1-5 in Figure 4-11). Spacecraft potential data with 0.2 second resolution measured by the EFW instrument [*Gustafsson et al.*, 1997] onboard Cluster have been used to do the timing analysis. Figure 4-12 shows the spacecraft potential for boundary crossings 1 and 2 shown in Figure 4-11. (a) Boundary crossing 1, from 01:19:40UT to 01:20:00UT (20 seconds time interval) on March 2, 2002. (b) Boundary crossing 2 from 01:33:15UT to 01:33:35UT (20 seconds time interval). The lines of different colors indicate data obtained by four Cluster spacecraft (C1-black, C2-red, C3-green and C4-blue). The spacecraft potential can provide information about electron density, so there is a sharp transition in the spacecraft potential during the boundary crossings from the cusp region to the high latitude trapping region. For the purpose of timing analysis, the spacecraft potential is a good proxy for the electron density. Although the separation of the Cluster spacecraft is only about 100 km, the crossing order can be clearly seen when Cluster crossed the interfaces labelled 1 to 5. The spacecraft crossing order in Figure 4-12 panel (b) (C1, C3, C2, C4) is opposite to that in Figure 4-12 panel (a) (C4, C2, C3, C1) which is consistent with the picture that the

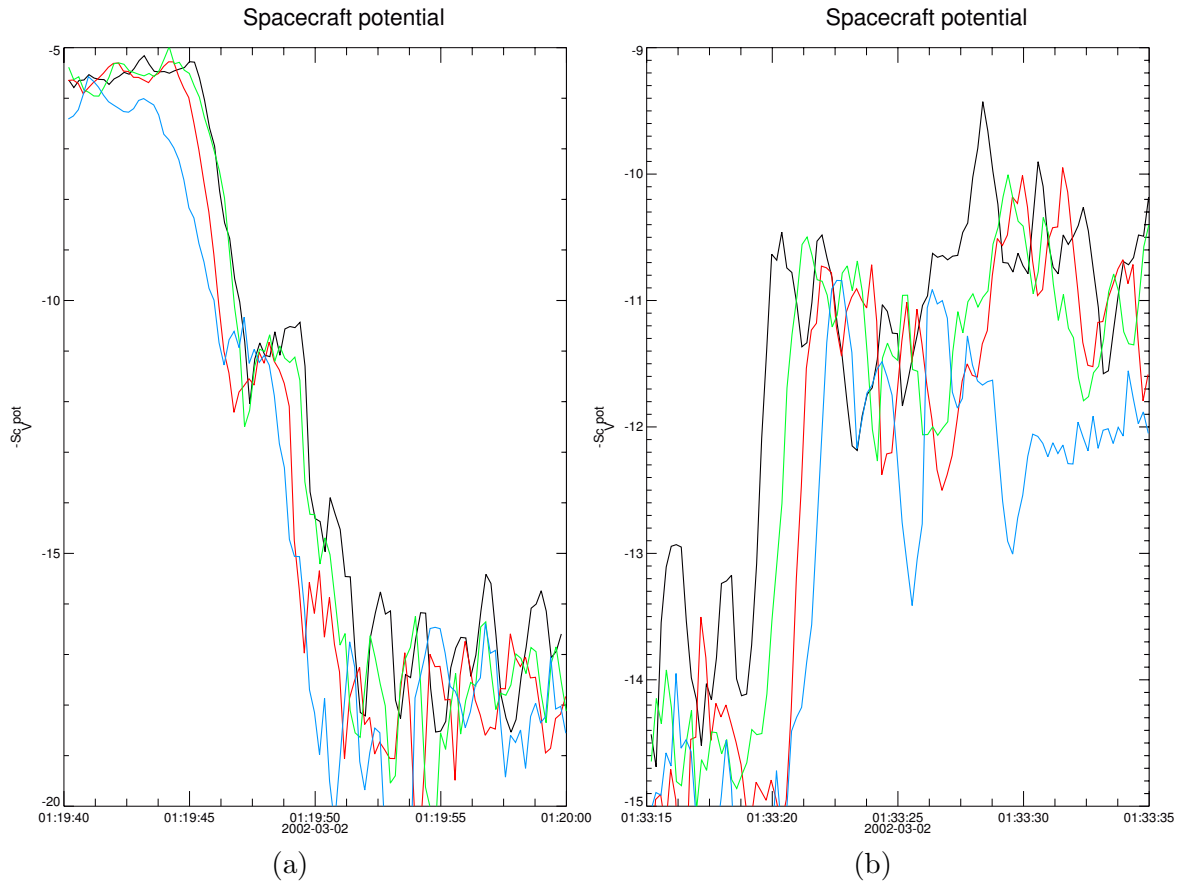


Figure 4-12: The spacecraft potential measured by EFW instrument [Gustafsson *et al.*, 1997] onboard Cluster for boundary crossings 1 and 2 shown in Figure 4-11. (a) Boundary crossing 1, from 01:19:40UT to 01:20:00UT (20 seconds time interval) on Mar 2, 2002. (b) Boundary crossing 2 from 01:33:15UT to 01:33:35UT (20 seconds time interval). The lines of different colors indicate data obtained by four Cluster spacecraft (C1-black, C2-red, C3-green and C4-blue). The spacecraft crossing order in panel (b) (C1, C3, C2, C4) is opposite to that in panel (a) (C4, C2, C3, C1). The boundary normals and the boundary moving speed along the normal directions obtained from multiple spacecraft timing method are given in Table 4.1. The normal directions are also plotted in Figure 4-10.

Table 4.1: Cusp- Dayside Magnetosphere Interface Crossing

	UT	Region	Speed(km/s)	$\mathbf{n}$ in GSE	Cluster Order	Moving direction
1	01:19:49	exit cusp	$v_n = 66.9$	(-0.76, 0.22, 0.61)	C4, C2, C3, C1	northward & anti-sunward
2	01:33:20	enter cusp	$v_n = 36.4$	(0.65, -0.30, -0.70)	C1, C3, C2, C4	southward & sunward
3	01:45:15	exit cusp	$v_n = 13.4$	(-0.60, 0.35, 0.72)	C4, C2, C3, C1	northward & anti-sunward
4	02:04:40	enter cusp	$v_n = 32.2$	(0.46, -0.15, -0.88)	C1, C3, C2, C4	southward & sunward
5	02:17:55	exit cusp	$v_n = 20.6$	(-0.47, 0.10, 0.88)	C4, C3, C2, C1	northward & anti-sunward

interface is moving back and forth.

The normal directions of the boundaries obtained from multiple spacecraft timing method were presented by red (northward motion) and blue (southward motion) arrows in Figure 4-10. As we can see from Figure 4-10, the northward boundary motion alternates with southward motion. The boundary normals and the boundary moving speed along the normal directions for all five boundary crossings are summarized in Table 4.1. The normal directions of boundaries 1, 3, 5 are opposite to those of the boundaries 2 and 4. The boundary crossing orders for boundaries 1 and 3 are also opposite to those for boundaries 2 and 4. We noticed that the crossing order for boundary 5 is different from boundaries 1 and 3. This difference is due to the fact that spacecraft 2 and 3 are almost lying in the plane perpendicular to the normal direction for the boundary crossing 5, so a small change in the normal direction can affect the crossing order of spacecraft 2 and 3. The boundary motion speed along the normal directions varies from 11.3 km/s to 66.9 km/s.

## 4.8 Conclusions

The Cluster spacecraft with its high-altitude polar orbit and its ensemble of scientific instruments has proved to be well suited to study the cusp region. From particle data recorded during two periods totaling 6 months we have been able to distinguish a well-defined region of high density (comparable to that in the magnetosheath) and small or stagnant plasma flow. This region is what we have defined as the SEC.

In summary, we have identified 40 clear SEC events from  $\sim 150$  cusp crossings (Jan. 1 to Apr. 30, 2001 and from Mar. 1 to Apr. 30, 2002) in the Cluster data. Statistically,

1. Energetic ions are observed in the high latitude magnetospheric region for most of

the SEC crossings (32 events of 40 opportunities, 80%). Energetic electrons are observed sometimes (9 events of 40 opportunities 22.5%).

2. The SEC lies predominantly within 10-13 MLT. However there are some cases where this region extends to both earlier and later MLTs.

3. 72.5% of the SEC events have depressed magnetic field.

4. The angular difference between the IMF and local clock angles is a good criterion in 72.5% of the 40 Stagnant Exterior Cusp events.

5. The particle spectra are characterized by a power law and the power law index is found to be closely related to solar wind velocity. The spectra seems to be harder for higher solar wind velocity.

6. There is no clear relationship between the power law index and IMF  $B_z$ , solar wind Mach number, Dst, magnetic turbulence or shear angle.

7. The larger the magnetic shear angle, the more turbulent is the magnetic field in the SEC. This result strongly suggests that the high latitude reconnection process is the major source of the magnetic turbulence in the SEC region.

We selected one multiple cusp event under variable IMF conditions for detailed study. From 0000UT to 0400UT on March 2, 2002 the Cluster spacecraft were on their outbound journey in the northern hemisphere. A normal cusp region was observed from from 00:06UT to 01:20UT, March 2, 2002. Two other cusp regions have been observed by all four spacecraft from 01:33UT to 01:45UT and from 02:05UT to 02:18UT. All three cusp-like encounters were characterized by shocked solar wind plasma and quasi-stagnant plasma flow. The boundary crossing orders and the timing analysis results for five clear boundaries between the cusp region and the high latitude trapping region obtained by all four spacecraft demonstrates temporal variation – the boundary between the dayside magnetosphere/trapping region and the cusp region was shifting in northward-antisunward/southward-sunward direction. So the Cluster spacecraft were observing the same cusp and it appeared as 3 cusp-like regions due to the boundary oscillations. The normal velocities  $v_n$  of the boundary motion varied from 13.4 km/s to 66.9 km/s.

We surveyed 2 years of Cluster data and found one more multiple ( $\geq 3$ ) cusp event of which each cusp lasts longer than 10 minutes. That event, on Feb. 25, 2002, also occurred under variable IMF condition. Multiple cusp events are observed under very different IMF conditions which is hard to be explained by the double reconnection model at different latitudes by *Wing et al.* [2001]. And the double reconnection model can only reproduce double cusps. Analysis (Feb. 25, 2002 event analysis is not shown) indicates that all of four multiple encounters were a temporal effect similar to the March 2, 2002 event.

## Chapter 5

# High Latitude Magnetopause

### 5.1 Introduction

The magnetopause is defined as the boundary between the magnetosphere and the magnetosheath [Sonnerup and Cahill, 1967]. The first subsolar magnetopause observations were made by Explorer 12 [Cahill and Amazeen, 1963]. The magnetometer usually records a sharp change in field direction, sometimes accompanied by a change in field magnitude. (If no such changes occur, the boundary can not be identified in the magnetic field data.) Thus, the magnetopause normally contains currents (from Ampere's law) to change the magnetic field direction [Sonnerup and Cahill, 1967].

The magnetopause is a transition layer between the magnetosheath and magnetosphere where the magnetosheath pressure is balanced by the magnetospheric pressure. Therefore magnetosheath pressure variations can move the position of the magnetopause back and forth [e.g. Sibeck *et al.*, 1991]. It has been observed that the interplanetary magnetic field (IMF) can also affect the position of the magnetopause. The magnetopause moves closer to the Earth when the IMF  $B_z$  is southward [Sibeck *et al.*, 1991; Petrinec and Russell, 1993]. Oscillations of the magnetospheric boundaries could also be driven by the IMF rotations [Laakso *et al.*, 1998].

The magnetospheric boundary layer is a region adjacent to the magnetopause in which magnetosheath plasma has strong influence. There are four subregions: plasma mantle, entry layer, exterior cusp, Low-Latitude Boundary Layer (LLBL).

The plasma mantle, which is located on the field lines where the injected magnetosheath plasma continues tailward, was first reported by Rosenbauer *et al.* [1975]. The low lati-

tude boundary layer contains both magnetosheath and magnetospheric plasma and is located earthward of the magnetopause [Eastman, 1976]. A systematic study of low-latitude boundary layer was carried out by Phan and Paschman [1996] and Phan *et al.* [1996] using the AMPTE/IRM data. However, these works are dealing with low latitude or subsolar magnetopause. Very few studies have addressed the high latitude boundaries. The term "Inner Edge of the Boundary Layer" (IEBL) is adopted from Phan and Paschman [1996] and Phan *et al.* [1996], who define the IEBL as the location where the density has dropped to 5% of its magnetosheath value. Whether the IEBL is formed by a further penetration of solar wind plasma into the trapping regions on closed field lines via diffusion processes (e.g. eddy effect [Haerendel *et al.*, 1978]) or the appearance of magnetosheath plasma on interconnected field lines whose flux tube has not had time to become empty of its ion population, remains an open question.

In addition there are two more boundary regions that are assumed to connect directly to the magnetosheath: the entry layer and the cusp region. The entry layer [Paschmann *et al.*, 1976] is located on the magnetospheric field lines just equatorward of the cusp. It is a region of diffusive, turbulent entry of magnetosheath plasma onto closed field lines probably caused by the eddy flow that maps to the low-altitude cusp [Haerendel *et al.*, 1978]. It has been indicated that in the entry layer the plasma density is almost as high as the magnetosheath but generally lacking the strong antisunward plasma flow. In fact sunward flow has even been reported by Paschmann *et al.* [1976]. Lundin [1985] suggested that a characteristic feature of the entry layer is a strong variability of magnetosheath plasma entry with frequent plasma injection. However, the entry layer is basically a region occurring during southward IMF [Zong *et al.*, 2005a] since the cusp geometry will be changed by the high latitude reconnection when the IMF is northward.

The first direct high-altitude cusp measurement was made by Frank [1971] using data from the IMP 5 satellite. The basic plasma and field properties in the cusp have been mapped by the HEOS spacecraft [Haerendel *et al.*, 1978; Paschmann *et al.*, 1976] and studies of cusp geometry were later carried out by Dunlop *et al.* [2005], by Zhou and Russell

[1997] and by *Eastman et al.* [2000]. Recently, Cluster measurements have revealed a more detailed picture of the presence of both inner and outer boundaries surrounding the high latitude cusp region [*Lavraud et al.*, 2002, 2004b; *Cargill et al.*, 2004; *Taylor et al.*, 2004; *Dunlop et al.*, 2005] (as illustrated schematically in Figure 5.1). *Lavraud et al.* [2004a] investigated the global characteristics of the high altitude cusp and its surrounding regions using three years of Cluster data. They found that the boundary between the cusp and the magnetosheath has a sharp bulk velocity gradient as well as a density decrease and a temperature increase as one goes from the magnetosheath to the exterior cusp. The cusp geometry has also been studied by MHD simulation [*Siscoe et al.*, 2005]. All of these studies show that the high altitude cusp is a very special region, not only because of the presence of magnetosheath plasma, but also because of its still uncertain geometry.

A primary goal of the Cluster mission is to study how magnetopause structure extends into high latitudes and the high-altitude cusp region in particular. This issue is the focus of our study.

Boundary 1 (as shown in Figure 5.1) is a transition from the plasma mantle to the cusp. This boundary is located on open field lines and is where the plasma density jumps from low levels to a value which is comparable to the sheath density and the plasma beta jumps from  $\beta \ll 1$  to  $\beta \approx 1$ .

Boundary 2 is the interface between the cusp and the magnetosheath. This boundary contains some level of turbulence and is sometimes called the turbulence boundary layer [e.g., *Savin et al.*, 2005; *Fritz and Zong*, 2005]. In this chapter, however, we will only address those cases when the interface is clearly identified. The definition of a clear boundary that we apply is a jump larger than 30 km/s in the plasma flow and jumps larger than 5 nT in at least two components of the magnetic field. This boundary appears to be a spatial structure under steady northward IMF conditions [*Lavraud et al.*, 2004b, 2005a].

The high-latitude, closed field-line region of the dayside magnetosphere is called here the high latitude trapping region or HLTR. There are other terms for this region (e.g. dayside plasma sheet [*Cowley and Lewis*, 1990], high latitude boundary layer [*Zong et al.*,

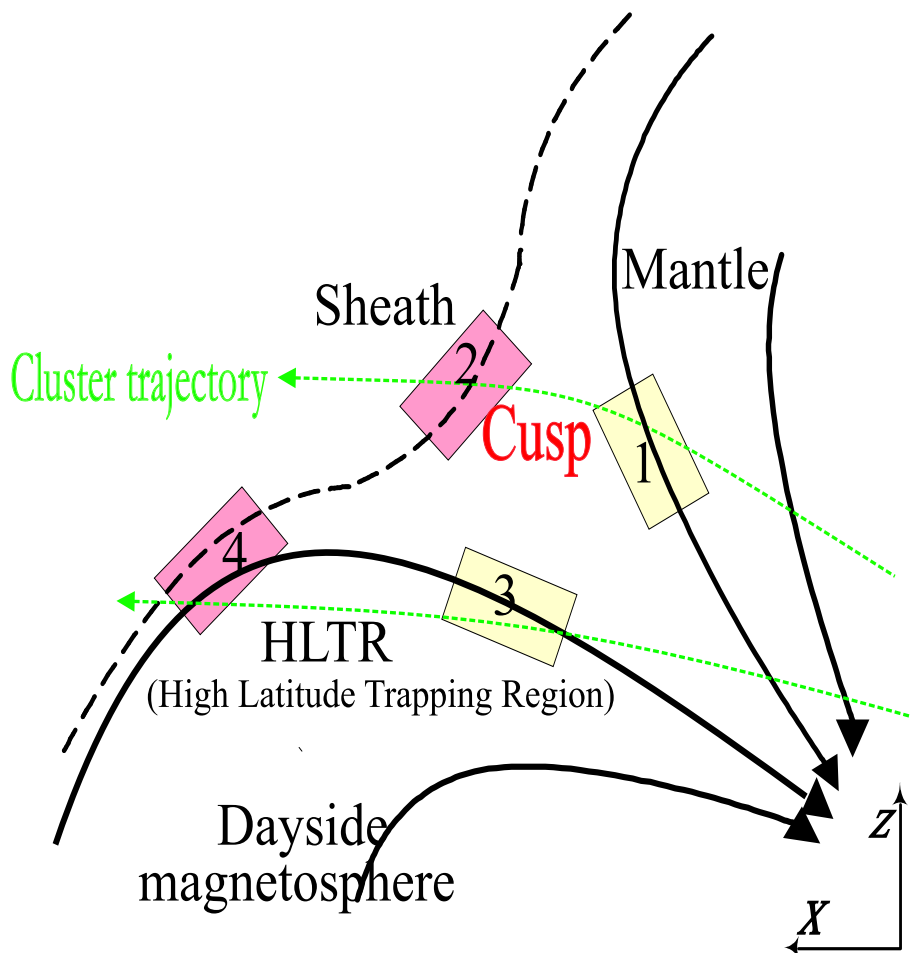


Figure 5-1: Schematic illustration of the high latitude boundaries viewed from dusk direction. Four boundaries are shown: the boundary between mantle and cusp, the boundary between cusp and magnetosheath, the boundary between cusp and HLTR(High Latitude Trapping Region) and the boundary between HLTR and magnetosheath.

2005a], etc.). Boundary 3 is a transition region between the cusp and HLTR which is often called the entry layer [*Paschmann et al.*, 1976]. This boundary is located on the magnetospheric field lines just equatorward of the cusp. The plasma density changes from high cusp levels to the low magnetospheric value.

Boundary 4 is the high latitude magnetopause between magnetosheath and HLTR. This boundary can be easily identified because, as for boundary 3, the density in the HLTR is much lower than that in the magnetosheath and there is a sharp transition in the magnetic field.

An important task in magnetospheric physics is to study the macroscopic and microscopic plasma processes at the magnetopause because these processes determine the rate of transport of mass, momentum and energy from the solar wind into the magnetosphere [*Sonnerup et al.*, 1987]. When the Interplanetary Magnetic Field (IMF) is southward, the subsolar reconnection opens the magnetopause [*Dungey*, 1961] which has been regarded as the main mechanism to transport mass, momentum and energy from the solar wind to the magnetosphere. When the IMF is northward, it is antiparallel to the earth's magnetic field in the high latitude region and there can be  $B_z$  reconnection. If the IMF  $B_y$  component dominates, there can be  $B_y$  reconnection in the dawn or dusk side depending on the sign of the IMF  $B_y$ . High latitude reconnections have been confirmed by MHD simulation and observations [*Crooker*, 1979; *Luhmann et al.*, 1984; *Phan et al.*, 2003; *Zong et al.*, 2005b]. The MHD theory predicts that the accelerated flow is Alfvénic in the HT frame. The HT frame is the reference frame in which the convective electric field is zero. *Paschmann et al.* [1979] and *Sonnerup et al.* [1981] first reported fast flows and the evidence for a rotational discontinuity at the dayside magnetopause. The Walén test was applied to the observed fast flows and it was shown that the flow was Alfvénic and hence consistent with reconnection.

There are four possible processes to break down the frozen-in flux condition so that

reconnection can happen. The terms on the right hand side of the generalized Ohm's law

$$\mathbf{E} + \mathbf{v} \times \mathbf{B} = \frac{1}{en} \mathbf{j} \times \mathbf{B} + \frac{1}{en} \nabla \cdot \mathbb{P} + \frac{1}{\epsilon_0 \omega_{pe}^2} \frac{d\mathbf{j}}{dt} + \eta \mathbf{j} \quad (5.1)$$

are the Hall term, the electron pressure term, the electron inertial term, and the resistive term respectively. The relative importance of these terms is related to four characteristic scale lengths, the ion inertial length  $\lambda_i = c/\omega_{pi}$ , the effective ion Larmor radius  $r_{ci} = (\kappa_B T_e/m_i)^{1/2}/\omega_{ci}$ , electron inertial length  $\lambda_e = c/\omega_{pe}$  and the resistive scale length  $\lambda_{res} = \eta/\mu_0|\mathbf{v}|$ . The process with the largest scale length dominates in the reconnection process. When the Hall term dominates, ions decouple from the magnetic field at the ion inertial length while electrons are still frozen in to the magnetic field but they will decouple with the magnetic field at the electron inertial length. The different behaviors of ions and electrons results in quadrupolar magnetic fields (Hall perturbation). Signatures of the Hall effect have been observed in the magnetotail [Oieroset *et al.*, 2001] and subsolar magnetopause [Mozer *et al.*, 2002]. In this chapter, we present several events showing the Hall reconnection signature for  $B_y$  reconnection at the high latitude magnetopause.

## 5.2 Boundary and Clock Angle of the IMF

In this chapter, we focus on the high latitude magnetopause (boundaries 2 and 4 in Figure 5.1). Figure 5.2 shows an example of the magnetopause crossing from the HLTR into the magnetosheath (boundary 4 in Figure 5.1). From the top the panels show: energetic ion flux (solid black line), energetic electron flux (red dashed line), plasma density, velocity  $V_x$  component, magnetic field components and magnitude. The magnetopause (at 03:31UT, marked by the vertical red line) is clearly identified by the sharp transition in the energetic electron flux, plasma density, velocity and magnetic field measurements. The region to the left of the magnetopause is the HLTR which is characterized by the presence of energetic particles, low plasma density (around  $1 \text{ cm}^{-3}$ ), stagnant plasma flow and relatively stable magnetic field. It can be clearly seen that the flux of energetic electrons drops immediately across the magnetopause, however the flux of the energetic ions extends into the magne-

tosheath due to their larger gyro radius. The region to the right of the magnetopause is the magnetosheath which is characterized by the high plasma density (around  $8 \text{ cm}^{-3}$ ), anti-sunward plasma flow and turbulent magnetic field.

We have surveyed two years of Cluster data and found that the magnetopause crossings from the HLTR to the magnetosheath have similar sharp transition features as the example shown in Figure 5-2, thus they can be clearly identified. However, the boundary between the magnetosheath and the cusp region (boundary 2 in Figure 5-1) is complicated. We have found that sometimes there is a clear boundary between the magnetosheath and the cusp which is associated with the sharp transition in the plasma flow and magnetic field data, and there is no such a clear boundary at other times.

Figure 5-3 shows an example for a clear and an unclear boundary. Figure 5-3 a) shows a clear boundary observed by Cluster when it travels outbound from the northern magnetosphere into the magnetosheath on March 16, 2002. From this figure we can see that all the parameters including energetic proton and electron flux, plasma density, velocity and magnetic field have clear boundaries. Figure 5-3 b) shows an unclear boundary observed by Cluster when it travels inbound from the magnetosheath into the southern magnetosphere on March 19, 2001. We can see from this figure that all the parameters except energetic proton flux have no clear boundaries. We do not know exactly where the boundary is since the parameters change smoothly from the magnetosheath into the magnetosphere.

We have surveyed Cluster data in 2001 and 2002 and found that the boundary between the cusp and magnetosheath is more complicated. Sometimes it is clear and sometimes it is unclear (as illustrated in 5-3 a) and b) respectively). We find that there is some relationship between the boundary and the clock angle of the IMF. In Figure 5-4, all the boundaries between the cusp and the magnetosheath in 2001 and 2002 are shown. The arrows indicate the IMF direction projected in the GSE  $YZ$  plane. The red arrows indicate unclear boundaries and green arrows indicate clear boundaries. In the shaded region, all the arrows are green which means when the IMF clock angle is between  $-65$  and  $81$  degree, the boundary between the magnetosheath and the cusp is clear. However this interface

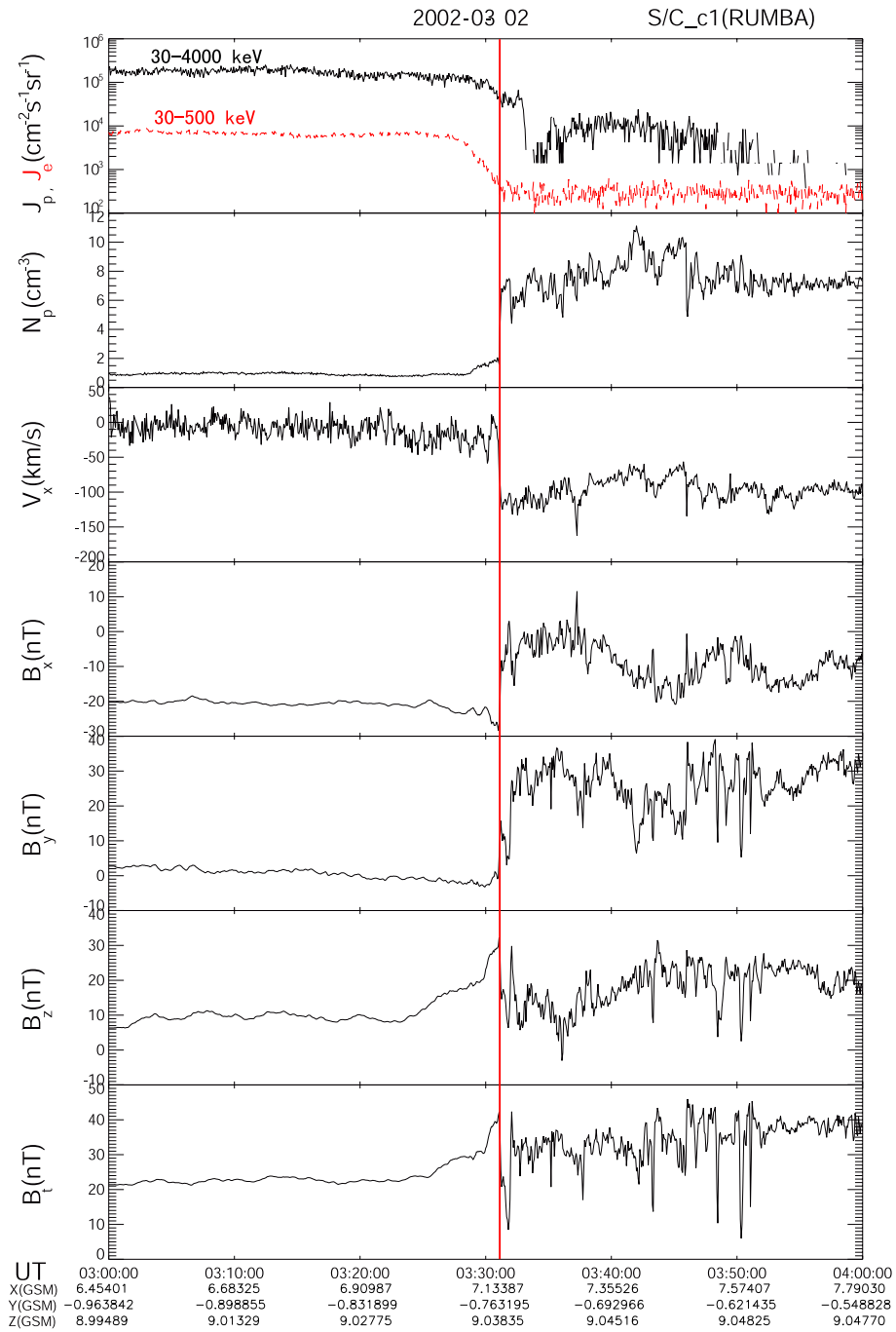


Figure 5-2: Cluster observation of the magnetopause crossing from the HLTR to the magnetosheath on March 2, 2002. From the top the panels show: energetic ion flux (solid black line), energetic electron flux (red dashed line), plasma density, velocity, magnetic field components and magnitude. The vertical red line marks the magnetopause. The region to the left (right) of the magnetopause is the HLTR (magnetosheath).

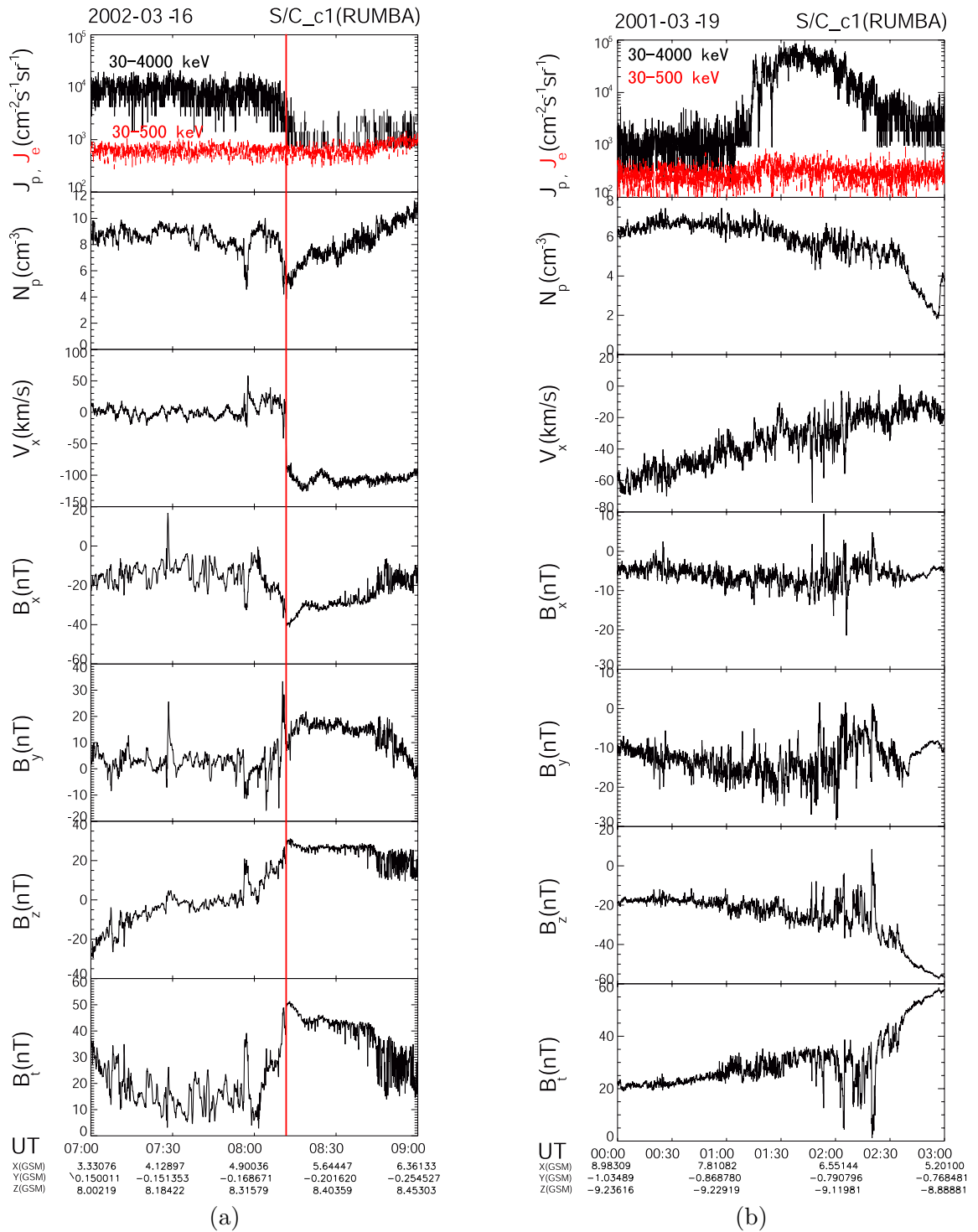


Figure 5-3: Examples for clear and unclear boundary between the cusp region and the magnetosheath. a) Clear boundary on Mar. 16, 2002 b) Unclear boundary on Mar. 19, 2001.

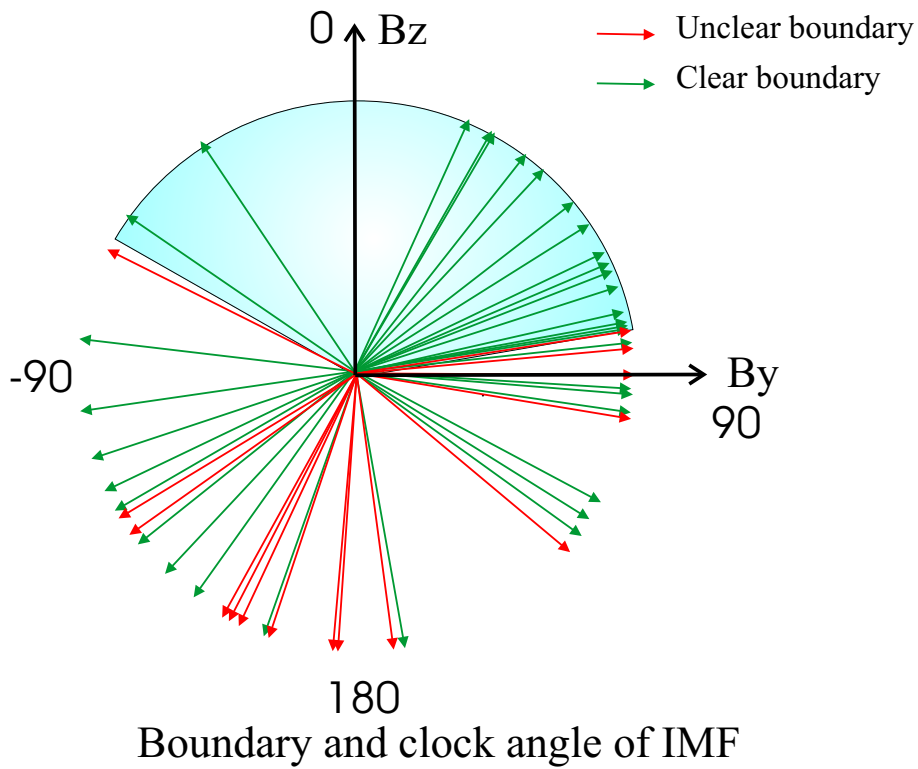


Figure 5.4: The IMF clock angle dependence of the boundary between the magnetosheath and cusp. The arrows indicate the IMF direction projected onto the GSE-YZ plane. In the shaded region, there are only green arrows which means when the IMF clock angle is between  $-65^\circ$  and  $81^\circ$ , the boundary between the magnetosheath and the cusp is clear.

becomes uncertain during southward IMF. The interface between magnetosheath and cusp loses its distinct well-defined signature during southward IMF might be due to the subsolar reconnection which opens the magnetosphere.

### 5.3 Average Structure of the Magnetopause

In this section, we present average structure of the high latitude magnetopause through a superposed epoch analysis based on the data set obtained by Cluster when these spacecraft were crossing the high latitude regions. We have surveyed Cluster data in 2001 and 2002 to select clear single magnetopause crossings to do the superposed epoch analysis. The criteria of a single magnetopause crossing is that Cluster crossed the magnetopause once within 20 minutes (10 minutes before and 10 minutes after the magnetopause crossing). The two types of magnetopause crossings (boundary 2 and boundary 4 shown in Figure 5.1) are distinguished by the plasma density since the plasma density in the cusp region is much higher than that in the HLTR.

Figure 5.5 (a) shows superposed epoch analysis (41 crossings) of the energetic particle flux, the plasma temperature, density, and velocity change from cusp region across the magnetopause (boundary 2 shown in Figure 5.1) in northern hemisphere. The vertical dashed line marked the magnetopause position which is identified by the sharp change in plasma parameters including temperature, density and velocity. The x axis is the minutes after outward magnetopause crossing. The time interval in this plot is 20 minutes, 10 minutes before and 10 minutes after the magnetopause crossing. The red lines show the median values.

Figure 5.5 (b) is similar to Figure 5.5 (a) except that Figure 5.5 (b) shows the boundary crossings (18 crossings) between the HLTR and the magnetosheath (boundary 4 shown in Figure 5.1).

Comparing Figure 5.5 (a) and (b), we can find that the plasma flow and density increase and the proton temperature decreases across the magnetopause from the magnetosphere into the magnetosheath. The amplitude of the flow change is about 100 km/s in both cases.

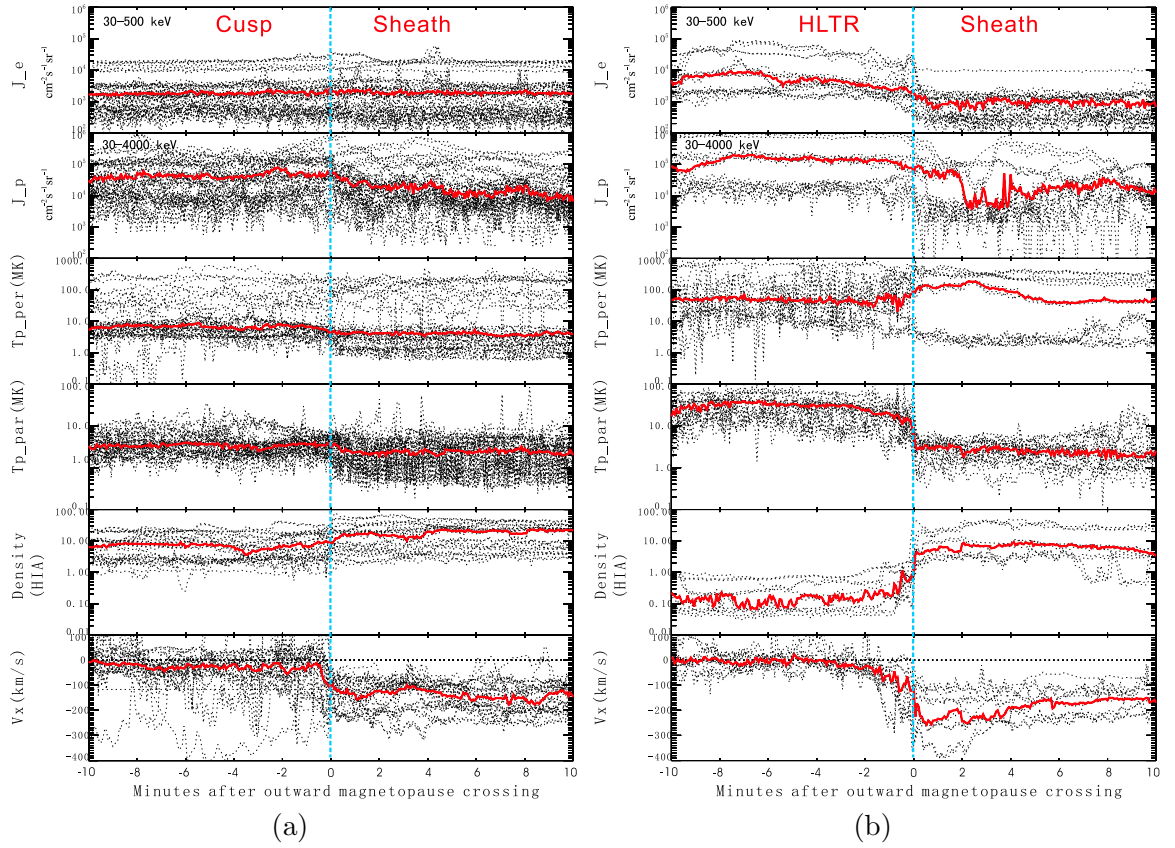


Figure 5-5: Superposed epoch analysis of the energetic particle flux, the plasma temperature, density, and velocity change (a) from cusp region (41 crossings) (b) from HLTR (18 crossings) across the magnetopause in northern hemisphere. The red lines show the median values for each 4 seconds of data.

The plasma density increases by a factor of 3 from the cusp region to the magnetosheath and it increases by two orders of magnitude from the HLTR to the magnetosheath. The parallel temperature decreases by a factor of 2 from the cusp region to the magnetosheath and it decreases by one order of magnitude from the HLTR to the magnetosheath. From the HLTR to the magnetosheath, the energetic electron flux drops immediately, and the energetic ion flux extends into the magnetosheath.

## 5.4 Under Extreme Solar Wind Conditions

In this section, we present statistical results of the plasma parameters of the boundary between magnetosheath and cusp (pink region shown in Figure 5-1) during extreme solar wind conditions based on the data set obtained by Cluster when these spacecraft were crossing the high latitude regions. The extreme solar wind conditions in this section include quiet time (Northward IMF), extreme storm time ( $Dst < -100nT$ ), high solar wind density ( $n > 40$  p/cc) and low solar wind density ( $n < 5$  p/cc). The superposed epoch analysis method was used to study the parameter changes across a boundary.

### 5.4.1 Quiet Time Vs. Extreme Storm Time

The properties of the high latitude boundaries vary rather dramatically under different solar wind conditions. In order to study the average variations of key plasma parameters in the vicinity of the magnetopause under different conditions, we perform a superposed epoch analysis. We present statistical results based on 4 years of data obtained by Cluster when these spacecraft were in the vicinity of the dayside magnetopause.

Figure 5-6 a) shows superposed epoch analysis of the energetic particle flux, the plasma temperature, density, and velocity change from cusp region across the magnetopause under northward IMF in the northern hemisphere. The vertical dashed line marks the magnetopause position which is identified by the jump in plasma parameters including temperature, density and velocity. The x axis is the minutes after outward magnetopause crossing. The time interval in this plot is 20 minutes, 10 minutes before and 10 minutes after the

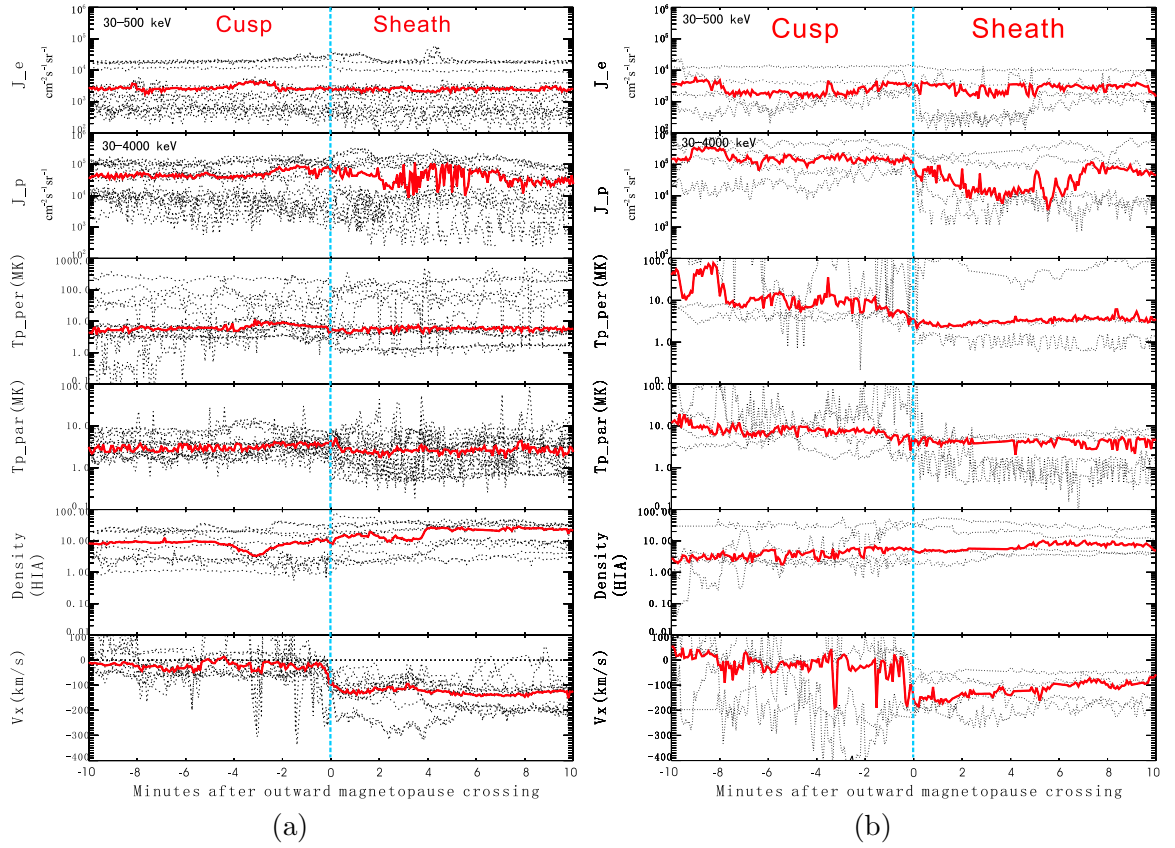


Figure 5-6: Superposed epoch analysis of the energetic particle flux, the plasma temperature, density, and velocity change from cusp region across the magnetopause (a) under northward IMF (17 crossings)(b) during extreme storm time ( $Dst < -100\text{nT}$ ) (5 crossings). The red lines show the median values for each 4 seconds of data.

magnetopause crossing. During northward IMF, the interfaces between the magnetosheath and the cusp are rather clear. The plasma flow and density increase and the proton temperature decreases across the magnetopause from the cusp into the magnetosheath.

Figure 5-6 b) shows superposed epoch analysis of the same parameters as a) but during extreme storm time ( $Dst < -100$  nT). By saying an event is during extreme storm time we mean that the most negative Dst during one storm is  $< -100$  nT and the event is observed during the storm time (initial phase, main phase or recovery phase). In Figure 5-6 b) all the events during extreme storm time from 2001 to 2004 are included. If the magnetopause crossing is in the southern hemisphere, we reverse the time sequence so that the crossing is still from the magnetosphere into the magnetosheath. Comparing Figure 5-6 b) and Figure 5-6 a), we can see that during extreme storm times, the cusp is more turbulent than during quiet times. We also noted that there is no clear plasma density change across the magnetopause during extreme storm time.

#### 5.4.2 High Solar Wind Density Vs. Low Solar Wind Density

The variations of the plasma parameters across the magnetopause when the solar wind density is very high ( $n > 40$  p/cc) and very low ( $n < 5$  p/cc) have also been studied.

Figure 5-7 shows superposed epoch analysis of the energetic particle flux, the plasma temperature, density, and velocity change from cusp region across the magnetopause under northward IMF when solar wind density is low ( $n < 5$  p/cc). The ratio means the 10 minutes averaged values in the cusp region over that in the magnetosheath. The ratios of the plasma perpendicular and parallel temperature are 2.3 and 3.2 respectively. The ratios of the plasma density and velocity are 0.43 and 0.23 respectively.

Figure 5-8 a) and b) show superposed epoch analysis of the energetic particle flux, the plasma temperature, density, and velocity change from cusp region across the magnetopause under southward IMF when solar wind density is high ( $n > 40$  p/cc) and low ( $n < 5$  p/cc) respectively. Comparing these two figures, we can see that during low density solar wind conditions, the magnitude of the parallel temperature change across the mag-

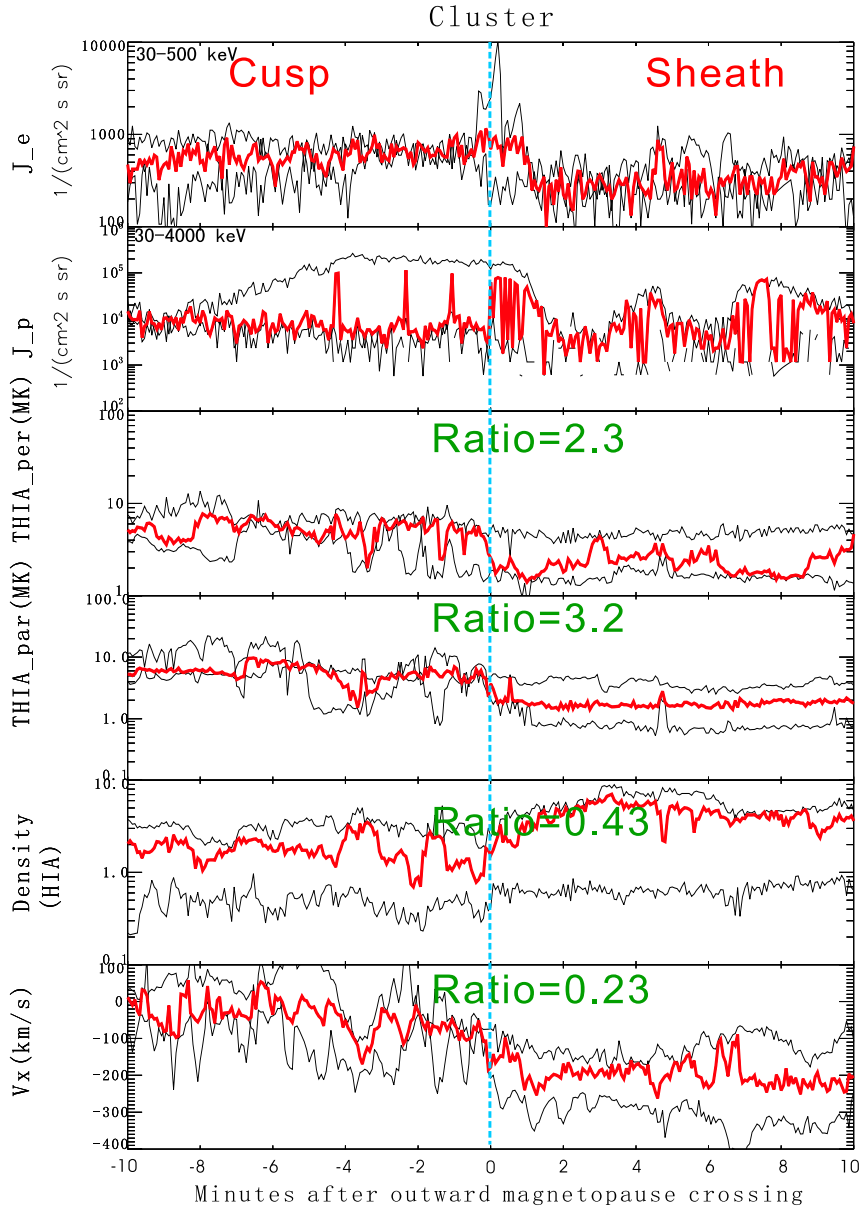


Figure 5-7: Superposed epoch analysis of the energetic particle flux, the plasma temperature, density, and velocity change from the cusp region across the magnetopause under northward IMF when solar wind density is low ( $n < 5$  p/cc). The red lines show the median values for each 4 seconds of data.

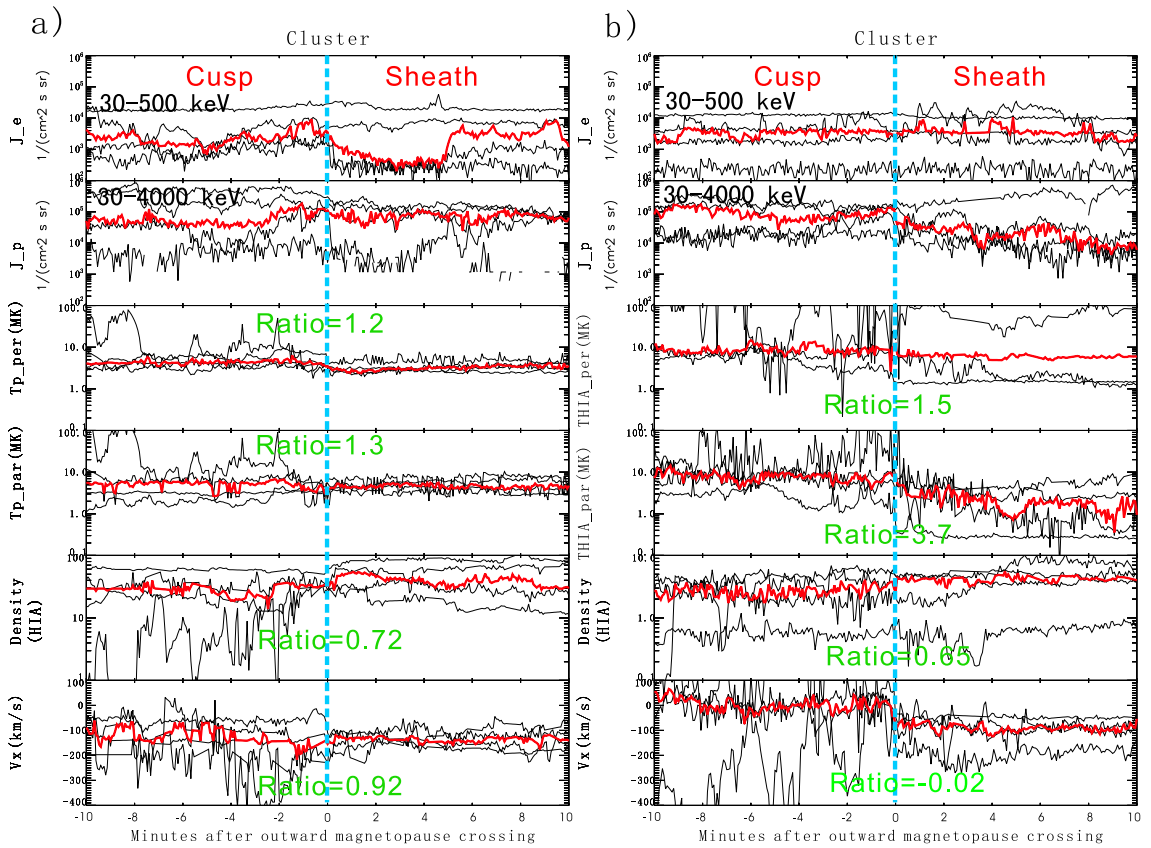


Figure 5-8: Superposed epoch analysis of the energetic particle flux, the plasma temperature, density, and velocity change from the cusp region across the magnetopause under southward IMF a) when solar wind density is high ( $n > 40$  p/cc). b) when solar wind density is low ( $n < 5$  p/cc). The red lines show the median values for each 4 seconds of data.

netopause is larger than during high density solar wind conditions. And the magnitude of the plasma density and velocity change is smaller than during high density solar wind conditions.

## 5.5 Geometry

In this section, we present initial statistical results of the orientation of the two outer boundaries (the pink regions shown in Figure 5.1): that between magnetosheath and cusp (boundary 2) and that between magnetosheath and the HLTR (boundary 4).

The analysis is based on the data set obtained by Cluster when all four spacecraft were crossing the high latitude regions and builds on the recent studies of *Lavraud et al.* [2004b] and *Dunlop et al.* [2005]. We also deduce the geometry of the other high latitude boundaries for particular IMF conditions, as inferred by a number of crossings. Minimum Variance Analysis (MVA, *Sonnerup and Cahill* [1967]) was primarily used to determine the normal direction of the boundary. The MVA method is based on the solenoidality of the magnetic field which results in the jump condition that the normal component of the magnetic field must be continuous across an infinite, thin interface. MVA associates the minimum direction of field variance with the normal magnetic field component, true in the case of a simple 1-D plasma boundary. We, therefore, utilize magnetic field data in this study, as taken by the FGM instrument on board the Cluster spacecraft [*Balogh et al.*, 1997]. The errors in this application are partly characterized by the separation in the principal values of the variance ellipsoid (eigenvalue ratios). Where the MVA gave ambiguous results (medium to minimum eigenvalue  $< 2$ ), the Discontinuity Analyzer (DA) technique was used, using the four spacecraft Cluster measurements, [*Dunlop et al.*, 2002]. All results selected have produced stable directions on all four spacecraft.

The boundary between the magnetosheath and the cusp has been studied before [e.g., *Onsager et al.*, 2001; *Lavraud et al.*, 2002; *Zong et al.*, 2005a]. For the single pass studied by *Lavraud et al.* [2002], the spacecraft exited into the magnetosheath from a central cusp position, so no clear indentation of the boundary between the exterior cusp and magne-

tosheath [Lavraud *et al.*, 2002] was expected or observed. Later papers by Lavraud *et al.* [2004b, 2005a], provided a statistical mapping of the region, but did not specifically address the geometry of the cusp/magnetosheath and cusp/HLTR boundaries. The cusp boundary geometry was also addressed by Dunlop *et al.* [2005], who showed that an indented cusp/magnetosheath boundary was possible in a small number of studied cases, perhaps relating to IMF conditions. With the help of MVA or DA methods, the normal direction at each magnetopause crossing can be estimated and the shape of the boundary between the magnetosheath and cusp can be deduced from the plasma context of the whole cusp traversal for that pass. Here, to confirm the suggestions of Dunlop *et al.* [2005], we extend the analysis to a larger set of crossings through a detailed identification of the nature of each boundary, using a set of both field and plasma conditions.

### 5.5.1 Case Events

In this section we focus first on four key events, which show the geometry of the inner and outer high-latitude boundaries, in order to establish a complete view of the whole cusp region. These results are assisted by the combination of MVA and four spacecraft timing estimates, and we calculate the normal direction at all boundaries to deduce the high latitude geometry, case by case.

The relative locations of the crossings are inferred from the field geometry and plasma character for each pass (as defined above). Figure 5.9 illustrates this process for one pass on 4 March 2002. Figure 5.9 shows the  $V_x$  component of the plasma flow, together with the magnetic field in GSM coordinates and clock angles of both interplanetary magnetic field (IMF) and local magnetic field. The stagnant exterior cusp (SEC) was identified as a region with high-density plasma, a stagnant plasma flow ( $V_x$  around 0) and a highly turbulent magnetic field which is uncorrelated with both the magnetosheath field and the IMF. The SEC region is also accompanied by a depressed magnetic field (compared to the T96 model [Tsyganenko and Stern, 1996]), and it is clear that large magnetic shears (changes in the field direction) are also present in this region.

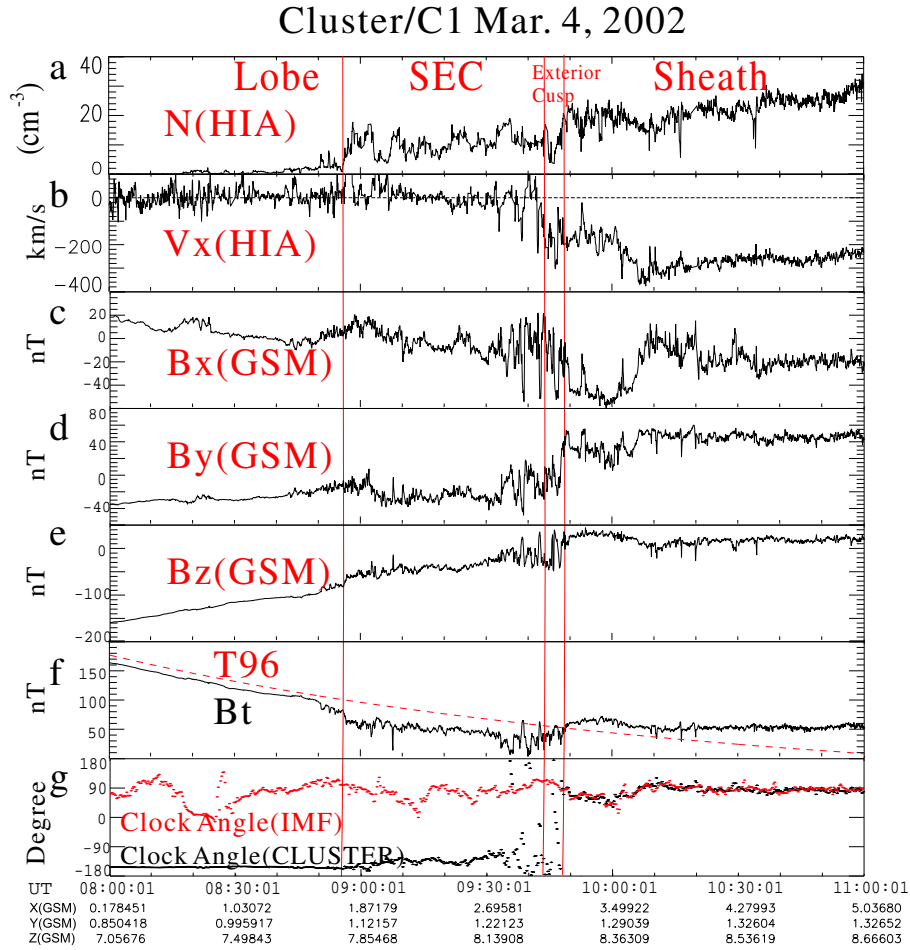


Figure 5-9: An overview of Cluster Ion Spectrometer (CIS), Fluxgate Magnetometer (FGM), and Advanced Composition Explorer (ACE) data from 0800 to 1100 UT on 4 March 2002. (a) shows the plasma density, (b) shows the plasma velocity  $V_x$  component, and (c-f) magnetic field components in the GSM coordinate system and magnitude (in nT) obtained by FGM on board Cluster. (g) shows the corresponding clock angles obtained from the ACE (interplanetary magnetic field, IMF) and Cluster spacecraft. The region between the first 2 vertical lines is identified as the stagnant exterior cusp (SEC). The characteristic of the plasma and magnetic field in the narrow region next to it on the right is very similar to SEC except the flow is not stagnant, so it is identified as the exterior cusp region. HIA is the hot ion analyzer component of CIS. The solar wind data were lagged by 50 min to allow for observed plasma to convect from the ACE spacecraft to the Cluster position.

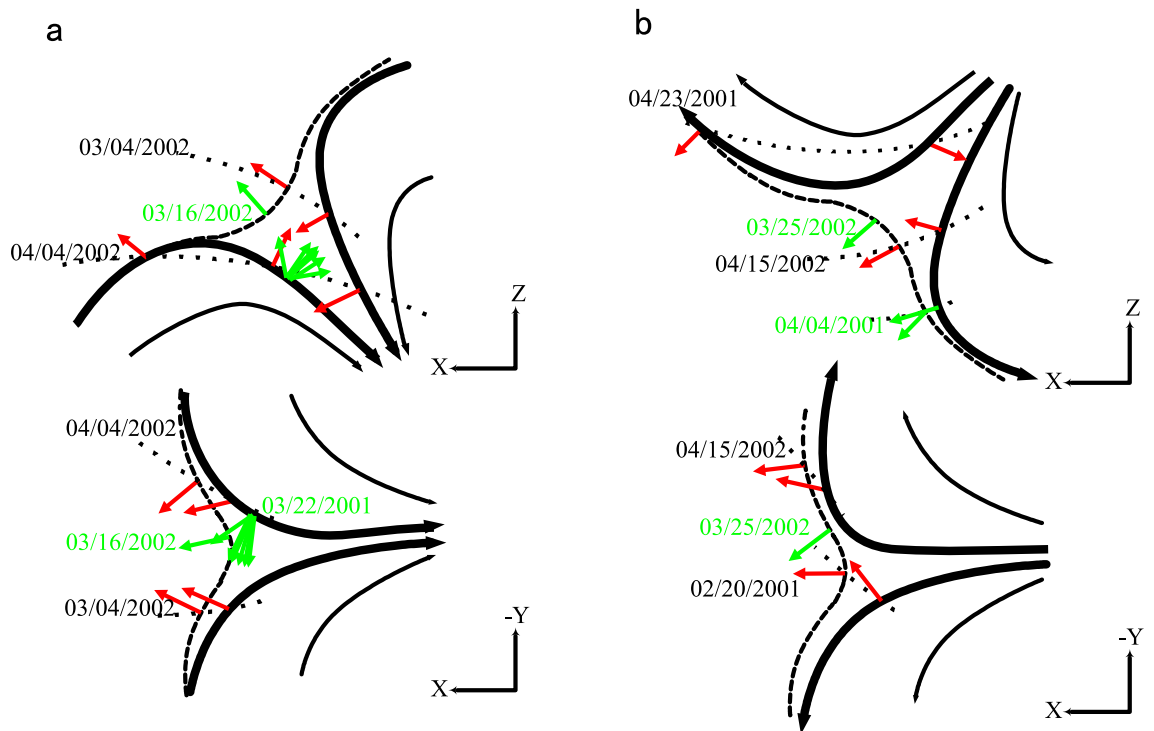


Figure 5-10: a) The geometry of the boundaries surrounding the cusp in the northern hemisphere deduced from a few crossings. The dotted lines show the implied trajectory of the Cluster spacecraft for each crossing with the date labelled on the left. The dashed lines indicate the probable geometry of the interface between the magnetosheath and cusp. b) The geometry of the boundaries in the southern hemisphere deduced from a few crossings.

The MVA method is used to obtain the normal direction of the boundary between the lobe and the cusp (SEC) region (at 9:00 UT) and also the boundary between the cusp and the magnetosheath (at 9:45 UT). The normal directions for each boundary for this and other passes are shown in Figure 5-10, as indicated. Figure 5-10 a) shows the implied geometry of the cusp and adjacent boundaries in the northern hemisphere and Figure 5-10 b) shows the geometry in the southern hemisphere. The indented boundary between the magnetosheath and cusp is drawn in the schematics such that it is most naturally consistent with the normal directions at the different, inferred locations. In these figures, and for each traversal used later, we have identified the boundaries individually and plotted these in an inferred relative location, based on the crossing sequence and plasma characteristics in each case. It is fairly apparent that the normals for both the inner and outer boundaries generally fit a crude geometry as shown. The examples used here correspond to a range of dipole tilt angles and exhibit a range of IMF clock angles (Figure 5-4), although the event set is selected from those events which have clearer and more stable plasma signatures. These results are therefore consistent with the preliminary findings of *Dunlop et al.* [2005] of an indented outer boundary.

### 5.5.2 Crossing Survey

In the previous section, the implications for a fixed cusp geometry were inferred by individually positioning the Cluster orbit relative to the cusp. In this section, we present results of a comparative survey of the outer boundaries only. We use GSM coordinates to reference the geometry of each crossing, given the selection criteria defined below (which by necessity does limit the data set, except as indicated in section 5.5.1). This procedure does not take account of any dynamic displacements of the cusp, but the crossing positions have been normalized as described below. In that context, the study provides a statistical check of the geometry trends implied in section 5.5.1, given the limitation arising from any cusp motions. The central cusp positions, in particular, are most likely to be affected by cusp displacements. We surveyed 6 months of Cluster data (from 1 January to 30 April

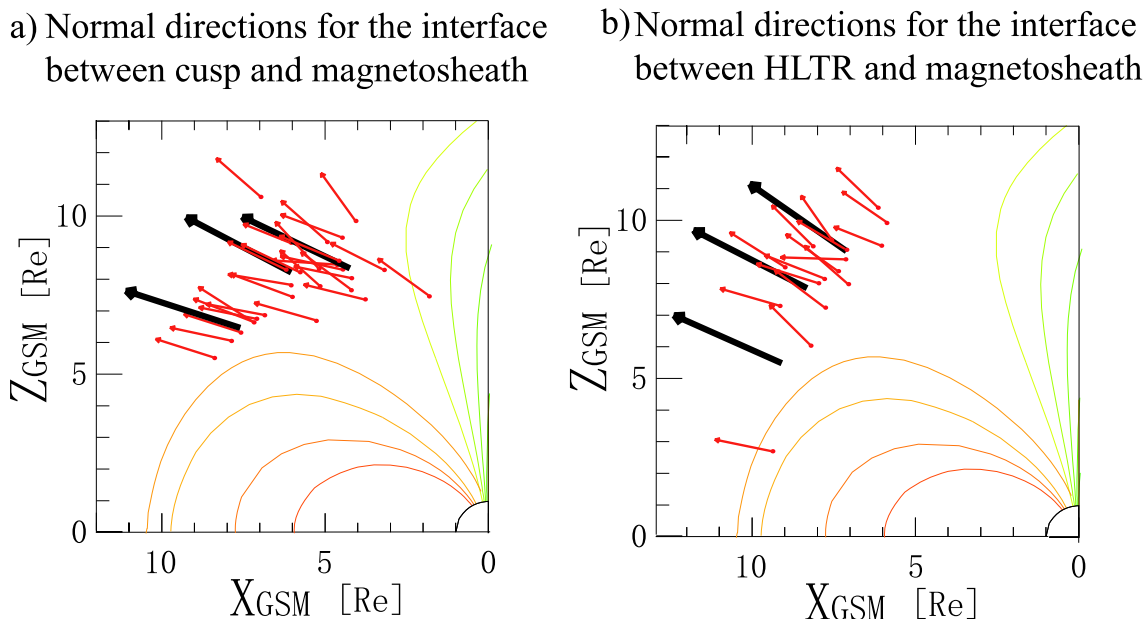


Figure 5-11: a) Normal directions for the interface between cusp and magnetosheath (38 events in 2001 and 2002, of which 11 events are in the southern hemisphere which can not be seen in this figure but can be seen in the X-Y plane in Figure 5-12) in the X-Z plane in the GSM coordinate system. Black arrows show the average normal directions over data with magnetic latitude  $\lambda < 50^\circ$ ,  $50^\circ \leq \lambda < 60^\circ$  and  $\lambda \geq 60^\circ$  respectively. The magnetic field lines are calculated from the T96 model [Tsyganenko and Stern, 1996]. The inputs for the T96 model are: Dynamic pressure = 2.5 nPa ; Dst = -10.0 nT ; IMF  $B_y = 2.0$  nT and IMF  $B_z = -0.1$  nT. b) Normal directions for the interface between HLTR and magnetosheath (19 events in 2001 and 2002) in the X-Z plane in the GSM coordinate system. Black arrows show the average normal directions over data with magnetic latitude  $\lambda < 40^\circ$ ,  $40^\circ \leq \lambda < 47^\circ$  and  $\lambda \geq 47^\circ$  respectively.

2001 and from 1 March to 30 April 2002). The identification of the cusp was made on the basis of the following criteria: 1. high density plasma (comparable to that in the sheath); 2. small or stagnant plasma flow ( $V_x < 60$  km/s). These criteria have been used by Zong *et al.* [2004a], Lavraud *et al.* [2002] and Zhang *et al.* [2005] and we use them here for this initial data set, since they effectively give clear stable boundaries.

In Figure 5-11 we selected only clear boundaries, given the criteria mentioned. Thirty-eight cusp-magnetosheath crossings in 2001 and 2002 have been identified, of which 11 crossings are in the southern hemisphere and cannot be seen in this figure, but can be seen in the X-Y plane in Figure 5-12. In addition, nineteen HLTR-magnetosheath crossings

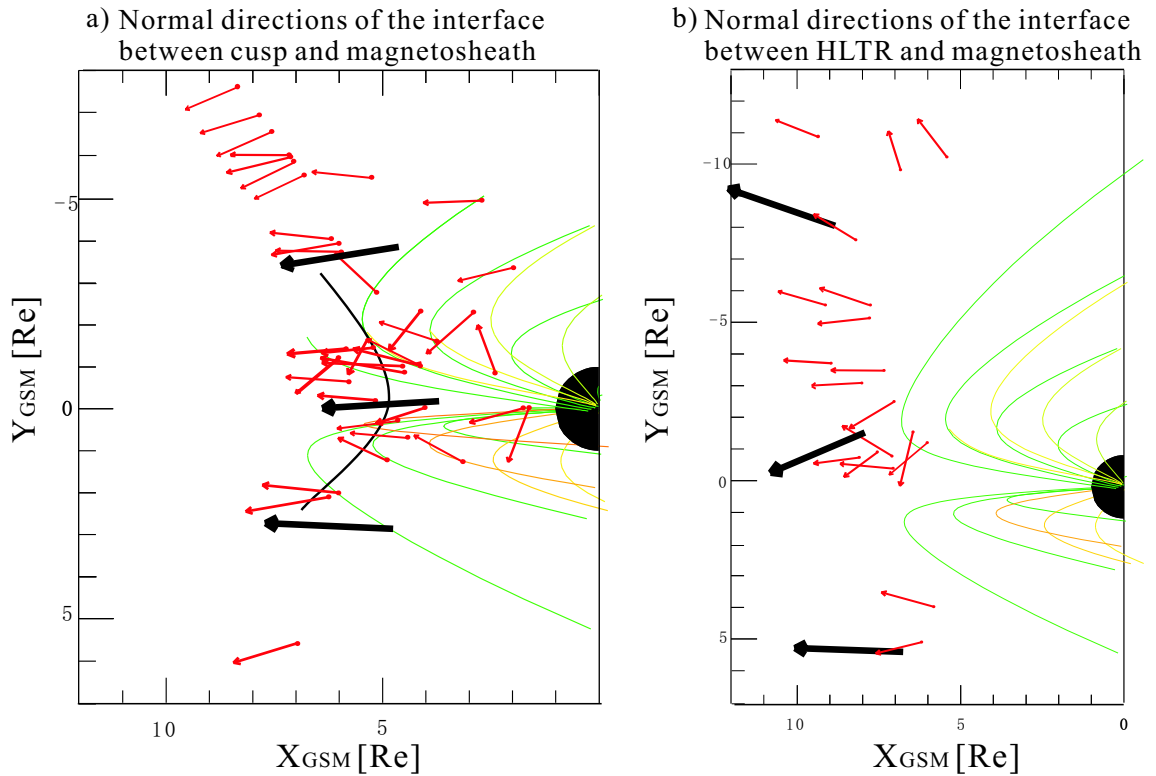


Figure 5-12: This figure shows the same crossing sets as those in Figure 5-11, but in the GSM-XY plane, where a) gives normal directions for the Cusp/magnetosheath interface and b) gives normal directions for the HLTR/magnetosheath boundary. Black arrows in a) show the average normal directions over data at noon ( $-15^\circ \leq \phi < 15^\circ$ ), at dawn side ( $\phi < -15^\circ$ ) and at dusk side ( $\phi \geq 15^\circ$ ) respectively. Black arrows in b) show the average normal directions over data at noon ( $-20^\circ \leq \phi < 20^\circ$ ), at dawn side ( $\phi < -20^\circ$ ) and at dusk side ( $\phi \geq 20^\circ$ ) respectively.

have been identified. Since the position of the cusp relative to each crossing point can vary, the magnetic field lines are shown for guidance only. We search for the combined effects of both the statistical trends overall (with respect to latitude, here) and the comparison between separate sets of crossings corresponding to the cusp/magnetosheath boundary (Figure 5-11a) and the HLTR/magnetosheath boundary (Figure 5-11b), respectively. We can see from Figure 5-11 a) that the normal directions are basically in the same direction. The angles between normal directions of data with magnetic latitude  $\lambda < 50^\circ$ ,  $50^\circ \leq \lambda < 60^\circ$  and  $\lambda \geq 60^\circ$  and equatorial plane are  $18^\circ$ ,  $28^\circ$  and  $26^\circ$  respectively. In Figure 5-11 b) these angles are  $25^\circ$ ,  $28^\circ$  and  $36^\circ$ .

Figure 5-12 shows the normal directions for the same crossing sets used for Figure 5-11, but now for the distribution in local time. Although all normal vectors point sunwards, the trends revealed in panel a) are quite different from those in panel b). In particular, Figure 5-12a) shows that the bunching seen in latitude for the cusp/magnetosheath interface is also present as we move from dawn to dusk in local time, in this case exhibiting inward pointing (toward noon) normals on either side of noon. On the dawn-side, most of the normal vectors are pointing into the dusk direction and on the dusk-side most of the normal vectors are pointing into the dawn direction. In the region near 12 MLT they are mixed because of the effect of displaced cusp positions relative to individual crossing points, possibly arising as a result of changing IMF  $B_y$ , as referred to earlier. Since the trend seen in local time is the direct opposite of that expected for an outwardly curved geometry, we can deduce that the interface between the magnetosheath and cusp is indented in the X-Y plane for this crossing set. In contrast, Figure 5-12b) shows normal vectors that are widely distributed in the Y direction. On the dawn-side, most of the normal vectors are pointing into the dawn direction and on the dusk-side they are pointing into the dusk direction. In the region near 12 MLT they show mixed directions. This is consistent with the classical picture of the magnetopause, not associated with the cusp region.

We have found that the outer cusp and adjacent boundaries show clear trends in the tilting of the boundary, such that the direction of the boundary normal points progressively toward noon as the local time of the crossing location occurs further away from local noon. This observed behavior of the normal directions suggests a possible indented geometry for this set of boundary crossings. Although the crossing set used covers a wide range of IMF clock angles, it is slightly biased towards those crossings for which a clear change (stagnation) in magnetosheath flow, together with a depressed (diamagnetic) magnetic field intensity, can be observed across the cusp/magnetosheath interface. The latter effect produces high beta plasma conditions, which may favor an indented geometry.

## 5.6 Reconnection at Magnetopause

Several measurements made by instruments onboard Cluster are employed to do the study of the reconnection at the magnetopause. The energetic particle flux data are from Research with Adaptive Particle Imaging Detectors (RAPID) [Wilken *et al.*, 1997], plasma moment data are from Cluster Ion Spectrometer (CIS) [Rème *et al.*, 1997] and the magnetic field data are from Fluxgate Magnetometer (FGM) [Balogh *et al.*, 1997]. In this section, we focus on the Mar. 23, 2002 event and list the characteristics of three  $B_y$  reconnection events at the end.

Figure 5-13 shows the satellite trajectory from 1000UT to 1300UT on Mar. 23, 2002, when Cluster was travelling outbound in the dawn side northern hemisphere. The magnetic field vectors are over plotted on the satellite trajectory in Figure 5-13. It is clear that Cluster crossed the magnetopause where the magnetic field changed its direction at around 1138UT.

Figure 5-14 gives an overview of Cluster CIS, FGM and RAPID data during the same time period of Figure 5-13. From the top the panels show the plasma density, plasma flow velocity  $V_x$  component, magnetic field and energetic electron, proton, helium and heavy ion fluxes. Cluster crossed the magnetopause from the cusp region into the magnetosheath at around 1138UT (marked by a red line). The interface between the cusp and the magnetosheath is clearly associated with sharp transitions of the magnetic field and plasma moments. These variations suggest that the interface is a clear current sheet. It is noticed that  $B_y$  changed around 40 nT across this boundary. Energetic electrons, protons, helium and oxygen ions were observed and their intensity peaked at this current sheet.

Figure 5-15 shows the local magnetic field data (black lines) in GSE coordinates and the interplanetary magnetic field (IMF, in red lines) obtained by the ACE spacecraft. The ACE data have been time-shifted to the Cluster position using a technique developed by Weimer *et al.* [2003]. This technique uses minimum variance analysis technique [Sonnerup and Cahill, 1967] to derive the tilting angles of the IMF phase front which is used for

*CLUSTER ORBIT*  
2002 03/23/10:00--03/23/13:00

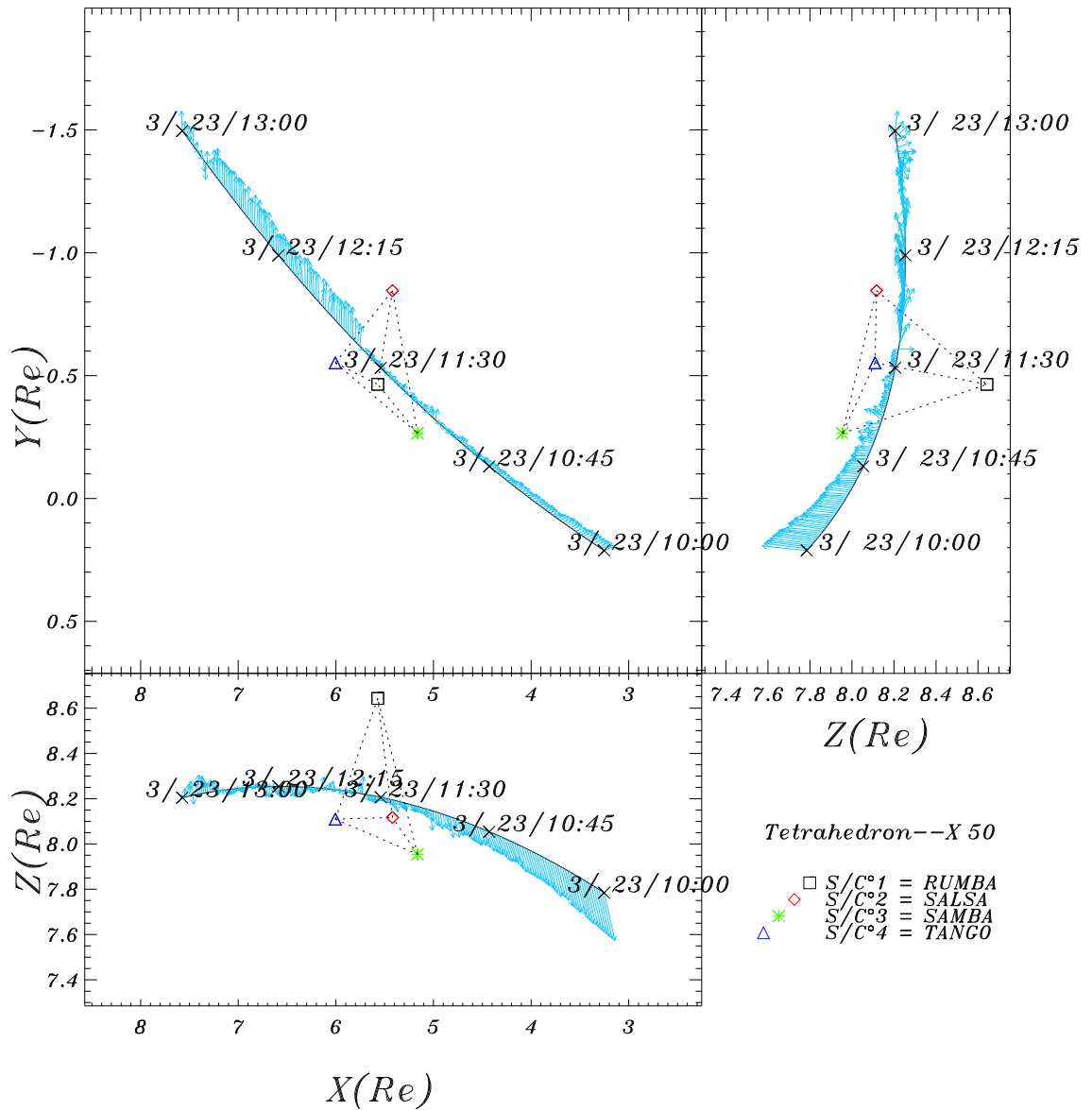


Figure 5-13: Cluster orbit on Mar. 23, 2002 plotted in the GSM coordinate system together with magnetic field vectors.

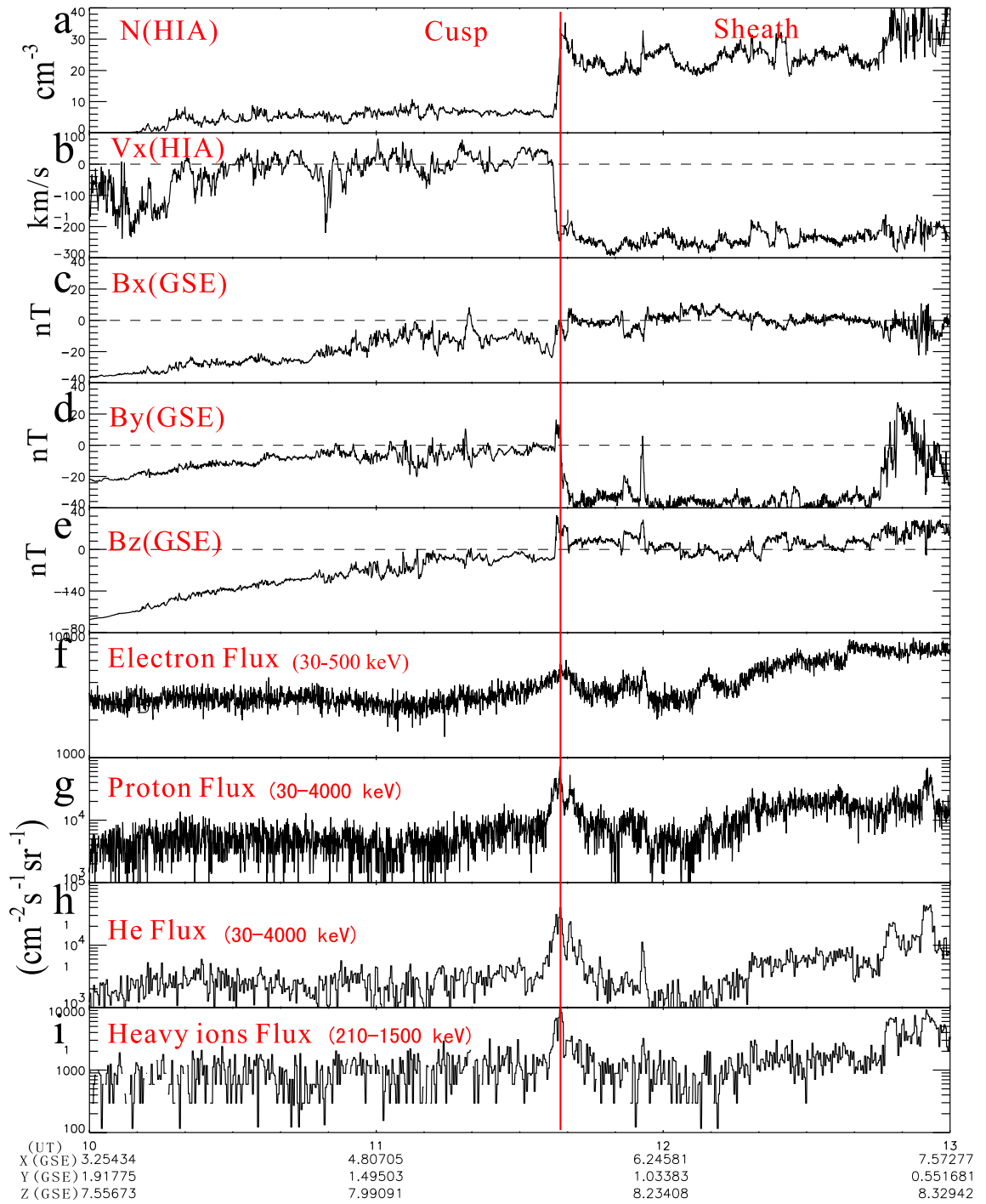


Figure 5-14: An overview of Cluster Ion Spectrometer (CIS), Fluxgate Magnetometer (FGM) and Research with Adaptive Particle Imaging Detectors (RAPID) data from 1000 to 1300 UT on 23 March 2002. (a) plasma density (b) plasma velocity  $V_x$  component, and (c-e) magnetic field components in the GSM coordinate system (in nT). (f-i) Energetic electron, proton, helium and heavy ion flux.

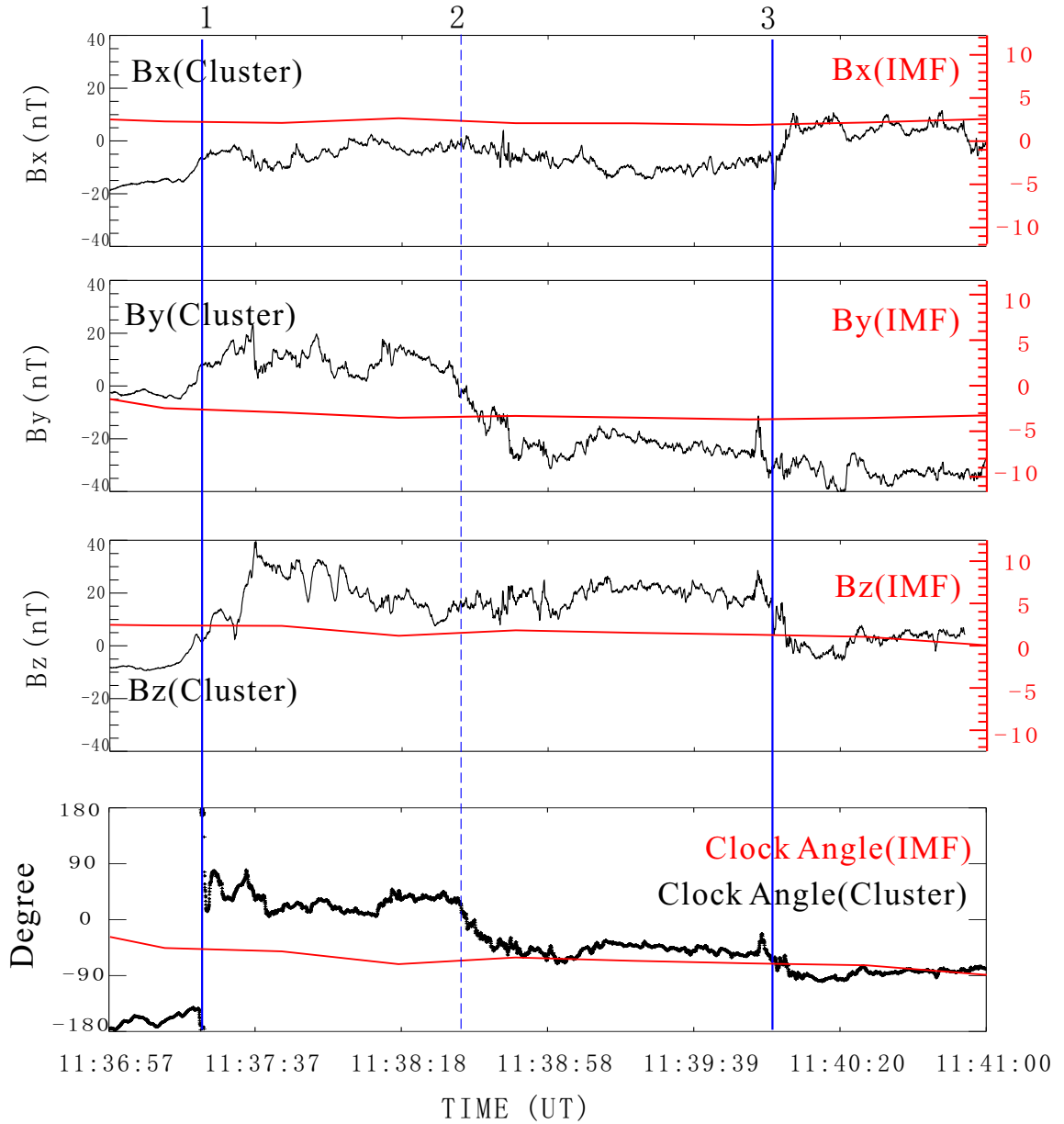


Figure 5-15: The magnetic field data obtained from the ACE (interplanetary magnetic field, IMF) and Cluster spacecraft. The solar wind data were time-shifted to allow for the plasma to travel from the ACE spacecraft to the position of Cluster. The vertical lines mark the region of the magnetopause crossing.

accurate calculation of the IMF time delay. The region between vertical lines 1 and line 3 is the transition region from the cusp into the magnetosheath which is determined based on the plasma (shown in Figure 5-16) and magnetic field signatures (shown in Figure 5-15 and Figure 5-16). The dashed vertical line 2 marks the time when  $B_y$  changes its sign from positive to negative. Lines 1, 2 and 3 are carried to Figure 5-16 and Figure 5-17. The clock angle of IMF is  $-90^\circ$  which indicates the IMF  $B_y$  dominates and favors  $B_y$  reconnection at dawn side of the cusp region.

Figure 5-16 is an overview plot for this boundary crossing for 12 mins time interval. In the transition region between lines 1 and 2, the ion density (panel a) is high and the peak density is  $32 \text{ cm}^{-3}$  which is even higher than the sheath level which is  $22 \text{ cm}^{-3}$ . The plasma flow jet which is the signature of reconnection is clearly seen in  $V_y$  component (panel d). The  $B_y$  component changes 42 nT across line 2 (panel f). Since Cluster has 4 identical satellites, from the magnetic field measured by the 4 satellites, the current can be calculated using the curlometer method. The total current is shown in panel g and panel h shows the error of current calculation [Robert *et al.*, 1998]. The curlometer method is invalid if the size of the Cluster tetrahedron is larger than the current structure. Although the current structure is thin (218 km), the separation of the satellites is small during this event (the largest separation in  $y$  direction is 76.4km). From panel h one can see that most of the values of  $\nabla \cdot \mathbf{B}/|\nabla \times \mathbf{B}|$  are between  $\pm 0.5$  which indicates that the current calculation is reliable in general. Filamentary current structures can be seen in panel g. The maximum current density is  $120 \text{ nA}/\text{m}^2$ . From panel i we can see there is a dawnward electric field measured by EFW instrument (black line) in this structure. The  $y$  component of  $-\mathbf{V} \times \mathbf{B}$  is over plotted (red line). If the magnetic fields are frozen into the plasma,  $\mathbf{E} = -\mathbf{V} \times \mathbf{B}$ , i.e., these two lines should coincide with each other. However between lines 1 and 2, the measured electric field (black line) differed significantly from  $(-\mathbf{V} \times \mathbf{B})_y$  which indicates that the ions did not obey  $\mathbf{E} = -\mathbf{V} \times \mathbf{B}$ . The difference between the red and black lines on the left hand side of line 1 might be due to the statistical error since the plasma density is low in that region.

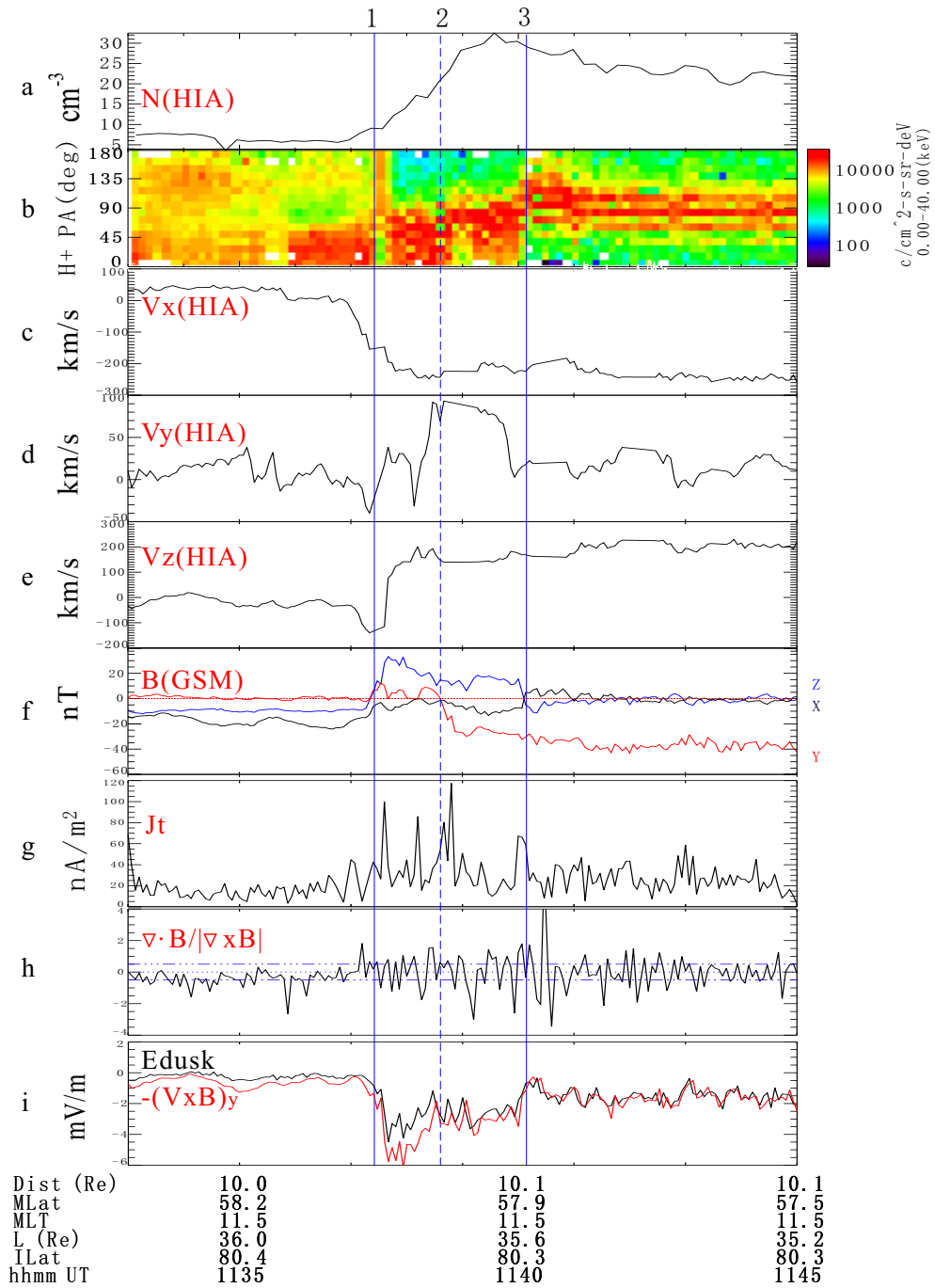


Figure 5-16: The detailed view of the magnetopause crossing (from 1133UT to 1145 UT, 12 minutes time interval). a) proton number density, b) hydrogen pitch angle, c), d) and e) plasma velocity components in GSM coordinate system, f) magnetic field components, g) total current, h) error of current calculation, and i) electric field in dawn dusk direction measured by EFW instrument (black line) and calculated by  $-V \times B$  (read line).

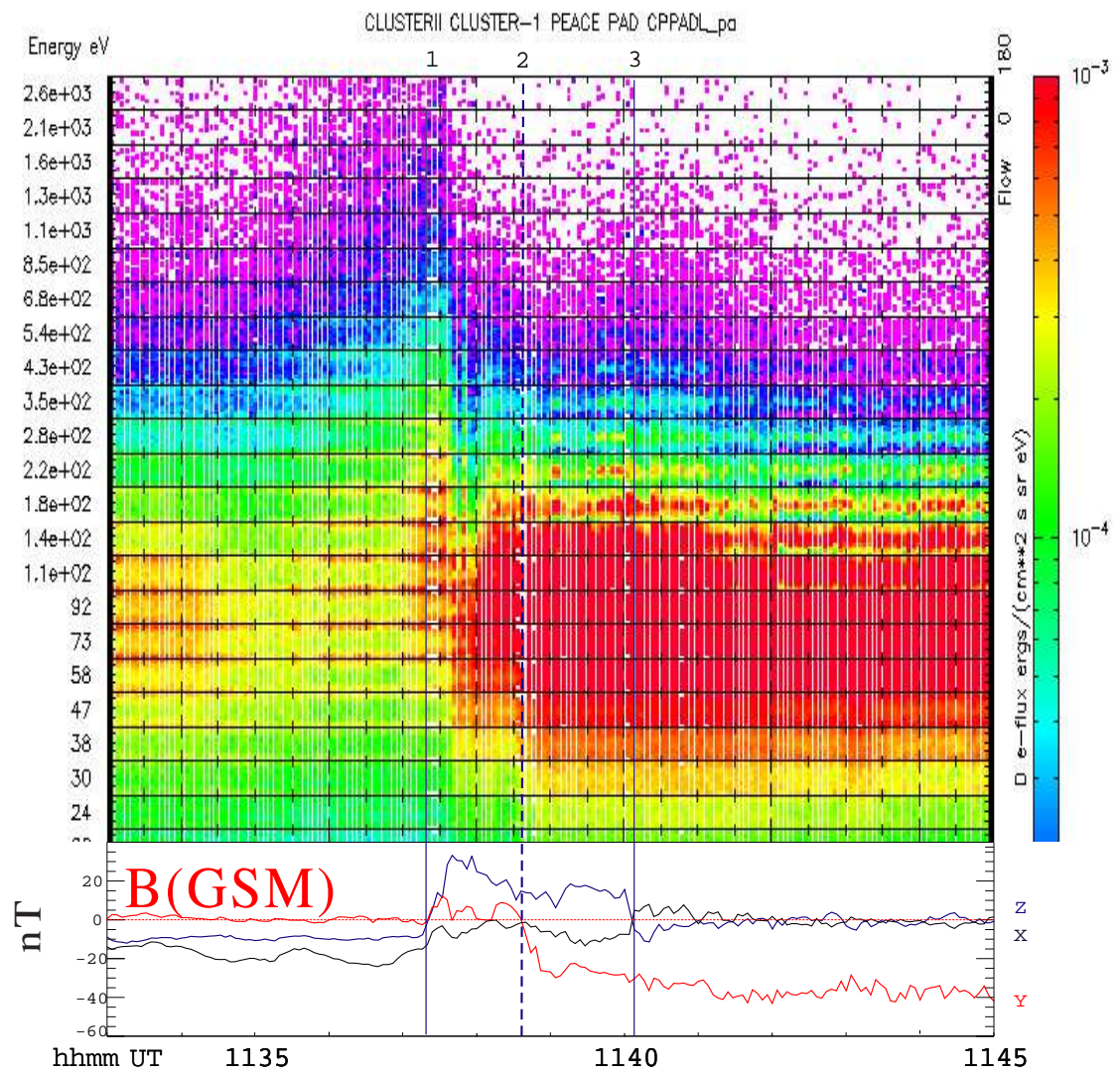


Figure 5-17: The pitch angles of electrons with different energies. In each energy channel panel the vertical scale displays the pitch angle from  $0^\circ$  to  $180^\circ$ .

Figure 5-17 shows the pitch angles of electrons with different energies lined up with the magnetic field data. The energy dispersion features are clearly seen. When Cluster encountered the magnetospheric edge of the reconnection region (line 1), the energy went up and the field aligned electrons indicated that they were on newly reconnected field lines. Then the energy decreased and the electrons changed from a field aligned distribution to an isotropic distribution. This variation probably results from the wave-particle scattering. The turbulent magnetic fields which could be signatures of electromagnetic waves can be clearly seen in the bottom panel of Figure 5-17. The electrons with higher energy experience stronger pitch angle scattering than those with lower energy and escape along open field lines in a very short time. The electrons with lower energy experience weaker pitch angle scattering and they can stay on open field lines for a longer time.

Figure 5-18 shows the geometry of the reconnection region viewed from  $x$  direction. The small box marks the electron diffusion region. Outside of the electron diffusion region is the ion diffusion region where ions are decoupled from the electrons and magnetic field, creating the Hall magnetic field in  $x$  direction. Hall currents are shown as dashed lines. The orange line is the Cluster trajectory deduced from the observations. Along this trajectory, Cluster observed the  $B_y$  component changing from positive to negative, a bipolar signature in  $B_x$  component, filamentary current sheet structure which is possibly the Hall current, and a plasma flow jet in  $+y$  direction.

Figure 5-19 shows the magnetic field data projected in local coordinate system where  $L$ ,  $M$  and  $N$  are the maximum, medium and minimum variance directions respectively. A clear bipolar signature is seen in the minimum variance direction which is basically in the GSE  $x$  direction (Table 5.1) with the  $+/-$  sense of the variation being as predicted for the Hall perturbation. The Hall magnetic field amplitude is around 30% of the total magnetic field which is consistent with a hybrid simulation [Shay *et al.*, 1999].

Figure 5-20 shows the high resolution magnetic field data from all 4 spacecraft for 20 seconds time interval when  $B_y$  changes its sign. Although the 4 spacecraft are very close to each other with separations of about 100 km, the magnetic fields observed by C3 (in

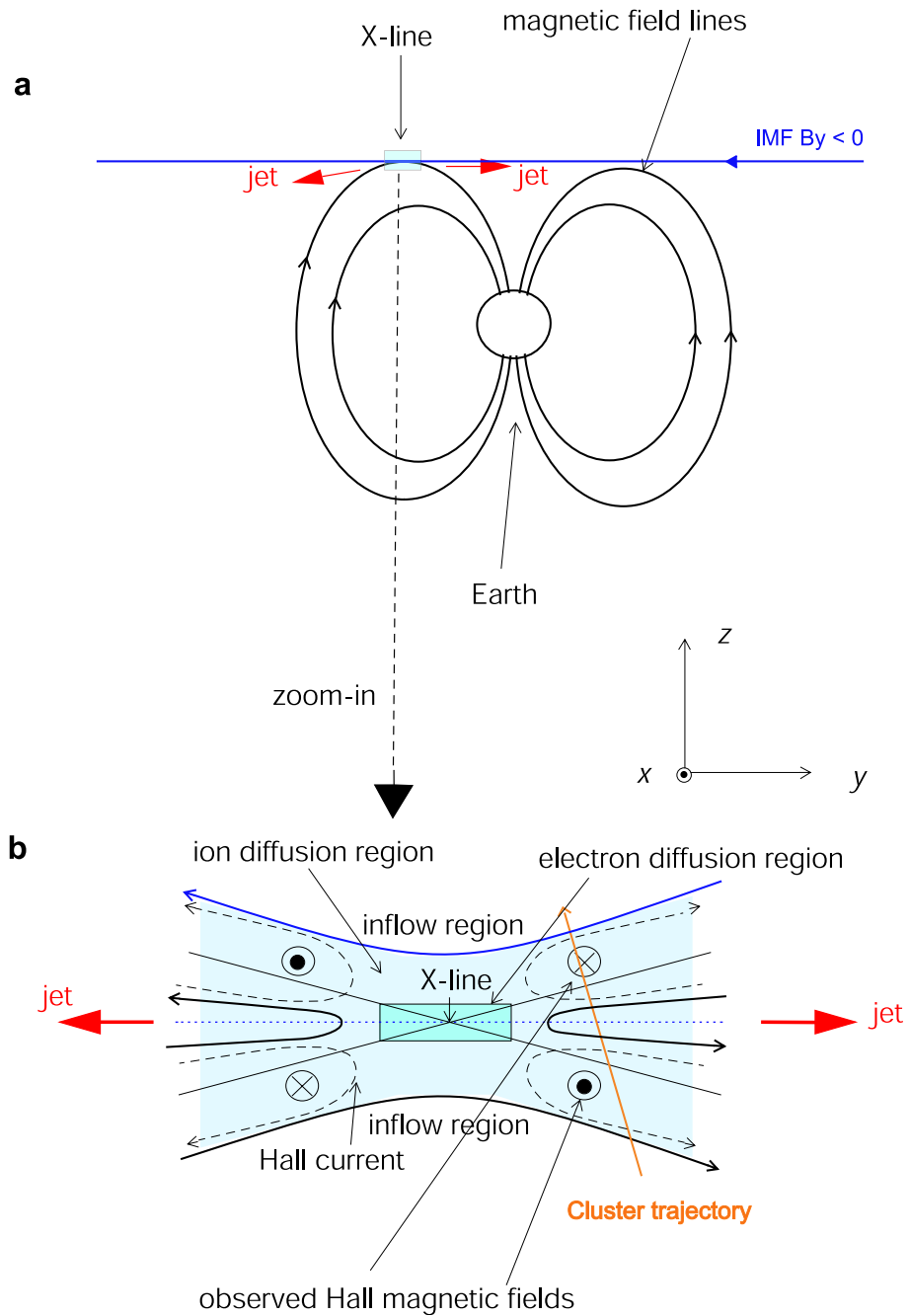


Figure 5-18: The geometry of the reconnection region. It is viewed from  $x$  direction. The small box marks the electron diffusion region. Outside of the electron diffusion region is the ion diffusion region. In this region ions are decoupled from the electrons and magnetic field, creating the Hall magnetic field in  $x$  direction and Hall currents shown as dashed lines. The orange arrow shows the Cluster trajectory. The red arrows indicate reconnection outflow jets.

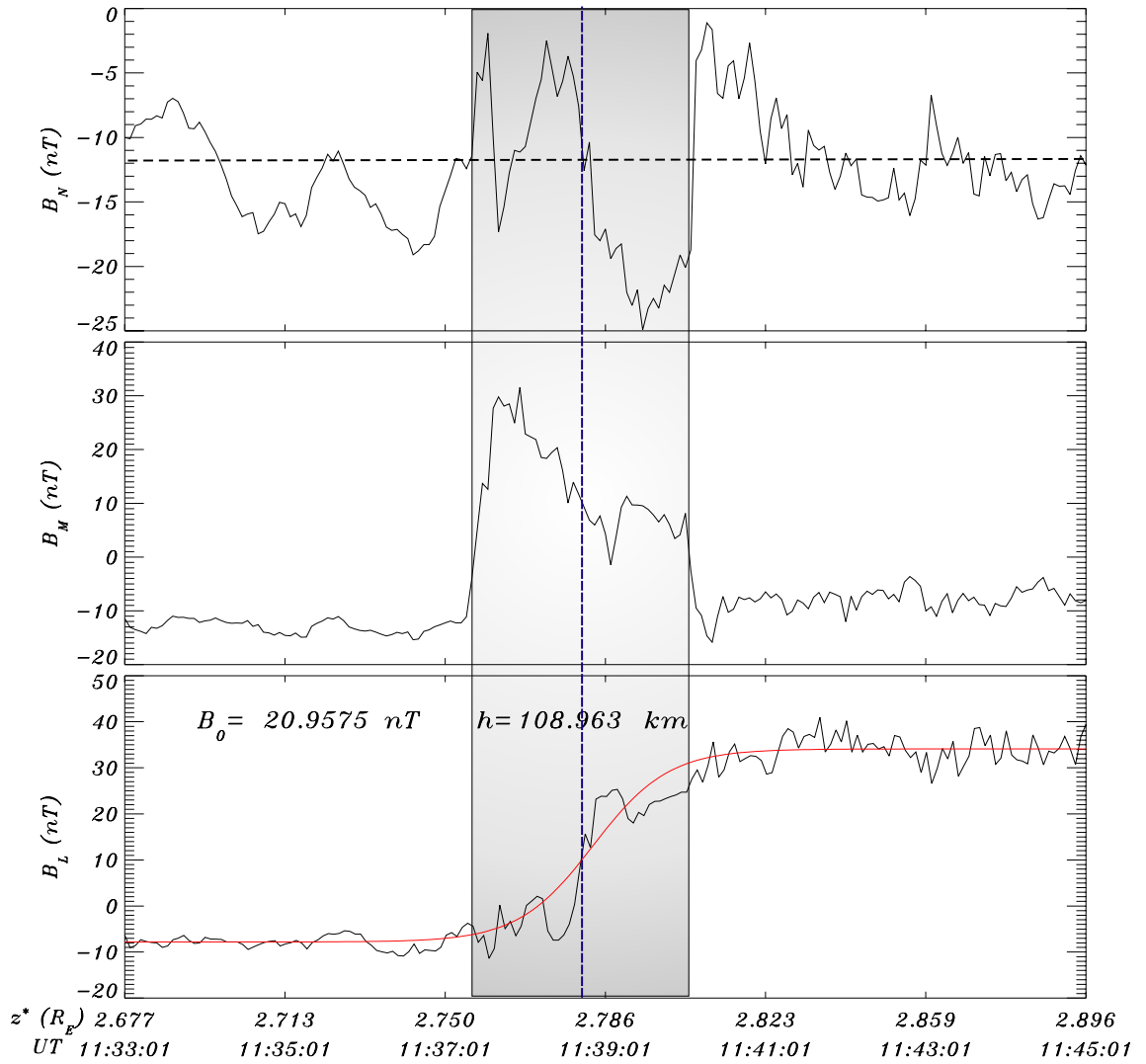


Figure 5-19: The magnetic field data projected in a local coordinate system where  $L$ ,  $M$  and  $N$  are the maximum, medium and minimum variance directions respectively. The red line in the last panel shows the nonlinear least-squares fit to Cluster C1 magnetopause crossing using a Harris sheet current model [Harris, 1962] on Mar. 23, 2002. The  $z^*$  at the bottom is the satellite  $N$  coordinate in the  $LMN$  coordinate system.

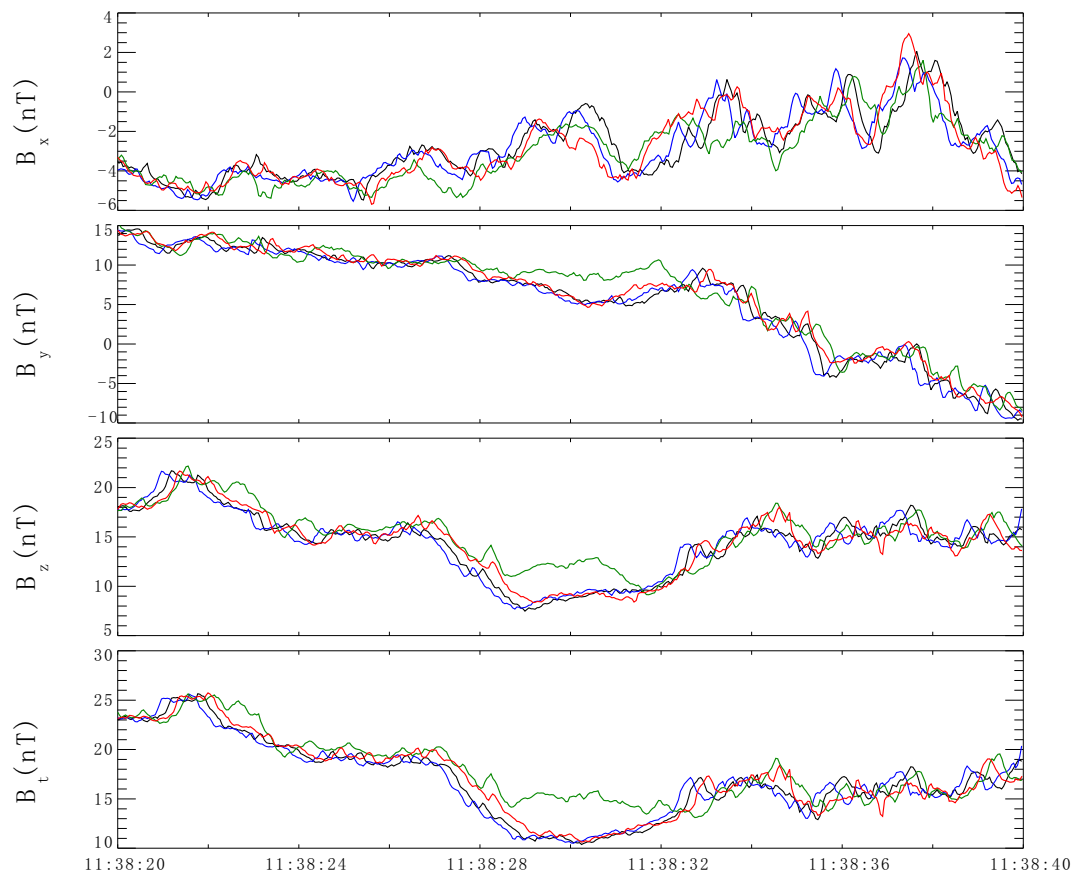


Figure 5-20: High resolution magnetic field data in GSE coordinate system from all 4 spacecraft.

Table 5.1: Events prefer  $B_y$  reconnection

Date mm/dd/yyyy	Time UT	Minimum	Medium	Maximum	$\Delta B_L$ (nT)	j (nA/m <sup>2</sup> )	thickness (km)	$\lambda_i$ (km)
03/23/2002	1133-1145	(0.88,0.29,-0.37)	(0.34,0.14,0.93)	(0.32,-0.95,0.02)	42	117	218	40.2
04/07/2001	1725-1745	(-0.96,-0.14,-0.24)	(-0.26,0.09,0.96)	(0.11,-0.99,0.12)	53	80	90	29.4
01/04/2003	1828-1840	(0.92,0.03,-0.39)	(0.32,0.51,0.80)	(0.23,-0.86,0.46)	25	N/A	40	65.6

green lines) are different from the other 3 spacecraft in the  $B_y$  and  $B_z$  components but not in the  $B_x$  component in a very short time period (4 sec). This difference could be the result of their different locations relative to the current sheet. The positions of the Cluster tetrahedron at 1130UT is shown in Figure 5.13. The distances among the 4 spacecraft are magnified 50 times. With the largest  $Y$ -coordinate, spacecraft C3 was furthest away from the X-line and observed stronger magnetic field than the other spacecraft.

$B_y$  reconnections are not rare in the cluster observations. Characteristics of 3  $B_y$  reconnection events are shown in Table 5.1. It is worth noting that these events are all during IMF  $B_y$  dominated time periods. The MVA results for these 3 events are very similar in the sense that the minimum, medium and maximum variance directions are mainly in GSE  $x/-x$ ,  $z$  and  $-y$  directions respectively. However the magnetic field variation and current sheet thickness are different.

## 5.7 Magnetopause Thickness

The simplest description of a current sheet structure is a one dimensional Harris sheet model [Harris, 1962]

$$B_x = B_0 \tanh\left(\frac{z - z_0}{h}\right) \quad (5.2)$$

For the March 23 event presented in section 5.6, Cluster crossed the high latitude magnetopause in a few minutes and during this short time interval the solar wind dynamic pressure is relatively stable. Therefore, a static Harris current sheet model should be employed to describe the observed current sheet. A nonlinear least-squares fit to the  $B_L$  component was shown as the red line in the last panel of Figure 5.19. The fitting parameters  $B_0$  and  $h$  are shown in the last panel of Figure 5.19. The thickness of the current

sheet is 218 km ( $2 \times h$ ). The  $z^*$  at the bottom is the satellite  $N$  coordinate in the  $LMN$  coordinate system.

The same method has been applied to estimate the thickness of the magnetopause for another two  $B_y$  reconnection events listed in Table 5.1. These events are all during IMF  $B_y$  dominated time periods. The magnetopause thicknesses are very different.

## 5.8 Discussion and Conclusions

We have seen from Figure 5-6 that during extreme storm time the cusp is more turbulent and the plasma density has no clear change across the boundary. This can be easily understood. During storm time, the whole magnetosphere is very active and the reconnected magnetic field lines convect from the subsolar point to the tail passing the cusp region. The magnetopause might be a rotational discontinuity during the storm time and in that case the density is constant across the rotational discontinuity. Therefore the density should not change across the magnetopause as is observed.

The fact that the plasma characteristics vary with solar wind density can be understood by the concept of pressure balance. When the solar wind density is very high (low), the plasma density is also very high (low) in the cusp region. To balance the magnetosheath pressure, the plasma temperature must be very low (high).

Previous Cluster analysis has identified both inner and outer boundaries surrounding the high-altitude cusp. The outer cusp/magnetosheath boundary appears to be a possible extension of the magnetopause boundary layer into the high-latitude and cusp region, whereas the inner boundaries define entry into the closed (equatorial) and open (polar) magnetospheric field regions. It is therefore of interest to understand the morphology of these boundaries, in particular relating to the external magnetosheath conditions. The recent study by *Lavraud et al.* [2004b] looked at the statistical extent of the cusp region by cusp characteristics, rather than direct identification of the boundary, and found no clear magnetosheath indentation. The current work has directly studied boundary orientation, both statistically and for individual crossing cases, and tested the expectation that the

outer boundary is typically indented on the magnetopause surface.

The crossing survey has selected only clear boundary crossings, which naturally biases the data set to lower IMF clock angles (northward orientation) since *Zhang et al.* [2006] showed that when IMF is northward, the boundary between the cusp and magnetosheath is clear. However a range of clock angles and a range of dipole tilt angles are nevertheless covered. The results in Figure 5-12 a) have shown, however, that the boundary between the magnetosheath and cusp shows a clear indentation on the dawn and dusk side of the cusp in the X-Y plane. For passes close to local noon, the normal vectors which point dawnward and duskward are mixed together as a result of displacements of the location of the cusp under different IMF and solar wind conditions. No attempt has yet been made, however, to separate the crossing set according to IMF and solar wind conditions to search for externally driven effects. Figure 5-10 also supports the indentation of the cusp. Because the spread of data points is wider in local time, the difference in the ordering of the normals between the Cusp and HLTR boundaries, is more dramatic in the X-Y plane.

Bipolar signatures which are possibly Hall perturbations have been observed by Cluster. If the Hall term dominates in the reconnection process, then the ion inertial length should be much larger than the resistive scale length. For Mar. 23, 2002 event, the ion inertial length is estimated as

$$\lambda_i = c/\omega_{pi} = 40.2km \quad (5.3)$$

the resistive scale length is

$$\lambda_{res} = \frac{\eta}{\mu_0|\mathbf{v}|} = \frac{1}{\mu_0\sigma|\mathbf{v}|} = 7.3km \quad (5.4)$$

where

$$D = \frac{1}{\mu_0\sigma} = 10^9 m^2/s \quad (5.5)$$

is adopted from *Sckopke et al.* [1981] and the Alfvén velocity is used for  $|\mathbf{v}|$ . The ion inertial

length is 6 times larger than the resistive scale length. The uncertainty of the value  $D$  is about an order of magnitude (personal communication with Prof. B. Sonnerup), so we conclude that the Hall term is important in the high latitude reconnection process.

We have studied the properties of the high latitude magnetopause (the one adjacent to the Cusp region, boundary 2 in Figure 5.1 and the one adjacent to the HLTR, boundary 4 in Figure 5.1) based on Cluster data. We found that the magnetopause adjacent to the HLTR is always associated with sharp change in plasma density ( $\sim 2$  orders of magnitude), velocity ( $\sim 100$  km/s), temperature ( $\sim$  one order of magnitude) and magnetic field. However the magnetopause adjacent to the cusp region is more complicated. When the IMF is northward, the magnetopause adjacent to the cusp region is associated with sharp change in plasma density, velocity, temperature and magnetic field. However, this interface will become uncertain when IMF turns southward.

We have done a superposed epoch analysis to study the average structure of the two different types of magnetopause crossings. We found that the plasma flow and density increase and the proton temperature decreases across the magnetopause from the magnetosphere into the magnetosheath with the amplitude of the flow change being about 100 km/s in both cases. The plasma density increases by a factor of 3 from the cusp region to the magnetosheath and it increases by two orders of magnitude from the HLTR to the magnetosheath. The parallel temperature decreases by a factor of 2 from the cusp region to the magnetosheath and it decreases by one order of magnitude from the HLTR to the magnetosheath. From the HLTR to the magnetosheath, the energetic electron flux drops immediately, and the energetic ion flux extends into the magnetosheath.

We have also studied the magnetopause adjacent to the cusp during extreme solar wind conditions based on four years of Cluster data. Our results can be summarized as follows:

During extreme storm times, the cusp is more turbulent than during quiet times and there is no clear plasma density change across the magnetopause. During low density solar wind conditions, the amplitude of the parallel temperature change across the magnetopause is larger than during high density solar wind conditions. And the amplitude of the plasma

density and velocity change is smaller than during high density solar wind conditions.

This study shows that solar wind conditions have strong influence on the cusp characteristics including density, plasma flow and ion temperature (not only location as shown in previous studies).

We have presented statistical results of the normal direction of the boundary between magnetosheath and cusp, and the boundary between magnetosheath and HLTR, based on the data set obtained by Cluster when these spacecraft were transiting the dayside cusp and magnetopause in 2001 and 2002. The geometry of all of the surrounding high latitude boundaries, deduced from a few selected crossings has also been presented. The boundary between the magnetosheath and the cusp seems to be indented in the X-Y plane, and is less clearly indented in the X-Z plane. Furthermore, the inner boundaries are consistent with a simple overall funnel-like geometry.

We also analyzed one event in detail to study the properties of the magnetic reconnection at the high latitude magnetopause. Clear high latitude magnetopause current sheets associated with  $B_y$  reconnection are observed. Energetic particles flux enhancements are associated with the high latitude magnetopause current sheet. The thickness of the current sheet for the Mar. 23, 2002 event is 218 km. In some cases, there is no clear high latitude magnetopause, however, the high latitude reconnection process can form a strong current sheet permitting a clear identification of the magnetopause. In the three events examined each showed bipolar signatures of the magnetic field which were consistent with the Hall effect in the reconnection process when the IMF  $B_y$  dominates.

## Chapter 6

# Comparison with MHD Simulations

### 6.1 Introduction to Global MHD Simulation

Global MHD simulation is the numerical simulation of the geospace environment with MHD equations as the governing equations. They are time dependent solutions of the MHD equations. Global MHD simulations have been widely used to study a variety of large scale problems associated with the dynamics of solar planetary interactions since 1978 [Brecht, 1985]. By obtaining global structure of the simulated system, the purpose of the global simulation is to aid in interpreting observations, testing theories, making prediction and so on.

In this Chapter, I will present the global MHD simulation results for a real event and compare the simulation with the Cluster observations which are presented in Chapter 4. The simulations provide a global context to help in interpreting Cluster measurements and the actual observations can test the capability of the MHD models to reproduce plasma parameters along the spacecraft orbit [Siscoe *et al.*, 2007].

Two global MHD models are used in this study, the Open Geospace General Circulation Model (Open GGCM) and the Block-Adaptive-Tree-Solarwind-Roe-Upwind-Scheme (BATSRUS) model. The Open GGCM was originally developed as a MHD model of the Earth's magnetosphere at UCLA in the early 90's by J. Raeder and was coupled with the Couple Thermosphere Ionosphere Model (CTIM) in the late 90's [Raeder *et al.*, 2001]. This model solves the MHD equations in a large volume surrounding the Earth including the bow shock, the magnetopause, and the magnetotail up to several hundred  $R_E$  from the Earth. It can be driven either by solar wind plasma and IMF observations or by idealized solar

wind and IMF conditions [Raeder *et al.*, 2001]. Open GGCM does not include the energetic particle drifts and ring current physics [<http://ccmc.gsfc.nasa.gov/models/openggcm.php>]. BATSRUS was designed as a very efficient, massively parallel MHD code for space physics applications by the Computational MHD Group at the University of Michigan [Powell *et al.*, 1999; Gombosi *et al.*, 2001]. It is based on a block adaptive Cartesian grid with block-based domain decomposition, and it employs the Message Passing Interface (MPI) standard for parallel execution. Both Open GGCM and BATSRUS have been successfully used for the global MHD simulation [e. g., Groth *et al.*, 2000; Gombosi *et al.*, 2004; Siscoe *et al.*, 2007].

## 6.2 Comparison of Observation and MHD Simulation for a Multiple Cusp Event

Both Open GGCM and BATSRUS have been used to simulate a multiple cusp event observed by Cluster on Mar 21 and Mar 22, 2001 which is presented in Chapter 4 (see Figure 4-8). The versions of the models used are those at Community Coordinated Modeling Center (CCMC) website [<http://ccmc.gsfc.nasa.gov/>].

### 6.2.1 General Properties

Figure 6-1 shows the model-derived parameters (magnetic field, plasma flow  $V_x$  component, pressure, density and temperature) along the Cluster trajectory together with the Cluster measurements. The ion pressure measured by Cluster has been multiplied by a factor of 1.1 to allow for electron pressure [Siscoe *et al.*, 2007]. The curves are time shifted (10 mins for Open GGCM and 12 min for BATSRUS) to achieve the best fit in the total magnetic field. This plot gives us a spatial-temporal comparison and a quantitative comparison between MHD models and Cluster observations. The magnetic field outputs (Figure 6-1, panel a-d) from both codes agree well with Cluster observations, however the plasma parameters (Figure 6-1, panel e-h) from both codes are very different from the Cluster observation. The magnetopause crossings in both codes (marked by a vertical red line) are about 2

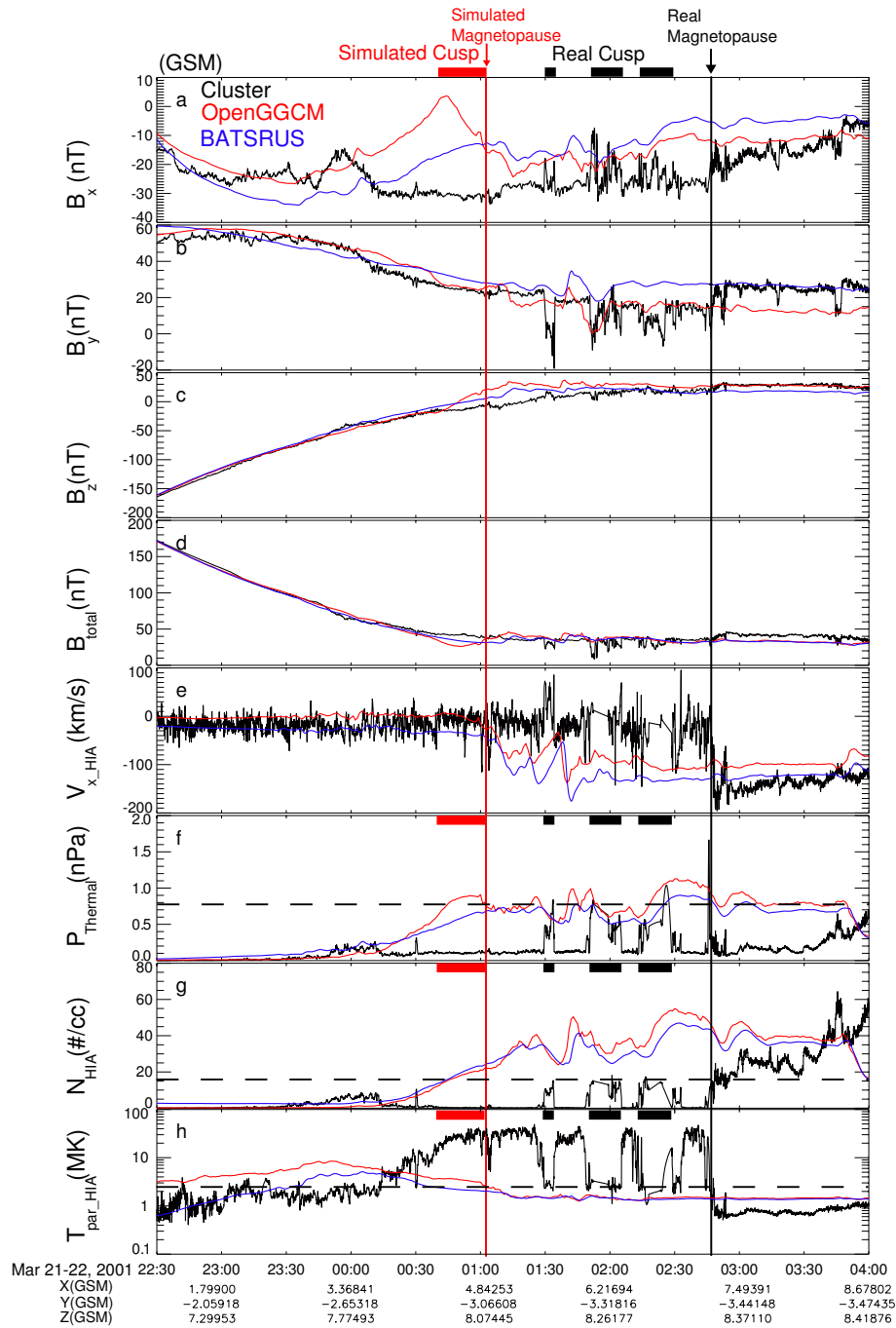


Figure 6-1: Comparison of Cluster C1 observation (black), outputs from the Open GGCM (red) and BATSURUS (blue) codes at CCMC (<http://ccmc.gsfc.nasa.gov/>), run numbers Hui\_Zhang\_050707\_1a and Hui\_Zhang\_051707\_2 respectively. (a-d) magnetic field (e) plasma flow  $V_x$  component (f) thermal pressure (the ion pressure measured by Cluster has been multiplied by a factor of 1.1 to allow for electron pressure) (g) density (h) temperature

hours earlier than the Cluster observation (marked by a vertical black line), indicating the simulated magnetosphere is smaller than the real one. The dayside magnetosphere did not show up in either codes calculation but is apparent in the Cluster observations as seen in the enhanced temperature (Figure 4-7, panel h) and the presence of energetic electrons (see Chapter 4, Figure 4-7, panel 8 and 11).

Although the size of the magnetosphere in the MHD simulation does not agree with Cluster observations well, all the amplitudes of model-derived parameters agree reasonably well with the Cluster observations. The thermal pressure (Figure 6-1, panel f) in the simulated cusp (marked by the red horizontal bars) and that observed by Cluster (marked by the black bars) are at the same level (0.8 nPa, use the horizontal dashed line as a guide line). The plasma flow  $V_x$  component, plasma density and temperature (Figure 6-1, panel e, g, h) from simulations also agree reasonably well with observations.

### 6.2.2 Responses of Cusp Position to the Solar Wind

In this section, I correlate the simulated cusp position with the solar wind azimuthal flow to see if it is consistent with the picture that the cusp shifts in an east-west direction due to the solar wind azimuthal flow.

The pressure contours are used to identify the center of the cusp. Figure 6-2 shows contours in  $xy$  plane of the thermal pressure calculated by BATSRUS code at the time Cluster crossed the magnetopause at 0248UT. The  $Z=7 R_E$  plane was selected for BATSRUS code because the magnetopause location is closest to the Cluster observation (GSM (7.3, -3.4, 8.3)  $R_E$ ) in this plane. Color scale shows the plasma density. The cusp is clearly outlined in the pressure contours. The position marked by "+" which indicates the maximum pressure is regarded as the center of the cusp. This method has been used by *Siscoe et al.* [2005].

Figure 6-3 shows the response of the cusp position to the solar wind azimuthal flow. The first panel shows the Y coordinate of the cusp position which is determined by the maximum thermal pressure for the time interval from 0100 to 0300, Mar. 22, 2001 (the Y

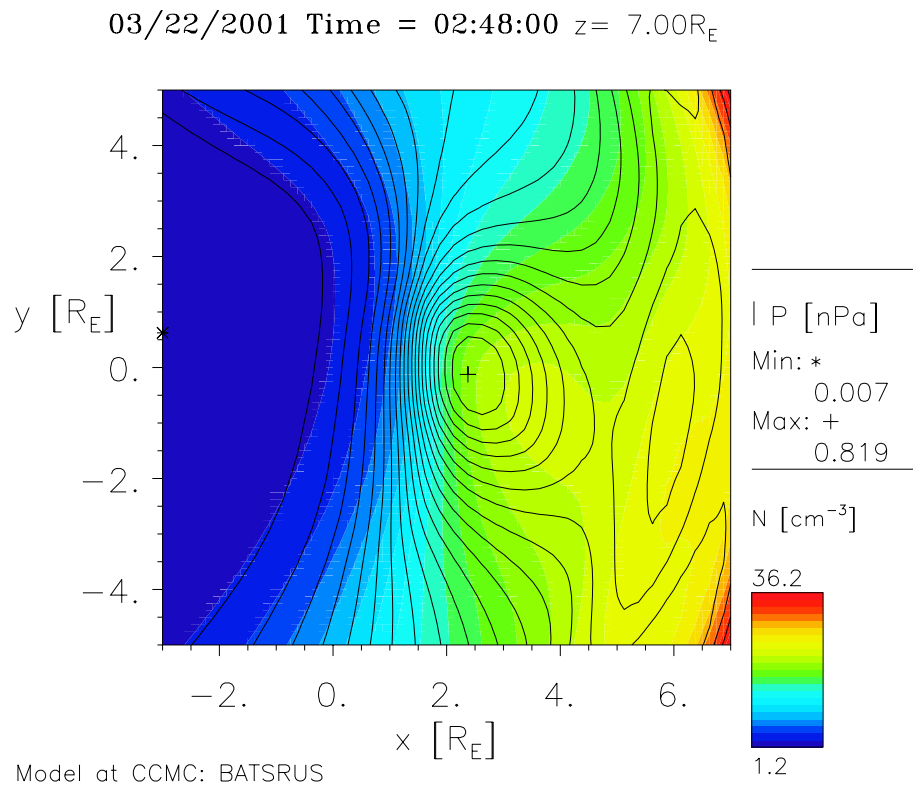


Figure 6.2: Contours in  $xy$  plane of the thermal pressure at the time Cluster crossed the magnetopause at 0248UT. This image is from BATSRUS code at CCMC (<http://ccmc.gsfc.nasa.gov/>), run number Hui\_Zhang\_051707.2.

## BATSRUS

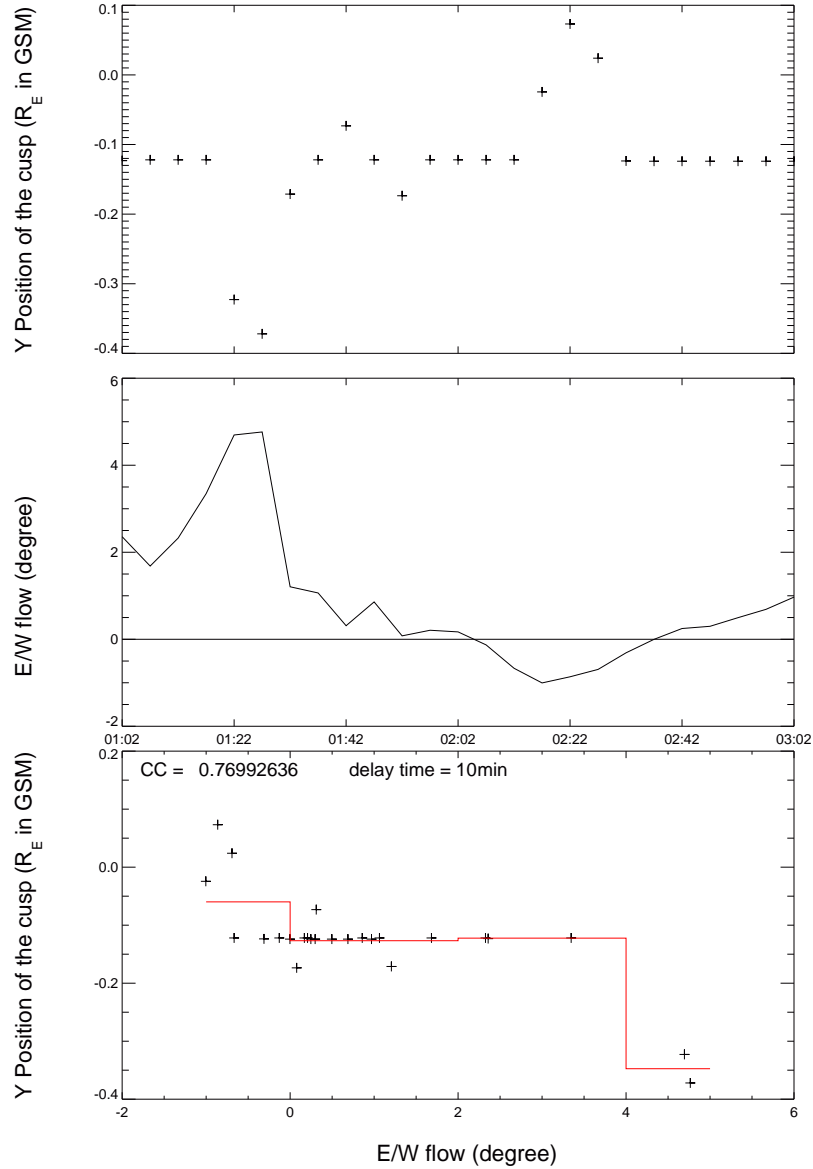


Figure 6-3: Response of the simulated cusp position to the solar wind azimuthal flow. The first panel shows the Y coordinates (averaged every 5 min) of the cusp position determined by the maximum thermal pressure. The second panel shows the solar wind E-W flow direction ( $angle = atan(-V_y/V_x)$ ) which is the Wind data used as the input for the simulation (projected to  $24 R_E$ ). The last panel shows the cusp position versus the solar wind azimuthal flow. The maximum correlation coefficient 0.77 is obtained when the Wind data are delayed 10 min as shown in this plot. The horizontal red bars indicate the average value of the cusp position. The result is from BATSRUS code at CCMC (<http://ccmc.gsfc.nasa.gov/>), run number Hui\_Zhang\_051707\_2.

coordinates are averaged every 5 min). The second panel shows the solar wind E-W flow direction ( $angle = atan(-V_y/V_x)$ , so positive angle means  $V_y$  is positive) determined using the Wind data which was used as the input for the simulation (projected to  $24 R_E$ ). There is a clear  $5^\circ$  deviation at around 01:22UT. The uncertainty of the solar wind flow angle is  $\sim 0.6^\circ$  derived from the uncertainties of the solar wind flow  $V_x$  and  $V_y$  (8 km/s and 3 km/s respectively) at 0122UT (<http://cdaweb.gsfc.nasa.gov/cdaweb/>). This uncertainty indicates the  $5^\circ$  deviation is significant statistically. The last panel shows the cusp position versus the solar wind azimuthal flow. The correlation coefficients are different when the shift time of the Wind data are different and the maximum correlation coefficient of 0.77 is obtained when the Wind data are delayed 10 min as shown in this plot. It is consistent with the picture that cusp position shifts in east-west direction due to the solar wind azimuthal flow (wind sock effect [Lundin *et al.*, 2001]). Since it takes the solar wind around 8 min to arrive at the center of the cusp ( $X=2 R_E$ , as seen in Figure 6.2) from  $24 R_E$ , the 10 min delay would indicate that it takes 2 min for the cusp to respond to the solar wind azimuthal flow.

### 6.2.3 Formation of the Cold Dense Plasma Sheet

When the Cluster spacecraft observed the multiple cusps, the Geotail spacecraft observed cold and dense plasma population in the dusk flank of the tail plasma sheet (Figure 6.4) which may be related to earlier high latitude reconnection [Zong *et al.*, 2007]. Global MHD simulation can help to demonstrate the formation of the cold dense plasma sheet.

Figure 6.5 shows  $z=3.10 R_E$  cut of the magnetosphere simulated by BATSRUS. Figure 6.5a is a snapshot at 00UT, Mar 22, 2001 and Figure 6.5b is a snapshot 3 hours later. The cold dense plasma population can be clearly seen on both dawn and dusk flanks. This figure shows that a CDPS is forming, presumably by two-point, sequential reconnection under northward IMF conditions. By comparing these two images, we can conclude that BATSRUS qualitatively simulated the formation of the cold dense plasma sheet on the flanks.

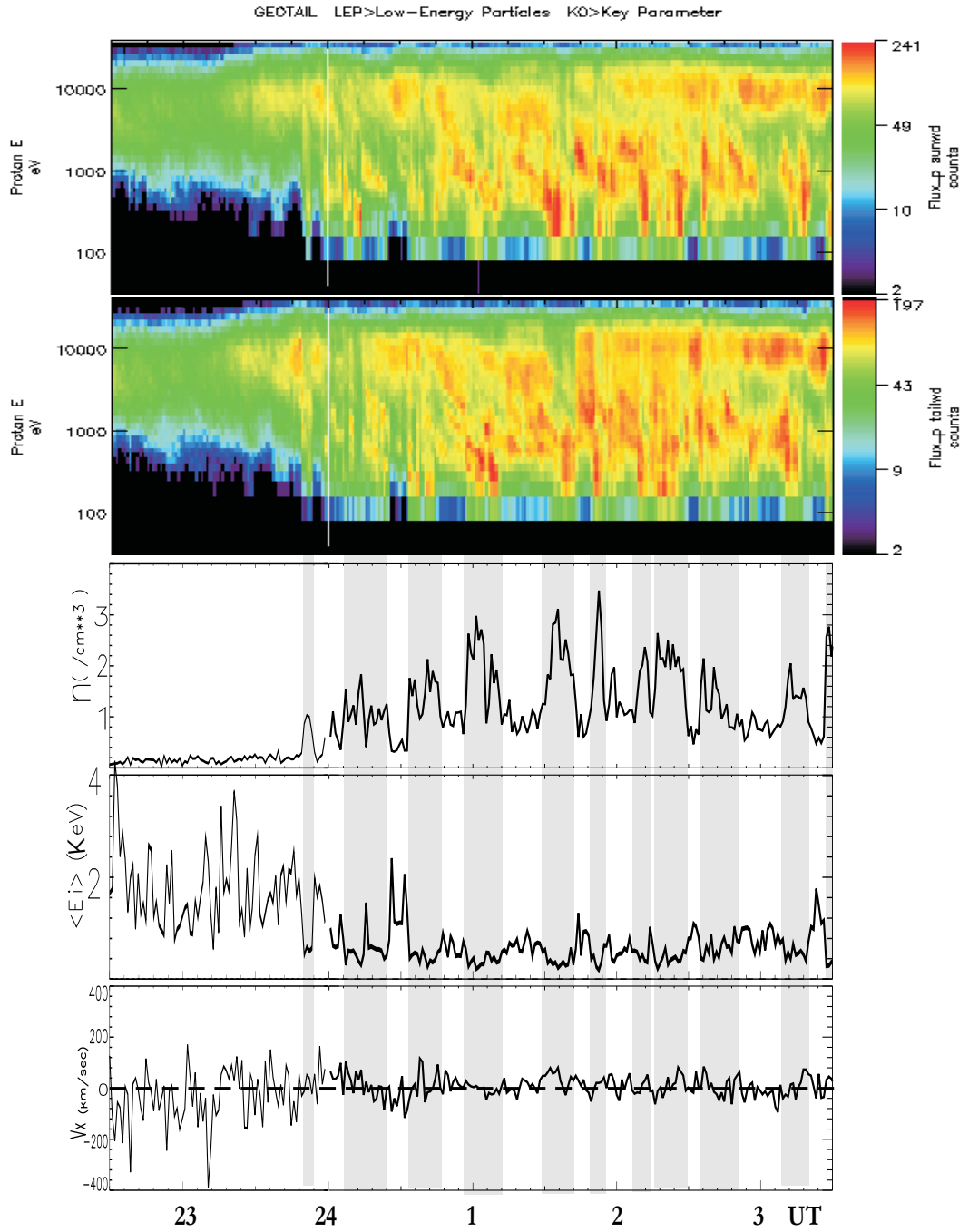


Figure 6-4: Geotail observations of the cold dense plasma population at the duskside tail-flank. The top 2 panels show spectra of sunward and tailward flowing protons respectively. The bottom 3 panels show the ion density, average energy (temperature, in keV) and the ion bulk velocity  $V_x$  in km/s. Bursty-like cold-dense plasma regions are shaded. (from [Zong *et al.*, 2007])

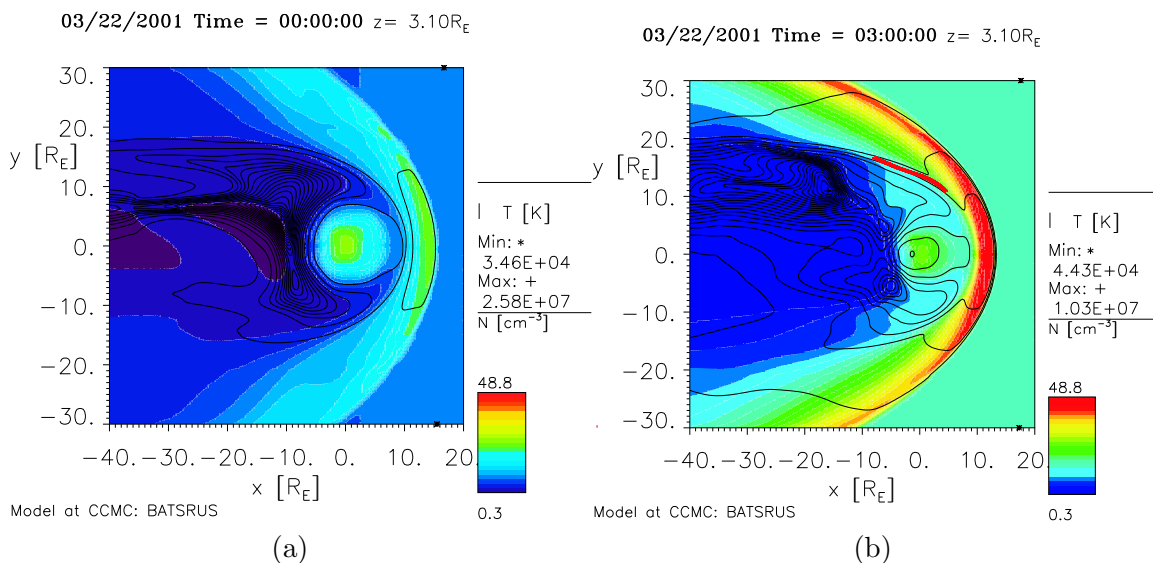


Figure 6-5: BATRUS simulation of the formation of the cold dense plasma sheet. Both plots show a  $z=3.10 R_E$  cut of the magnetosphere. The color scale is for the density and the contours are for the temperature. (a) A snapshot at 00UT, Mar 22, 2001. No cold dense plasma sheet has formed. (b) A snapshot at 03UT, Mar 22, 2001. Cold dense plasma sheet has formed at both dawn and dusk flanks. The red solid line is the projection of the Geotail orbit from 16UT, Mar 21 to 04 UT, Mar 22, 2001.

Figure 6-6 shows the plasma density, temperature and flow  $V_x$  component along the straight line which connecting two points  $(-7, -30, 2)$  GSM  $R_E$  and  $(-7, 30, 2)$  GSM  $R_E$ . The shaded regions are the magnetosheath which can be identified by the strong anti-sunward flow ( $\sim 250$  km/s). The hot tenuous central plasma sheet is surrounded by the cold dense plasma populations on both dawn and dusk flanks. The density at the flank is as high as  $10 \text{ cm}^{-3}$  which is comparable to the Geotail observation of  $3 \text{ cm}^{-3}$  (the blue dot) and the temperature is as low as  $2 \times 10^6$  K which is also comparable to  $4 \times 10^6$  K (the red dot) as measured by Geotail when it observed the cold dense plasma sheet on the dusk flank.

### 6.3 Discussion and Conclusions

The MHD outputs are very different from the Cluster observation because the volume of the magnetosphere from both codes are smaller than the observation. Figure 6-7 shows the profile of the magnetosphere in  $xz$ -plane plane as seen in contours of plasma pressure at

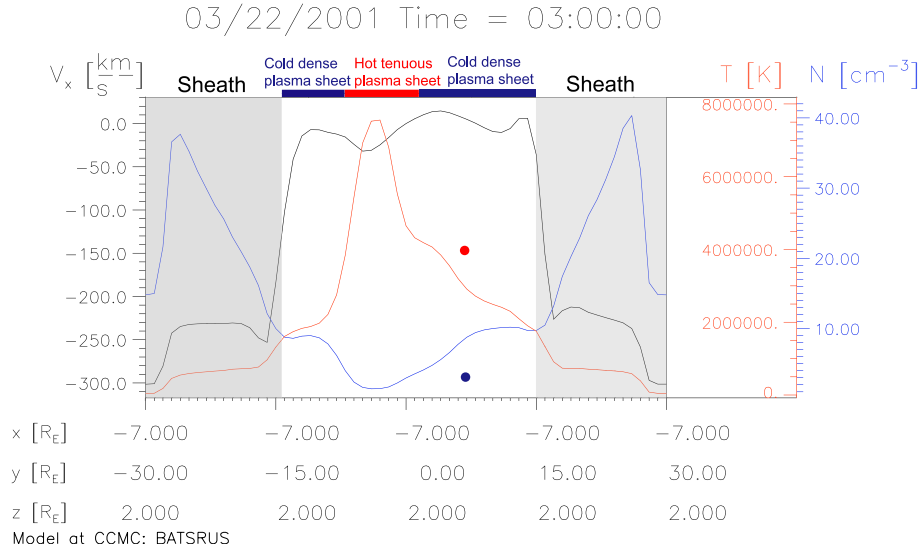


Figure 6-6: The plasma density, temperature and flow  $V_x$  component derived by BATSRUS along the straight line which connecting two points  $(-7, -30, 2) \text{ GSM } R_E$  and  $(-7, 30, 2) \text{ GSM } R_E$ . The shaded regions are the magnetosheath. The hot tenuous plasma sheet and cold dense plasma sheet are marked by red and blue horizontal bars on the top the plot respectively. The red (blue) dot marks the density (temperature) measured by the Geotail spacecraft when it observed the cold dense plasma sheet on the dusk flank.

0248UT when Cluster crossed the magnetopause at  $(7.3, 1.0, 8.9) \text{ GSE } R_E$  ( $(7.3, -3.4, 8.3) R_E$  in GSM). Panel a shows  $Y=1 R_E$  plane from Open GGCM code and panel b shows  $Y=-3.4 R_E$  (GSM) plane from BATSRUS code. These two planes are selected because Cluster was located in these two planes at 0248UT. The two planes are just from different coordinate systems used in Open GGCM and BATSRUS codes, i.e., GSE and GSM coordinate system respectively. The red lines shows the Cluster trajectory from 21UT, Mar. 21 to 03UT, Mar. 22, 2001. From this figure it is clearly seen that Cluster exits the cusp region into the magnetosheath directly in the MHD simulation which is different from the observation in which Cluster entered the dayside magnetosphere after passing the cusp region as shown in Chapter 4. Also, the magnetopause observed by Cluster (marked as blue tick marks on the Cluster trajectory) is several  $R_E$  outside of the simulated magnetopause which is identified by the sharp change in the plasma thermal pressure contours. The cusp in the BATSRUS plot is not very clear because the cusp in BATSRUS is not wide enough to extend to  $Y$

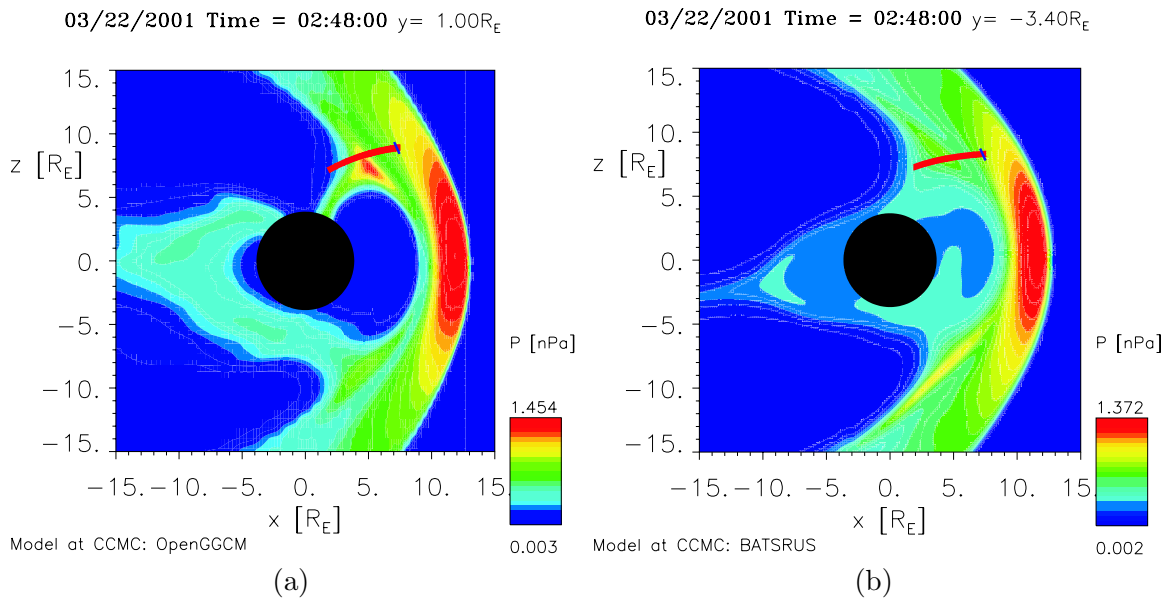


Figure 6-7: The profile of the magnetosphere in  $xz$ -plane as seen in contours of plasma pressure at 0248UT when Cluster crossed the magnetopause at (7.3, 1.0, 8.9) GSE ((7.3, -3.4, 8.3)  $R_E$  in GSM). The color bar gives pressure in the units of nPa. The red line shows the Cluster trajectory from 21UT, Mar. 21 to 03UT, Mar. 22, 2001. The Cluster spacecraft is moving sunward. The blue tick mark on the trajectory marks the position when Cluster crossed the magnetopause. (a) Plot from Open GGCM in GSE coordinate system. (b) Plot from BATSRUS in GSM coordinate system. The images are from the CCMC (<http://ccmc.gsfc.nasa.gov/>), run numbers Hui\_Zhang\_050707\_1a and Hui\_Zhang\_051707\_2 respectively.

$=-3.4 R_E$ .

This event is during the recover phase of a storm (minimum Dst is -149 nT) and the Dst index is -44 nT for the cusp crossing. Regarding the 2-hour offset in the location of the boundary between Cluster and the codes (the real magnetosphere is bigger), this could be owing to inflation from the residual ring current, which the codes do not include.

In this chapter, we compared the Cluster and Geotail observations with the MHD simulations. We find that although the simulated magnetospheres are smaller than the real magnetosphere due to the absence of the ring current model, the simulated magnetic fields and the amplitude of the model-derived plasma parameters (velocity, density, temperature and thermal pressure) in the cusp region agree reasonably well with Cluster observations. The MHD code qualitatively simulated the responses of the cusp positions to the solar wind azimuthal flow (the wind sock effect). The MHD code qualitatively simulated the formation of the cold sense plasma sheet on the flanks which is consistent with the Geotail observations.

## Chapter 7

# Conclusions and Future Work

### 7.1 Conclusions

The Cluster spacecraft with its high-altitude polar orbit and its ensemble of scientific instruments provides a good opportunity to investigate the structure and dynamics of the high latitude magnetospheric boundaries including the high latitude magnetopause and cusp region. Moreover, global MHD simulations can provide a global context to help in interpreting observations. In this dissertation, the magnetospheric cusp region and high latitude magnetopause are investigated via extensive Cluster data analysis and comparison with global MHD simulations. The following long standing questions have been addressed in Chapter 4, 5 and 6 of this dissertation. What is the magnetic structure of high latitude boundaries during southward and northward interplanetary magnetic field (IMF) conditions? Do the boundaries lose their distinct well-defined and sharp edge during southward IMF conditions? How do they respond to outside (solar wind) and inside (magnetic storm and substorm) conditions? What is the behavior of energetic particles in these regions?

We focus on the magnetospheric cusp region in Chapter 4. As presented in the first half of Chapter 4, we surveyed 2 years (2001 and 2002) of Cluster data when its apogee was at the dayside (totaling 6 months,  $\sim 150$  cusp crossings) and distinguished a well-defined region of high density (comparable to that in the magnetosheath) and small or stagnant plasma flow. This region is what we have defined as the Stagnant Exterior Cusp (SEC). Based on 40 clearly identified SEC events, the property of the SEC has been investigated. We found that the SEC lies predominantly within 10-13 MLT, however there are some cases where this region extends to both earlier and later MLTs. We also found that 72.5%

of the SEC events have depressed magnetic field. The angular difference between the IMF and local clock angles is a good criterion to identify the cusp region in 72.5% of the 40 SEC events. Energetic ions are observed in the high latitude magnetospheric region for most of the SEC crossings (32 events of 40 opportunities, 80%). Energetic electrons are observed sometimes (9 events of 40 opportunities 22.5%). It is interesting to find that the particle spectra are characterized by a power law and the power law index is found to be closely related to solar wind velocity. The spectra seems to be harder (flatter) for higher solar wind velocity. There is no clear relationship between the power law index and IMF  $B_z$ , solar wind Mach number, Dst, magnetic turbulence or shear angle. The larger the magnetic shear angle, the more turbulent is the magnetic field in the SEC. This result strongly suggests that the high latitude reconnection process is the major source of the magnetic turbulence in the SEC region.

To understand the dynamics of the cusp region, in the second half of Chapter 4, we analyzed one multiple cusp event under variable IMF conditions. From 0000UT to 0400UT on March 2, 2002 the Cluster spacecraft were on its outbound journey in the northern hemisphere. A normal cusp region was observed from from 00:06UT to 01:20UT, March 2, 2002. Two other cusp regions have been observed by all four spacecraft from 01:33UT to 01:45UT and from 02:05UT to 02:18UT. All three cusp-like encounters were characterized by shocked solar wind plasma and quasi-stagnant plasma flow. The order of boundary crossings and timing analysis results for the four satellites for five clear boundaries between the cusp region and the high latitude trapping region demonstrates temporal variation – the boundary between the dayside magnetosphere/trapping region and the cusp region was shifting alternately in a northward-antisunward or southward-sunward direction. So the Cluster spacecraft were observing the same cusp and it appeared as 3 cusp-like regions due to the boundary oscillations. The normal velocities  $v_n$  of the boundary motion varied from 13.4 km/s to 66.9 km/s. In a survey of 2 years of Cluster data, one more multiple ( $\geq 3$ ) cusp event of which each cusp lasts longer than 10 minutes was found. The Feb. 25, 2002 event was also under variable IMF condition. Multiple cusp events are observed under very

different IMF conditions which is hard to be explained by the double reconnection model at different latitudes proposed by *Wing et al.* [2001]. The double reconnection model can only reproduce double cusps. Analysis (Feb. 25, 2002 event analysis is not shown) indicates that all of four multiple encounters were a temporal effect similar to the March 2, 2002 event.

In Chapter 5, we focus on the high latitude magnetopause (the one adjacent to the cusp region, boundary 2 in Figure 5-1 and the one adjacent to the HLTR, boundary 4 in Figure 5-1). To study the high latitude magnetopause, we need first to identify it. After surveying the first two years of Cluster data, we found that the magnetopause adjacent to the HLTR is always associated with sharp changes in plasma density ( $\sim 2$  orders of magnitude), velocity ( $\sim 100$  km/s), temperature ( $\sim$  one order of magnitude) and magnetic field. However the magnetopause adjacent to the cusp region is more complicated. When the IMF is northward, the magnetopause adjacent to the cusp region is associated with sharp changes in plasma density, velocity, temperature and magnetic field. However, this interface becomes uncertain when the IMF turns southward.

After the identification of the high latitude magnetopause crossing, as presented in section 5.3, we have done a superposed epoch analysis to study the average structure of the two different types of magnetopause crossings. We found that the plasma flow and density increase and the proton temperature decreases across the magnetopause from the magnetosphere into the magnetosheath with the amplitude of the flow change being about 100 km/s in both cases. The plasma density increases by a factor of 3 from the cusp region to the magnetosheath and it increases by two orders of magnitude from the HLTR to the magnetosheath. The parallel temperature decreases by a factor of 2 from the cusp region to the magnetosheath and it decreases by one order of magnitude from the HLTR to the magnetosheath. From the HLTR to the magnetosheath, the energetic electron flux drops immediately, and the energetic ion flux extends into the magnetosheath.

To understand how the solar wind condition and the geomagnetic activity affect the magnetopause, we have studied the magnetopause adjacent to the cusp during extreme

solar wind conditions based on four years of Cluster data (section 5.4). We found that during extreme storm times, the cusp is more turbulent than during quiet times and there is no clear plasma density change across the magnetopause. During low density solar wind conditions, the amplitude of the parallel temperature change across the magnetopause is larger than during high density solar wind conditions. In addition, the amplitude of the plasma density and velocity change is smaller than during high density solar wind conditions. This study shows that solar wind conditions have strong influence on the cusp characteristics including density, plasma flow and ion temperature (not only location as shown in previous studies).

The geometry of the high latitude boundaries are investigated and presented in section 5.5 of this dissertation. We have presented statistical results of the normal direction (obtained by MVA method and four spacecraft timing method) of the boundary between magnetosheath and cusp, and the boundary between magnetosheath and HLTR, based on the data set obtained by Cluster when these spacecraft were transiting the dayside cusp and magnetopause in 2001 and 2002. The geometry of all of the surrounding high latitude boundaries, deduced from a few selected crossings has also been presented. The boundary between the magnetosheath and the cusp seems to be indented in the X-Y plane, and is less clearly indented in the X-Z plane. Furthermore, the inner boundaries are consistent with a simple overall funnel-like geometry.

The magnetic reconnection process is one of the most important mechanism for the energy transfer via the magnetopause. In section 5.6, we reported the first in-situ observation of collisionless Hall reconnection at the high latitude magnetopause when the IMF  $B_y$  dominates. Clear high latitude magnetopause current sheets associated with  $B_y$  reconnection are observed by the Cluster spacecraft. Energetic particles flux enhancements are associated with the high latitude magnetopause current sheet. In some cases, there is no clear high latitude magnetopause, however, the high latitude reconnection process can form a strong current sheet allowing the magnetopause to become clearly defined. In the three events examined each showed bipolar signatures of the magnetic field which were

consistent with the Hall effect in the reconnection process.

The thickness of the magnetopause current sheet varies from case to case. The magnetic reconnection process may happen when the current sheet is thin enough so the frozen in condition is broken. In section 5.7, we estimated the thickness of the high latitude magnetopause by a Harris sheet model for the March 23, 2002 reconnection event. The thickness of the current sheet for this event is 218 km which is about 5 ion inertial lengths,  $\lambda_i$ .

As mentioned before, the global MHD simulation can provide a global context to help in interpreting observations and observations can test the capability of the MHD codes in reproducing the plasma parameters along the spacecraft trajectory. In chapter 6, we compared the Cluster and Geotail observations with the MHD simulations for a real multiple cusp event. We find that although the simulated magnetospheres are smaller than the real magnetosphere due to the absence of the ring current model, the simulated magnetic fields and the amplitude of the model-derived plasma parameters (velocity, density, temperature and thermal pressure) in the cusp region agree well with Cluster observations. The MHD code successfully simulated the responses of the cusp positions to the solar wind azimuthal flow (the wind sock effect). The MHD code successfully simulated the formation of the cold dense plasma sheet on the flanks which is consistent with the Geotail observations.

In summary, the high latitude magnetopause and cusp region are strongly affected by the upstream solar wind and IMF conditions. When the IMF is northward, the magnetopause adjacent to the cusp region is associated with sharp changes in plasma density, velocity, temperature and magnetic field. However, this interface becomes uncertain when the IMF turns southward. The magnetopause adjacent to the cusp region show clear indentation in X-Y plane. The magnetic turbulence in the cusp region is stronger during northward IMF time period than during southward IMF period which implies the high latitude reconnection is the major source of the turbulence in the cusp region. Energetic protons (30 to 4000 keV) are found to be present 80% of the cusp crossings. The spectrum of energetic particles in the cusp region is harder for faster solar wind.

## 7.2 Future Work

As presented in Chapter 4, the energetic proton spectra in the cusp region were found to be closely related to solar wind velocity. It would be of interest to check if it is the same case for the electron, helium ion and heavy ion spectra. It would also be interesting to investigate the particle spectra in the HLTR and compare them with those in the cusp region which may provide information on whether they are from the same source.

In Chapter 5, we showed that the magnetopause between the magnetosheath and the cusp seems to be indented in the X-Y plane. Theoretical work needs to be done to interpret the indentation.

All of the three reconnection events we presented in Chapter 5 are associated with the enhancement of the energetic particle flux in the current sheet which could be accelerated locally by reconnection or come from somewhere else and become trapped in the current sheet. If these particles are accelerated by the reconnection process, the next important question would be how are they getting accelerated? How long can these energetic particles stay there? Further study on this might be helpful for us to understand the behavior of energetic particles in the current sheet. For the March 23, 2002 event, there is a strong  $B_z$  component (or  $B_M$  component in  $LMN$  coordinates) in the reconnection region which is significantly larger than outside of the reconnection region. Where does this strong field come from? Is it the result of reconnection? It would be interesting to further investigate the macro and micro structure of reconnection region. In the discussion section of Chapter 5, we calculated the characteristic scale length of the Hall term and the resistive term. In the calculation of the resistive scale length, we adopted diffusion coefficient from *Scopke et al.* [1981], although *Scopke et al.* [1981] obtained this diffusion coefficient value based on the measurements of a single magnetopause crossing, it would be more reliable if this value could be obtained based on the in-situ measurement of our own event. It would be interesting to calculate the scale length for the remaining terms. If both anti-parallel reconnection and component reconnection processes can occur, which process will take

place under what conditions? What is the relation between anti-parallel and component reconnection? Can both take place and be observed in the high latitude magnetopause/cusp region? More theoretical and observational work needs to be done to answer these questions about reconnection.

In Chapter 6, we showed that the BATSRUS MHD code successfully simulated the formation of the cold dense plasma sheet on the flanks and this was consistent with the Geotail observations. We traced the cold dense plasma population back with simulation time and found that this cold dense plasma population appeared first at dayside and then extended to the nightside from the flank. These simulation results show that the CDPS is forming, presumably by two-point, sequential reconnection under northward IMF conditions. The Dual-Lobe Reconnection Model seems to be a promising description of CDPS formation. However, more evidence is needed in order to determine positively the high latitude origin of CDPS plasma and to better determine the relevant transport processes.

## List of Journal Abbreviations

Adv. Space Res.	.....	Advances In Space Research
Ann. Geophys.	.....	Annales Geophysicae
Astrophys. J.	.....	Astrophysical Journal
Geophys. Monogr. Ser.	.....	Geophysical Monograph Series
Geophys. Res. Lett.	.....	Geophysical Research Letters
J. Atmos. Terr. Phys.	.....	Journal of Atmospheric and Terrestrial Physics
J. Geophys. Res.	.....	Journal of Geophysical Research
Phil. Trans. Roy. Soc.	.....	Philosophical Transactions of the Royal Society
Phys. Rev.	.....	Physical Review
Phys. Scr.	.....	Physica Scripta
Planet. Space Sci.	.....	Planetary and Space Science
Rev. Geophys.	.....	Reviews of Geophysics
Rep. Prog. Phys.	.....	Reports on Progress in Physics
Sol. Phys.	.....	Solar Physics
Space Sci. Rev.	.....	Space Science Reviews
Terr. Magn. Atmos. Elect.	.....	Terrestrial Magnetism Atmospheric Electricity

## References

- Anderson, B. J., and S. A. Fuselier, Magnetic pulsations from 0.1 to 4.0 Hz and associated plasma properties in the earth's subsolar magnetosheath and plasma depletion layer, *J. Geophys. Res.*, *98*, 1461–1479, 1993.
- Anderson, K. A., H. K. Harris, and R. J. Paoli, Energetic Electron Fluxes in and beyond the Earth's Outer Magnetosphere, *J. Geophys. Res.*, *70*, 1039–+, 1965.
- Aparcio, B., B. Thelin, and R. Lundin, The polar cusp from a particle point of view: A statistical study based on the viking data, *J. Geophys. Res.*, *96*, 14,023–14,031, 1991.
- Balogh, A., et al., The cluster magnetic field investigation, *Space Sci. Rev.*, *79*, 65–91, 1997.
- Beard, D. B., Interaction of the Solar Plasma with the Earth's Magnetic Field, *Physical Review Letters*, *5*, 89–91, doi:10.1103/PhysRevLett.5.89, 1960.
- Beard, D. B., The solar wind, *Rep. Prog. Phys.*, *30*, 409–444, doi:10.1088/0034-4885/30/2/302, 1967.
- Biermann, L., untitled letter, *Observatory*, *77*, 109, 1957.
- Biskamp, D., Magnetic reconnection via current sheets, *Physics of Fluids*, *29*, 1520–1531, 1986.
- Biskamp, D., and H. Welter, Coalescence of magnetic islands, *Physical Review Letters*, *44*, 1069–1072, 1980.
- Boardsen, S. A., T. E. Eastman, T. Sotirelis, and J. L. Green, An empirical model of the high-latitude magnetopause, *J. Geophys. Res.*, *105*, 23,193–23,219, 2000.
- Bogdanova, Y. V., et al., On the formation of the high-altitude stagnant cusp: Cluster observations, *Geophys. Res. Lett.*, *32*, L12,101, doi:10.1029/2005GL022813, 2005.
- Boudouridis, A., H. E. Spence, and T. G. Onsager, Investigation of magnetopause reconnection models using two colocated, low-altitude satellites: A unifying reconnection geometry, *J. Geophys. Res.*, *106*, 29,431–29,466, 2001.
- Brecht, S. H., Global simulations using MHD codes: A few points to consider before you try one, *Space Sci. Rev.*, *42*, 169–185, 1985.
- Burch, J. L., Effects of interplanetary magnetic sector structure on auroral zone and polar cap magnetic activity., *J. Geophys. Res.*, *78*, 1047–1057, 1973.

- Cahill, L. J., Jr., and P. G. Amazeen, The boundary of the geomagnetic field, *J. Geophys. Res.*, *68*, 1835–1843, 1963.
- Cargill, P. J., M. W. Dunlop, B. Lavraud, R. C. Elphic, D. L. Holland, K. Nykyri, A. Balogh, I. Dandouras, and H. Reme, CLUSTER encounters with the high altitude cusp: Boundary structure and magnetic field depletions, *Ann. Geophys.*, *22*, 1739–1754, 2004.
- Chang, S. W., et al., Cusp energetic ions: A bow shock source, *Geophys. Res. Lett.*, *25*, 3729–3732, 1998.
- Chang, S. W., et al., Energetic magnetosheath ions connected to the earth's bow shock: Possible source of CEP's, *J. Geophys. Res.*, *105*, 5471–, 2000.
- Chapman, S., and J. Bartels, Theories of magnetic storms and aurorae, in *Geomagnetism*, Vol. II, pp. 850–861, Clarendon Press, Oxford, 1940.
- Chapman, S., and V. C. A. Ferraro, A new theory of magnetic storms, part 1, the initial phase, *Terr. Magn. Atmos. Elect.*, *36*, 77–97, 171–186, 1931.
- Chen, J., T. A. Fritz, R. B. Sheldon, H. E. Spence, W. N. Spjeldvik, J. F. Fennell, and S. Livi, A new, temporarily confined population in the polar cap during the August 27, 1996 geomagnetic field distortion period, *Geophys. Res. Lett.*, *24*, 1447–1450, 1997.
- Choe, J. Y., D. B. Beard, and E. C. Sullivan, Precise calculation of the magnetosphere surface for a tilted dipole, , *21*, 485–498, doi:10.1016/0032-0633(73)90045-7, 1973.
- Coroniti, F. V., and A. Eviatar, Magnetic field reconnection in a collisionless plasma, , *33*, 189–210, 1977.
- Cowley, S. W. H., Plasma populations in a simple open model magnetosphere, *Space Sci. Rev.*, *26*, 217–275, 1980.
- Cowley, S. W. H., Theoretical perspectives of the magnetopause: A tutorial review, in *Physics of the Magnetopause*, *Geophys. Monogr. Ser.*, vol. 90, edited by P. Song, B. U. Ö. Sonnerup, and M. F. Thomsen, pp. 29–43, AGU, Washington, D. C., 1995.
- Cowley, S. W. H., and Z. V. Lewis, Magnetic trapping of energetic particles on open dayside boundary layer flux tubes, *Planet. Space Sci.*, *38*, 1343–1350, 1990.
- Crooker, N. U., Dayside merging and cusp geometry, *J. Geophys. Res.*, *84*, 951–959, 1979.
- de Hoffman, F., and E. Teller, Magneto-hydrodynamic shocks, *Phys. Rev.*, *80*, 692, 1950.
- Delcourt, D. C., and J.-A. Sauvaud, Recirculation of plasma sheet particles into the high-latitude boundary layer, *J. Geophys. Res.*, *103*, 26,521, 1998.
- Delcourt, D. C., and J.-A. Sauvaud, Populating of cusp and boundary layers by energetic (hundreds of keV) equatorial particles, *J. Geophys. Res.*, *104*, 22,635–22,648, 1999.
- Dessler, A. J., The Propagation Velocity of World-Wide Sudden Commencements of Magnetic Storms, *J. Geophys. Res.*, *63*, 405–, 1958.

- Dessler, A. J., and E. N. Parker, Hydromagnetic theory of geomagnetic storms, *J. Geophys. Res.*, *64*, 2239–2252, 1959.
- Drake, J. F., Magnetic Reconnection: A Kinetic Treatment, pp. 155–165, 1995.
- Drake, J. F., and M. A. Shay, Fundamentals of collisionless reconnection, in *Reconnection of Magnetic Fields*, edited by J. Birn and E. R. Priest, pp. 87–107, Cambridge University Press, Cambridge, UK, 2007.
- Drake, J. F., M. Swisdak, M. A. Shay, B. N. Rogers, A. Zeiler, and C. Cattell, Formation of electron holes and particle energization during magnetic reconnection, *Science*, *299*, 873–, 2003.
- Dungey, J. W., *Cosmic Electrodynamics*, Cambridge Univ. Press, Cambridge, 1958.
- Dungey, J. W., Interplanetary magnetic field and the auroral zones, *Phys. Rev. Letters*, *6*, 47–48, 1961.
- Dungey, J. W., The structure of the exosphere or adventures in velocity space, in *Geophysics The Earth's Environment*, edited by C. DeWitt and J. Hieblot, p. 503, Gordon and Breach, New York, 1963.
- Dunlop, M. W., A. Balogh, and K. H. Glassmeier, Four-point cluster application of magnetic field analysis tools: The discontinuity analyzer, *J. Geophys. Res.*, *107(A11)*, 1385, doi:10.1029/2001JA005,089, 2002.
- Dunlop, M. W., et al., Cluster observations of the Cusp: Magnetic structure and dynamics, *Surveys in Geophysics*, *26*, 5–55, doi:10.1007/s10,712–005–1871–7, 2005.
- Eastman, T. E., The plasma sheet boundary layer, *Geophys. Res. Lett.*, *3*, 685–688, 1976.
- Eastman, T. E., S. A. Boardsen, S.-H. Chen, S. F. Fung, and R. L. Kessel, Configuration of high-latitude and high-altitude boundary layers, *J. Geophys. Res.*, *105*, 23,221–23,238, 2000.
- Eccles, A. A., and T. A. Fritz, Energetic particle observations at the subsolar magnetopause, *Annales Geophysicae*, *20*, 445–460, 2002.
- Escoubet, C. P., R. Schmidt, and M. L. Goldstein, Cluster - Science and Mission Overview, *Space Science Reviews*, *79*, 11–32, 1997.
- Fairfield, D. H., Average and unusual locations of the Earth's magnetopause and bow shock, *J. Geophys. Res.*, *76*, 6700–6716, 1971.
- Ferraro, V. C. A., O the Theory of the First Phase of a Geomagnetic Storm: a New Illustrative Calculation Based on AN Idealised (plane not Cylindrical) Model Field Distribution, *J. Geophys. Res.*, *57*, 15–+, 1952.
- Ferraro, V. C. A., An Approximate Method of Estimating the Size and Shape of the Stationary Hollow Carved Out in a Neutral Ionized Stream of Corpuscles Impinging on the Geomagnetic Field, *J. Geophys. Res.*, *65*, 3951–+, 1960.

- Formisano, V., V. Domingo, and K.-P. Wenzel, The three-dimensional shape of the magnetopause, *Planet. Space Sci.*, *27*, 1137–1149, doi:10.1016/0032-0633(79)90134-X, 1979.
- Frank, L. A., Plasma in the earth's polar magnetosphere, *J. Geophys. Res.*, *76*, 5202, 1971.
- Frey, H. U., S. B. Mende, T. J. Immel, S. A. Fuselier, E. S. Claffin, J.-C. Gerard, and B. Hubert, Proton aurora in the cusp, *J. Geophys. Res.*, *107*, 755–758, doi:10.1029/2001JA900161, 2002.
- Fritz, T. A., The role of the cusp as a source for magnetospheric particles: A new paradigm, in *Proc. Cluster-II workshop on Multiscale/Multipoint Plasma Measurements*, pp. 203–209, Eur. Space Agency Spec. Publ., SP - 449, ESA, 2000.
- Fritz, T. A., The cusp as a source of magnetospheric energetic particles, currents, and electric fields: new paradigm, *Space Sci. Rev.*, *95*, 469–488, 2001.
- Fritz, T. A., and Q. G. Zong, The magnetospheric cusps: a summary, *Surveys in Geophysics*, *26*, 409–414, 2005.
- Fritz, T. A., J. Chen, R. B. Sheldon, H. E. Spence, and J. F. Fennell, Cusp energetic particle events measured by polar spacecraft, *Physics and Chemistry of the Earth*, *24*, 135–140, 1999.
- Fritz, T. A., J. Chen, and G. L. Siscoe, Energetic ions, large diamagnetic cavities, and chapman-ferraro cusp, *J. Geophys. Res.*, *108*, 1028, doi:10.1029/2002JA009476, 2003.
- Fujimoto, M., and T. Terasawa, Anomalous ion mixing within an MHD scale Kelvin-Helmholtz vortex, *J. Geophys. Res.*, *99*, 8601–8613, 1994.
- Fuselier, S. A., Kinetic Aspects of Reconnection at the Magnetopause, in *Physics of the Magnetopause*, *Geophys. Monogr. Ser.*, vol. 90, edited by P. Song, B. U. Ö. Sonnerup, and M. F. Thomsen, pp. 181–187, AGU, Washington, D. C., 1995.
- Fuselier, S. A., D. M. Klumper, and E. G. Shelley, Ion reflection and transmission during reconnection at the earth's subsolar magnetopause, *Geophys. Res. Lett.*, *16*, 139–142, 1991.
- Fuselier, S. A., B. J. Anderson, and T. G. Onsager, Electron and ion signatures of field line topology at the low-shear magnetopause, *J. Geophys. Res.*, *102*, 4847–4863, 1997.
- Galeev, A. A., and R. Z. Sagdeev, Current instabilities and anomalous resistivity of plasma, in *Basic Plasma Physics: Selected Chapters, Handbook of Plasma Physics, Volume 1*, edited by A. A. Galeev and R. N. Sudan, pp. 270–303, 1984.
- Ganguli, G., and P. Palmadesso, Electrostatic ion instabilities in the presence of parallel currents and transverse electric fields, *Geophys. Res. Lett.*, *15*, 103, 1988.
- Giovanelli, R.-G., Magnetic and electric phenomena in the Sun's atmosphere associated with sunspots, *MNRAS*, *107*, 1947.

- Gold, T., Motions in the magnetosphere of the Earth, *J. Geophys. Res.*, *64*, 1219–1224, 1959.
- Gombosi, T. I., G. Tth, D. L. D. Zeeuw, K. G. Powell, and Q. F. Stout, Adaptive Mesh Refinement MHD for Global Simulations, in *Proceedings of ISSS-6*, pp. 1–8, Copernicus Gesellschaft, 2001.
- Gombosi, T. I., et al., Solution Adaptive MHD for Space Plasmas: Sun-to-Earth Simulations, *Computing in Science and Engineering*, *6*, 14–35, 2004.
- Gosling, J. T., J. R. Asbridge, S. J. Bame, W. C. Feldman, G. Paschmann, N. Sckopke, and C. T. Russell, Evidence for quasi-stationary reconnection at the dayside magnetopause, *J. Geophys. Res.*, *87*, 2147–2158, 1982.
- Gosling, J. T., M. F. Thomsen, S. J. Bame, T. G. Onsager, and C. T. Russell, The electron edge of the low latitude boundary layer during accelerated flow events, *Geophys. Res. Lett.*, *17*, 1833–1836, 1990.
- Gosling, J. T., D. J. McComas, J. L. Phillips, and S. J. Bame, Geomagnetic activity associated with earth passage of interplanetary shock disturbance and coronal mass ejections, *J. Geophys. Res.*, *96*, 7831–7839, 1991.
- Groth, C. P. T., D. L. D. Zeeuw, T. I. Gombosi, and K. G. Powell, Global three-dimensional MHD simulation of a space weather event: CME formation, interplanetary propagation, and interaction with the magnetosphere, *J. Geophys. Res.*, *105*, 25,053–, 2000.
- Gustafsson, G., et al., The Electric Field and Wave Experiment for the Cluster Mission, *Space Science Reviews*, *79*, 137–156, 1997.
- Haerendel, G., G. Paschmann, N. Sckopke, H. Rosenbauer, and P. C. Hedgecock, The frontside boundary layer of the magnetopause and the problem of reconnection, *J. Geophys. Res.*, *83*, 3195–3216, 1978.
- Harris, E. G., On a plasma sheet separating regions of oppositely directed magnetic field, *Nuovo Cimento*, *23*, 115–, 1962.
- Hasegawa, H., M. Fujimoto, T.-D. Phan, H. Reme, A. Balogh, M. W. Dunlop, C. Hashimoto, and R. TanDokoro, Transport of solar wind into Earth’s magnetosphere through rolled-up Kelvin-Helmholtz vortices, *Nature*, *430*, 755–758, doi:10.1038/nature02799, 2004.
- Haskell, G. P., Anisotropic fluxes of energetic particles in the outer magnetosphere, *Planet. Space Sci.*, *74*, 1740–1748, 1969.
- Heikkila, W. J., and J. D. Winningham, Penetration of magnetosheath plasma to low altitudes through the dayside magnetospheric cusps, *J. Geophys. Res.*, *76*, 883–, 1971.
- Holzer, R. E., and J. A. Slavin, Magnetic flux transfer associated with expansions and contractions of the dayside magnetosphere, *J. Geophys. Res.*, *83*, 3831–3839, 1978.

- Huba, J. D., N. T. Gladd, and K. Papadopoulos, The lower-hybrid-drift instability as a source of anomalous resistivity for magnetic field line reconnection, *Geophys. Res. Lett.*, *4*, 125–126, 1977.
- Hudson, P. D., Discontinuities in an anisotropic plasma and their identification in the solar wind, *Planet. Space Sci.*, *18*, 1611–1622, 1970.
- Johnstone, A. D., et al., Peace: A plasma electron and current experiment, *Space Sci. Rev.*, *79*, 351–398, 1997.
- Kaymaz, Z., G. Siscoe, and J. G. Luhmann, IMF draping around the geotail: IMP 8 observations, *Geophys. Res. Lett.*, *19*, 829–832, 1992.
- Kessel, R. L., S. H. Chen, J. L. G., S. F. Fung, S. A. Boardsen, L. C. Tan, , and L. A. Frank, Evidence of high-latitude reconnection during northward imf: Hawkeye observations, *Geophys. Res. Lett.*, *23*, 583–586, 1996.
- Khotyaintsev, Y., A. Vaivads, Y. Ogawa, B. Popielawska, M. Andre, S. Buchert, P. Decreau, B. Lavraud, and H. Reme, Cluster observations of high-frequency waves in the exterior cusp, *Ann. Geophys.*, *22*, 2403–2411, 2004.
- Kivelson, M. G., and C. T. Russell, *Introduction to Space Physics*, Introduction to Space Physics, Edited by Margaret G. Kivelson and Christopher T. Russell, pp. 586. ISBN 0521451043. Cambridge, UK: Cambridge University Press, April 1995., 1995.
- Kremser, G., J. Woch, K. Mursula, P. Tanskanen, B. Wilken, and R. Lundin, Origin of energetic ions in the polar cusp inferred from ion composition measurements by the viking satellite, *Ann. Geophys.*, *13*, 595–607, 1995.
- Kudela, K., D. Sibeck, M. Slivka, and V. Lutsenko, Energetic ions in the magnetosheath: Statistical study of spectra and anisotropy, *Adv. Space Res.*, *21*, 633–636, 1998.
- Laakso, H., et al., Oscillations of magnetospheric boundaries driven by IMF rotations, *Geophys. Res. Lett.*, *25*, 3007–3010, 1998.
- Lavraud, B., A. Fedorov, E. Budnik, A. Grigoriev, P. J. Cargill, M. Dunlop, H. Rème, I. Dandouras, and A. Balogh, Cluster survey of the high-altitude cusp properties: A three-year statistical study, *Ann. Geophys.*, *22(8)*, 3009–3019, 2004a.
- Lavraud, B., et al., Cluster observations of the exterior cusp and its surrounding boundaries under northward IMF, *Geophys. Res. Lett.*, *29*, 1995, doi:10.1029/2002GL015,464, 2002.
- Lavraud, B., et al., The exterior cusp and its boundary with the magnetosheath: Cluster multi-event analysis, *Ann. Geophys.*, *22*, 3039–3054, 2004b.
- Lavraud, B., et al., Cluster observes the high-altitude cusp region, *Survey Geophysics*, *26*, 135–175, doi:10.1007/s10,712–005–1875–3, 2005a.
- Lavraud, B., et al., High-altitude cusp flow dependence on imf orientation: A 3-year cluster statistical study, *J. Geophys. Res.*, *110*, A02,209, doi:10.1029/2004JA010,804, 2005b.

- Le, G., C. T. Russell, J. T. Gosling, and M. F. Thomsen, observations of low-latitude boundary layer for northward interplanetary magnetic field: Implications for cusp reconnection, *J. Geophys. Res.*, *101*, 27,239–27,249, 1996.
- Lemaire, J., and M. Roth, Penetration of solar wind plasma elements into the magnetosphere, *J. Atmos. Terr. Phys.*, *40*, 331, 1978.
- Lockwood, M., and M. F. Smith, The variation of reconnection rate at the dayside magnetopause and cusp ion precipitation, *J. Geophys. Res.*, *97*, 14,841–14,847, 1992.
- Lotko, W., and B. U. Ö. Sonnerup, The Low-Latitude Boundary Layer on Closed Field Lines, in *Physics of the Magnetopause*, *Geophys. Monogr. Ser.*, vol. 90, edited by P. Song, B. U. Ö. Sonnerup, and M. F. Thomsen, pp. 371–383, AGU, Washington, D. C., 1995.
- Luhmann, J. G., R. J. Walker, C. T. Russell, N. U. Crooker, J. R. Spreiter, and S. S. Stahara, Patterns of potential magnetic field merging sites on the dayside magnetopause, *J. Geophys. Res.*, *89*, 1739–1745, 1984.
- Lundin, R., plasma composition and flow characteristic in the magnetospheric boundary layers connected to the polar cusp, in *The polar Cusp*, edited by J. A. Holtet and A. Egeland, pp. 9–32, Kluwer Academic Publishers, Dordrecht, the Netherlands, 1985.
- Lundin, R., L. Eliasson, and I. Sandahl, First Viking results: Hot plasma, *Phys. Scr.*, *37*, 482–490, 1988.
- Lundin, R., B. Aparicio, and M. Yamauchi, On the solar wind flow control of the polar cusp, *J. Geophys. Res.*, *106*, 13,023–13,035, 2001.
- Lundin, R., et al., Evidence for impulsive solar wind plasma penetration through the dayside magnetopause, *Ann. Geophys.*, *21*, 457–472, 2003.
- Maynard, N. C., et al., Polar, cluster and superdarn evidence for high latitude merging during southward IMF: temporal/spatial evolution, *Annales Geophysicae*, *21*, 2233–2258, 2003.
- Mead, G. D., and D. B. Beard, Shape of the Geomagnetic Field Solar Wind Boundary, *J. Geophys. Res.*, *69*, 1169–+, 1964.
- Meng, C. I., A. T. Y. Lui, S. M. Krimigis, S. Ismail, and D. J. Williams, Spatial distribution of energetic particles in the distant magnetotail, *J. Geophys. Res.*, *86*, 5682–5700, 1981.
- Menietti, J., and J. Burch, Spatial extent of the plasma injection in the cusp-magnetosheath interface, *J. Geophys. Res.*, *93*, 105–, 1988.
- Merka, J., J. Safrankova, and Z. Nemecek, Cusp-like plasma in the high altitudes: a statistical study of the width and location of the cusp from magion-4, *Ann. Geophys.*, *20*, 311–320, 2002.

- Midgeley, J. E., and L. Davis, Jr., Calculation by a moment technique of the perturbation of the geomagnetic field by the solar wind, *J. Geophys. Res.*, *68*, 5111–5123, 1963.
- Mozer, F. S., S. Bale, and T. D. Phan, Evidence of diffusion regions at a subsolar magnetopause crossing, *Phys. Rev. Lett.*, *89*, DOI: 10.1103/PhysRevLett.89.015,002, 2002.
- Nemecek, Z., J. Simunek, J. Safrankova, and L. Prech, Spatial and temporal variations of the high-altitude cusp precipitation, *Ann. Geophys.*, *22*, 2441–2450, 2004.
- Newell, P. T., and C. I. Meng, The cusp and the cleft/boundary layer: Lower-altitude identification and statistical local time variation, *J. Geophys. Res.*, *93*, 14,549–14,556, 1988.
- Newell, P. T., and C.-I. Meng, Ionospheric projections of magnetospheric regions under low and high solar wind pressure conditions, *J. Geophys. Res.*, *99*, 273, 1994.
- Newell, P. T., C. I. Meng, and D. G. S. and R. Lepping, Some low-altitude dependencies on the interplanetary magnetic field, *J. Geophys. Res.*, *94*, 8921–8927, 1989.
- Nykyri, K., and A. Otto, Plasma transport at the magnetospheric boundary due to reconnection in Kelvin-Helmholtz vortices, *Geophys. Res. Lett.*, *28*, 3565–3568, doi: 10.1029/2001GL013239, 2001.
- Nykyri, K., et al., Cluster observations of magnetic field fluctuations in the high-altitude cusp, *Ann. Geophys.*, *22*, 2413–2429, 2004.
- Oieroset, M., T. D. Phan, , M. Fujimoto, R. P. Lin, and R. P. Lepping, In situ detection of collisionless reconnection in the Earth's magnetotail, *Nature*, *412*, 414–417, 2001.
- Olson, W. P., The shape of the tilted magnetopause., *J. Geophys. Res.*, *74*, 5642–5651, 1969.
- Onsager, T. G., J. D. Scudder, M. Lockwood, and C. T. Russell, Reconnection at the high latitude magnetopause during northward interplanetary magnetic field conditions, *J. Geophys. Res.*, *106*, 25,467–25,488, 2001.
- Papadopoulos, K., A review of anomalous resistivity for the ionosphere, *Rev. Geophys.*, *15*, 113–127, 1977.
- Parker, E., Extension of the Solar Corona into Interplanetary Space, *J. Geophys. Res.*, *64*, 1675–, 1959.
- Parker, E. N., Newtonian development of the dynamical properties of ionized gases of low density, *Physical Rev.*, *107*, 924–933, 1957.
- Parker, E. N., Dynamics of the Interplanetary Gas and Magnetic Fields., *Astrophys. J.*, *128*, 664C676, 1958.
- Parks, G. K., *Physics of space plasmas : an introduction*, Physics of space plasmas : an introduction / George K Parks. Boulder, Colo. : Westview Press, Advanced Book Program, c2004., 2004.

- Paschmann, G., Plasma structure of the magnetopause and boundary layer, in *Magnetospheric Boundary Layers, ESA Special Publication*, vol. 148, edited by J. Lemaire, pp. 25–36, 1979.
- Paschmann, G., G. Haerendel, N. Sckopke, and H. Rosenbauer, Plasma and field characteristics of the distant polar cusp near local noon: The entry layer, *J. Geophys. Res.*, *81*, 2883–2899, 1976.
- Paschmann, G., et al., Plasma acceleration at the earth’s magnetopause: Evidence for reconnection, *Nature*, *282*, 243–246, 1979.
- Paulikas, G. A., and J. B. Blake, Effects of the solar wind on magnetospheric dynamics: energetic electrons at the synchronous orbit, in *Quantitative Modeling of Magnetospheric Process*, edited by W. P. Olson, pp. 180–202, AGU monograph 21, Washiton, D. C., 1979.
- Petrinec, S. M., and C. T. Russell, External and internal influences on the size of dayside terrestrial magnetosphere, *Geophys. Res. Lett.*, *20*, 339–342, 1993.
- Petrinec, S. P., P. Song, and C. T. Russell, Solar cycle variations in the size and shape of the magnetopause, *J. Geophys. Res.*, *96*, 7893–7896, 1991.
- Petschek, H. E., Magnetic Field Annihilation, in *The Physics of Solar Flares*, edited by W. N. Hess, p. 425, 1964.
- Phan, T. D., and G. Paschman, Low-latitude dayside magnetopause and boundary layer for high magnetic shear 1. Structure and motion, *J. Geophys. Res.*, *2101*, 7801–7815, 1996.
- Phan, T.-D., G. Paschmann, W. Baumjohann, N. Sckopke, and H. Luehr, The magnetosheath region adjacent to the dayside magnetopause: AMPTE/IRM observations, *J. Geophys. Res.*, *99*, 121–141, 1994.
- Phan, T. D., G. Paschman, and B. U. Ö. Sonnerup, Low-latitude dayside magnetopause and boundary layer for high magnetic shear 2. Occurrence of magnetic reconnection, *J. Geophys. Res.*, *2101*, 7817–7828, 1996.
- Phan, T. D., et al., Simultaneous Cluster and IMAGE observations of cusp reconnection and auroral proton spot for northward IMF, *Geophys. Res. Lett.*, *30*, 16–1, doi:10.1029/2003GL016885, 2003.
- Pitout, F., C. P. Escoubet, Y. V. Bogdanova, E. Georgescu, A. N. Fazakerley, and H. Rème, Response of the mid-altitude cusp to rapid rotations of the IMF, *Geophys. Res. Lett.*, *33*, L11,107, doi:10.1029/2005GL025,460, 2006.
- Powell, K. G., P. L. Roe, T. J. Linde, T. I. Gombosi, and D. L. De Zeeuw, A solution-adaptive upwind scheme for ideal magnetohydrodynamics, *Journal of Computational Physics*, *154*, 284–309, 1999.

- Priest, E., and T. Forbes, *Magnetic Reconnection*, Magnetic Reconnection, by Eric Priest and Terry Forbes, pp. 612. ISBN 0521481791. Cambridge, UK: Cambridge University Press, June 2000., 2000.
- Raeder, J., J. Berchem, M. Ashour-Abdalla, L. A. Frank, W. R. Paterson, K. L. Ackerson, S. Kokubun, and J. A. Slavin, Boundary layer formation in the magnetotail: Geotail observations and comparisons with a global mhd simulation, *Geophys. Res. Lett.*, *24*, 951–954, 1997.
- Raeder, J., Y. L. Wang, and T. J. Fuller-Rowell, Geomagnetic storm simulation with a coupled magnetosphere-ionosphere-thermosphere model, in *Space Weather: Progress and Challenges in Research and Applications*, edited by P. Song, H. Singer, and G. Siscoe, pp. 377–384, Geophysical Monograph, 125, AGU, Washington, D.C., 2001.
- Rème, H., et al., The cluster ion spectrometry(CIS) experiment, *Space Sci. Rev.*, *79*, 303–350, 1997.
- Robert, P., M. W. Dunlop, A. Roux, and G. Chanteur, Accuracy of current determination, in *Analysis Methods for Multi Spacecraft Data*, edited by G. Paschmann and P. W. Daly, p. 395, ESA, Bern, Switzerland, 1998.
- Roederer, J. G., *Dynamics of geomagnetically Trapped radiation*, Springer-Verlag, New York, 1970.
- Rosenbauer, H., H. Gruenwaldt, M. D. Montgomery, G. Paschmann, and N. Skopke, HEOS 2 plasma observations in the distant polar magnetosphere: the plasma mantle, *J. Geophys. Res.*, *80*, 2723–2737, 1975.
- Russell, C. T., and R. C. Elphic, Initial ISEE magnetometer results: Magnetopause observations, *Space Sci. Rev.*, *22*, 681–715, 1978.
- Russell, C. T., and R. C. Elphic, Observation of magnetic flux ropes in the Venus ionosphere, *Nature*, *279*, 616–618, 1979.
- Russell, C. T., M. M. Mellot, E. J. Smith, and J. H. King, Multiple spacecraft observations of interplanetary shocks : four spacecraft determination of the shock normals, *J. Geophys. Res.*, *88*, 4739–4748, 1983.
- Russell, C. T., E. R. Priest, and L. C. Lee, *Physics of Magnetic Flux Ropes*, pp. 439–453, American Geophysical Union, Washington, D.C., 1990.
- Sato, T., and T. Hayashi, Externally driven magnetic reconnection and a powerful magnetic energy converter, *Physics of Fluids*, *22*, 1189–1202, 1979.
- Savin, S., et al., Magnetosheath interaction with the high latitude magnetopause, *Surveys in Geophysics*, *26*, 95–133, 2005.
- Scholer, M., Undriven magnetic reconnection in an isolated current sheet, *J. Geophys. Res.*, *94*, 8805–8812, 1989.

- Sckopke, N., G. Paschmann, G. Haerendel, B. U. Ö. Sonnerup, S. J. Bame, T. G. Forbes, E. W. Hones, Jr., and C. T. Russell, Structure of the low latitude boundary layer, *J. Geophys. Res.*, *86*, 2099–2110, 1981.
- Shay, M. A., J. F. Drake, B. N. Rogers, and R. E. Denton, The scaling of collisionless, magnetic reconnection for large systems, *Geophys. Res. Lett.*, *26*, 2163–2166, 1999.
- Sheldon, R. B., H. E. Spence, J. D. Sullivan, T. A. Fritz, and J. Chen, The discovery of trapped energetic electrons in the outer cusp, *Geophys. Res. Lett.*, *25*, 1825–1828, 1998.
- Shue, J.-H., J. K. Chao, H. C. Fu, C. T. Russell, P. Song, K. K. Khurana, and H. J. Singer, A new functional form to study the solar wind control of the magnetopause size and shape, *J. Geophys. Res.*, *102*, 9497–9512, doi:10.1029/97JA00196, 1997.
- Sibeck, D. G., R. E. Lopez, and E. C. Roelof, Solar wind control of the magnetopause shape, location, and motion, *J. Geophys. Res.*, *96*, 5489–5495, 1991.
- Sibeck, D. G., et al., Plasma transfer processes at the magnetopause, in *Magnetospheric Plasma Sources and Losses*, edited by B. Hultqvist and M. Oieroset, pp. 207–283, Kluwer Acade., Norwell, Mass., 1999.
- Siscoe, G., Z. Kaymaz, and Y. V. Bogdanova, Magnetospheric Cusps under Extreme Conditions: Cluster Observations and MHD Simulations Compared, *Sol. Phys.*, *244*, 189–199, doi:10.1007/s11207-007-0359-7, 2007.
- Siscoe, G. L., N. Crooker, K. Siebert, N. Maynard, D. Weimer, and W. White, Cusp geometry in MHD simulations, *Surveys in Geophysics*, *26*, 387–407, 2005.
- Song, P., and C. T. Russell, Model of the formation of low- latitude boundary layer for strongly northward interplanetary magnetic field, *J. Geophys. Res.*, *97*, 1411–, 1992.
- Song, P., C. T. Russell, R. C. Elphic, J. T. Gosling, and C. A. Cattell, Structure and properties of the subsolar magnetopause for northward IMF - ISEE observations, *J. Geophys. Res.*, *95*, 6375–6387, 1990.
- Song, P., C. T. Russell, and M. F. Thomsen, Slow mode transition in the frontside magnetosheath, *J. Geophys. Res.*, *97*, 8295, 1992.
- Song, P., C. T. Russell, R. J. Strangeway, J. R. Wygant, C. A. Cattell, R. J. Fitzenreiter, and R. R. Anderson, Wave properties near the subsolar magnetopause - Pc 3-4 energy coupling for northward interplanetary magnetic field, *J. Geophys. Res.*, *98*, 187–196, 1993.
- Sonnerup, B. U. Ö., and L. J. Cahill, Jr., Magnetopause structure and attitude from Explorer 12 observations, *J. Geophys. Res.*, *72*, 171–183, 1967.
- Sonnerup, B. U. Ö., and B. G. Ledley, Electromagnetic structure of the magnetopause and boundary layer, in *Proceeding of Magnetospheric Boundary Layers Conference*, edited by ESA, pp. 401–411, ESA Sp-148, Alpbach, 1979.

- Sonnerup, B. U. Ö., G. Paschmann, I. Papamastorkis, N. Sckopke, G. Haerendel, S. J. Bame, J. R. Asbridge, J. T. Gosling, and C. T. Russell, Evidence for magnetic field reconnection at the earth's magnetopause, *J. Geophys. Res.*, *86*, 10,049–10,067, 1981.
- Sonnerup, B. U. Ö., I. Papamastorkis, G. Paschmann, and H. Lühr, Magnetopause properties from AMPTE/IRM observations of the convection electric field: Method development, *J. Geophys. Res.*, *92*, 12,137–12,159, 1987.
- Sonnerup, B. U. O., I. Papamastorakis, G. Paschmann, and H. Luehr, The magnetopause for large magnetic shear - Analysis of convection electric fields from AMPTE/IRM, *J. Geophys. Res.*, *95*, 10,541–10,557, 1990.
- Sonnerup, B. U. Ö., G. Paschmann, and T.-D. Phan, Fluid Aspects of Reconnection at the Magnetopause: In Situ Observations, pp. 167–180, 1995.
- Sonnerup, U. O., Magnetic field reconnection, in *Solar system plasma physics. (A79-53667 24-46) Amsterdam, North-Holland Publishing Co.*, vol. 3, pp. 45–108, 1979.
- Spreiter, J. R., and B. R. Briggs, Theoretical Determination of the Form of the Boundary of the Solar Corpuscular Strea Produced by Interaction with the Magnetic Dipole Field of the Earth, *J. Geophys. Res.*, *67*, 37–+, 1962.
- Spreiter, J. R., and S. S. Stahara, A new predictive model for determining solar wind -terrestrial planet interactions, *J. Geophys. Res.*, *85*, 6769–6777, 1980.
- Storey, L. R. O., An investigation of whistling atmospherics, *Phil. Trans. Roy. Soc.*, *246*, 113, 1953.
- Sweet, P. A., The neutral point theory of solar flares, in *Electromagnetic Phenomena in Cosmical Physics*, edited by B. Lehnert, pp. 123–134, Cambridge Univeristy Press, New York, 1958.
- Taylor, M. G. G. T., et al., Cluster observations of a complex high-altitude cusp passage during highly variable IMF, *Ann. Geophys.*, *22*, 3707–3719, 2004.
- Terasawa, T., et al., Solar wind control of density and temperature in the near-earth plasma sheet: WIND/GEOTAIL collaboration, *Geophys. Res. Lett.*, *24*, 935–938, 1997.
- Trattner, K. J., E. Mobius, B. Klecker, M. Hilchenbach, and H. Luhr, Statistical analysis of diffuse ion events upstream of the Earth's bow shock, *J. Geophys. Res.*, *99*, 13,389–, 1994.
- Trattner, K. J., S. A. Fuselier, W. K. Peterson, S. W. Chang, R. Friedel, and M. R. Aellig, Origins of energetic ions in the cusp, *J. Geophys. Res.*, *106*, 5967–5976, 2001.
- Trattner, K. J., S. A. Fuselier, W. K. Peterson, and C. W. Carlson, Spatial features observed in the cusp under steady solar wind conditions, *J. Geophys. Res.*, *107*, 1288–, doi: 10.1029/2001JA000262, 2002.

- Tsyganenko, N. A., and D. P. Stern, Modeling the global magnetic field of the large-scale Birkeland current system, *J. Geophys. Res.*, *101*, 27,187–27,198, 1996.
- Ugai, M., and T. Tsuda, Magnetic field-line reconnection by localized enhancement of resistivity. I - Evolution in a compressible MHD fluid, *Journal of Plasma Physics*, *17*, 337–356, 1977.
- Walén, C., On the Theory of Sunspots, *Arkiv for Astronomi*, *30*, 1–87, 1944.
- Weimer, D. R., D. M. Ober, N. C. Maynard, M. R. Collier, D. J. McComas, N. F. Ness, C. W. Smith, and J. Watermann, Predicting interplanetary magnetic field (IMF) propagation delay times using the minimum variance technique, *J. Geophys. Res.*, *108*, 1026–+, doi:10.1029/2002JA009405, 2003.
- Weiss, L. A., P. H. Reiff, E. J. Weber, H. C. Carlson, M. Lockwood, and W. K. Peterson, Flow-aligned jets in the magnetospheric cusp: Results from the geospace environment modeling pilot program, *J. Geophys. Res.*, *100*, 7649–7659, 1995.
- West, H. I., and R. M. Buck, Observations of  $> 100$  keV protons in the Earth's magnetosheath, *J. Geophys. Res.*, *81*, 569–584, 1976.
- Wilken, B., and Q. Zong, Die CLUSTER-Flotte. Ein Beitrag der ESA zur Erforschung der Magnetosphäre, *Sterne und Weltraum*, *40*, 836–844, 2001.
- Wilken, B., et al., RAPID: The imaging energetic particle spectrometer on Cluster, *Space Sci. Rev.*, *79*, 399–473, 1997.
- Wilken, B., et al., First results from the rapid imaging energetic particle spectrometer on board cluster, *Ann. Geophys.*, *19*, 1355–1366, 2001.
- Williams, D. J., Dynamic of the earth's ring current: theory and observation, *Space Sci. Rev.*, *42*, 375–396, 1985.
- Wing, S., P. T. Newell, and J. M. Ruohoniemi, Double cusp: Model prediction and observational verification, *J. Geophys. Res.*, *106*, 25,571–25,593, 2001.
- Yamauchi, M., and R. Lundin, Physical signatures of magnetospheric boundary layer processes, in *Physical Signatures of Magnetospheric Boundary Layer Processes*, edited by J. A. Holtet and A. Egeland, pp. 99–109, Kluwer Academic Publishers, Dordrecht, the Netherlands, 1998.
- Zhang, H., T. A. Fritz, Q. G. Zong, and P. W. Daly, Stagnant exterior cusp region as viewed by energetic electrons and ions: A statistical study using Cluster Research with Adaptive Particle Imaging Detectors (RAPID) data, *J. Geophys. Res.*, *110*, doi:10.1029/2004JA010562, 2005.
- Zhang, H., T. A. Fritz, Q. G. Zong, and P. W. Daly, The high latitude boundaries under extreme solar wind conditions: A Cluster perspective, in *Advances in Geosciences, Volume 2: Solar Terrestrial(ST)*, edited by W.-H. Ip, pp. 163–172, World Scientific Publishing Co. Pte. Ltd., 5 Toh Tuck Link, Singapore, 2006.

- Zhou, X.-W., and C. T. Russell, The location of the high-latitude polar cusp and the shape of the surrounding magnetopause, *J. Geophys. Res.*, *102*, 105–110, 1997.
- Zhou, X. W., C. T. Russell, G. Le, S. A. Fuselier, and J. D. Scudder, Solar wind control of the polar cusp at high-altitude, *J. Geophys. Res.*, *105*, 245–251, 2000.
- Zong, Q.-G., B. Wilken, S.-Y. Fu, T. A. Fritz, Z.-Y. Pu, N. Hasebe, and D. J. Williams, Ring current oxygen ions in the magnetosheath caused by magnetic storm, *J. Geophys. Res.*, *106*, 25,541–25,556, 2001.
- Zong, Q.-G., T. A. Fritz, B. Wilken, and P. W. Daly, Energetic ions in the high latitude boundary layer of the magnetosphere - rapid/cluster observation, in *The Lower-Latitude Boundary Layer*, edited by P. T. Newell and T. G. Onsager, pp. 101–110, AGU, AGU, Washington, D.C., 2002.
- Zong, Q.-G., T. A. Fritz, H. Spence, M. Dunlop, A. Balogh, A. Korth, P. W. Daly, Z. Y. Pu, and H. Reme, Bursty energetic electrons in the cusp region, *Planet. Space Sci.*, *51*, 821–830, 2003.
- Zong, Q.-G., T. A. Fritz, H. Zhang, A. Korth, P. W. Daly, M. W. Dunlop, K.-H. Glassmeier, H. Reme, and A. Balogh, Triple cusps observed by Cluster: temporal or spatial effect?, *Geophys. Res. Lett.*, *31*, L09,810, doi:10.1029/2003GL019,128, 2004a.
- Zong, Q.-G., et al., Energetic oxygen ion bursts in distant magnetotail as a product of intense substorms: Three case studies, *J. Geophys. Res.*, *103*, 20,339–20,363, 1998.
- Zong, Q.-G., et al., Cluster observations of earthward flowing plasmoid in the tail, *Geophys. Res. Lett.*, *31*, L18,803, doi:10.1029/2004GL020,692, 2004b.
- Zong, Q.-G., et al., Energetic electrons as a field line topology tracer in the high latitude boundary / cusp region: Cluster rapid observations, *Surveys in Geophysics*, *26*, 213–238, doi:10.1007/s10,712–005–1879–z, 2005a.
- Zong, Q.-G., et al., Plasmoid in the high latitude boundary/cusp region observed by cluster, *Geophys. Res. Lett.*, *32*, L01,101, doi:10.1029/2004GL020,960, 2005b.
- Zong, Q.-G., et al., Multiple cusps during an extended northward IMF period with a significant  $B_y$  component, *J. Geophys. Res.*, 2007.

# Curriculum Vitae

**Hui Zhang**

## Contact Information

Center for Space Physics, Boston University  
 725 Commonwealth Ave., Boston, MA, 02215, USA  
 Phone (office): (617)3535611 Fax: (617) 353-6463  
 Email: [zhang@bu.edu](mailto:zhang@bu.edu)  
 WWW: <http://people.bu.edu/zhang>

## Research Interests

Boundary layers including magnetosheath, magnetopause, plasma mantle, cusp and so on, multiple satellites data analysis.

## Education

Boston University, Boston, MA, USA

M.S., Astronomy, Boston University, USA, September, 2004

Ph.D. candidate, Astronomy, Boston University, USA, July 2002 - present (PhD expected 01/2008)

- Dissertation Topic: Structure and dynamics of high latitude dayside magnetospheric boundaries
- Advisor: T. A. Fritz

Peking University, Beijing, P. R. China

B.A., Space physics, Peking University, Beijing, P. R. China, June 2002.

## Awards

1. 2006, Outstanding Student Paper Awards in American Geophysical Union 2006 Spring Meeting
2. 2002, Outstanding Graduate, Peking University, P. R. China
3. 2000-2001, Outstanding Student, Peking University, P. R. China
4. 2000-2001, Baogang Scholarship, Peking University, P. R. China
5. 1999-2000, Antai Scholarship, Peking University, P. R. China

## Research Experience

Boston University, Boston, MA, USA

Graduate Research Assistant, Department of Astronomy, Boston University, July 2002 - Present.

- Study the structure and dynamics of high latitude magnetospheric boundaries by analyzing multi-year Cluster datasets.

Peking University, Beijing, P. R. China

Research Assistant, Space Physics, Peking University, Beijing, P. R. China, June 2000 - June 2002.

- Hall-MHD simulation of vortex-induced reconnection at the magnetopause

### **Teaching Experience**

Graduate Teaching Assistant for AS101, The Solar System, Department of Astronomy, Boston University, 2006 spring semester.

Taught 3 lab sections per week, graded homework, lab reports and exams, held office hours, and advised 40 students.

### **Professional Activities**

#### Society Membership

Student Member of the American Geophysical Union 2002 - Present Student member of Geospace Environment Modeling (GEM), 2003 - Present.

#### Referee Service

Referee of a paper submitted to *Advances in Geoscience* (2006)

Referee of a paper submitted to *J. Geophys. Res* (2007)

#### Invited Talks

"High Latitude Magnetospheric Boundaries Cluster Observations" **University of Massachusetts Lowell/CAR Weekly Seminar Series**, Nov., 2006

"Structure and Dynamics of High Latitude Magnetospheric Boundaries"

**Peking University**, Beijing, P. R. China, Weekly Seminar Series, May, 2005

"Structure and Dynamics of High Latitude Magnetospheric Boundaries"

**NASA Goddard Space Flight Center**, Weekly Seminar Series, Apr., 2007

### **Fundamental Skills**

- Scientific background: Physics, Mathematics, Astronomy, Space Physics, Computer Science
- Programming Languages: C, Fortran77, IDL, Matlab, Maple, L<sup>A</sup>T<sub>E</sub>X
- Languages: English, Chinese

### **Publications**

#### Refereed Journal Articles

**H. Zhang**, T. A. Fritz, Q.-G. Zong, and P. W. Daly, Stagnant exterior cusp region as viewed by energetic electrons and ions: A statistical study using Cluster Research with Adaptive Particle Imaging Detectors (RAPID) data, *J. Geophys. Res.*, 110, A05211, doi:10.1029/2004JA010562, 2005.

**H. Zhang**, T. A. Fritz, Q. -G. Zong, M. W. Dunlop and P. W. Daly, The high latitude boundaries under extreme solar wind conditions: a Cluster perspective, pp163-172, *Advances in Geosciences*, Vol.2 - Solar Terrestrial (ST), 2006.

**H. Zhang**, M. W. Dunlop, Q. -G. Zong, T. A. Fritz, A. Balogh and Y. Wang, Geometry

of the high-latitude magnetopause as observed by Cluster, *J. Geophys. Res.*, 112, A02204, doi:10.1029/2006JA011774, 2007.

**H. Zhang**, Q.-G. Zong, T. A. Fritz, S. Y. Fu, S. Schaefer, K.-H. Glassmeier, P. W. Daly, H. Reme and A. Balogh, Cluster observations of collisionless Hall reconnection at high-latitude magnetopause, *J. Geophys. Res.*, 2007JA012769, 2007, in press.

Q.-G. Zong, T. A. Fritz, **H. Zhang**, A. Korth, P. W. Daly, M. W. Dunlop, K.-H. Glassmeier, H. Reme, and A. Balogh, Triple cusps observed by Cluster-Temporal or spatial effect?, *Geophys. Res. Lett.*, 31, doi:10.1029/2003GL019128, 2004.

Q.-G. Zong, T. A. Fritz, Z. Y. Pu, S. Y. Fu, D. N. Baker, **H. Zhang**, A. T. Lui, I. Vogiatzis, K.-H. Glassmeier, A. Korth, P. W. Daly, A. Balogh, and H. Reme, Cluster observations of earthward flowing plasmoid in the tail, *Geophys. Res. Lett.*, 31, doi:10.1029/2004GL020692, 2004.

Q.-G. Zong, T. A. Fritz, H. Spence, **H. Zhang**, Z. Y. Huang, Z. Y. Pu, K.-H. Glassmeier, A. Korth, P. W. Daly, A. Balogh, and H. Reme, Plasmoid in the high latitude boundary/cusp region observed by Cluster, *Geophys. Res. Lett.*, 32, doi:10.1029/2004GL020960, 2005.

Q. Q. Shi, Z. Y. Pu, **H. Zhang**, S. Y. Fu, C. J. Xiao, Q.-G. Zong, T. A. Fritz and Z. X. Liu, Simulation studies of high-latitude magnetospheric boundary dynamics, *Surveys in Geophysics*, 26, 369-386, DOI 10.1007/s10712-005-1900-6, 2005.

Q. Q. Shi, C. Shen, Z. Y. Pu, M. W. Dunlop, Q.-G. Zong, **H. Zhang**, C. J. Xiao, Z. X. Liu, and A. Balogh, Dimensional analysis of observed structures using multipoint magnetic field measurements: Application to Cluster, *Geophys. Res. Lett.*, 32, doi:10.1029/2005GL022454, 2005

Y. L. Wang, R. C. Elphic, B. Lavraud, M.G.G.T. Taylor, J. Birn, J. Raeder, C.T. Russell, H. Kawano, Q.-G. Zong, **H. Zhang**, X. X. Zhang and R. H. Friedel, Initial results of high-latitude magnetopause and low-latitude flank Flux transfer events from three years of Cluster observations, *J. Geophys. Res.*, 110, A11221, doi:10.1029/2005JA011150, 2005.

Q.-G. Zong, **H. Zhang**, T. A. Fritz, M. L. Goldstein, S. Wing, W. Keith, J. D. Winningham, R. Frahm, M. W. Dunlop, A. Korth, P. W. Daly, H. Reme, A. Balogh and A. N. Fazakerley, Multiple Cusps During an Extended Northward IMF Period With a Significant  $B_y$  Component, *J. Geophys. Res.*, 2007, in press.

#### **Selected Oral Presentations**

**Zhang, H.**, Q.-G. Zong, T. A. Fritz, S. Y. Fu, S. Schaefer, K. H. Glassmeier, P. W. Daly, H. Reme, A. Balogh, "Cluster Observations of Collisionless Hall Reconnection at High-Latitude Magnetopause" contributed talk at AOGS 2007 4th Annual Meeting, Bangkok, 30 July-4 August 2007, Abstract ST06-10-A0005.

**Zhang, H.**, "Structure and Dynamics of High Latitude Magnetospheric Boundaries" **Invited** talk at **NASA Goddard Space Flight Center** Weekly Seminar Series, Apr., 2007.

**Zhang, H.**, T. A. Fritz, Q.-G. Zong, H. Reme, A. Balogh, "High latitude plasmoids observed on the dayside by Cluster", contributed talk at 2006 Fall AGU meeting, San Francisco, 11-15 December 2006, Abstract SM44B-08.

**Zhang, H.**, "High Latitude Magnetospheric Boundaries: Cluster Observations" **Invited**

talk at **University of Massachusetts Lowell**/CAR Weekly Seminar Series, Nov., 2006  
**Zhang, H.**, T. A. Fritz, Q.-G. Zong, S. Y. Fu, M. G. G. T. Taylor, S. Schaefer, K. H. Glassmeier, P. W. Daly, H. Reme, A. Balogh, "High Latitude Magnetopause Current Sheet During Northward IMF Condition" contributed talk at 2006 Joint Assembly, Baltimore, 23-26 May 2006, Abstract SM21A-06.

**Zhang, H.**, T. A. Fritz, Q.-G. Zong, S. Y. Fu, M. G. G. T. Taylor, S. Schaefer, K. H. Glassmeier, P. W. Daly, H. Reme, A. Balogh, "High Latitude Magnetopause Current Sheet", contributed talk at 2005 Fall AGU meeting, San Francisco, 5-9 December 2005, Abstract SM23C-05.

**Zhang, H.**, "The magnetospheric cusp" GEM student Tutorial Talk, Santa Fe, July, 2005

**Zhang, H.**, T. A. Fritz, Q.-G. Zong, P. W. Daly, A. Balogh, "Dayside Boundary Layer under Extreme Solar Wind Conditions: A Cluster Perspective", contributed talk at Asia Oceania Geosciences Society 2nd annual meeting, Singapore, 20-24 June 2005, Abstract ST11/1A-02-4.

**Zhang, H.**, "Structure and Dynamics of High Latitude Magnetospheric Boundaries" **Invited talk at Peking University**, Beijing, P. R. China, Weekly Seminar Series, May, 2005

#### **Selected Poster Presentations**

**Zhang, H.**, Q.-G. Zong, T. A. Fritz, S. Y. Fu, M. G. G. T. Taylor, S. Schaefer, K. H. Glassmeier, P. W. Daly, H. Reme, A. Balogh, "High latitude magnetopause current sheet during an IMF By dominated period" COSPA meeting and 2006 Western Pacific Geophysics Meeting, Beijing, 17-27 July 2006

**Zhang, H.**, T. A. Fritz, Q.-G. Zong, P. W. Daly, Dayside boundary layer under northward IMF: A Cluster perspective, San Francisco, 2004 AGU Fall meeting, 13-17 December, 2004, Abstract SM13B1218

**Zhang, H.**, T. A. Fritz, Q.-G. Zong, P. W. Daly, High latitude boundary observed by Cluster, 2004 Joint Assembly, Montreal, 17-21 May 2004, Abstract SM43C..04

**Zhang, H.**, T. A. Fritz, Q.-G. Zong, P. W. Daly, Cusp Region as Viewed by Energetic Electrons and Ions: A Statistical Study Using Cluster Rapid Data, 2003 Fall Meeting, San Francisco, 8-12 December 2003, Abstract SM12A1197

**Zhang, H.**, T. A. Fritz, Q.-G. Zong, P. W. Daly, Cusp Region as Viewed by Energetic Electrons and Ions: A Statistical Study Using Cluster Rapid Data, 2002 Fall Meeting, San Francisco, 6-10 December 2002, Abstract SM62A0502